Search for New Physics at the future Lepton Colliders

Sahabub Jahedi

A thesis
submitted for the degree of

Doctor of Philosophy

Supervisor
Dr. Subhaditya Bhattacharya

Department of Physics
Indian Institute of Technology Guwahati
Guwahati - 781039, Assam, India

Search for New Physics at the future Lepton Colliders

A thesis submitted by

Sahabub Jahedi

to

Indian Institute of Technology Guwahati
in partial fulfillment of the requirements
for the award of the degree of
Doctor of Philosophy in Physics

Supervisor

Dr. Subhaditya Bhattacharya

Department of Physics
Indian Institute of Technology Guwahati
Guwahati - 781039, Assam, India

To
my
Grandmother

> "If you want to master something, teach it.
> The more you teach, the better you learn.
> Teaching is a powerful tool to learning."
>
> **-Richard P. Feynman**

Declaration

Sahabub Jahedi
Roll No. 186121021
Department of Physics
Indian Institute of Technology, Guwahati
Guwahati, India
E-mail: sahabub@iitg.ac.in

I hereby declare that works presented in the thesis entitled “**Search for New Physics at the future Lepton Colliders**” has been carried out by me under the supervision of Dr. Subhaditya Bhattacharya at the Department of Physics, Indian Institute of Technology Guwahati, India. The thesis has not been submitted anywhere else for any degree. Works presented in the thesis are all my own unless referenced to the contrary in the thesis.

Sahabub Jahedi

Date: 23/04/2024 **Sahabub Jahedi**

Certificate

Dr. Subhaditya Bhattacharya
Associate Professor
Department of Physics
Indian Institute of Technology, Guwahati
Guwahati, India
E-mail: subhab@iitg.ac.in

It is certified that the work contained in the thesis entitled "**Search for New Physics at the future Lepton Colliders**" by Mr. Sahabub Jahedi (Roll No - 186121021), a Ph.D. student in the Department of Physics, Indian Institute of Technology, Guwahati is carried out under my supervision and has not been submitted elsewhere for the award of any other degree.

Subhaditya Bhattacharya.

Date: 23/04/2024

Subhaditya Bhattacharya

Acknowledgements

First and foremost, I would like to convey my sincere gratitude toward my supervisor Dr. Subhaditya Bhattacharya for his constant support, guidance, and advice throughout my Ph.D. journey. I am truly privileged to have him as my supervisor, as he has not only assisted me academically but also consistently kept me motivated, especially during challenging times. His suggestions on becoming a proficient speaker have always aided me in refining my presentation skills. I genuinely appreciate his understanding and patience in accommodating my limitations. With him, it has indeed been a profoundly enriching learning experience for me.

I am indebted to Prof. Jose Wudka for his insightful guidance throughout my PhD journey. His expertise has been invaluable in shaping my research and academic growth.

I am grateful to my doctoral committee members Prof. Poulose, Dr. Sovan Chakraborty, and Dr. Meduri C. Kumar, for their valuable comments and suggestions during the yearly evaluation of my research work. I appreciate all HEP Journal Club members for keeping me informed about the latest trends in high-energy physics.

I thank all of my collaborators and co-authors: Dr. Basabendu Barman, Dr. Sudhakantha Girmohanta, Dr. Jayita Lahiri, Dr. Soumitra Nandi, Abhik Sarkar, and Prof. Jose Wudka for providing me with opportunities to engage in diverse problem-solving abilities. Through these experiences, I have gained extensive knowledge and valuable expertise. Special acknowledgment to Prof. Alexander S. Belyaev and Prof. Alexander Pukhov for assistance via the CalcHEP launchpad. Thanks to Dr. Sunando Patra for guiding my early statistical analysis learning. I thank Prof. Sudhir Vempati's small visit arrangement at IISc Bangalore. My thanks go to Dr. Biswajit Karmakar and Prof. Janusz Gluza for all the arrangements during my stay in Ustron, Poland, for MTTD 23.

I would like to thank my seniors: Dr. Purusottam Ghosh, Dr. Dibyendu Nanda, Dr. Kajol Samanta, Dr. Lopamudra Mukherjee, Dr. Sayandeep Ghosh, Dr. Surojit Dalui, Dr. Arghyajit Datta, Dr. Madhurima Chakraborty, Dr. Ipsita Ray, Dr. Pritam Das, Dr. Devabrat Mahanta, Dr. Riajul Haque, Dr. Subhajit Barman, Dr. Shilpi Roy, Rajesh Karmakar and others for engaging in both academic and non-academic discussions. As an integral part of my doctoral expedition, I am thankful to Suruj, Prantik, Sumit, Golam, Tarik, Mrinal, Danny, Debabrata, Mandira, Dipankar, Lipika, Soumen, Swarup, Abhik, Niloy, Nayan and others. Their presence has turned my time at IITG into a delightful and unforgettable experience. I acknowledge the efforts of hostel mess workers and cleaning staff for making my life comfortable. Engaging in weekend football matches at IITG has been one of the highlights of my PhD endeavor. I express my gratitude to all the players from various departments who joined me in the joy of playing football. I thank Abhishek, Shubhajit, Ankur, Abhijit, Sudipta, Rouf, Arnob, Asif, and other close friends for their consistent support. I especially thank Gargi, my constant companion, for standing with me through highs and lows and teaching me to value the little things. Cheers to all!

Finally, I wish to express my deepest gratitude to my parents and my sister for their enduring love, invaluable support, and unwavering understanding that have been pillars of strength throughout my life.

Acronyms

SM	: Standard Model
EW	: Electroweak
EWSB	: Electroweak Symmetry Breaking
SSB	: Spontaneous Symmetry Breaking
VEV	: Vacuum Expectation Value
QCD	: Quantum Chromodynamics
BSM	: Beyond Standard Model
NP	: New Physics
BBN	: Big Bang nucleosynthesis
CMB	: Cosmic Microwave Background
DM	: Dark Matter
WIMP	: Weakly Interacting Massive Particles
FIMP	: Feebly Interacting Massive Particles
SIMP	: Strongly Interacting Massive Particles
CERN	: European Organization for Nuclear Research
LHC	: Large Hadron Collider
HL-LHC	: High Luminosity Large Hadron Collider
SLAC	: Stanford Linear Accelerator Center
PETRA	: Positron Electron Tandem Ring Accelerator
CDF	: Collider Detector at Fermilab
SPS	: Super Proton Synchrotron
ISRs	: The Intersecting Storage Rings
ILC	: International Linear Collider
CLIC	: Compact Linear Collider
CEPC	: Circular Electron Positron Collider

FCC	Future Circular Collider
OOT	Optimal Observable Technique
ML	Maximum Likelihood
C.L.	Confidence Level
RGE	Renormalization Group Evolution
BR	Branching Ratio
H.c.	Hermitian Conjugate
d.o.f	Degrees of freedom
UFO	Universal FeynRule Output
LFV	Lepton Flavour Violation
MeV	Mega electron Volt
GeV	Giga electron Volt
TeV	Tera electron Volt
CM	Center of Mass
UV	Ultraviolet
ISR	Initial State Radiation
FSR	Final State Radiation
NLO	Next Leading Order
LG	Loop-Generated
PTG	Potentially-Tree-Generated
GIM	Glashow-Iliopoulos-Maiani
EFT	Effective Field Theory
SMEFT	Standard Model Effective Field Theory
HEFT	Higgs Effective Field Theory
ChPT	Chiral Perturbation Theory
HQET	Heavy Quark Effective Theory
SCET	Soft Collinear Effective Theory
FC	Flavor Changing
FCNC	Flavour Changing Neutral Current
FCCC	Flavour Changing Charge Current
nTGCs	Neutral triple gauge couplings
ALPs	Axion Like Particles
PDG	Particle Data Group
FLAG	Flavour Averaging Lattice Group
VVF	Vector boson fusion

Abstract

The Standard Model (SM) of particle physics has effectively explained the forces of nature namely strong, weak, and electromagnetic, demonstrating its reliability through consistent agreement with experimental findings so far. After the discovery of Higgs boson at the Large Hadron Collider (LHC), the particle spectrum of the SM is complete. Yet, there are different theoretical and experimental reasons compelling us to explore beyond the SM (BSM). Statistical analysis plays a crucial role to look for several BSM scenarios in both model-dependent and model-independent ways in different collider experiments. In Chapter 1, we discuss the particle spectrum of the SM and mass generation of gauge bosons via spontaneous symmetry breaking (SSB). Our discussion extends to the limitations of the SM, where we explore both model-dependent and model-independent approaches to address these challenges. After that, we provide a concise overview of the outlook for past, present, and future colliders and outline the physics issues tackled by the future lepton colliders. Chapter 2 encompasses a detailed study of two distinct statistical techniques: binned analysis and the optimal observable technique (OOT). Chapter 3 elaborates the example of OOT in the case of BSM dominated scenario. In this chapter, we study the optimal estimation of Z couplings (vector, chiral, and pure axial-vector) with heavy charged fermions at the e^+e^- collider. Dark matter (DM) phenomenology and collider analysis of a UV complete model that contains these heavy charge fermions are discussed. Moving forward to Chapter 4, we shift our focus to scenarios where the SM dominates in the context of OOT. In this scenario, we investigate the optimal determination of anomalous neutral triple gauge couplings (nTGCs) via di-boson productions at the e^+e^- colliders using the dimension-8 Standard Model effective field theory (SMEFT) framework. In another case, we estimate the optimal uncertainty of scalar and tensor-mediated dimension-6 effective couplings through top-quark pair production at the e^+e^- collider. UV completion of dim-6 scalar mediated SMEFT operator is studied. The optimal uncertainty of new physics (NP) couplings in that UV complete model (2-Higgs doublet model) is also discussed. A comparison of optimal sensitivity with the binned sensitivity is drawn. In Chapter 5, we determine the experimental constraint on dimension-6 four-Fermi SMEFT operators from flavour and top-quark observables. We then explore the flavour probe of these SMEFT operators through flavour-changing tc production at the muon collider. A comparison of flavour uncertainty with optimal uncertainty for dimension-6 effective couplings is also discussed. In Chapter 6, our focus turns to the study of optimal sensitivity of NP couplings in the presence of non-interfering SM background with a generic numerical technique. Finally, in Chapter 7, we present a summary of the thesis and briefly outline potential future directions.

List of publications/preprints included in this thesis

1. Probing heavy charged fermions at the e^+e^- colliders using the optimal observable technique,
   Author(s): Subhaditya Bhattacharya, **Sahabub Jahedi** (IIT Guwahati), and Jose Wudka (UC Riverside, California),
   *e*print: arXiv: 2106.02846 (hep-ph),
   Published in **JHEP 05 (2022) 009**.

2. Probing anomalous $ZZ\gamma$ and $Z\gamma\gamma$ couplings at the e^+e^- colliders using optimal observable technique,
   Author(s): **Sahabub Jahedi** and Jayita Lahiri (University of Hamburg),
   *e*print: arXiv: 2212.05121 (hep-ph),
   Published in **JHEP 04 (2023) 085**.

3. Optimal determination of new physics couplings: a comparative study,
   Author(s): Subhaditya Bhattacharya, **Sahabub Jahedi** (IIT Guwahati), Jose Wudka (UC Riverside, California),
   *e*print: arXiv: 2301.07721 (hep-ph),
   Published in **JHEP 12 (2023) 026**.

4. Optimal estimation of dimension-8 neutral triple gauge couplings at the e^+e^- colliders,
   Author(s): **Sahabub Jahedi** (IIT, Guwahati),
   *e*print: arXiv: 2305.11266 (hep-ph),
   Published in **JHEP 12 (2023) 031**.

5. Optimal New Physics estimation in presence of Standard Model backgrounds,
   Author(s): Subhaditya Bhattacharya, **Sahabub Jahedi** (IIT, Guwahati), Jayita Lahiri (University of Hamburg), and Jose Wudka (UC Riverside, California),
   *e*print: arXiv: 2312.12514 (hep-ph).

6. Probing flavour constrained SMEFT operators through tc production at the Muon collider,
   Author(s): Subhaditya Bhattacharya, **Sahabub Jahedi**, Soumitra Nandi, and Abhik Sarkar (IIT, Guwahati),
   *e*print: arXiv: 2312.14872 (hep-ph).

Publication not included in this thesis

7. Effective Leptophilic WIMPs at the e^+e^- collider,
   Author(s): Basabendu Barman (SRM University, Amaravati), Subhaditya Bhattacharya (IIT, Guwahati), Sudhakantha Girmohanta (Tsung-Dao Lee Institute, Shanghai), and **Sahabub Jahedi** (IIT, Guwahati),
   *e*print: arXiv: 2109.10936 (hep-ph),
   Published in **JHEP 04 (2022) 146**.

Permissions and Attributions

- The content of the Chapter 3 is based on following work
  (a) **JHEP 05 (2022) 009**, in collaboration with Subhaditya Bhattacharya and Jose Wudka.
- The content of the Chapter 4 is based on following works
  (a) **JHEP 04 (2023) 085**, in collaboration with Jayita Lahiri.
  (b) **JHEP 12 (2023) 026**, in collaboration with Subhaditya Bhattacharya and Jose Wudka.
  (c) **JHEP 12 (2023) 031**.
- The content of the Chapter 5 is based on following work
  (a) **arXiv:2312.14872**, in collaboration with Subhaditya Bhattacharya, Soumitra nandi, and Abhik Sarkar.
- The content of the Chapter 6 is based on following work
  (a) **arXiv:2312.12514**, in collaboration with Subhaditya Bhattacharya, Jaiyta Lahiri, and Jose Wudka.

Contents

Chapter 1

Introduction

Contents

1.1 Standard Model of particle physics

Over the past century, exceptional experimental efforts and profound theoretical developments together have uncovered the fundamental structure of our universe to a great extent. The outcome of these efforts is the very construct of the Standard Model (SM) of particle physics, a framework elucidating the characteristics of elementary particles and their interactions via weak, strong, and electromagnetic forces. The predictions of SM has been confirmed quite accurately by experiments like Stanford Linear Accelerator Centre (SLAC), Tevatron, Large Electron-positron Collider (LEP), Large Hadron Collider (LHC), thus bolstering its credibility and correctness. The journey has been fascinating to say the least, but in this thesis we will provide a short account of this model, which is central to develop the ideas exploited further.

1.1.1 The basic construct

The particle spectrum of the SM consists of spin-1/2 matter particles with six flavours of quarks (up, down, charm, strange, top, and bottom) and three flavours of charged leptons (electron, muon, and tau) and three flavours of neutrinos. Neutrinos possess no electric charge and very tiny mass. The interactions between quarks and leptons are mediated by spin-1 gauge bosons. The strong interaction is mediated by Gluons (G), massless, and electromagnetic charge neutral. Massive gauge bosons $W^{\pm}$ and Z take the role of mediating weak interaction whereas electromagnetic interaction is carried by massless photon (A). The only scalar particle in the SM is the Higgs boson and is responsible for providing mass to all the massive particles. The complete spectrum of the SM is shown in Fig. 1.1. SM is a renormalizable quan-

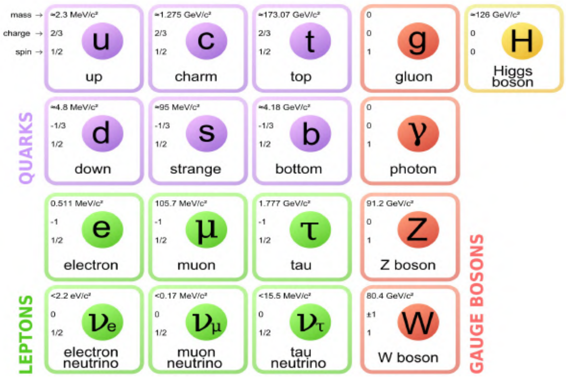

Figure 1.1: The particle spectrum of the SM. Source: quantumdiaries.org.

tum field theory based upon the gauge group $SU(3)_C \times SU(2)_L \times U(1)_Y$, where the gauge symmetry dictates the characteristics of different interactions. Strong interaction arises out of $SU(3)_C$ symmetry, where C represents color quantum numbers. $SU(2)_L \times U(1)_Y$ gauge group describes the framework for weak and electromagnetic interactions together, which is often called electroweak interactions. L represents (left) handedness or chirality, while Y represents hypercharge. Our thesis will mainly focus on the electroweak sector of SM and extensions of similar kind. The electroweak Lagrangian respecting $SU(2)_L \times U(1)_Y$ symmetry and Lorentz invariance can be written as

$$\mathcal{L}_{EW} = \mathcal{L}_{gauge} + \mathcal{L}^{f}_{int}\,, \tag{1.1}$$

where

$$\mathcal{L}_{gauge} = -\frac{1}{4}W^a_{\mu\nu}W^{\mu\nu,a} - \frac{1}{4}B_{\mu\nu}B^{\mu\nu} \quad \text{and} \quad \mathcal{L}^{f}_{int} = i\bar{\psi}\gamma^\mu D_\mu \psi. \tag{1.2}$$

Here $B_{\mu\nu}$ and $W^a_{\mu\nu}$ are the $U(1)$ and $SU(2)$ field strength tensors, given by

$$\begin{aligned} B_{\mu\nu} &= \partial_\mu B_\nu - \partial_\nu B_\mu, \\ W^a_{\mu\nu} &= \left(\partial_\mu W^a_\nu - \partial_\nu W^a_\mu - g\epsilon_{abc}W^b_\mu W^c_\nu\right), \end{aligned} \tag{1.3}$$

where g is the $SU(2)_L$ coupling constant and ϵ_{abc} are completely antisymmetric tensors, representing the structure constant associated with the $SU(2)_L$ group algebra. W^a_μ $(a = 1, 2, 3)$ and B_μ are the gauge fields associated with $SU(2)_L$ and $U(1)_Y$ groups respectively. $\mathcal{L}^f_{int}$ possesses the kinetic and interaction terms of the fermions (ψ), where D_μ represents the gauge covariant derivative defined as

$$D_\mu = \partial_\mu - ig\frac{\sigma^a}{2}W^a_\mu - ig^{'}\frac{Y}{2}B_\mu, \tag{1.4}$$

where g' denotes the $U(1)_Y$ coupling constant and Y is the hypercharge, σ^a's ($a = 1, 2, 3$) represent Pauli matrices. The left (ψ_L) and right-handed (ψ_R) components of Dirac fermions (ψ) are defined by

$$\psi_{L(R)} = \frac{1-(+)\gamma 5}{2} = P_{L(R)}\psi. \tag{1.5}$$

ψ_L and ψ_R transform differently under $SU(2)_L$ transformations, which is the key source of parity violation in weak interactions. The left handed parts form a doublet, while the right handed parts form singlet under $SU(2)_R$ as shown below (for all three families),

$$\begin{aligned} \text{Quarks}: \ Q_L &= \begin{pmatrix} q^u_L \\ q^d_L \end{pmatrix}, \quad q^u_R, q^d_R; \quad (q^u : u, c, t; \ q^d : d, s, b); \\ \text{Leptons}: \ L_L &= \begin{pmatrix} \nu_{\ell L} \\ \ell_L \end{pmatrix}, \quad \ell_R; \quad (\ell : e, \mu, \tau)\,. \end{aligned} \tag{1.6}$$

Both leptons and quarks take part in the electroweak interactions (no right handed neutrino ν_R in SM however). The other part of SM is governed by QCD Lagrangian, dictated by $SU(3)_C$ gauge group as

$$\mathcal{L}_{QCD} = -\frac{1}{4} G^a_{\mu\nu} G^{\mu\nu,a} + g_S \sum_{i=u,d,c,s,t,b} \bar{q}_i \gamma^\mu t^a q_i G^a_\mu \,, \tag{1.7}$$

where g_s represents strong coupling constant and t^a's are the $SU(3)_C$ group generators with color index a running from 1 to 8. G^a_μ is the gluon field and $G^a_{\mu\nu}$ represents $SU(3)_C$ field strength tensor

$$G^a_{\mu\nu} = \left(\partial_\mu G^a_\nu - \partial_\nu G^a_\mu - g_s f_{abc} G^b_\mu G^c_\nu\right), \tag{1.8}$$

where f_{abc} are the $SU(3)_C$ group structure constants. Only quarks (having three colour charges) take part in the strong interaction. All the terms in the Lagrangian mentioned above respect SM gauge symmetry and no mass term is allowed for either fermions or for gauge bosons. The breaking of SM gauge symmetry is necessary for mass generation of fermions and gauge bosons. This is achieved via spontaneous symmetry breaking (SSB) mechanism discussed next.

1.1.2 Spontaneous Symmetry Breaking (SSB)

The basic idea of spontaneous symmetry breaking is that while the Lagrangian remains invariant under the SM gauge group, a scalar field having interaction with the SM fields acquires a non-zero vacuum expectation value (VEV) at the minimum of the scalar potential and thus breaks the gauge symmetry. This in turn generates the masses for the SM particles. This can be accomplished by introducing a complex scalar $SU(2)_L$ doublet with hypercharge $Y_\phi = 1$ as

$$\Phi = \begin{pmatrix} \phi^+ \\ \phi^0 \end{pmatrix} = \frac{1}{\sqrt{2}} \begin{pmatrix} \phi_1 + i\phi_2 \\ \phi_3 + i\phi_4 \end{pmatrix}. \tag{1.9}$$

The Lagrangian of Φ is written as

$$\mathcal{L}_{scalar} = (D_\mu \Phi)^\dagger (D_\mu \Phi) - V(\Phi^\dagger, \Phi)\,, \tag{1.10}$$

where

$$D_\mu \Phi = (\partial_\mu - ig\frac{\sigma^a}{2} W^a_\mu - ig'\frac{Y}{2} B_\mu)\Phi\,, \ \ V(\Phi^\dagger, \Phi) = -\mu^2 \Phi^\dagger \Phi + \lambda (\Phi^\dagger \Phi)^2. \tag{1.11}$$

When $\mu^2 < 0$ and $\lambda > 0$, the minima of the potential is located at zero, whereas for $\mu^2 > 0$ and $\lambda > 0$, the degenerate minima of this potential occurs at

$$\Phi^\dagger \Phi = \frac{1}{2}(\phi_1^2 + \phi_2^2 + \phi_3^2 + \phi_4^2) = \frac{v^2}{2}; \quad v = \sqrt{\frac{\mu^2}{\lambda}}. \tag{1.12}$$

We can select the VEV of Φ to be both real and aligned along the direction of electrically neutral component ϕ_3. This choice effectively leads to $\phi_1 = \phi_2 = \phi_4 = 0$ and $\phi_3 = v$, so that the scalar doublet can be written as

$$\Phi = \frac{1}{\sqrt{2}} \begin{pmatrix} 0 \\ v + h(x) \end{pmatrix} , \tag{1.13}$$

resulting in the spontaneous breaking of the $SU(2)_L \times U(1)_Y$ symmetry. One can write Eq. (1.9) as

$$\Phi = e^{i\boldsymbol{\tau}.\boldsymbol{\theta}(\boldsymbol{x})/v} \begin{pmatrix} 0 \\ \frac{v+h(x)}{2} \end{pmatrix} , \tag{1.14}$$

where $(\phi_1, \phi_2, \phi_3, \phi_4)$ are replaced by $(\theta_2, \theta_1, v + h(x), -\theta_3)$. Leveraging the $SU(2)_L$ invariance of $\mathcal{L}_{scalar}$, we can eliminate the three massless Goldstone boson fields, denoted as θ_i (where i = 1, 2, 3), through the following transformation

$$\Phi = e^{-i\boldsymbol{\tau}.\boldsymbol{\theta}(\boldsymbol{x})/v}\Phi. \tag{1.15}$$

These degrees of freedom (d.o.f) will subsequently manifest themselves as the longitudinal d.o.f of the gauge bosons stemming from the broken $SU(2)_L$ group. Following the execution of a rotation, the physical gauge bosons are expressed as

$$\begin{pmatrix} Z_\mu \\ A_\mu \end{pmatrix} = \begin{pmatrix} c_w & -s_w \\ s_w & c_w \end{pmatrix} \begin{pmatrix} W_\mu^3 \\ B_\mu \end{pmatrix} ; \qquad W_\mu^\pm = \frac{1}{2}(W_\mu^1 \mp iW_\mu^2), \tag{1.16}$$

where s_w (c_w) is the sine (cosine) of the weak mixing angle θ_w defined as

$$\theta_w = \tan^{-1}\left(\frac{g_1}{g_2}\right). \tag{1.17}$$

Putting Eq. (1.14) in the first term of $\mathcal{L}_{scalar}$ the masses of gauge bosons are obtained as

$$M_{W^\pm} = \frac{1}{2}gv, \quad M_Z = \frac{1}{2}v\sqrt{(g^2 + g'^2)}, \quad M_A = 0. \tag{1.18}$$

The gauge fields $(W^\pm, Z)$ have acquired mass as if by 'eating up' the Goldstone modes. This is loosely referred as the *Higgs mechanism* [1–5]. The photon (γ) remains massless, so are the Gluons. This is an artefact of the SSB, $SU(3)_C \times SU(2)_L \times U(1)_Y \xrightarrow{SSB} SU(3)_C \times U(1)_{em}$, leaving electromagnetic and colour symmetry intact.

Let us now turn to the generation of charged fermion masses. The Yukawa Lagrangian involving the interactions between the Higgs doublet with leptons and quarks is written as

$$\mathcal{L}_Y = -y^\ell \bar{\ell_L} \Phi e_R - y^u \bar{q_L} \tilde{\Phi} u_R - y^d \bar{q_L} \Phi d_R + H.c., \tag{1.19}$$

where ℓ_L (e_R) is the left (right)-handed lepton doublet (singlet), q_L is the left-handed quark doublet and u_R (d_R) is the up (down) type right-handed quark singlet. y^i's (i=ℓ, u, d) are the Yukawa couplings associated with different charged fermions. $\tilde{\Phi}$ is conjugate of Φ which is defined as $\tilde{\Phi} = i\sigma_2\Phi$ with σ_2 denoting Pauli matrix. When Higgs acquires a VEV (v) after SSB, charged fermions get the masses, and the mass terms are written as

$$m_\ell = \frac{y^\ell v}{\sqrt{2}}, \quad m_u = \frac{y^u v}{\sqrt{2}}, \quad m_d = \frac{y^d v}{\sqrt{2}}. \tag{1.20}$$

The hierarchy of fermion masses then indicates a large hierarchy in the Yukawa couplings. The properties of the Higgs boson discovered at the LHC largely mimic the Higgs boson of the SM as described here. However, we are yet to conclude that there exists no extension of the scalar sector. We will discuss them individually when we take up specific Higgs properties for study.

To conclude this section, the SM stands as a mathematically consistent theoretical framework based upon the principles of gauge symmetry and quantum field theory. Within this premise, the SM proficiently elucidates the interactions of elementary particles that have been unveiled through experimental explorations till date. Although the SM has achieved remarkable success, it falls short to account for various theoretical and experimental outcomes as we discuss next.

1.2 Limitations of the Standard Model

After the discovery of the Higgs boson at the LHC [6, 7], the ATLAS and CMS experiments have measured most of the Higgs properties with good precision. Despite the compelling agreement of the SM with experimental data, there exists both theoretical and experimental incentives to explore physics beyond the Standard Model (BSM). We highlight a few key issues here.

1.2.1 Hierarchy Problem

Due to the absence of symmetry principles, the mass of the Higgs boson undergoes significant modifications due to radiative corrections along with its tree-level value. Experimentally observed Higgs boson mass (M_H) in terms of the bare mass term (M_H^0) and 1-loop radiative correction (δM_H) can be expressed as $M_H^2 = {M_H^0}^2 + \delta M_H^2$, the radiative correction exhibits quadratic sensitivity to the cutoff scale, Λ. The dominant contribution to 1-loop correction arises from top-quark, W, Z, and Higgs itself. The loop correction of the Higgs mass is expressed as [8]

$$\delta M_H^2 = \frac{3g^2\Lambda^2}{32\pi^2 M_W^2}(M_H^2 + 2M_W^2 + M_Z^2 - 4M_t^2). \tag{1.21}$$

In principle, Λ can go up to the Planck scale ($M_P \sim 10^{19}$ GeV), where the quantum theory of gravity should arise. The quadratically divergent loop corrections to the Higgs mass have the potential to push its mass to extremely high values. This issue essentially stems from the hierarchy between the EW scale and the scale of gravity, so it is called hierarchy problem. However, as SM is a renormalizable theory, there will be a counterterm to cancel this divergence and provide a finite Higgs mass at the observed value (*e.g.* 125 GeV). But unmistakably this constitutes a fine-tuning of the theory's parameters to have the cancellation of terms several orders of magnitude larger than the measured one. Given that the Higgs mass term establishes the scale for all other particles within the SM, any adjustment to the Higgs mass essentially entails fine-tuning of the entire spectrum of SM particles. Thus hierarchy problem is also known as the *fine-tuning problem*.

1.2.2 Presence of a Dark Matter

Cosmic Microwave Background (CMB) observations lead to an estimated present energy density (ρ_0) that closely matches its critical value ($\rho_{\texttt{crit}}$):

$$\rho_0 = \rho_{\texttt{crit}} = \frac{3H_0^2}{8\pi G_N} \sim 10^{-29}\ \mathrm{g/cm}^3, \tag{1.22}$$

with $H_0 = 70$ km/s/Mpc is the Hubble constant and $G_N = 6.67 \times 10^{-11}\ \mathrm{Nm}^2/\mathrm{kg}^2$ indicates the Newton's gravitational constant. Fitting the CMB anisotropies to the ΛCDM model, one finds an amazing result. The total energy density comprises of roughly 70% Dark Energy (DE), 26% Dark Matter (DM), and (only) 4% ordinary (baryonic) matter. This raises the question what are DM and DE? Having a satisfactory answer for DE is not easy within the particle physics paradigm, but a huge amount of effort and energy has been devoted to particle DM explanation.

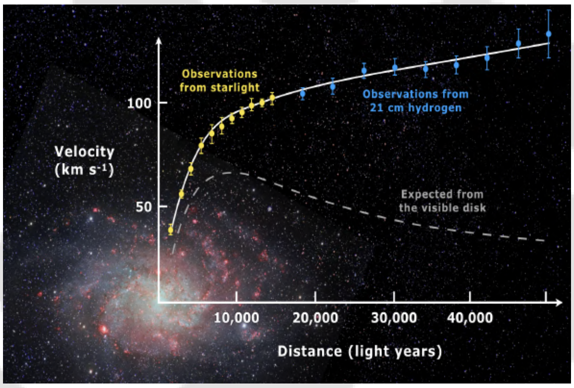

Figure 1.2: Galaxy rotation curve. Source: Wikipedia.

Different astrophysical phenomena like Galaxy rotation curve [9] (Fig. 1.2), gravitational lensing [10], structure formation [11], etc., provide concrete evidence of the existence of DM. When considering particle DM, a broad range of possible masses (eV to Plank mass) is available. Depending on the interactions between the visible sector and the dark sector particles, we classify several DM candidates. Weakly Interacting Massive Particles (WIMP) are one of the most popular candidates for DM having moderate interactions with the visible sector, which produces the observed relic density of DM [12, 13]

$$\Omega_{\mathrm{DM}} h^2 = 0.11933 \pm 0.00091\,, \tag{1.23}$$

where $\Omega = \rho/\rho_c$ denotes cosmological energy density parameter and h is the reduced Hubble constant. WIMP are assumed to be in thermal equilibrium with the visible sector particles in the early universe. When the DM interaction rate falls short of the Hubble expansion rate, then WIMP freeze out to provide present-day DM relic. Feebly Interacting Massive Particles (FIMP) are another potential DM candidates that remain out of thermal equilibrium due to their feeble interaction with the visible sector, but get produced through the decay and scattering of thermal bath particles to 'freeze in' when the temperature falls down DM mass. Strongly Interacting Massive Particles (SIMP) are another possibility characterized by strong interactions within the dark sector, which freezes out due to number-changing processes within the dark sector, but is constrained from the self-interaction limits. There are many other possibilities. In this thesis, we will touch upon some WIMP-like DM candidates and their discovery potential at colliders.

1.2.3 Neutrino mass

Observation of neutrino oscillations [14–16] suggests that at least two SM neutrinos must possess non-zero mass. It has also been established that neutrinos don't only possess non-zero mass but also exhibit mixing between different flavors, transitioning from one flavor to another over time[1]. This contradicts the fundamental assumption of the SM, which assumes the existence of only left-handed neutrinos without right-handed neutrinos. While it is conceivable to generate neutrino masses by introducing right-handed neutrinos and employing Yukawa couplings similar to those for up-type quarks, comprehending their minuteness relative to other fermions, one requires $Y_\nu \sim 10^{-10}$ in order to be consistent with the observed light neutrino mass and remains a puzzling issue. However, it is possible to generate such a mass term in a gauge invariant way from the dimension-5 Weinberg operator (we will briefly discuss effective operator frameworks in the next section)

$$\frac{Y_\nu}{\Lambda}(\bar{l}^c \tilde{H}^*)(\tilde{H}^\dagger l), \tag{1.24}$$

where Λ is some NP scale and small Majorana mass is obtained after SSB via

$$m_\nu = \frac{Y_\nu \langle H \rangle^2}{2\Lambda} = \frac{Y v^2}{2\Lambda}. \tag{1.25}$$

With $\Lambda \sim 10^{14}$ GeV one can generate correct neutrino mass without fine tuning. There are several 'NP' possibilities that can generate the dimension five operator; for example, type-I seesaw [17, 18] , type-II seesaw [19–21], type-III seesaw [22, 23] etc. We will have a brief sketch of such frameworks in the next section.

1.2.4 Matter anti-matter asymmetry

When we look around, we see only matter, and anti-matter is very rare which suggests that our universe is predominantly composed of matter compared to antimatter. Anti-matter, like anti-protons, is found mainly in cosmic rays and is about 10,000 times less than matter. We can also create anti-matter in collider experiments like LHC. Expressed as the ratio of baryon density to photon density, the asymmetry is quantified as $(n_b - n_{\bar{b}})/n_\gamma = (6.10 \pm 0.4) \times 10^{-10}$ following CMB [25] measurement and Big Bang Nucleosynthesis (BBN), where n_γ and $n_b(n_{\bar{b}})$ represent the present number densities of photon and baryon (anti-baryon), respectively. Inflation erases

---

[1] A concise overview of the most accurate estimate for neutrino oscillation parameters after performing global fit is shown in Table 1.1.

		Normal Ordering		Inverted Ordering	
		bfp $\pm 1\sigma$	3σ range	bfp $\pm 1\sigma$	3σ range
without SK atmospheric data	$\sin^2\theta_{12}$	$0.304^{+0.013}_{-0.012}$	$0.269 \to 0.343$	$0.304^{+0.013}_{-0.012}$	$0.269 \to 0.343$
	$\theta_{12}/^\circ$	$33.44^{+0.78}_{-0.75}$	$31.27 \to 35.86$	$33.45^{+0.78}_{-0.75}$	$31.27 \to 35.87$
	$\sin^2\theta_{23}$	$0.570^{+0.018}_{-0.024}$	$0.407 \to 0.618$	$0.575^{+0.017}_{-0.021}$	$0.411 \to 0.621$
	$\theta_{23}/^\circ$	$49.0^{+1.1}_{-1.4}$	$39.6 \to 51.8$	$49.3^{+1.0}_{-1.2}$	$39.9 \to 52.0$
	$\sin^2\theta_{13}$	$0.02221^{+0.00068}_{-0.00062}$	$0.02034 \to 0.02430$	$0.02240^{+0.00062}_{-0.00062}$	$0.02053 \to 0.02436$
	$\theta_{13}/^\circ$	$8.57^{+0.13}_{-0.12}$	$8.20 \to 8.97$	$8.61^{+0.12}_{-0.12}$	$8.24 \to 8.98$
	$\delta_{\rm CP}/^\circ$	195^{+51}_{-25}	$107 \to 403$	286^{+27}_{-32}	$192 \to 360$
	$\frac{\Delta m^2_{21}}{10^{-5}\ \mathrm{eV}^2}$	$7.42^{+0.21}_{-0.20}$	$6.82 \to 8.04$	$7.42^{+0.21}_{-0.20}$	$6.82 \to 8.04$
	$\frac{\Delta m^2_{3\ell}}{10^{-3}\ \mathrm{eV}^2}$	$+2.514^{+0.028}_{-0.027}$	$+2.431 \to +2.598$	$-2.497^{+0.028}_{-0.028}$	$-2.583 \to -2.412$

		Normal Ordering		Inverted Ordering	
		bfp $\pm 1\sigma$	3σ range	bfp $\pm 1\sigma$	3σ range
with SK atmospheric data	$\sin^2\theta_{12}$	$0.304^{+0.012}_{-0.012}$	$0.269 \to 0.343$	$0.304^{+0.013}_{-0.012}$	$0.269 \to 0.343$
	$\theta_{12}/^\circ$	$33.44^{+0.77}_{-0.74}$	$31.27 \to 35.86$	$33.45^{+0.78}_{-0.75}$	$31.27 \to 35.87$
	$\sin^2\theta_{23}$	$0.573^{+0.016}_{-0.020}$	$0.415 \to 0.616$	$0.575^{+0.016}_{-0.019}$	$0.419 \to 0.617$
	$\theta_{23}/^\circ$	$49.2^{+0.9}_{-1.2}$	$40.1 \to 51.7$	$49.3^{+0.9}_{-1.1}$	$40.3 \to 51.8$
	$\sin^2\theta_{13}$	$0.02219^{+0.00062}_{-0.00063}$	$0.02032 \to 0.02410$	$0.02238^{+0.00063}_{-0.00062}$	$0.02052 \to 0.02428$
	$\theta_{13}/^\circ$	$8.57^{+0.12}_{-0.12}$	$8.20 \to 8.93$	$8.60^{+0.12}_{-0.12}$	$8.24 \to 8.96$
	$\delta_{\rm CP}/^\circ$	197^{+27}_{-24}	$120 \to 369$	282^{+26}_{-30}	$193 \to 352$
	$\frac{\Delta m^2_{21}}{10^{-5}\ \mathrm{eV}^2}$	$7.42^{+0.21}_{-0.20}$	$6.82 \to 8.04$	$7.42^{+0.21}_{-0.20}$	$6.82 \to 8.04$
	$\frac{\Delta m^2_{3\ell}}{10^{-3}\ \mathrm{eV}^2}$	$+2.517^{+0.026}_{-0.028}$	$+2.435 \to +2.598$	$-2.498^{+0.028}_{-0.028}$	$-2.581 \to -2.414$

Table 1.1: Best fit values of different neutrino mass parameters from three-flavor oscillation. This global fit has been done by νFIT Collaboration [24].

most of the initial conditions, therefore, it prescribes that such asymmetry must be generated dynamically. The mechanism of generating matter-antimatter symmetry is called *baryogenesis* [26, 27] and follows Sakharov conditions [28]. A standard approach to achieve baryon asymmetry through *leptogenesis* [29, 30] where a non-zero lepton asymmetry is generated which can be later gets convert into baryon asymmetry via electroweak sphalerons [31].

1.2.5 Experimental Anomalies

Although most of the experimental outcomes have validated the SM with good precision, there are still some experimental results that show some deviation. For example, in the context of flavor physics, the anomalous magnetic moment of muon ($(g-2)_\mu$) shows 4.2σ deviation [32], $R(D^*)$ has been measured with a 2.2σ deviation [33, 34]. Recently, the LHC has measured Higgs decays to Z and a photon with 3.4σ deviation [35]. The CMS experiment has provided a hint of a new neutral scalar with a mass around 95 GeV at 2.8σ global significance [36].

In addition to the aforementioned issues, there are strong CP problem in the QCD sector [37, 38], gauge coupling unification [39–42], Higgs vacuum stability [43–45], etc. which can not be explained within the SM framework.

1.3 Examples of physics beyond the Standard Model

There exists a huge literature on BSM physics, addressing one or a few of the problems listed above. It is impossible and out of the scope of this thesis to have a systematic discussion on a majority of them. In the following, we will sketch a few UV complete scenarios that are referred later and we also discuss the SMEFT framework, which we use extensively.

1.3.1 UV complete BSM models

- Minimal supersymmetric standard model (MSSM): Supersymmetry is one of the most promising candidates for BSM physics. In this framework, new particles are called the superpartners of SM with spin differing by half a unit. The spin-$1/2$ quarks and leptons in supersymmetry have spin-0 scalar partners known as sfermions (squarks and sleptons), while the superpartners of spin-1 gauge bosons are spin-$1/2$ gauginos. In addition to the SM like Higgs doublet, an extra Higgs doublet is required to provide masses to the (s)fermions is supersymmetry. The superpartners of Higgses are called Higgsinos. The minimal and economic choice to extend the SM with supersymmetry is MSSM [46–48] that incorporates softly broken $N = 1$ global supersymmetry in SM. Supersymmetry provides a natural solution to the hierarchy problem, with cancellation between SM and superpartner's loop contribution to the Higgs mass. On top of that, it provides a suitable DM candidate as well. Null results for supersymmetry searches at the LHC have resulted in high mass limits for the superpartners.

- 2-Higgs doublet model (2HDM): Given that we are yet to decide upon the exact nature of the scalar boson discovered at the LHC, and to address the issue of vacuum stability, extension of the scalar sector of SM is widely studied. 2HDM is a simple extension of SM with an extra $SU(2)_L$ Higgs doublet (let's call it Φ_2) that contains three neutral Higgses along with a pair of charged Higgs bosons [49–52]. Depending on the interactions of the quarks and leptons with the scalar doublets, there are four types of possibilities:

  i) Type-I: All quarks and leptons couples only to the additional doublet (Φ_2) [53],

  ii) Type-II: Φ_1 couples to down-type quarks and charged leptons [53],

  iii) Type-X: Φ_1 couples to all leptons whereas Φ_2 couples to all quarks [53],

  iv) Type-Y: Φ_1 couples to all down-type quarks, Φ_2 couples to up-type quarks and leptons [53].

  Flavour Changing Neutral Currents (FCNC) emerge at the tree level in 2HDM [54–58], a phenomenon that is absent in SM. If the additional doublet is odd under discrete $\mathbb{Z}_2$ symmetry then 2HDM called *Inert* Higgs doublet model (IDM) [49] and the lightest component of the neutral Higgs serves as a DM candidate. IDM with right-handed neutrinos is often categorized into *scotogenic* model [59, 60] which provides loop-generated neutrino mass, having DM in the loop.

- Seesaw models: Seesaw models are one of the most prominent BSM scenarios to explain the smallness of neutrino mass. The heaviness of the NP scale in the denominator makes the neutrino mass tiny, that's how they are referred as seesaw models. There are majorly three types of seesaw models, all of which generate the dimension five Weinberg operator when integrated out:

  i) Type-I seesaw: This is the simplest extension of SM, where we assume the presence of three right-handed Majorana neutrinos (RHN). The neutrino masses are generated by the interactions of RHNs with the SM left-handed neutrinos via Yukawa couplings [17, 18].

  ii) Type-II seesaw: A scalar triplet is added to the SM. The triplet couples to the SM leptons and acquires a VEV. The interaction of the triplet with the SM leptons leads to the generation of neutrino masses. The smallness of the neutrino masses is attributed to the small VEV of the triplet [19–21].

  iii) Type-III seesaw: In this case, heavy fermion triplet is introduced to the SM that interacts with the left-handed SM doublets [22, 23]. The smallness of neutrino mass is attributed to heavy triplet mass. The schematic Feynman graphs for all three possibilities are shown in the Fig. 1.3. Seesaw models play a crucial role not only in elucidating the origin of tiny neutrino masses but also in providing a theoretical framework of the observed baryon asymmetry of the universe, Seesaw-I model, in particular.

- Singlet scalar extension: The simplest model to accommodate a DM, is to extend the SM by a scalar singlet stabilised by $\mathbb{Z}_2$ symmetry. This DM couples to SM via Higgs portal interaction. Both the possibilities of WIMP [61–64], and FIMP [65, 66] have been studied widely in this context, along with the detection possibilities. Some features of multi-particle DM in the extended version of this model have also been carried out.

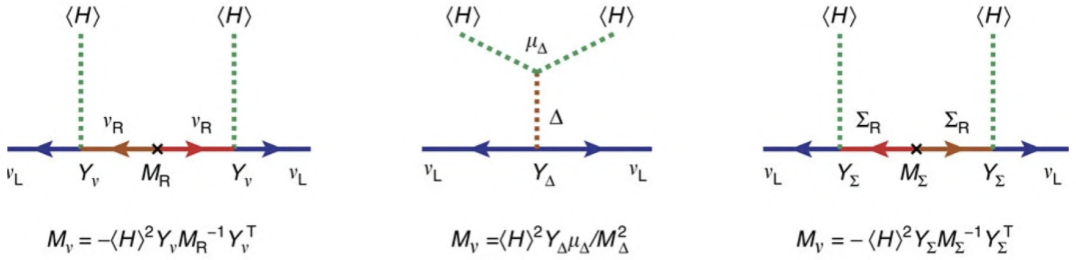

Figure 1.3: Feynman graphs for different types of neutrino mass generation, Type-I Seesaw (left), Type-II Seesaw (middle) and Type-III seesaw (right).

There are many possibilities that we left out, some which we still would like to mention are the composite Higgs model [63, 67], extra-dimensional set ups [68, 69], left-right symmetric model (LRSM) [70–73], $U(1)_X$ models [74–84], etc.

1.3.2 Standard Model Effective Field Theory (SMEFT)

The Effective field theory (EFT) mainly deals with the degrees of freedom of a theory that are difficult to achieve. For example, Fermi theory has been a classic example of an effective theory of weak interactions when the scale of W boson couldn't be reached. Chiral perturbation theory (ChPT) is an example of an EFT that has been incredibly successful in describing the interactions of pions and other hadrons, similarly heavy quark effective theory (HQET) is an EFT that has been instrumental in understanding the physics of charm and bottom quarks within the context of QCD. Soft-Collinear Effective Theory (SCET) is used to study the behaviour of particles that are either very energetic (collinear) or very soft in high-energy collisions in different experiments at the LHC.

The Standard Model Effective Field Theory (SMEFT) [85–89] is a framework where the low energy incarnation is assumed to be the SM, with its particle content and symmetries. To be more precise, below a cut-off scale Λ, SM with its mass dimension-four interactions at the leading order is assumed to be the 'known' theory. However one can construct higher dimensional operators with the SM fields (and their derivatives), respecting the SM symmetry, suppressed by appropriate powers of Λ, which can bring forth the effects of NP having a mass scale larger than Λ. The Lagrangian under the SMEFT framework can be written as

$$\mathcal{L} = \mathcal{L}_{\texttt{SM}} + \sum_i \sum_{d\geq 5} \frac{C_i}{\Lambda^{d-4}} \mathcal{O}^d, \tag{1.26}$$

where Λ is the scale of NP, C_i are the dimensionless Wilson coefficients (WCs) and $\mathcal{O}^d$ are the higher dimensional effective operators of dimension d constituted of SM fields and their derivatives. The EFT is favoured as a model-independent benchmark to study the deviations from the SM observations, as no confirmation of a specific UV set up could be made so far.

At the dimension five level, there exists a lone operator known as the Weinberg operator [90]

$$\mathcal{L}^{5}_{\texttt{EFT}} = \frac{C}{\Lambda}(\bar{l}^{c}\tilde{H}^{*})(\tilde{H}^{\dagger}l) + H.c.; \tag{1.27}$$

where H and l are the SM Higgs and lepton doublets, respectively. When the Higgs field obtains its VEV, this operator is responsible for inducing Majorana neutrino masses. As we already touched upon in the last section, there are several possible NP implications of this operator, in terms of seesaw frameworks. In the top-down approach, one starts with a UV complete theory that integrates out the heavy degrees of freedom and then matches with the SMEFT to study this theory in low energy limit. On the other hand, in the case of the bottom-up approach, we are agnostic about the UV completion of a theory/model and use the low-energy data to constrain WCs. In most of the phenomenological approaches, people consider the bottom-up approach to study different BSM scenarios. In this thesis, we take up the bottom-up approach mostly. For example, at the neutrino mass generation level, all the seesaw frameworks are effectively the same, but at the scale larger than Λ, the possible distinctions between a right handed neutrino, or a triplet scalar or fermion can be done. Weinberg operator violates lepton number by two units [2]. If right handed neutrinos are included, there are two more operators in dimension five.

At dimension six level, there are several operators that are of interest. Buchmüller and Wyler in 1986 defined a consistent basis for the SMEFT at dimension six [85]. More than two decades later, the first non-redundant basis of dimension-6 operators was established [86] in 2010. This set of operators is known as the "Warsaw basis". Under the assumption of flavor universality, this basis consists of 59 dimension-6 operators, see Table 1.2 and 1.3. The guiding principle behind creating the Warsaw basis is to minimize the use of derivatives in operators and remove the redundancy by using the equations of motion. Over the past two decades, various sets of bases have been developed to address specific issues. One example is the strongly interacting light Higgs (SILH) basis [91], which is especially useful in dealing with a strongly interacting Higgs sector. Another noteworthy operator basis in dimension-6 SMEFT is the HISZ basis [92]. This operator basis plays a crucial role to study self-interactions of γ and Z bosons with $W^{\pm}$ along with CP violation. In this thesis, we mostly focus on operators of dimension six, in Warsaw basis. We also do have a classification of operators; when the operators can only be generated at the loop level (LG) to that of potential tree generated (PTG), for details, see [93].

---

[2] Actually operators with odd dimension violates Baryon or Lepton numbers.

X^3 **(LG)**		H^6 and H^4D^2 **(PTG)**		ψ^2H^3 **(PTG)**	
$\mathcal{O}_G$	$f^{ABC}G_\mu^{A\nu}G_\nu^{B\rho}G_\rho^{C\mu}$	$\mathcal{O}_H$	$(H^\dagger H)^3$	$\mathcal{O}_{eH}$	$(\lvert H\rvert^2)(\bar{l}_p e_r H)$
$\mathcal{O}_{\widetilde{G}}$	$f^{ABC}\widetilde{G}_\mu^{A\nu}G_\nu^{B\rho}G_\rho^{C\mu}$	$\mathcal{O}_{H\Box}$	$\lvert H\rvert^2\Box\lvert H\rvert^2$	$\mathcal{O}_{uH}$	$(\lvert H\rvert^2)(\bar{q}_p u_r \tilde{H})$
$\mathcal{O}_W$	$\varepsilon^{IJK}W_\mu^{I\nu}W_\nu^{J\rho}W_\rho^{K\mu}$	$\mathcal{O}_{HD}$	$\left\lvert H^\dagger D_\mu H\right\rvert^2$	$\mathcal{O}_{dH}$	$(\lvert H\rvert^2)(\bar{q}_p d_r H)$
$\mathcal{O}_{\widetilde{W}}$	$\varepsilon^{IJK}\widetilde{W}_\mu^{I\nu}W_\nu^{J\rho}W_\rho^{K\mu}$				
X^2H^2 **(LG)**		ψ^2XH **(LG)**		ψ^2H^2D **(PTG)**	
$\mathcal{O}_{HG}$	$\lvert H\rvert^2\, G_{\mu\nu}^A G^{A\mu\nu}$	$\mathcal{O}_{eW}$	$(\bar{l}_p\sigma^{\mu\nu}e_r)\tau^I H W_{\mu\nu}^I$	$\mathcal{O}_{Hl}^{(1)}$	$(H^\dagger i\overleftrightarrow{D}_\mu H)(\bar{l}_p\gamma^\mu l_r)$
$\mathcal{O}_{H\widetilde{G}}$	$\lvert H\rvert^2\, \widetilde{G}_{\mu\nu}^A G^{A\mu\nu}$	$\mathcal{O}_{eB}$	$(\bar{l}_p\sigma^{\mu\nu}e_r)H B_{\mu\nu}$	$\mathcal{O}_{Hl}^{(3)}$	$(H^\dagger i\overleftrightarrow{D}_\mu H)(\bar{l}_p\tau^I\gamma^\mu l_r)$
$\mathcal{O}_{HW}$	$\lvert H\rvert^2\, W_{\mu\nu}^I W^{I\mu\nu}$	$\mathcal{O}_{uG}$	$(\bar{q}_p\sigma^{\mu\nu}T^A u_r)\tilde{H}\, G_{\mu\nu}^A$	$\mathcal{O}_{He}$	$(H^\dagger i\overleftrightarrow{D}_\mu H)(\bar{e}_p\gamma^\mu e_r)$
$\mathcal{O}_{H\widetilde{W}}$	$\lvert H\rvert^2\, \widetilde{W}_{\mu\nu}^I W^{I\mu\nu}$	$\mathcal{O}_{uW}$	$(\bar{q}_p\sigma^{\mu\nu}u_r)\tau^I\tilde{H}\, W_{\mu\nu}^I$	$\mathcal{O}_{Hq}^{(1)}$	$(H^\dagger i\overleftrightarrow{D}_\mu H)(\bar{q}_p\gamma^\mu q_r)$
$\mathcal{O}_{HB}$	$\lvert H\rvert^2\, B_{\mu\nu}B^{\mu\nu}$	$\mathcal{O}_{uB}$	$(\bar{q}_p\sigma^{\mu\nu}u_r)\tilde{H}\, B_{\mu\nu}$	$\mathcal{O}_{Hq}^{(3)}$	$(H^\dagger i\overleftrightarrow{D}_\mu^I H)(\bar{q}_p\tau^I\gamma^\mu q_r)$
$\mathcal{O}_{H\widetilde{B}}$	$\lvert H\rvert^2\, \widetilde{B}_{\mu\nu}B^{\mu\nu}$	$\mathcal{O}_{dG}$	$(\bar{q}_p\sigma^{\mu\nu}T^A d_r)H\, G_{\mu\nu}^A$	$\mathcal{O}_{Hu}$	$(H^\dagger i\overleftrightarrow{D}_\mu H)(\bar{u}_p\gamma^\mu u_r)$
$\mathcal{O}_{HWB}$	$(H^\dagger i\overleftrightarrow{D}_\mu^I H)\tau^I H\, W_{\mu\nu}^I B^{\mu\nu}$	$\mathcal{O}_{dW}$	$(\bar{q}_p\sigma^{\mu\nu}d_r)\tau^I H\, W_{\mu\nu}^I$	$\mathcal{O}_{Hd}$	$(H^\dagger i\overleftrightarrow{D}_\mu^I H)(\bar{d}_p\gamma^\mu d_r)$
$\mathcal{O}_{H\widetilde{W}B}$	$H^\dagger\tau^I H\, \widetilde{W}_{\mu\nu}^I B^{\mu\nu}$	$\mathcal{O}_{dB}$	$(\bar{q}_p\sigma^{\mu\nu}d_r)H\, B_{\mu\nu}$	$\mathcal{O}_{Hud}$	$i(\tilde{H}^\dagger D_\mu H)(\bar{u}_p\gamma^\mu d_r)$

Table 1.2: Dimension-6 operators other than the four-fermion ones ($\tilde{H} = i\sigma_2 H^*$, and the subindices p, r denote family labels).

The dimension-7 operators [94, 95] offer valuable tools for investigating potential signals of new physics in various phenomena and processes. Specifically, due to their lepton and baryon number-violating characteristics, these operators can be used to explore baryogenesis and leptogenesis. The next level of correction is anticipated to emerge from dimension-8 operators. These operators have been a topic of investigation for some time, and recently an operator basis has been identified [88]. The significance of dimension-8 SMEFT operators becomes apparent in their pivotal role in unraveling the self-interactions of neutral gauge bosons. These interactions are notably absent in both the SM and dimension-6 SMEFT at tree level. In this thesis, we use some of these dimension-8 effective operators within the context of neutral gauge boson self-interactions. Beyond dimension-8, a complete set of dimension-9 SMEFT operators are also available in the literature [96].

In SMEFT framework, EWSB is linearly realized, i.e. the Higgs field undergoes transformation as a doublet under the $SU(2)_L$ gauge group, as elaborated above. Within this setup, the Goldstone bosons are integrated to the Higgs doublet making the Higgs self-couplings and HVV couplings correlated. Certain models, like the dilaton model, pose challenges for accurate description of low-energy behaviour within the SMEFT framework [97]. In such cases, an alternative EFT framework known as the Higgs Effective Field Theory (HEFT) [98, 99] is employed to effectively capture the low energy dynamics or IR behaviour. In contrast to SMEFT, HEFT framework is expressed in EWSB phase, utilizing the physical Higgs boson, without inherent relationship between the Higgs and the Goldstone bosons. Therefore, there are larger number of operators and no correlation between the Higgs self couplings and HVV couplings here, providing a broader platform for Higgs related studies as well as to probe NP via Higgs window in HEFT set up. While both SMEFT and HEFT are valuable tools for studying BSM physics, SMEFT is sometimes favoured

$(\bar{L}L)(\bar{L}L)$ **(PTG)**		$(\bar{R}R)(\bar{R}R)$ **(PTG)**		$(\bar{L}L)(\bar{R}R$ **(PTG)**$)$	
$\mathcal{O}_{ll}$	$(\bar{l}_p\gamma_\mu l_r)(\bar{l}_s\gamma^\mu l_t)$	$\mathcal{O}_{ee}$	$(\bar{e}_p\gamma_\mu e_r)(\bar{e}_s\gamma^\mu e_t)$	$\mathcal{O}_{le}$	$(\bar{l}_p\gamma_\mu l_r)(\bar{e}_s\gamma^\mu e_t)$
$\mathcal{O}_{qq}^{(1)}$	$(\bar{q}_p\gamma_\mu q_r)(\bar{q}_s\gamma^\mu q_t)$	$\mathcal{O}_{uu}$	$(\bar{u}_p\gamma_\mu u_r)(\bar{u}_s\gamma^\mu u_t)$	$\mathcal{O}_{lu}$	$(\bar{l}_p\gamma_\mu l_r)(\bar{u}_s\gamma^\mu u_t)$
$\mathcal{O}_{qq}^{(3)}$	$(\bar{q}_p\gamma_\mu\tau^I q_r)(\bar{q}_s\gamma^\mu\tau^I q_t)$	$\mathcal{O}_{dd}$	$(\bar{d}_p\gamma_\mu d_r)(\bar{d}_s\gamma^\mu d_t)$	$\mathcal{O}_{ld}$	$(\bar{l}_p\gamma_\mu l_r)(\bar{d}_s\gamma^\mu d_t)$
$\mathcal{O}_{lq}^{(1)}$	$(\bar{l}_p\gamma_\mu l_r)(\bar{q}_s\gamma^\mu q_t)$	$\mathcal{O}_{eu}$	$(\bar{e}_p\gamma_\mu e_r)(\bar{u}_s\gamma^\mu u_t)$	$\mathcal{O}_{qe}$	$(\bar{q}_p\gamma_\mu q_r)(\bar{e}_s\gamma^\mu e_t)$
$\mathcal{O}_{lq}^{(3)}$	$(\bar{l}_p\gamma_\mu\tau^I l_r)(\bar{q}_s\gamma^\mu\tau^I q_t)$	$\mathcal{O}_{ed}$	$(\bar{e}_p\gamma_\mu e_r)(\bar{d}_s\gamma^\mu d_t)$	$\mathcal{O}_{qu}^{(1)}$	$(\bar{q}_p\gamma_\mu q_r)(\bar{u}_s\gamma^\mu u_t)$
		$\mathcal{O}_{ud}^{(1)}$	$(\bar{u}_p\gamma_\mu u_r)(\bar{d}_s\gamma^\mu d_t)$	$\mathcal{O}_{qu}^{(8)}$	$(\bar{q}_p\gamma_\mu T^A q_r)(\bar{u}_s\gamma^\mu T^A u_t)$
		$\mathcal{O}_{ud}^{(8)}$	$(\bar{u}_p\gamma_\mu T^A u_r)(\bar{d}_s\gamma^\mu T^A d_t)$	$\mathcal{O}_{qd}^{(1)}$	$(\bar{q}_p\gamma_\mu q_r)(\bar{d}_s\gamma^\mu d_t)$
				$\mathcal{O}_{qd}^{(8)}$	$(\bar{q}_p\gamma_\mu T^A q_r)(\bar{d}_s\gamma^\mu T^A d_t)$

$(\bar{L}R)(\bar{R}L)$ and $(\bar{L}R)(\bar{L}R)$ **(PTG)**	
$\mathcal{O}_{ledq}$	$(\bar{l}_p^j e_r)(\bar{d}_s q_t^j)$
$\mathcal{O}_{quqd}^{(1)}$	$(\bar{q}_p^j u_r)\varepsilon_{jk}(\bar{q}_s^k d_t)$
$\mathcal{O}_{quqd}^{(8)}$	$(\bar{q}_p^j T^A u_r)\varepsilon_{jk}(\bar{q}_s^k T^A d_t)$
$\mathcal{O}_{lequ}^{(1)}$	$(\bar{l}_p^j e_r)\varepsilon_{jk}(\bar{q}_s^k u_t)$
$\mathcal{O}_{lequ}^{(3)}$	$(\bar{l}_p^j \sigma_{\mu\nu} e_r)\varepsilon_{jk}(\bar{q}_s^k \sigma^{\mu\nu} u_t)$

Table 1.3: Four-fermion operators conserving baryon number (the subindices p, r, s and t denote family labels).

as it is consistent with LHC, LEP, and other low-energy experimental data, which indicates SM to be the prevalent low energy theory. In this thesis, we will therefore mainly involve SMEFT framework. However, considering the possibility of a new particle discovery during Run 3 of LHC or the high luminosity LHC (HL-LHC), within the energy range proximate to lepton colliders, the new particle will also contribute to the construction of higher dimensional operators and the EFT will have to be modified accordingly. For example, a right handed neutrino, if found within the proximity of next generation colliders, the relevant EFT framework should include this particle to yield νSMEFT, see for example, [94].

1.4 Particle colliders

Particle colliders have been essential tools for studying the fundamental constituents of the universe. Over the years, several types of colliders have been built to explore different energy regimes. Here, we provide a short overview of the Hadron colliders, following that we discuss Lepton colliders with some more details.

1.4.1 Hadron colliders

A hadron collider is a type of particle accelerator that is designed to accelerate and collide beams of hadrons, which are composite particles made up of quarks and sometimes heavy ions as well. The Intersecting Storage Rings (ISRs) located at CERN was the world's first hadron collider that ran from 1971 to 1984 with a maximum CM energy of 62 GeV. The Super Proton Synchrotron (SPS) is a hadron collider that ran from 1981 to 1991 at CERN. In July 1981, 1st $p\bar{p}$ collisions were observed at CM energy $\sqrt{s}$ = 540 GeV. The UA1 and UA2 collaborations independently reported the discovery of the W and Z bosons in January 1983. The Tevatron at Fermilab was a hadron collider that was functional from 1983 to 2011. The highest CM energy reached by Tevatron was 1.96 TeV. The Tevatron, under the collaborative efforts of CDF and D0, achieved a milestone with the remarkable discovery of the top quark. The latest Hadron collider, LHC, is the world's largest and most powerful collider. The first collisions at the LHC were achieved at 3.5 TeV CM energy. The crowning achievement of the LHC is the discovery of the last missing piece of the SM, the Higgs boson in 2012 at a mass 125 GeV. In addition to the groundbreaking Higgs discovery, the LHC plays a pivotal role in affirming various properties of the SM. Currently, the LHC is running with 14 TeV CM energy to investigate different properties of SM and look for possible BSM physics. The luminosity at which many physics studies have already been done is 39 fb^{-1}, whereas the HL-LHC has been proposed to accumulate 3 ab^{-1} data. In spite of the remarkable success, the LHC grapples with a whopping QCD background. This challenge implies that potential NP signals may be overshadowed by the prevalent SM backgrounds. In light of this, our focus is more devoted to the proposed lepton colliders and their different discovery potentials.

1.4.2 Lepton colliders

As we have stated before, particle physics has entered into an era of unprecedented precision, and in this context, lepton colliders have emerged as vital tools for conducting precision analyses within both SM and BSM scenarios. These high-energy accelerators, which collide elementary charged leptons, offer distinct advantages for studying the characteristic fundamental particles and their interactions, making them indispensable in advancing our understanding of particle physics. In the past, different lepton colliders played a significant role in discovering crucial phenomena. At the Positron-Electron Tandem Ring Accelerator (PETRA), gluon was discovered in 1979. The discovery of the tau lepton occurred through a series of experiments conducted from 1974 to 1977 at the Stanford Linear Accelerator Center (SLAC). Besides the tau lepton discovery, SLAC was instrumental in revealing the existence of partons within protons and neutrons, revolutionizing our understanding of the hadron structure. The discovery of charmed quark also took place at the SLAC in 1974. Another lepton collider named Large Electron Positron (LEP) collider has helped us to shed light on the determination of the number of light neutrino species. The outcomes from the LEP experiments played a pivotal role in establishing precise values for various parameters in the SM, with a particular emphasis on determining the masses of W and Z bosons. Prior to its final shutdown at CERN, the LEP provided a lower limit for the Higgs boson's mass. This critical lower limit proved to be highly influential in guiding and supporting the subsequent discovery of the Higgs boson at the LHC. Following the Higgs discovery, a lepton collider with adequate energy would serve as an ideal companion with the LHC to facilitate precision measurements. We discuss below a few important aspects of the lepton colliders:

- **Detail:** Lepton colliders offer a distinct advantage with their well-defined CM energy ($\sqrt{s} = 2E_{\texttt{beam}}$) resulting from the collision of two elementary particles.

This eliminates the uncertainty surrounding initial kinematic configurations, allowing for the use of full kinematic information during event reconstruction, including the application of kinematic fits. In contrast, pp colliders face the challenge of an unknown kinematic configuration for each collision since two composite particles collide. Due to the wide energy distributions of gluons within protons, governed by probability through parton distribution functions, the energy at which particle collisions occur remains uncertain. At high-energy lepton colliders like electron-positron setups, particle acceleration generates two primary forms of radiation: bremsstrahlung and beamstrahlung. Bremsstrahlung arises from the acceleration of charged particles, while beamstrahlung results from the radiation due to the electromagnetic field of the other beam of charged particles. These radiations have significant implications for collider operations, causing a reduction in the CM energy available for collisions, as particles emit radiation and lose energy. Careful consideration in collider design and operation is required for minimum energy loss and maintain superlative experimental conditions [100, 101].

- **Cleanliness:** QCD background is absent in the lepton colliders as leptons do not carry colors. This absence of QCD background in lepton colliders results in a cleaner experimental environment, making it easier to study electroweak processes with better precision. The primary contributors to machine background are photon-photon collisions, which have a cross-section that is six orders of magnitude smaller compared to the backgrounds encountered at the LHC. This characteristic ensures manageable background levels, even at high luminosities. As a result, the cleaner experimental environment significantly simplifies the process of event reconstruction.

- **Polarization:** Beam polarization at linear lepton colliders plays an important role in precision analyses and NP searches. Both longitudinal and transverse polarization of initial beams provide in-depth studies of helicity structures of different processes. Judicious choice of polarized beams offers the benefit of effectively diminishing the SM background, thereby enabling the potential detection of NP signals. Along with better statistical accuracy of NP couplings, the chiral character of the different NP couplings can also be well studied by using beam polarization.

- **Calculability:** In the case of electron-positron collision, all the processes are primarily governed by electro-weak interactions. Therefore, the calculation of the next leading order (NLO) correction to cross-sections for different processes is straightforward and estimated to be the order of a few percent. This enhances the theoretical uncertainty of the projected cross-sections. Precise knowledge of theoretical and experimental uncertainties render lepton colliders capable of detecting even subtle quantum correction to cross sections that subsequently leads to observe NP even when it falls beyond the direct kinematic range.

- **Democracy:** In e^+e^- colliders, the couplings of Z boson and photon to all other particles exhibit uniform strength, and production rates are primarily constrained by the available phase space within the reaction. This characteristic results in a lack of substantial hierarchy between SM and BSM physics, eliminating the need for specific triggers and enabling the use of continuous readout. Furthermore, all possible final states of decaying particles can be harnessed for physics analyses, offering the unique opportunity to measure absolute branching ratios, total widths, and the identification of hadronic W and Z decays. This versatility and comprehensiveness make e^+e^- colliders valuable tools for a wide range of particle physics investigations.

Based on the discussions described above, the High Energy Physics community has taken significant initiative to build different lepton colliders across the globe. We provide a brief overview of notable future lepton colliders.

- **International Linear Collider:** The International Linear Collider (ILC) [102–105] is a proposed 31 KM long next-generation electron-positron collider that uses advanced 1.3 GHz superconducting radio-frequency technology with high luminosity. Initial operation of ILC is planned in the range between 250-500 GeV CM energy with a possible upgradation up to 1 TeV. It will start with a luminosity of 420 fb^{-1} and after 11 years, it will be able to accumulate a total integrated luminosity of 2 ab^{-1}. This will be attainable following an energy upgrade, during which the CM energy will be doubled compared to its previous value. It is presumed that up to 500 GeV CM energy, ILC beams will maintain a minimum of 80% electron polarization along with a 30% positron polarization. The positron beam can be upgraded up to 60% with the incorporation of a photon collimator. Japan has initially shown interest to build ILC but the exact location has not been finalized yet.

- **Compact Linear Collider:** The Compact Linear Collider (CLIC) [106–109] is a high-energy and high-luminosity electron-positron collider under development by worldwide 'CLIC' collaboration. This accelerator has been considered for operation at three distinct CM energy levels: 380 GeV, 1.5 TeV, and 3 TeV. Each stage's timeframe is set based on the integrated luminosity of 500 fb^{-1} at 380 GeV, 1.5 ab^{-1} at 1.5 TeV, and 3 ab^{-1} at 3 TeV. The electron source generates spin-polarized electrons with a degree of polarization of 80% or greater whereas the positron source aims to provide only an unpolarized beam. CLIC is proposed to be constructed at CERN.

- **Circular Electron Positron Collider:** The Circular Electron Positron Collider (CEPC) [110–112] is a circular electron-positron collider with a 100 km circumference proposed by the particle physics community immediately after the discovery of the Higgs boson. It is planned to operate at CM energy around 91.2 GeV as Z boson factory, 160 GeV which is the W boson production threshold, and 240 GeV that can be served as a Higgs factory. The CM energy of CEPC can be enhanced to 360 GeV, facilitating top-quark pair production. Over a ten-year period, the planned operation aims to generate a combined integrated luminosity of 16 ab^{-1} for Z operations, 2.6 ab^{-1} for W operations, and 5.6 ab^{-1} for Higgs operations. The CEPC study group is striving to secure project approval by approximately 2027 and China is foreseen as the location for this initiative.

- **Future Circular Collider:** The initial phase of the Future Circular Collider is an electron-positron collider known as FCC-ee [113–115], designed to function as a Higgs production facility, electroweak, and top-quark factory. It will operate at four distinct CM energies: the Z pole, the WW threshold, the ZH production peak, and the $t\bar{t}$ threshold. After four years of running, FCC-ee is proposed to achieve 150 ab^{-1} luminosity at Z pole CM energy. With the upgradation of CM energy up to 365 GeV, integrated luminosity would be around 1 ab^{-1}. FCC-ee is planned to be situated in the Lake Geneva basin, with connection to the existing CERN facilities.

- **Muon Collider:** A high-energy muon collider [116–118] stands out for its unparalleled capability to deliver precision measurements and attain the highest energy levels within a single machine, a feat beyond the reach of any currently existing technology. Experimental outcomes from flavor physics suggest that we require very high CM energy to probe NP. Now, using traditional technology, electron-based colliders are unable to attain such a magnitude of CM energy. Muon's mass is approximately 206 times greater than that of an electron, resulting in a billion-fold reduction in synchrotron radiation. This significant decrease in radiation loss makes it feasible to build circular colliders with significantly higher design energies compared to electron-positron colliders of the same class. Likewise, electrons and muons are also fundamental particles that focus all their energy on close-range interactions, rather than spreading it out like in protons. This means a 14 TeV muon collider can be as effective as a 100 TeV proton-proton collider [119]. Therefore, a 10+ TeV muon collider will be the ideal choice to probe such NP scenarios. Possible CM energies of muon collider with integrated luminosity are noted as

$$\sqrt{s} = 3, 6, 10, 14 \text{ and } 30 \text{ TeV} \quad \text{with} \quad \mathfrak{L}_{\texttt{int}} = 1, 4, 10, 20, \text{ and } 90 \text{ ab}^{-1}. \tag{1.28}$$

  An international collaboration named 'International Muon Collider Collaboration (IMCC)' has been formed to study muon collider prospect.

After the exploration of past and future lepton colliders, their advantages, energy capabilities, and luminosity projections, we discuss the physics objectives across various lepton colliders in the next subsection.

1.4.3 Physics issues at lepton colliders

Future lepton colliders, powerful machines designed for particle physics research, are instrumental in pushing the energy frontier to explore the unknown. In this section we discuss the important physics issues these colliders tackle, shedding light on their significant role in expanding our understanding of the nature of the fundamental particles and their interactions.

- As mentioned earlier, CEPC plans to operate at CM energy around Z-pole (91.2 GeV), WW threshold (160 GeV), and also can be served as Higgs factory (240 GeV). Therefore, the primary motivation of this collider is to study Z, W, and H precision measurements. Although LEP has already measured the W and Z properties with satisfactory precision, CEPC will relook into it. In the 360 GeV run, the cross-section of ZH production is 36% lower compared to the 240 GeV run. Meanwhile, the cross-sections of the WW and ZZ fusion for Higgs production are 3.8 and 4.6 times higher, respectively. These channels are crucial for determining the Higgs width. In the context of the BSM scenarios, the

CEPC serves as a platform for exploring various possibilities like charged lepton flavor violation through tau (τ) physics, exotic Higgs decays (particularly those involving hidden sector dynamics, and asymmetric dark matter). ZH measurement at 240 GeV provides a model-independent evaluation of HZZ coupling, which serves as a crucial normalization for gauging other Higgs boson couplings and CP violation estimations in the Higgs sector [112].

- FCC-ee plans to operate at 360 GeV on top of all CEPC ranges. Therefore it will provide precise measurements of top-quark mass, width, and top-quark electroweak and Yukawa coupling and help estimating underlying NP effects in addition to the W, Z, and H precision measurements. One of the most important aims of HEP community is to determine the Higgs boson self-coupling, crucial for understanding the Higgs boson potential shape. Projections for HL-LHC anticipate a 50% precision in measuring this, while combined HL-LHC and FCC-ee results can improve it to 33% [115].

- ILC at 250 GeV CM energy, aims to measure Higgs invisible decays precisely, which offers unparalleled opportunities to explore a wide range of NP models. The production of the Higgs boson at 250 GeV, primarily in association with a Z boson, allows for the identification of events featuring a single isolated Z boson – a hallmark for Higgs decaying entirely to invisible states. While SM predicts a decay branching of $H \to 4\nu$ as 0.1%, an observed precision in this channel will open the window for estimating invisible decays stemming from NP. In absence of observing this mode, a 95% confidence upper limit on the branching ratio of 0.16% can be established. Along with the precision measurements of the W boson's properties like mass, width, and branching ratios, a primary objective of the ILC is to enhance the accuracy of $WWV(V = \gamma, Z)$ couplings through direct measurement. The $WW \to \ell\nu qq'$ final state plays a pivotal role in scrutinizing these couplings. Additionally, the HVV and $h\gamma Z$ couplings are regarded as significant case studies. With CM energy of 1 TeV, the ILC aims to explore the presence of Z' bosons, new scalars, and heavy neutral neutrinos (HNL) up to 1 TeV. In the pursuit of WIMP search via effective operators, a 500 GeV ILC could estimate the presence of NP scale upto $\Lambda = 3$ TeV, while a 1 TeV ILC could push this limit to $\Lambda = 4.5$ TeV [105]. It also has the capability to probe charged fermions originating from the type-III seesaw model with masses below 900 GeV. We discuss various possibilities at ILC including heavy fermion production in Chapter 3.

- CLIC at the initial stage (with $\sqrt{s}$ =380 GeV) also plans to explore the Higgsstrahlung process (Zh production), which enables the identification of the Higgs via recoil against the Z boson, providing model-independent measurement of Higgs branching ratios and width. This method is advantageous for lepton colliders as it doesn't rely on assumptions about BSM invisible decays. An upper limit on BR (Higgs $\to$ inv.) $< 0.69\%$ at 90% C.L. can be achieved through this process. Additionally, precise top quark mass measurements can be conducted via threshold scans. In the subsequent stages (1.5 TeV), the ZHH and $HH\nu\nu$ processes will be examined for triple Higgs coupling measurements in a complementary manner. Moving to the final stage (3 TeV), CLIC has the capability to search for heavy Leptons with masses up to 3 TeV. A better precision on WWV couplings can also be achieved at 3 TeV. Further, CLIC is well-equipped to investigate DM models characterized by significant mass-splitting, allowing for the detection of signals comprising prompt jets, leptons, photons, and missing momentum [107]. The CLIC program can be invaluable in refining the precision of anomalous neutral triple gauge couplings (nTGCs), as discussed in Chapter 4.

- A muon collider serves as a complementary probe to CLIC at initial stage ($\sqrt{s}$ =3 TeV), enabling precision test in the electroweak sector of the SM. At 10 TeV CM energy, single Higgs and Di-Higgs production cross-sections through vector boson fusion (VVF) is higher compared to 3 TeV; thus provides a better probe of Higgs properties. The high-energy muon collider emerges as the primary and most reliable avenue for investigating heavy electroweak DM, such as higgsino, devoid of astrophysical uncertainties. Moreover, a 10 TeV muon collider holds the potential to explore the compositeness scale through indirect precision measurements, achieving scales as high as $m^* \sim$ 45 TeV with 10 ab^{-1} data. Some of the most robust constraints on NP emerge from investigations into flavor and/or CP violation, as well as other accidental symmetries within the SM. These encompass searches for electron and neutron electric dipole moments (EDMs), lepton flavor-violating (LFV) muon decays, and measurements of Kaon (or other meson) mixing. A high-energy muon collider possibly is an ideal laboratory for complementing these low-energy probes, for example, to explore the novel realms of $(g-2)_\mu$ physics. In the scenario where a new SM singlet, scalar or vector, resolves the $(g-2)_\mu$ anomaly, and if it exclusively interacts with the muon, only a muon beam holds the capability to investigate the singlet coupling responsible for $(g-2)_\mu$. Even if the singlet proves too massive to be produced on-shell, its impact on muonic Bhabha scattering can still be directly investigated at a muon collider. At 10 TeV, we can probe $U_{\mu N}^2 \sim 10^{-7}$ for 10 TeV HNL mass, where $U_{\mu N}$ is the heavy-light neutrino mixing angle. Another possibility is to investigate flavor violation within the quark sector that is constrained by different flavor and top-quark observables [118], which necessitates high CM energy, as detailed in Chapter 5.

Chapter 2

Statistical Analysis

Contents

2.1 Maximum likelihood and χ^2 function

Particle physicists heavily rely on statistical analysis to scrutinize complex theoretical models, seeking to determine the optimal parameter values that assess the compatibility of experimental/simulated data with hypotheses about new particles or novel physical theories. In the past decade, particle physics has transitioned into the precision era. This transition necessitates a thorough understanding of experimental uncertainties, encompassing both statistical and systematic aspects. It's crucial to establish confidence intervals for measuring any parameter using different observables from experimental/simulated data. These confidence intervals are equally important for hypothesis testing which confirms the existence of NP or anomalies. In the discussion below and throughout the thesis, we adhere to only statistical error in estimating NP parameters and leave systematics aside. The methodology involves a statistical approach via the principle of maximum likelihood (ML). Let's consider a data set with N independent measurement, $\{y_1, y_2, ..., y_N\}$ to determine a parameter θ at known points x_i, then the likelihood of the data sample is defined as

$$L(y_i, x_i; \theta) = \prod_i P(y_i, x_i, \theta), \tag{2.1}$$

where $P(y_i, x_i; \theta))$ probability distribution function (p.d.f) involving y_i. If we assume that the measurement "y_i" follow a Gaussian distribution with a mean μ and standard deviation of σ_i, then $P(y_i, x_i; \theta)$ is

$$P(y_i, x_i; \theta) = \frac{1}{\sqrt{2\pi}\sigma_i} e^{-\dfrac{(y_i - \mu(x_i, \theta))^2}{2\sigma_i^2}}. \tag{2.2}$$

Now, the χ^2 function in terms of the logarithm of the likelihood is

$$\chi^2 = -\ln L + \text{constant} = \sum_{\mathrm{i}} \frac{(\mathrm{y_i} - \mu)^2}{\sigma_{\mathrm{i}}^2}. \tag{2.3}$$

In order to determine the parameter, one has to maximize the likelihood ($i.e.$, probability) which is equivalent to minimizing the χ^2 function. If the measurement y_i's are not independent then χ^2 function is defined as

$$\chi^2 = \sum_{i,j} (y_i - \mu(x_i;\theta))(y_j - \mu(x_j;\theta))V_{ij}^{-1}, \tag{2.4}$$

where the V_{ij} is the covariance matrix. Therefore, using the expression of χ^2, $\Delta\chi^2$ is defined as

$$\Delta\chi^2 = \chi^2 - \chi^2_{min}, \tag{2.5}$$

where χ^2_{min} is the value of χ^2 at the best-fit value of the parameter θ. This $\Delta\chi^2 = n$ provides the $\sqrt{n}\sigma$ deviation from the best-fit value of the parameter. Depending on the number of parameters, n indicates different confidence levels (C.L.). C.L. is a statistical range that provides an estimated range of values for a parameter, with a specified value of probability, indicating the uncertainty in the best-fit value. For instance, in case of 1 parameter scenario, $n = 1$ denotes 68.3% C.L. In Table 2.1, probabilities corresponding to different parameters are tabulated for various $n\sigma$ levels.

$n\sigma$	Confidence level (C.L.) (%)		
	1 parameter	2 parameter	3 parameter
1σ	68.27	39.34	19.87
2σ	95.4	86.47	73.85
3σ	99.73	98.89	97.07

Table 2.1: Numerical values representing confidence levels (C.L.) corresponding to various standard deviation levels ($n\sigma$) for different parameters.

2.1.1 Regular χ^2 analysis

Let us consider we have some observational/simulated data for an observable ($e.g.$, differential cross-section) that we can organize into different bins. Alongside this data, we have a model or hypothesis that tries to predict the number of events within each of these bins. If N_i^{obs} is the number of events in i^{th} bin from an experiment or Monte Carlo simulation and $N_i^{\texttt{theo}}$ as the expected values for an observable distribution from a model/hypothesis, the χ^2 function is defined as

$$\chi^2 = \sum_i \frac{(N_i^{\texttt{obs}} - N_i^{\texttt{theo}})^2}{\sigma_i^2}. \tag{2.6}$$

In the above, $\sigma_i = \sqrt{N_i^{\texttt{obs}}}$ is the statistical uncertainty in the $i^{\texttt{th}}$ bin. Here, we consider the fact that the determination of the number of events in each bin is independent of the other bins and the number of events in each bin follows Poisson distribution. In order to estimate NP parameters in a collider environment from Monte Carlo simulated data, we start by examining a specific final state signal. We must ensure that the SM contribution to that final state signal is well-understood and reduced as much as possible using appropriate collider variables. Thereafter, we collect $N^{\texttt{obs}}$ from the binned observable distribution to feed Eq. (2.4) and minimize the χ^2 with respect to NP parameters to determine the statistical sensitivity of NP parameters with certain C.L.

2.2 The optimal observable technique (OOT)

The optimal observable technique (OOT) [120–123] estimates the statistical uncertainty of NP parameters by minimizing the covariance matrix. The covariance matrix is found out using the probability distribution function of a simulated number of events for a particular observable with appropriate phase space information. In Fig. 2.1, we show a schematic, where the interfering contributions of SM and BSM has been shown to the signal state. Contributions from other SM production processes to the same final state may arise, which are called non-interfering SM background. In this following section, we elaborate on the derivation of the OOT for different NP scenarios, (i) when NP dominates the signal, (ii) when SM interference contribution dominates over NP, and (iii) when we have large non-interfering SM background.

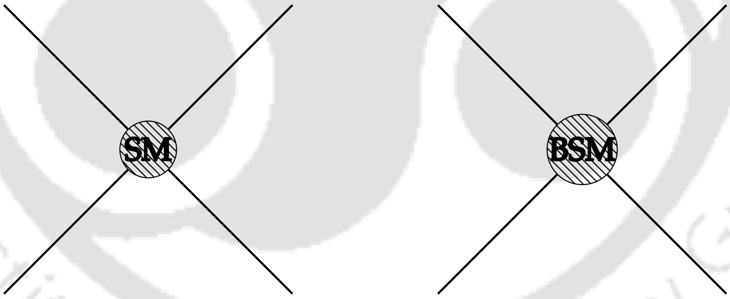

Figure 2.1: Schematic Feynman diagrams for a hypothetical signal with SM (left) and BSM (right) contributions.

2.2.1 BSM dominance over SM

In this scenario, we consider processes in which either SM does not have any substantial contribution or exerts only a marginal influence. Within this context, an observable such as differential cross-section can be expressed as follows:

$$\mathcal{O}_{\texttt{BSM}} = \frac{d\sigma_{\texttt{theo}}}{d\phi} = \sum_i g_i f_i(\phi)\,, \tag{2.7}$$

where g_i denotes non-linear functions of NP parameters and f_i's are sets of linearly independent functions of the phase-space coordinates ϕ. In the following discussions, as we delve into the $2 \to 2$ scattering processes, ϕ is the cosine of the scattering angle in the CM frame. In principle, one can have the flexibility to select any ϕ, depending on the specific nature of the process. Our aim now is to provide observables that allow for the most efficient measurement of the g_i parameters.

The total cross-section for the process is

$$\Sigma_{\texttt{theo}} = \left\langle \frac{d\sigma_{\texttt{theo}}}{d\phi} \right\rangle , \tag{2.8}$$

where to simplify notation, we define the bracket $\langle \cdots \rangle$ such that for any quantity W depending on ϕ

$$\langle W \rangle = \int d\phi \, W(\phi) \, . \tag{2.9}$$

In reality, experiments occur over a length of time, in which case the probability to observe a number A follows Poisson distribution. If $\mathfrak{L}_{\texttt{int}}$ is the integrated luminosity over that period, the average event number in a fixed period is

$$\mathfrak{N}_{\texttt{theo}} = \mathfrak{L}_{\texttt{int}} \Sigma_{\texttt{theo}} \, . \tag{2.10}$$

So, assuming the events occur at a constant rate and are independent of one another [1], the probability of observing A events is given by

$$\frac{\mathfrak{N}^A_{\texttt{theo}}}{A!} e^{-\mathfrak{N}_{\texttt{theo}}} . \tag{2.11}$$

Therefore the probability of observing A events in regions $\Delta\phi_a$ around phase-space points ϕ_a, $a = 1, \dots, A$ is

$$\mathfrak{F}_{\texttt{theo}}(A; \Phi_A)\, \Delta\Phi_A = \frac{\mathfrak{N}^A_{\texttt{theo}}}{A!} e^{-\mathfrak{N}_{\texttt{theo}}} \prod_{a=1}^{A} p_{\texttt{theo}}(\phi_a) \Delta\phi_a \, ; \; \Phi_A = (\phi_1, \dots, \xi_A) \, , \; \Delta\Phi_A = \prod_{a=1}^{A} \Delta\phi_a \, , \tag{2.12}$$

$$\Rightarrow \mathfrak{F}_{\texttt{theo}}(A; \Phi_A) = \frac{e^{-\mathfrak{N}_{\texttt{theo}}}}{A!} \prod_{a=1}^{A} \mathfrak{p}_{\texttt{theo}} \, , \quad \mathfrak{p}_{\texttt{theo}} = \mathfrak{N}_{\texttt{theo}} p_{\texttt{theo}} = \mathfrak{L}_{\texttt{int}} \frac{d\sigma_{\texttt{theo}}}{d\phi} \, , \tag{2.13}$$

and $\Phi_A = (\phi_1, \dots, \phi_A)$. Choose now a set of observables $o_i(\phi)$ and let

$$O_i(A; \Phi_A) = \sum_{a=1}^{A} o_i(\phi_a) \, . \tag{2.14}$$

In the following, we will need the expectation values of quantities using $\mathfrak{F}_{\texttt{theo}}$ as the probability density function. These averages involve an integration over phase-space variables and a summation of the number of events. To simplify notation we also define $\langle\!\langle \cdots \rangle\!\rangle$ such that for any quantity U that depends on A and Φ_A,

$$\langle\!\langle U \rangle\!\rangle = \sum_{A=0}^{\infty} \int d\Phi_A U(A; \Phi_A) = \sum_{A=0}^{\infty} \int \prod_{c=1}^{A} d\phi_c U(A; \Phi_A) \, . \tag{2.15}$$

---

[1] Situations where this may not be true usually require a very large number of events. In such cases events may not be independent because of effects such as Bose enhancement of Pauli blocking.

With these preliminaries, the average of $\mathcal{O}_i$ is

$$\langle\!\langle \mathfrak{F}_{\texttt{theo}}\,\mathcal{O}_i \rangle\!\rangle = \sum_{A=1}^{\infty} \frac{e^{-\mathfrak{N}_{\texttt{theo}}}}{A!} \mathfrak{N}_{\texttt{theo}}^{A-1} A \left\langle \mathfrak{p}_{\texttt{theo}}\, o_i \right\rangle = \left\langle \mathfrak{p}_{\texttt{theo}}\, o_i \right\rangle = \mathfrak{L}_{\texttt{int}} \left\langle o_i f_j \right\rangle g_j \,. \tag{2.16}$$

Let then

$$\Gamma_i = \left(M^{-1}\right)_{ij} \mathcal{O}_j \,, \quad \text{where} \quad M_{ij} = \mathfrak{L}_{\texttt{int}} \left\langle o_i f_j \right\rangle \,, \tag{2.17}$$

in which case

$$g_i = \langle\!\langle \mathfrak{F}_{\texttt{theo}} \Gamma_i \rangle\!\rangle^{2} \,. \tag{2.18}$$

Therefore, any Γ_i that has the above form can be used to determine the g_i. The idea now is to choose the Γ_i that has the smallest covariance matrix.

Consider a dataset comprising N pairs of numbers, denoted as $\{x_i, y_i\}$. The generic expression of covariance matrix associated with this dataset is defined as

$$V = \frac{1}{N} \sum_i (x_i - \langle x \rangle)(y_i - \langle y \rangle) = \langle xy \rangle - \langle x \rangle \langle y \rangle \,. \tag{2.19}$$

Therefore, the covariance matrix in our case (OOT) is given by

$$V_{ij} = \left\langle \mathfrak{F}_{\texttt{theo}} \Gamma'_i \Gamma'_j \right\rangle = \langle\!\langle \mathfrak{F}_{\texttt{theo}} \Gamma_i \Gamma_j \rangle\!\rangle - g_i g_j \,; \quad \text{where } \Gamma'_i = \Gamma_i - g_i; \tag{2.20}$$

which we extremize as a function of the o_i:

$$\delta \left(\frac{1}{2} a_i a_j V_{ij} \right) = \langle\!\langle \mathfrak{F}_{\texttt{theo}} (b\mathcal{O}) \left(b_i \, \delta\mathcal{O}_i - b_i \, \delta M_{ij} \, \Gamma_j \right) \rangle\!\rangle = 0, \tag{2.21}$$

where a_i and b_i are arbitary vectors with $b_i = a_j M^{-1}_{ji}$.

Now,

$$\begin{aligned} \langle\!\langle \mathfrak{F}_{\texttt{theo}}\, \mathcal{O}_k \, \delta \mathcal{O}_i \rangle\!\rangle &= \int d\Xi \sum_{A=1}^{\infty} \frac{e^{-\mathfrak{N}_{\texttt{theo}}}}{A!} \prod_{a=1}^{A} \mathfrak{p}_{\texttt{theo}}(\xi_a) \sum_{b=1}^{A} o_k(\xi_b) \sum_{c=1}^{A} \delta o_i(\xi_c), \\ &= \left\langle \mathfrak{p}_{\texttt{theo}}\, o_k \delta o_i \right\rangle + \left\langle \mathfrak{p}_{\texttt{theo}}\, o_k \right\rangle \left\langle \mathfrak{p}_{\texttt{theo}} \delta o_i \right\rangle \,. \end{aligned} \tag{2.22}$$

Similary, we can write

$$\langle\!\langle \mathfrak{F}_{\texttt{theo}}\, \mathcal{O}_k \Gamma_j \rangle\!\rangle = M^{-1}_{jl} \left\langle \mathfrak{p}_{\texttt{theo}}\, o_k \, o_l \right\rangle + \left\langle \mathfrak{p}_{\texttt{theo}}\, o_k \right\rangle g_j, \tag{2.23}$$

where we use $M^{-1}_{jl} \left\langle \mathfrak{p}_{\texttt{theo}}\, o_l \right\rangle = g_j$. Therefore, the extremum condition is

$$b_i b_k \left\{ \mathfrak{p}_{\texttt{theo}}\, o_k + \left\langle \mathfrak{p}_{\texttt{theo}}\, o_k \right\rangle \mathfrak{p}_{\texttt{theo}} - \mathfrak{L}_{\texttt{int}}\, s_j \left[M^{-1}_{jl} \left\langle \mathfrak{p}_{\texttt{theo}}\, o_k \, o_l \right\rangle + \left\langle \mathfrak{p}_{\texttt{theo}}\, o_k \right\rangle g_j \right] \right\} = 0. \tag{2.24}$$

As we know $\mathfrak{L}_{\texttt{int}} f_i g_j = \mathfrak{p}_{\texttt{theo}}$ then

$$\mathfrak{p}_{\texttt{theo}}\, o_k = \mathfrak{L}_{\texttt{int}} f_j M^{-1}_{jl} \left\langle \mathfrak{p}_{\texttt{theo}}\, o_k \, o_l \right\rangle \Rightarrow o_k = \frac{f_k}{\mathfrak{p}_{\texttt{theo}}}, \tag{2.25}$$

for which the condition $\langle f_k \rangle = M_{kl} g_l$ is satisfied and the expression of optimal covariance matrix derived as

$$V^{\Gamma}_{ij} = \frac{1}{\mathfrak{L}_{\texttt{int}}} M^{-1} \,; \qquad M_{ij} = \mathfrak{L}_{\texttt{int}} \left\langle \frac{f_i f_j}{\mathfrak{p}_{\texttt{theo}}} \right\rangle = \left\langle \frac{f_i f_j}{\mathcal{O}_{\texttt{BSM}}} \right\rangle \,. \tag{2.26}$$

---

[2] Γ_i are the sets of function that follow the distribution $\mathfrak{F}_{\texttt{theo}}$, so that g_i are the expectation values of Γ_i.

2.2.2 SM dominance over BSM

In this section, we will calculate the expression of the optimal covariance matrix when SM dominates over BSM contribution for a specific process. A similar mathematical description has been elaborated in [122]. The observable which we take the differential cross-section, is defined as

$$\mathcal{O} = \frac{d\sigma_{\mathtt{SM}}}{d\phi} + \sum_i g_i f_i(\phi)\,, \qquad \mathcal{O}_{\mathtt{SM}} = \frac{d\sigma_{\mathtt{SM}}}{d\phi}, \tag{2.27}$$

where $\mathcal{O}_{SM}$ denotes the SM contribution to the observable and the BSM contribution ($\sum_i g_i f_i$) is considered to be small compared to SM. The probability distribution function for observing A events follows similar expression as Eq. (2.13) with $\mathfrak{N}_{\mathtt{theo}} = (\mathfrak{N}_{\mathtt{SM}} + \mathfrak{N}_{\mathtt{NP}})$ is

$$P_{\mathtt{theo}} = \frac{1}{\Sigma_{\mathtt{theo}}}\frac{d\sigma_{\mathtt{theo}}}{d\xi} = \frac{d\sigma_{\mathtt{SM}}/d\xi + g_i f_i}{\Sigma_{\mathtt{SM}} + g_i \langle f_i \rangle}\,, \tag{2.28}$$

$$= P_{\mathtt{SM}} + g_i \left(\frac{f_i - P_{\mathtt{SM}} \langle f_i \rangle}{\Sigma_{\mathtt{SM}}} \right) + O(g^2)\,; \qquad P_{\mathtt{SM}} = \frac{1}{\Sigma_{\mathtt{SM}}}\frac{d\sigma_{\mathtt{SM}}}{d\phi}. \tag{2.29}$$

Now, likewise Eq. (2.13), we define

$$\mathfrak{p}_{\mathtt{SM}} = \mathfrak{N}_{\mathtt{SM}} P_{\mathtt{SM}} = \mathfrak{L}_{\mathtt{int}} \frac{d\sigma_{\mathtt{SM}}}{d\phi}. \tag{2.30}$$

Similar to the previous case, here we choose a set of observables $o_i(\phi)$ and define

$$\mathcal{O}_i(A;\, \Phi_A) = \frac{1}{\mathfrak{N}_{\mathtt{SM}}} \sum_{a=1}^{A} o_i(\phi_a). \tag{2.31}$$

Using Eq. (2.13) and Eq. (2.29), following term can be expanded as

$$\langle\!\langle \mathfrak{F}_{\mathtt{theo}} \mathcal{O}_i \rangle\!\rangle = \langle P_{\mathtt{sm}} o_i \rangle + \frac{1}{\mathfrak{N}_{\mathtt{SM}}} \sum_j C_{ij} g_j + \cdots\,, \qquad C_{ij} = \mathfrak{L}_{\mathtt{int}} \langle o_i f_j \rangle\,, \tag{2.32}$$

so,

$$\langle\!\langle \mathfrak{F}_{\mathtt{theo}} \Gamma_j \rangle\!\rangle = g_j\,, \qquad \Gamma_j = \mathfrak{N}_{\mathtt{SM}} \sum_i C^{-1}_{ji} \left[\mathcal{O}_i - \langle P_{\mathtt{sm}} o_i \rangle \right]. \tag{2.33}$$

Now, putting the expression of Γ_j into Eq. (2.20), it is straightforward to show that

$$\delta \left(\frac{1}{2} V^{\Gamma}_{ij} a_i a_j \right) = 0 \Rightarrow o_i = \frac{f_i}{P_{\mathtt{sm}}}. \tag{2.34}$$

Substituting Eq. (2.34) into Eq. (2.17), we get

$$C_{ij} = \mathfrak{L}_{\mathtt{int}} \left\langle \frac{f_i f_j}{P_{\mathtt{sm}}} \right\rangle = \frac{\mathfrak{L}_{\mathtt{int}}}{\Sigma_{\mathtt{SM}}} \left\langle \frac{f_i f_j}{\mathcal{O}_{\mathtt{SM}}} \right\rangle. \tag{2.35}$$

Therefore, the optimal covariance matrix can be expressed as

$$\begin{aligned} V_{ij} =& \Sigma_{\mathtt{SM}} C^{-1}_{ij} = \frac{1}{\mathfrak{L}_{\mathtt{int}}} \left\langle \frac{f_i f_j}{\mathcal{O}_{\mathtt{SM}}} \right\rangle^{-1}, \\ =& \frac{M^{-1}_{ij}}{\mathfrak{L}_{\mathtt{int}}}, \quad M_{ij} = \left\langle \frac{f_i f_j}{\mathcal{O}_{\mathtt{SM}}} \right\rangle. \end{aligned} \tag{2.36}$$

2.2.3 OOT with non-interfering SM background

In the previous two cases, the discussion on evaluating the optimal covariance matrix (V_{ij}) is based on a signal-based hypothesis where we have assumed negligible SM backgrounds. The exclusion of SM backgrounds is justified as long as cuts on a collider variable(s) can be used to reduce the SM backgrounds maximally. Now if the whole SM background can not be nearly eliminated after employing cut on a particular or several collider variables, then the estimation of NP uncertainties will have deviation from the actual value when we use the above expressions of covariance matrix. Moreover, the above analyses rely on the utilization of the analytical expression of a specific observable at the production level, incorporating an efficiency factor (ϵ) to imitate the final state. If we assume that the cut efficiencies do not alter the phase space correlations of either the signal or the background, then, we can write the observable including the SM background contribution as

$$\mathcal{O} = \frac{d\sigma_{\texttt{theo}}}{d\phi} = \epsilon_s \mathcal{O}_{\texttt{sig}} + \epsilon_b \mathcal{O}_{\texttt{bkg}} = \sum_i g_i f_i(\phi)\,. \tag{2.37}$$

The presence of the second term in the observable, i.e. the SM background makes an important distinction of Eq. (2.37) from the previous ones. Here g_i are the non-linear functions of NP couplings and f_i are the function of phase-space co-ordinate ϕ and ϵ_s (ϵ_b) is the signal (background) efficiencies in estimating the signal (and background) after using judicious cuts. This methodology relies on the fact that we have analytical expressions of both signal and background productions, the reconstruction of final state events to the hard production level is possible within the efficiency factor(s) included above and in the process of successive cuts, the phase space orientations of the observable do not change significantly, other than reducing the number of events. We will provide an example later where Eq. (2.37) can be used to estimate OOT in presence of SM background. However, there are ample cases where either or all of the above approximations won't work and we need to think of some alternative way to do the optimization of the covariance matrix. In this section, we will discuss a numerical method to incorporate the SM background to estimate the uncertainties of NP couplings for a particular final state using OOT.

Suppose the theory under study has 2 parameters of interest, a, b, and that the amplitude is linear in these parameters. It follows that the differential cross-section takes the form

$$\frac{d\sigma}{d\phi} = \mathcal{O}_{\texttt{tot}} = f_0 + af_1 + bf_2 + a^2 f_3 + abf_4 + b^2 f_5 = \sum_{i=0}^{5} g_i f_i, \tag{2.38}$$

where, f_i are the phase space functions and $g_0 = 1,\ g_1 = a,\ g_2 = b,\ g_3 = a^2,\ g_4 = ab,\ g_5 = b^2$. Now, we divide the phase space into $\texttt{R}$ bins $b_1,\ b_2, \ldots, b_{\texttt{R}}$ and then define

$$\Delta_{\texttt{r}} = \int_{b_{\texttt{r}}} d\phi, \tag{2.39}$$

and

$$n_{\texttt{r}i} = \mathfrak{L}_{\texttt{int}} \int_{b_{\texttt{r}}} d\phi f_i. \tag{2.40}$$

The total number of events in b_{r} is

$$N_r = \mathfrak{L}_{\mathtt{int}} \int_{b_{\mathrm{r}}} d\phi \mathcal{O} = \sum_i g_i n_{\mathrm{r}i}. \tag{2.41}$$

Now, if the bins are small enough the f_i will be approximately constant inside them, then

$$\begin{aligned} f_i|_{b_{\mathrm{r}}} &\simeq \frac{1}{\Delta_{\mathrm{r}}} \int_{b_{\mathrm{r}}} d\phi f_i = \frac{1}{\Delta_{\mathrm{r}}} \frac{n_{\mathrm{r}i}}{\mathfrak{L}_{\mathtt{int}}}, \\ \mathcal{O}|_{b_{\mathrm{r}}} &\simeq \frac{1}{\Delta_{\mathrm{r}}} \int_{b_{\mathrm{r}}} d\phi \mathcal{O} = \frac{1}{\Delta_{\mathrm{r}}} \frac{N_{\mathrm{r}}}{\mathfrak{L}_{\mathtt{int}}}, \end{aligned} \tag{2.42}$$

whence

$$M_{ij} = \sum_r \int_{b_{\mathrm{r}}} d\phi \frac{f_i f_j}{\mathcal{O}} \simeq \sum_r \frac{1}{\mathfrak{L}_{\mathtt{int}} \Delta_{\mathrm{r}}} \frac{n_{\mathrm{r}i} n_{\mathrm{r}j}}{N_{\mathrm{r}}}, \tag{2.43}$$

with the approximation becoming increasingly accurate as $\Delta r \to 0$ and $R \to \infty$.

Now, in order to extract the $n_{\mathrm{r}i}$ note that N_r is a function of a and b, namely,

$$N_{\mathrm{r}}(a, b) = \sum_{i=0}^{5} g_i n_{\mathrm{r}i}. \tag{2.44}$$

Now, one can evaluate $n_{\mathrm{r}i}$ as

$$\begin{aligned} n_{\mathrm{r}0} =& N_{\mathrm{r}}(0,0), \\ n_{\mathrm{r}1} =& \frac{1}{2}[-3N_{\mathrm{r}}(0,0) + 4N_{\mathrm{r}}(1,0) - 3N_{\mathrm{r}}(2,0)], \\ n_{\mathrm{r}2} =& \frac{1}{2}[-3N_{\mathrm{r}}(0,0) + 4N_{\mathrm{r}}(0,1) - 3N_{\mathrm{r}}(0,2)], \\ n_{\mathrm{r}3} =& \frac{1}{2}[N_{\mathrm{r}}(0,0) - 2N_{\mathrm{r}}(1,0) + N_{\mathrm{r}}(2,0)], \\ n_{\mathrm{r}4} =& N_{\mathrm{r}}(0,0) - 2N_{\mathrm{r}}(0,1) - N_{\mathrm{r}}(1,0) + N_{\mathrm{r}}(1,1), \\ n_{\mathrm{r}5} =& \frac{1}{2}[N_{\mathrm{r}}(0,0) - 2N_{\mathrm{r}}(0,1) + N_{\mathrm{r}}(0,2)]. \end{aligned} \tag{2.45}$$

To evaluate M_{ij} for some set of seed parameters $a^{(0)}, b^{(0)}$

$$M_{ij} = \sum_r \frac{1}{\mathfrak{L}_{\mathtt{int}} \Delta_{\mathrm{r}}} \frac{n_{\mathrm{r}i} n_{\mathrm{r}j}}{N_{\mathrm{r}}}, \tag{2.46}$$

where the covariance matrix is defined as $V_{ij} = \frac{M_{ij}^{-1}}{\mathfrak{L}_{\mathtt{int}}}$. If the number of NP parameters is changed, Eq. (2.45) is also modified to evaluate M_{ij}.
Now, using the information of V_{ij} in different scenarios, χ^2 function can be written as

$$\chi^2 = \sum_{ij} (g_i - g_i^0)(g_j - g_j^0) V_{ij}^{-1}, \tag{2.47}$$

where g_i^0 are the seed values or input values that depend on the specific model or hypothesis. The limit dictated by $\chi^2 \leq n^2$ corresponds to $n\sigma$ standard deviation from seed values (g^0) is the optimal limit for any NP couplings as the covariance matrix (V_{ij}) is minimal. In the rest of the thesis, we utilise the above mentioned techniques to find optimal estimation of NP parameters for several cases of interest, compare them with the standard likelihood analysis and comment on the collider variables like CM energy, luminosity and beam polarizations, that best elicit them.

A few comments before we end this chapter. OOT is a statistical technique to estimate the future sensitivities of NP couplings in an optimal way, so that the covariance matrix is minimal w.r.t the NP coupling(s). In presence of data, for example at current luminosities of LHC, there is not much scope of statistical optimization of NP couplings, although optimization is possible to reduce systematic uncertainties, for example, by considering the ratios of observables. In such circumstances, one rather focuses to the question, which model/theory provides the best fit to that dataset for a given observable. OOT on the other hand, can indicate how precise estimation of the particular NP, dictated by the present data, is possible in future sensitivities of collider run. While this thesis primarily focuses on discussing the OOT within the context of lepton colliders, it can also be done for future LHC searches. Although a few practical challenges in precision extraction of NP couplings at the LHC persists, like the huge SM background contribution, and the lack of an analytical cross-section due to hadron scattering. However, as elaborated in Section 2.2.3, the OOT methodology enables the study of various NP scenarios across different colliders. This underscores the versatility and applicability of the OOT across diverse experimental setups.

Chapter 3

BSM dominance: Heavy charged fermions at the e^+e^- colliders

Contents

3.1 Introduction

In this chapter, we discuss an example of the optimal estimation of NP couplings in BSM dominated scenario. Concerning this, we will first study the detectability of a singly-charged lepton with mass of either 150 GeV or 245 GeV at the ILC, with a CM energy of 500 GeV and determine the optimal statistical precision to which its couplings to the Z boson can be measured using the OOT for judicious choice of beam polarization. Charged fermion pair production in the context of the type-III seesaw framework has been studied in literature [124, 125], but no study has been done yet using the optimal observable approach. We will then consider this particle in the context of a specific NP model and provide an event-level collider simulation of its dominating decay channel; this model has the added feature of containing a viable dark matter candidate, some of whose effects at the ILC will also be considered. We will discuss the effects of beam polarization and the extent to which the conclusions drawn for these specific cases can be generalized.

The current bounds on heavy lepton masses depend on their nature (chiral or vector-like) and dominating decay channels. For example, LEP put a bound on the mass of 101.2 GeV (95% CL) on the mass of heavy, unstable, singly-charged fermion [126] when its main decay channel is $\nu W^{\pm}$, while the bound is 102.6 GeV (95% C.L.)

if it is stable [127]. Searches at LHC have been so far in three main directions: *(i)* triplet leptons associated with type III seesaw mechanism for neutrino mass generation [128]; *(ii)* stable or long-lived charged leptons; and *(iii)* superpartners of the SM gauge bosons (neutralino and chargino). In the first case, CMS has put a (3σ) bound of 840 GeV [128] (using $137\,\mathrm{fb}^{-1}$ of data at $\sqrt{s} = 13$ TeV). The current bound for a long-lived singly charged fermion is $\sim$ 574 GeV [129] (CMS, using $18.8\,\mathrm{fb}^{-1}$ of data at $\sqrt{s} = 8$ TeV). The limit on chargino mass in supersymmetric theories from the production of chargino pairs [130] is $\sim$ 400 GeV when the neutralino mass is zero, and ~ 250 GeV from chargino-neutralino pair production [131] (both obtained at CM energy $\sqrt{s} = 13$ TeV).

The OOT has been used previously in a variety of studies, including the estimation of the uncertainty of the Higgs couplings [132, 133] and top-quark couplings at e^+e^- colliders [134–138], of the top-quark interactions in a $\gamma\gamma$ collider [139–141], of the CP properties of Higgs boson at a muon collider [142], and of possible non-standard top-quark couplings at the LHC [143–145]; other studies using this technique include estimating the sensitivity to NP effects in flavor physics [146–148] and NP searches in top-quark production at the $e\gamma$ colliders [149].

This chapter is organized as follows: the phenomenological framework that we will use to study the Z couplings of a heavy charged lepton is presented in Section 3.2; Section 3.3 and Section 3.4 discuss the relevant cross-section calculations and OOT for this framework; the UV-complete model and associated collider signals are examined in Section 3.5 and Section 3.6; with Section 3.7 containing parting comments and summary.

3.2 Phenomenological framework

In this and the following sections, we will use the OOT to determine the accuracy to which the parameters of a simple model of BSM physics can be measured at the ILC. The model we consider is a simple extension of the SM by the addition of a heavy charged fermion $\psi^\pm$, that can be produced by Z and photon exchange (Fig. 3.1). We will discuss the precision to which the OOT allows the determination of the ψ couplings to the Z at an e^+e^- collider.

This type of heavy fermion appears in various extensions of SM; *e.g.* those containing a fermion isodoublet (ψ^0, ψ^-) with hypercharge $Y_\psi = -1$; we elaborate upon a possible model framework in Section 3.5. Here we adopt a purely phenomenological approach, allowing $\psi^\pm$ to have general chiral couplings to the Z boson[1]:

$$\psi^+\psi^- Z : -\frac{ie_0}{s_{2\mathrm{w}}}\gamma^\mu\left(a + b\gamma^5\right) \,, \tag{3.1}$$

where $s_{2\mathrm{w}} = \sin(2\theta_\mathrm{w})$; θ_w is the weak-mixing angle. We assume [2] that $\psi^\pm$ has the usual minimal coupling to the photon:

$$\psi^+\psi^-\gamma : -ie_0\gamma^\mu \,. \tag{3.2}$$

The parameters $a,\ b$ correspond to the p_a discussed briefly at the end of section 2.2.1.

---

[1] We postpone any constraints coming from chiral anomalies to our discussion of a specific model.

[2] It is worth noting that in weakly-coupled theories modifications to the photon minimal coupling are generated at 1 or higher loops and are correspondingly suppressed.

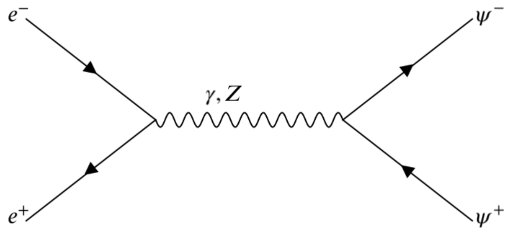

Figure 3.1: Production of heavy charged fermions ($\psi^+\psi^-$) at e^-e^+ collision (ILC).

We will call any specific choice of $\{a,\, b\}$ a *hypothesis* and the corresponding parameters as *seed parameters*, of which we will consider the following:

- $a = \pm 1, b = 0$ (pure vector coupling).
- $a = 0, b = \pm 1$ (pure axial vector coupling).
- $a = \pm 1, b = \pm 1$ (chiral coupling).

We note that, for this simple model, $b \to -b$ is under a parity transformation, so we need to consider only $b \geq 0$.

Using the couplings in Eqs. (3.1) and (3.2), we can evaluate $d\sigma_{\mathtt{theo}}$ and, upon selection of the f_i, extract the coefficients $g_i = g_i(a, b)$; the hypothesis $a = a^0$, $b = b^0$ corresponds to assuming that these coefficients have seed values $g_i^0 = g_i(a^0, b^0)$. We then use Eq. (2.26) to compute the covariance matrix V and corresponding χ^2; the regions χ^2 <const. determine the optimal statistical uncertainties and the accuracy to which different hypotheses can be differentiated.

For the calculations below we will assume the following collider parameters:

$$m_{\psi^\pm} = 150 \text{ GeV}\,, \text{ or } 245 \text{ GeV}\,, \qquad \sqrt{s} = 500 \text{ GeV}\,; \quad \mathfrak{L}_{\mathtt{int}} = 567 \text{ fb}^{-1}\,, \tag{3.3}$$

where $\sqrt{s}$ is the CM energy of the collider and integrated luminosity $\mathfrak{L}_{\mathtt{int}}$, whose values were taken from the ILC design parameters [102]. The lower value of $m_{\psi^\pm}$ is chosen above the current collider limit of $O(100)$ GeV [127] (Section 3.1) [3]; the higher value is chosen to be close to the threshold.

3.3 The $\psi^+\psi^-$ production cross-section

The amplitude for the process $e^+e^- \to \psi^+\psi^-$, which we denote by $\mathcal{M}(\lambda_{e^-},\, \lambda_{e^+},\, \lambda_\psi,\, \lambda_{\bar{\psi}})$ (where $\lambda_i = \pm 1$ denotes the helicity of particle i), is easily calculated [150]:

$$\begin{aligned} \mathcal{M}(\lambda_{e^-},\, -\lambda_{e^-},\, \lambda_\psi,\, -\lambda_\psi) &= -ee_0\, (P_{e^-}\lambda_\psi + \cos\theta)\, [1 + \xi\, (a + b\lambda_\psi\beta_\psi)]\ ; \quad \xi = \xi_1 + \lambda_{e^-}\xi_2 \\ \mathcal{M}(\lambda_{e^-},\, -\lambda_{e^-},\, \lambda_\psi,\, \lambda_\psi) &= -ee_0 \left(\frac{2m_{\psi^\pm}\lambda_\psi \sin\theta}{\sqrt{s}} \right) (1 + \xi a)\ , \end{aligned} \tag{3.4}$$

where e is the electron charge, $\sqrt{s}$ is the CM energy, $\beta_\psi = \sqrt{1 - 4m_{\psi^\pm}^2/s}$, and

$$\xi_1 = \frac{C_v}{s_{2\mathtt{w}}^2(1 - m_{\mathtt{z}}^2/s)}\,, \qquad \xi_2 = \frac{C_a}{s_{2\mathtt{w}}^2(1 - m_{\mathtt{z}}^2/s)}\,, \tag{3.5}$$

---

[3] This limit is obtained using the $\psi^\pm \to W^\pm$+neutral decay, which naturally occurs in the simplest models containing a $\psi^\pm$; see Section 3.5.

with $C_v = (4s_w^2 - 1)/2$, $C_a = 1/2$, the vector and axial couplings of the electron to the Z, respectively (and $s_w = \sin\theta_w$). If $\hat{\mathbf{p}}_{e^-}$ and $\hat{\mathbf{p}}_{\psi^-}$ are unit vectors parallel to the corresponding momenta, then the scattering angle θ is defined by $\cos\theta = \hat{\mathbf{p}}_{e^-} \cdot \hat{\mathbf{p}}_{\psi^-}$.

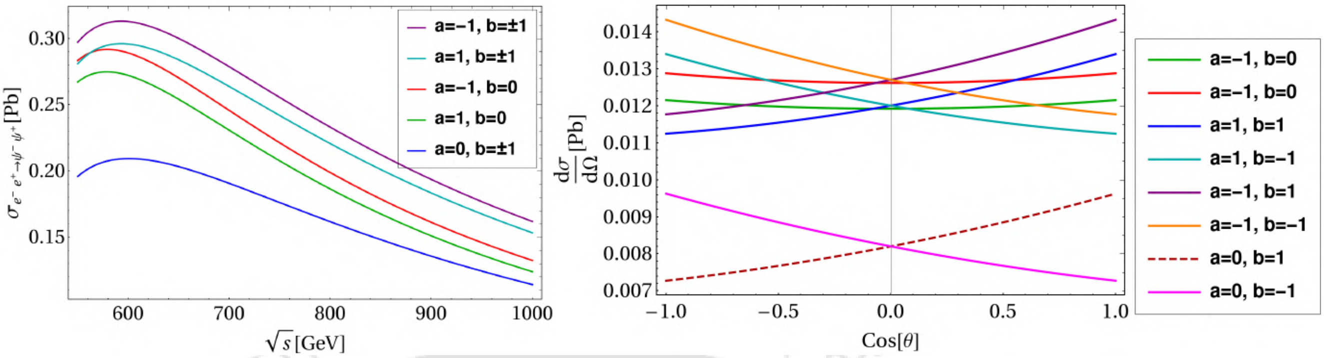

Figure 3.2: Left: Total spin-averaged cross-section for $e^+e^- \to \psi^+\psi^-$ as a function of the CM energy $\sqrt{s}$; right: differential spin-averaged cross-section as a function of the scattering angle for CM energy $(\sqrt{s}) = 500$ GeV. We took $m_{\psi^\pm} = 245$ GeV and the collider parameters of Eq. (3.3).

Using Eq. (3.4), the cross-section when the $e^\pm$ beams have partial polarizations $P_{e^\pm}$ (with $-1 \le P_{e^\pm} \le 1$) is given by[4]

$$\begin{aligned}\frac{d\sigma(P_{e^+}, P_{e^-})}{d\Omega} &= \sum_{\lambda_e^+ = \pm 1} \sum_{\lambda_e^- = \pm 1} \frac{(1 + \lambda_{e^-} P_{e^-})(1 + \lambda_{e^+} P_{e^+})}{4} \left(\frac{d\sigma}{d\Omega}\right)_{\lambda_{e^-}, \lambda_{e^+}}; \\ &= \sum c_i f_i\,,\end{aligned} \tag{3.6}$$

where we choose [5]

$$\{f_1,\, f_2,\, f_3\} = \frac{\beta_\psi}{2s}\left\{(2 - \beta_\psi^2),\, \beta_\psi \cos\theta,\, \beta_\psi^2 \cos^2\theta\right\}\,, \tag{3.7}$$

and

$$\begin{aligned}\frac{g_1}{\alpha\alpha_0} &= \frac{1 - P_{e^-} P_{e^+}}{2}\left[1 + 2\xi_1 a + (\xi_1^2 + \xi_2^2)\left(a^2 + \frac{\beta_\psi^2}{2 - \beta_\psi^2} b^2\right) - 2P_{\tt eff}\left\{\xi_2 a + \xi_1\xi_2 a^2 + \frac{\beta_\psi^2}{2 - \beta_\psi^2}\xi_1\xi_2 b^2\right\}\right]; \\ \frac{g_2}{\alpha\alpha_0} &= \frac{1 - P_{e^-} P_{e^+}}{2}\left[2\xi_2 b + 4\xi_1\xi_2 ab - P_{\tt eff}\left\{2\xi_1 b + (\xi_1^2 + \xi_2^2) ab\right\}\right]; \\ \frac{g_3}{\alpha\alpha_0} &= \frac{1 - P_{e^-} P_{e^+}}{2}\left[1 + 2\xi_1 a + (\xi_1^2 + \xi_2^2)(a^2 + b^2) - 2P_{\tt eff}\left\{\xi_2 a + \xi_1\xi_2(a^2 + b^2)\right\}\right];\end{aligned} \tag{3.8}$$

We defined

$$P_{\tt eff} = \frac{P_{e^-} - P_{e^+}}{1 - P_{e^-} P_{e^+}}. \tag{3.9}$$

and $\alpha_0 = e_0^2/(4\pi)$, while $\alpha = e^2/(4\pi)$ is the usual fine-structure constant. It is also useful to note that $d\sigma/d\Omega$ is invariant under $b \to -b$ and $\theta \to \pi - \theta$, a consequence of the invariance of Eqs. (3.1) and (3.2) under CP.

---

[4] $\lambda_i = +1(-1)$ denotes right (left)-handed helicity.

[5] It is straightforward to verify that these functions are linearly independent.

The spin-averaged total and differential cross-sections (corresponding to $P_{e^\pm} = 0$) for different seed values of $\{a, b\}$ are plotted in Fig. 3.2. It is worth noting that the total cross sections exhibit the same behavior for the values of a and b considered, especially at large s; this is due to a combination of two effects. First, since $s_{\rm w}^2 \simeq 1/4$, $\xi_1 \sim 0$; second, for large s, $\beta_\psi \simeq 1$; it follows that the average cross section $\sigma \propto 1 + \xi_2^2(a^2 + b^2)$, explicitly displaying its dependence on a and b. In contrast, the unpolarized *differential* cross section depends on $c_2 \simeq \xi_2 b$ and will have very different behavior depending on the values of b. As expected from unitarity, the total cross-section drops with increasing CM energy.

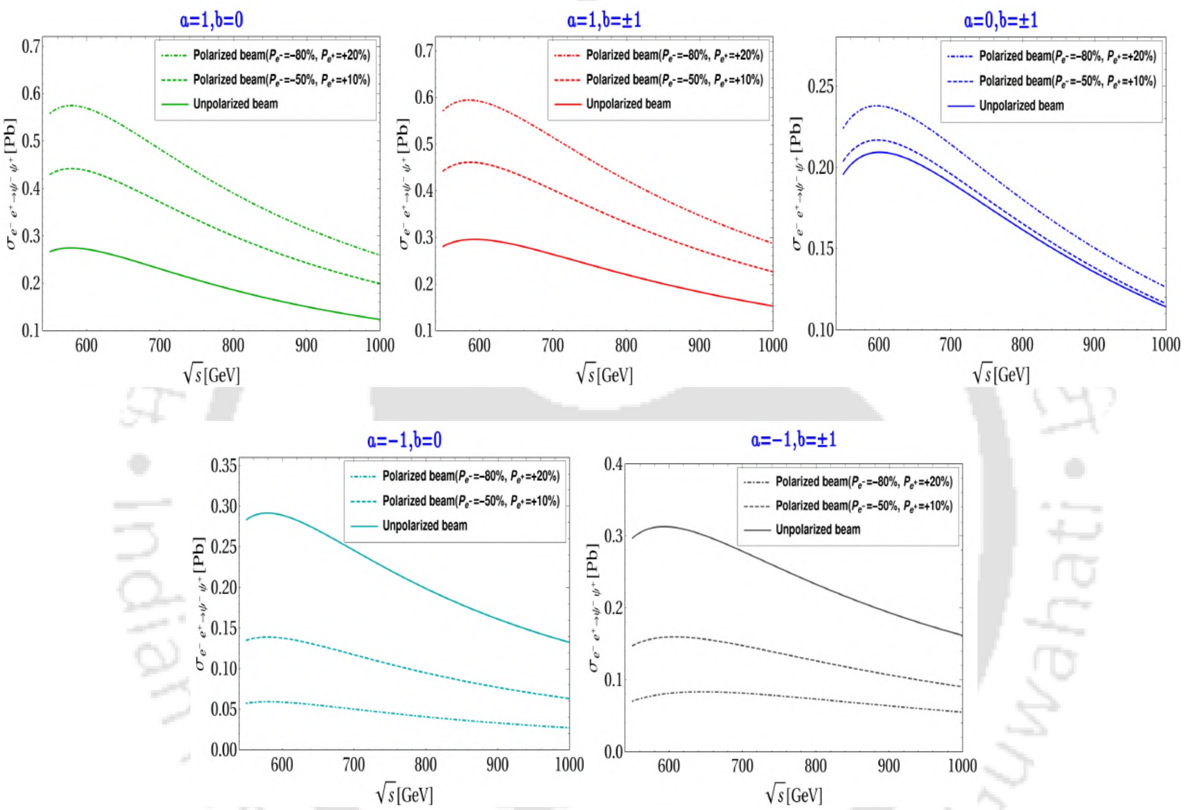

Figure 3.3: Total cross-section as a function of the CM energy for unpolarized ($P_{e^\pm} = 0$) beams (solid line); $P_{e^\mp} =^{-50\%}_{+10\%}$ (dashed line), and $P_{e^\mp} =^{-80\%}_{+20\%}$ (dashed-dot line) for various seed values of a and b.

According to the design report [102], the ILC will produce highly polarized electron beam and moderately polarized positron beam; we will choose $P_{e^-} = -0.8,\ P_{e^+} = +0.2$ when considering this option. Also, for polarized beams we have

$$\begin{aligned} a > 0: &\quad \sigma\left(P_{e^-},\, P_{e^+}\right) \geq \sigma\left(P_{e^\pm} = 0\right)\,, \\ a < 0: &\quad \sigma\left(P_{e^-},\, P_{e^+}\right) \leq \sigma\left(P_{e^\pm} = 0\right)\,, \end{aligned} \tag{3.10}$$

whence it follows that polarization will enhance detectability. We illustrate these features in Fig. 3.3 where we plot the total cross section for various seed values of a, b and choices of $P_{e^\pm}$.

The covariance matrix (V_{ij}) as defined in Eq. (2.26) has been derived at the production level ($\psi^+\psi^-$). It is straightforward to show that for a particular final state signal, V_{ij} is scaled by a efficiency factor (ϵ). In the following we will consider the (electron-positron) collider production of NP which in turn decays to SM states; symbolically, $e^+e^- \to$NP$\to$SM. We denote the 'hard' cross section for $e^+e^- \to$NP production by $\sigma^{\mathtt{NP}}$, and by $\sigma^{\mathtt{FS}}$ the final-state cross section $e^+e^- \to$NP$\to$SM, including all event selection cuts aimed at reducing and SM background and enhancing the NP contribution. The efficiency factor is defined by the ratio

$$\epsilon = \frac{\sigma^{\mathtt{FS}}}{\sigma^{\mathtt{NP}}}. \tag{3.11}$$

We would also like to note further that the statistical analysis done in Section 3.4 is based on the NP signal process without including the effects of SM backgrounds, since this requires a specific model for a detailed characterization of the final state events (we return to this in Section 3.5). However, the efficiency ϵ in Eq. (3.11) includes not only the branching ratio of NP$\to$ SM final state, but also the effects of event selection cuts that suppress the SM background contamination. The values of ϵ must be then estimated using a complete model of NP production and decay; in the next section we will assume $\epsilon = 0.001$ and 0.005, justified by the analysis of the specific model in Section 3.6. The use of ϵ to include these effects is, of course, an approximation; it is appropriate for the type of situations we consider: the resonant production of new particles which then decay into a SM final state. This approximation would not be appropriate in processes where on-shell NP particle is similar in mass and spin to that of a SM particle leading to same signal and providing large interference (for example, a new $Z^{'}$ boson having similar mass to SM Z boson), or when the new particle contribution to the signal is virtual or in narrow-width s-channel resonance. In all such cases the cross section in Eq. (2.7) receives also a non-interfering SM background contribution, and the corresponding OOT must be modified; we will return to this issue in Chapter 6. However, the procedure as adopted here, will be less conclusive, given a large irreducible SM background contribution and the estimation of ϵ will be limited in this case.

3.4 Optimal statistical analysis

We now apply the OOT described in Section 2.2.1 to the case of $\psi^\pm$ production at the ILC, using the parameters of Eq. (3.3); the cases of 250 GeV and 2 TeV CM energy collider are briefly discussed in appendix A.1.

$\sqrt{s} = 500\,\text{GeV}\,,\quad P_{e^\pm} = 0$		
$m_{\psi^\pm}$ (GeV)	$c_i/(\alpha\alpha_0)$	$f_i \times 10^{-8}\,\text{GeV}^2$
150	$i=1: \ \frac{1}{2}(1 - 0.086a + 0.522a^2 + 0.245b^2)$	$i=1: \ 217.60$
	$i=2: \ \frac{1}{2}(1.442b - 0.124ab)$	$i=2: \ 128.00\cos\theta$
	$i=3: \ \frac{1}{2}(1 - 0.086a + 0.552(a^2+b^2))$	$i=3: \ 102.40\cos^2\theta$
245	$i=1: \ \frac{1}{2}(1 - 0.086a + 0.522a^2 + 0.011b^2)$	$i=1: \ 78.02$
	$i=2: \ \frac{1}{2}(1.442b - 0.124ab)$	$i=2: \ 7.92\cos\theta$
	$i=3: \ \frac{1}{2}(1 - 0.086a + 0.552(a^2+b^2))$	$i=3: \ 1.58\cos^2\theta.$

(3.12)

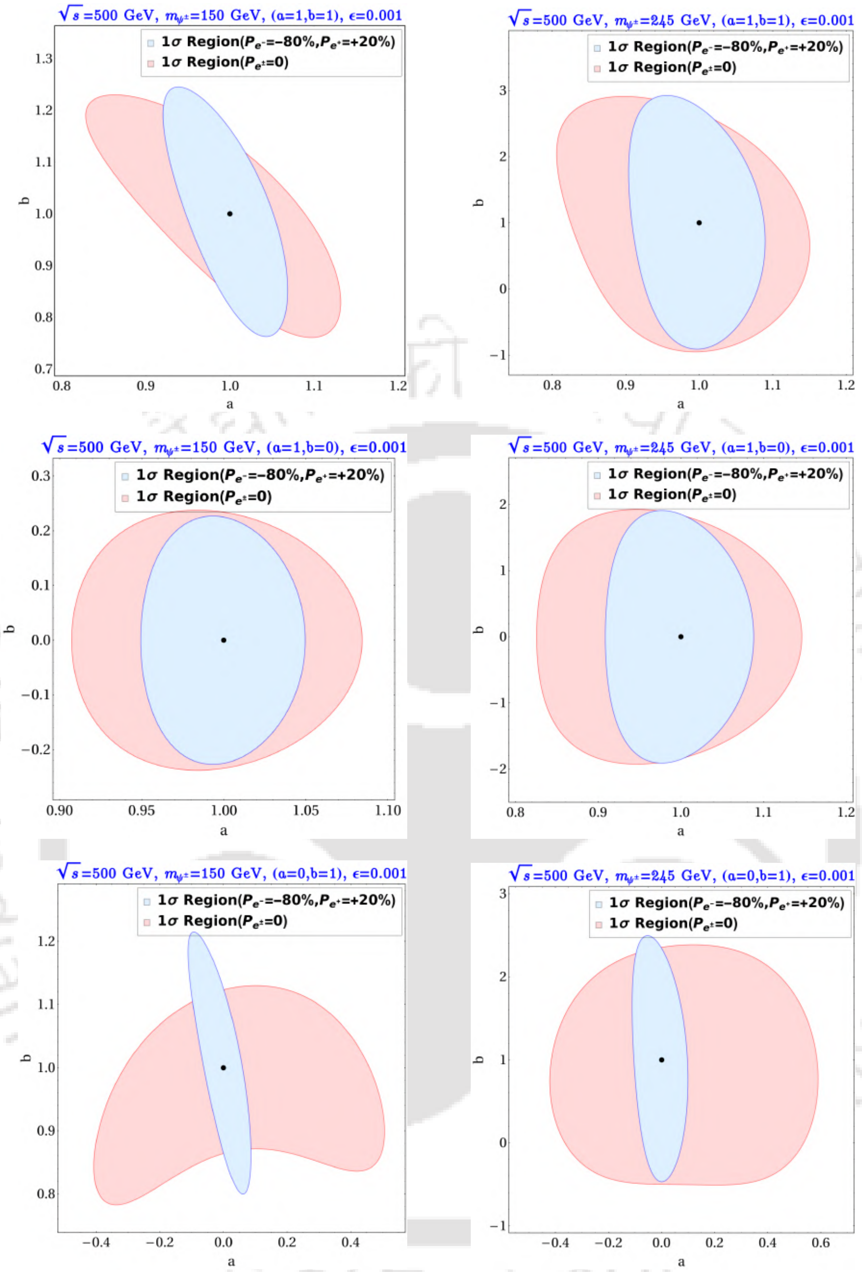

Figure 3.4: $\chi^2 = 1$ surfaces for hypotheses with $a^0 \geq 0$, $P_{e^\pm} = 0$ and $P_{e^\pm} = ^{+20\%}_{-80\%}$, and $\epsilon = 0.001$. Left (right) column: $m_{\psi^\pm} = 150\,(245)$ GeV. Note: the scales in the graphs are not all equal.

Next, the optimal 1σ statistical uncertainties in the NP parameters a, b are obtained from the $\chi^2 \leq 1$ regions using Eqs. (2.26) and (2.47) for the parameters in Eq. (3.3). As illustrative examples we the seed values listed at the beginning of this section, and take $\epsilon = 0.001, 0.005$ as reasonable estimates of the efficiency of signal identification (see Section 3.6 for a discussion); we consider both unpolarized ($P_{e^\pm} = 0$) and polarized ($P_{e^\pm} = ^{+20\%}_{-80\%}$) beams. The results are presented in Fig. 3.4 (for $a^0 \geq 0$), Fig. 3.5 (for $a^0 = -1$) and Table 3.1. These results illustrate the advan-

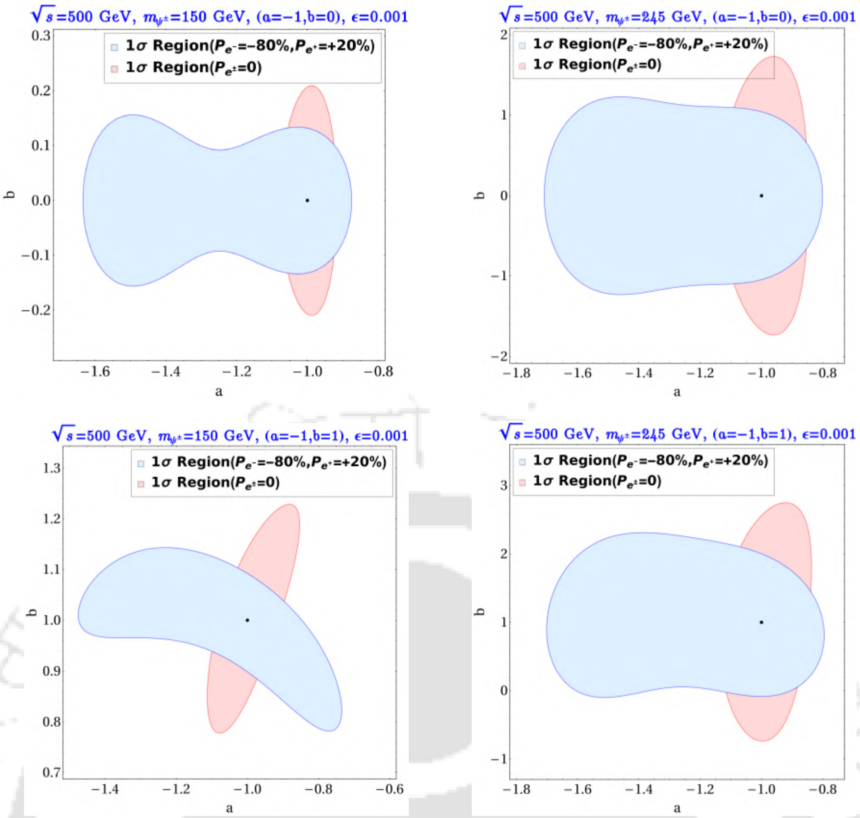

Figure 3.5: Same as Fig. 3.4 for $a^0 < 0$.

tages that polarization provides in the determination of the couplings of these new particles.

From these results we can see that of the cases considered, the $a^0 = 0$, $b^0 = \pm 1$ (pure axial coupling) hypothesis has the largest statistical errors and is, therefore, the most challenging. Also worth noting is that, while the magnitude of the total cross-section strongly affects the statistical uncertainties, it is not the only factor; this is illustrated by considering the $a^0 = -1$ case where the unpolarized cross-section is larger than the polarized one (Fig. 3.3) but the uncertainties are larger (Fig. 3.5). We also note that 1σ regions for the lower mass (150 GeV) are smaller than those for higher mass (245 GeV), making the determination of the NP couplings for the latter case more difficult.

3.4.1 Differentiation of models

One of the most important uses of the OOT is the ability to estimate the extent to which different hypotheses can be distinguished. Specifically, we consider a "base" hypothesis $a = a^0$, $b = b^0$ and, using Eq. (2.26), define

$$\left[\Delta\sigma(a^0, b^0; \bar{a}, \bar{b})\right]^2 = \epsilon \sum_{i,j} \left(g_i^0 - \bar{g}_i\right)\left(g_j^0 - \bar{g}_j\right)\left(V_0^{-1}\right)_{ij}, \quad V_0 = V(g = g^0); \tag{3.13}$$

Seed parameters		$P_{e^\pm} = 0$				$P_{e^\pm} =^{+20\%}_{-80\%}$			
		$\epsilon = 0.005$		$\epsilon = 0.001$		$\epsilon = 0.005$		$\epsilon = 0.001$	
model	$m_{\psi^\pm}$(GeV)	$\pm\Delta a$	$\pm\Delta b$	$\pm\Delta a$	$\pm\Delta b$	$\pm\Delta a$	$\pm\Delta b$	$\pm\Delta a$	$\pm\Delta b$
$a = 1,\ b = 0$	150	$+0.04$	$+0.11$	$+0.08$	$+0.24$	$+0.02$	$+0.10$	$+0.05$	$+0.23$
		-0.04	-0.11	-0.09	-0.24	-0.02	-0.10	-0.05	-0.23
	245	$+0.07$	$+0.87$	$+0.15$	$+1.95$	$+0.04$	$+0.05$	$+0.09$	$+0.91$
		-0.07	-0.87	-0.17	-1.95	-0.04	-0.05	-0.09	-0.91
$a = 1,\ b = \pm 1$	150	$+0.06$	$+0.10$	$+0.13$	$+0.23$	$+0.03$	$+0.11$	$+0.07$	$+0.25$
		-0.06	-0.10	-0.18	-0.24	-0.03	-0.11	-0.08	-0.24
	245	$+0.07$	$+0.87$	$+0.15$	$+1.96$	$+0.04$	$+0.86$	$+0.09$	$+1.93$
		-0.07	-0.87	-0.21	-1.96	-0.04	-0.86	-0.10	-1.92
$a = 0,\ b = \pm 1$	150	$+0.35$	$+0.06$	$+0.51$	$+0.13$	$+0.04$	$+0.09$	$+0.07$	$+0.22$
		-0.27	-0.11	-0.41	-0.22	-0.05	-0.09	-0.11	-0.22
	245	$+0.43$	$+0.66$	$+0.59$	$+1.39$	$+0.04$	$+0.66$	$+0.10$	$+1.50$
		-0.26	-0.67	-0.13	-1.51	-0.04	-0.66	-0.11	-1.47
$a = -1,\ b = 0$	150	$+0.04$	$+0.09$	$+0.07$	$+0.21$	$+0.06$	$+0.06$	$+0.12$	-0.16
		-0.04	-0.09	-0.07	-0.21	-0.08	-0.06	-0.63	-0.16
	245	$+0.06$	$+0.76$	$+0.15$	$+1.75$	$+0.10$	$+0.48$	$+0.20$	$+1.23$
		-0.06	-0.76	-0.15	-1.75	-0.21	-0.48	-0.71	-1.23
$a = -1,\ b = \pm 1$	150	$+0.06$	$+0.10$	$+0.15$	$+0.22$	$+0.17$	$+0.11$	$+0.26$	$+0.14$
		-0.05	-0.10	-0.11	-0.22	-0.34	-0.11	-0.48	-0.22
	245	$+0.07$	$+0.78$	$+0.17$	$+1.79$	$+0.11$	$+0.71$	$+0.20$	$+1.31$
		-0.06	-0.78	-0.14	-1.74	-0.60	-0.49	-0.70	-1.11

Table 3.1: Optimal 1σ statistical uncertainty in the a, b couplings for both unpolarized and polarized ($P_{e^\pm} =^{+20\%}_{-80\%}$) beams and two values of ϵ; we used the parameters in Eq. (3.3).

(where $g_i^0 = g_i(a^0, b^0)$, $\bar{g}_i = g_i(\bar{a}, \bar{b})$) which we take as a measure of the degree to which the $a = \bar{a}$, $b = \bar{b}$ hypothesis can be distinguished from the base hypothesis; we refer to $\Delta\sigma$ as the statistical significance of the $\bar{a}$, $\bar{b}$ hypothesis (which depends on the base model chosen).

We will use $\Delta\sigma$ as a measure of the separation of an alternate model from the base one. The distribution of $\Delta\sigma$ can also be used to determine the probability that $\Delta\sigma \leq \ell$ occurs; in general this distribution is not simple, but for the cases where g_0 and $\bar{g}$ have normal distributions with averages $\mathbb{g}_0$, $\bar{\mathbb{g}}$, and correlation matrices V_0 and $\bar{V}$ that are approximately proportional to the unit matrix, $\sigma_0^2\mathbb{I}$, $\bar{\sigma}^2\mathbb{I}$ respectively, then $\sqrt{\Delta\sigma}$ is approximately normally distributed with average $|\mathbb{g}_0 - \bar{\mathbb{g}}|/\sigma_0$ and variance $1 + (\bar{\sigma}/\sigma_0)^2$; in practice this means that the values quoted for $\Delta\sigma$ will have errors approximately $\pm\sqrt{1 + (\bar{\sigma}/\sigma_0)^2}$. Similar results hold when $\Delta\sigma$ is written in terms of a and b provided they also are normally distributed.

We now consider a few examples[6] corresponding to some of the cases presented in Table 3.2 or in Fig. 3.6, 3.7, and 3.8. If $a^0 = 1$, $b^0 = 1$ and $\bar{a} = -1$, $\bar{b} = 0$, and we choose $m_\psi = 150$ GeV, unpolarized beams, $\epsilon = 0.005$, and $\mathfrak{L}_{\texttt{int}} = 567\,\text{fb}^{-1}$, we find $\Delta\sigma \simeq 9$ with a ± 1.43 uncertainty. Assuming now $m_\psi = 245$ GeV, polarized beam ($P_{e^\pm} = ^{+20\%}_{-80\%}$), $\epsilon = 0.001$, and $\mathfrak{L}_{\texttt{int}} = 567\,\text{fb}^{-1}$ and taking $a^0 = 0$, $b^0 = 0$ as the base model, we find that when $\bar{a} = 1$, $\bar{b} = 0$ (the purely vector-like case) $\Delta\sigma = 13.96$ with ± 1.05 uncertainty; if $\bar{a} = 1$, $\bar{b} = 1$ we find $\Delta\sigma = 14.09$ with an uncertainty of ± 1.07. We do not consider the $a^0 = 0, b^0 = \pm 1$ cases since the $\Delta\sigma$ distribution is not normal, however, we expect that the uncertainties in these cases will continue to be $O(\lesssim 10\%)$.

It is worth noting that, as expected, larger efficiency ϵ and luminosity $\mathfrak{L}_{\texttt{int}}$ increase the significance, while larger masses reduce it. It is also important to note that though the significance $\Delta\sigma$ depends on the magnitude of the cross-section of the base model, this is not the only factor. For the example considered, the unpolarized cross section of the base model $a^0 = b^0 = 0$ is smaller than the one for polarized beams by about 30%, yet the significance of the $\bar{a} = 0$, $|\bar{b}| = 1$ models is the same, while that of $\bar{a} = 1$, $\bar{b} = 0$ is larger than expected from the cross-section alone.

3.5 Model example and dark matter phenomenology

The above analysis focused on the application of the OOT to the study and detectability of the properties of a hypothetical new heavy lepton. In this section, we turn to a possible underlying economical and UV complete model that contains such a particle. This model provides a viable theoretical underpinning of the previous discussion, a framework for studying other aspects of its detectability at the ILC, and can be used to obtain an estimate of the efficiency ϵ. In addition, the study of this model using event-level simulation allows for a comparison of the expected ILC sensitivity to the optimal statistical uncertainties derived above. Finally, we will see that the model proposed contains a viable dark matter candidate, satisfying the relic density, direct-search, and electroweak constraints in a large region of parameter space.

---

[6] For these choices V_0, $\bar{V}$ are approximately proportional to $\mathbb{I}$.

model	ϵ	$\mathfrak{L}_{\texttt{int}}$ (fb^{-1})	significance($\Delta\sigma$)			
			$m_{\psi^\pm} = 150$ GeV		$m_{\psi^\pm} = 245$ GeV	
			$P_{e^\pm} = 0$	$P_{e^\pm} = {}^{+20\%}_{-80\%}$	$P_{e^\pm} = 0$	$P_{e^\pm} = {}^{+20\%}_{-80\%}$
$\bar{a} = 1,\ \bar{b} = 0$	0.001	567	6.13	25.03	3.42	13.96
	0.001	2000	11.51	47.03	6.62	26.22
	0.005	567	13.72	55.98	7.65	31.21
$\bar{a} = 1,\ \bar{b} = \pm 1$	0.001	567	11.46	29.81	3.58	14.09
	0.001	2000	21.52	56.00	6.73	26.46
	0.005	567	25.62	66.67	8.01	31.50
$\bar{a} = 0,\ \bar{b} = \pm 1$	0.001	567	7.07	7.09	0.68	0.69
	0.001	2000	13.28	13.32	1.28	1.29
	0.005	567	15.81	15.86	1.52	1.54
$\bar{a} = -1,\ \bar{b} = 0$	0.001	567	8.65	10.81	4.82	6.01
	0.001	2000	16.24	20.30	9.05	11.28
	0.005	567	19.33	24.17	10.78	13.44
$\bar{a} = -1\ ,\bar{b} = \pm 1$	0.001	567	14.15	14.92	4.99	5.92
	0.001	2000	26.57	28.02	9.36	11.12
	0.005	567	31.63	33.36	11.15	13.24

Table 3.2: Statistical significance $\Delta\sigma$ (see Eq. (3.13)) of hypotheses $\bar{a}$, $\bar{b}$ with respect to the base hypothesis $a^0 = b^0 = 0$.

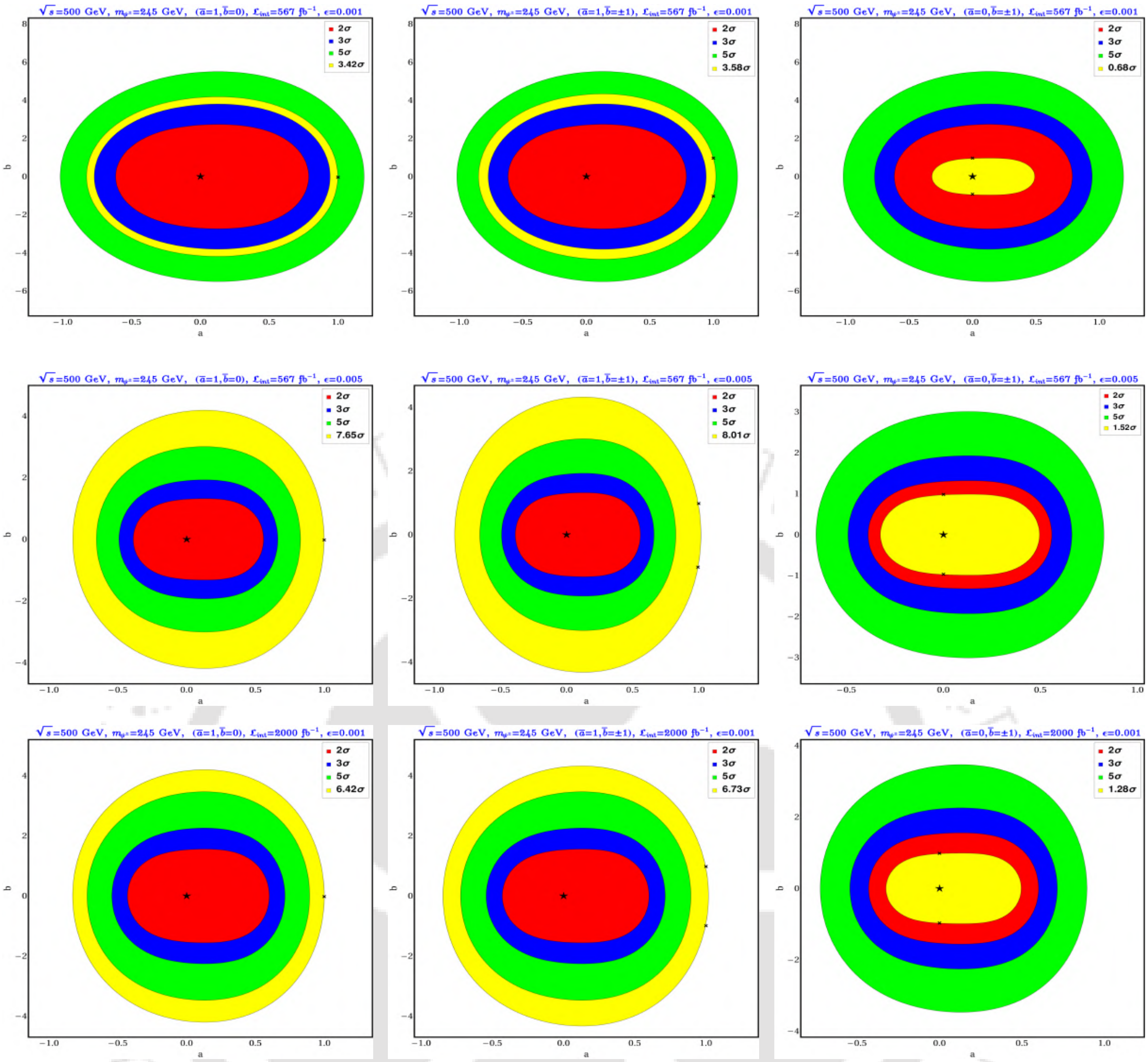

Figure 3.6: 2σ, 3σ, and 5σ regions (red, blue, and green, respectively) when $a^0 = b^0 = 0$, indicated by a star. The yellow area denotes the significance, Eq. (3.13), of alternate hypotheses $a = \bar{a}$, $b = \bar{b}$ (indicated by crosses) for various choices of luminosity ($\mathfrak{L}_{\mathtt{int}}$) and efficiency ($\epsilon$): $\bar{a} = 1$, $\bar{b} = 0$ (left column), $\bar{a} = 1$, $\bar{b} = \pm 1$ (middle column) and $\bar{a} = 0$, $\bar{b} = \pm 1$ (right column). We assumed $m_{\psi^\pm} = 245$ GeV and unpolarized beams.

The model consists of an extension of the SM by two vector-like leptons: a weak iso-doublet, $\psi = (\psi^0, \psi^-)$ of hypercharge -1, and an iso-singlet χ of zero hypercharge; both ψ and χ are odd under an exact $\mathbb{Z}_2$ symmetry under which all the SM fields are even [151, 152]. Upon electroweak symmetry breaking (EWSB) the $\psi\chi H$ Yukawa coupling (see Eq. (3.14) below) generates a mixing between the neutral component ψ^0 and χ, the resulting lighter mass eigenstate will be odd under $\mathbb{Z}_2$ and therefore stable and serves as a DM candidate. The quantum numbers under the SM$\times\mathbb{Z}_2$ symmetry are summarized in Table 3.3.

The Lagrangian of the model is

$$\mathcal{L}^{\mathtt{VF}} = \bar{\psi}\left[i\left(\not{\partial} - i\frac{g}{2}\sigma\cdot\not{W} - i\frac{g'}{2}\not{B}\right) - m_{\psi^\pm}\right]\psi + \bar{\chi}\left(i\not{\partial} - m_\chi\right)\chi - \left(Y_1\bar{\psi}\widetilde{H}\chi + \text{H.c}\right)\,, \tag{3.14}$$

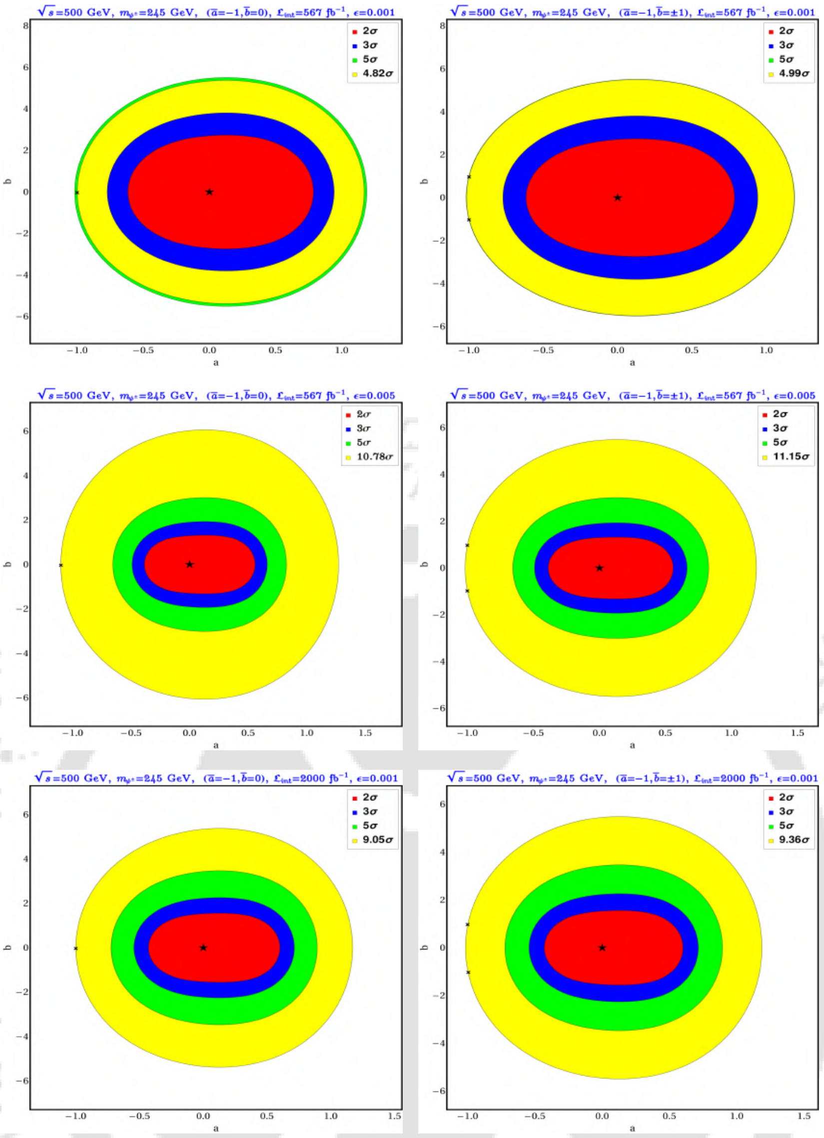

Figure 3.7: Same as Fig. 3.6 for $\bar{a} = -1,\ \bar{b} = 0$ (left column) and $\bar{a} = -1,\ \bar{b} = \pm 1$ (right column).

with the usual SM terms. After electroweak symmetry breaking H acquires a vev $v/\sqrt{2}$:

$$H \to \frac{v+h}{\sqrt{2}} \begin{pmatrix} 1 \\ 0 \end{pmatrix}, \tag{3.15}$$

and, as noted above, the χ and ψ_0 will mix through the Yukawa interaction $\propto Y_1$. The mass Lagrangian then becomes

$$-\mathcal{L}_{\texttt{mass}} = (\bar{\chi}, \bar{\psi}^0) \begin{pmatrix} m_\chi & \mu \\ \mu & m_{\psi^\pm} \end{pmatrix} \begin{pmatrix} \chi \\ \psi^0 \end{pmatrix} + m_{\psi^\pm} \psi^+ \psi^-; \qquad \mu = \frac{Y_1 v}{\sqrt{2}}. \tag{3.16}$$

The mass eigenstates $\psi_{1,2}$ are then given by

$$\begin{pmatrix} \chi \\ \psi^0 \end{pmatrix} = \begin{pmatrix} \cos\gamma & \sin\gamma \\ -\sin\gamma & \cos\gamma \end{pmatrix} \begin{pmatrix} \psi_1 \\ \psi_2 \end{pmatrix}; \qquad \tan 2\gamma = \frac{2\mu}{m_\chi - m_{\psi^\pm}}. \tag{3.17}$$

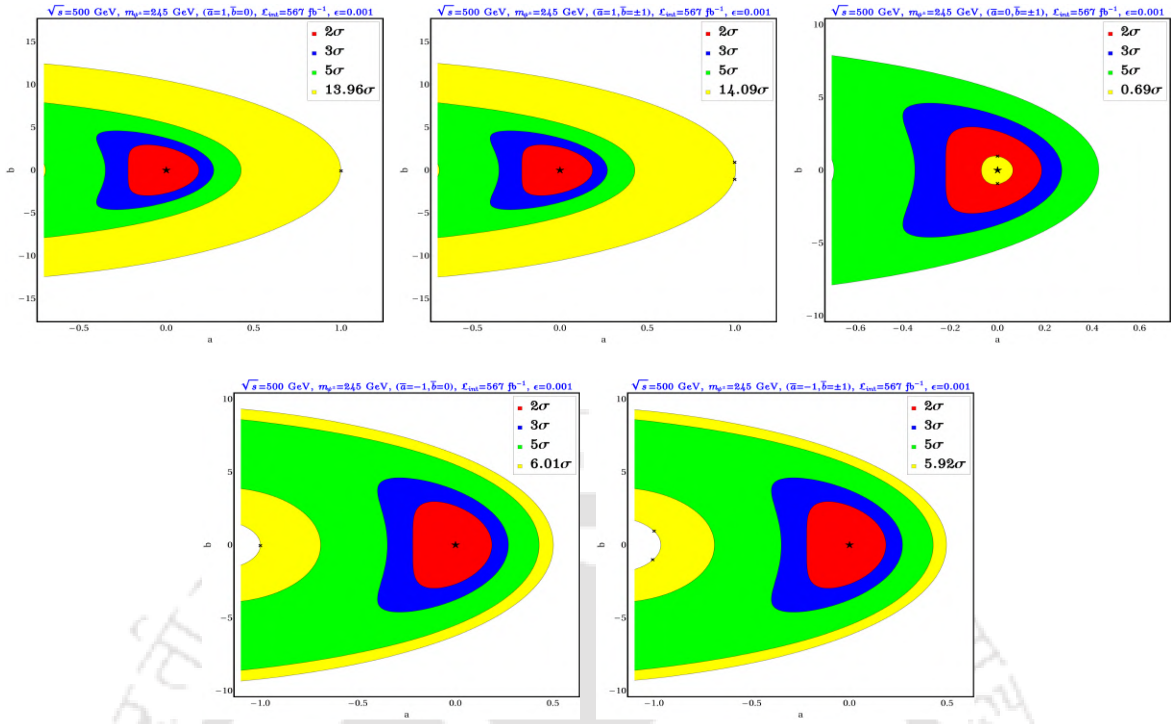

Figure 3.8: Same as Fig. 3.6 for polarized beams ($P_{e^\pm} = ^{+20\%}_{-80\%}$).

field	$SU(3)_\mathrm{C}$	$SU(2)_\mathrm{L}$	$U(1)_\mathrm{Y}$	$\mathbb{Z}_2$
ψ	1	2	-1	odd
χ	1	1	0	odd

Table 3.3: Quantum numbers of the additional dark-sector fermions under $SU(3)_\mathrm{C}\times SU(2)_\mathrm{L}\times U(1)_\mathrm{Y}\times \mathbb{Z}_2$. SM fields have the usual gauge quantum numbers and are even under $\mathbb{Z}_2$.

We will assume [7] $|\mu| \ll m_\chi < m_{\psi^\pm}$ so that $2\mu \ll |m_\chi - m_{\psi^\pm}|$; in this case γ is small and

$$m_{\psi_1} \simeq m_\chi - \frac{\mu^2}{m_{\psi^\pm} - m_\chi}\,, \qquad m_{\psi_2} \simeq m_{\psi^\pm} + \frac{\mu^2}{m_{\psi^\pm} - m_\chi}; \tag{3.18}$$

so that $m_{\psi_2} > m_{\psi^\pm} > m_{\psi_1}$ and ψ_1 is the DM candidate. Note that we also have

$$Y_1 = -\sin(2\gamma)\frac{\Delta m}{\sqrt{2}\,v}\,, \qquad \Delta m = m_{\psi_2} - m_{\psi_1} > 0. \tag{3.19}$$

---

[7] The case $|\mu| < m_\chi \ll m_{\psi^\pm}$ is excluded by DM direct-detection and relic abundance constraints.

In the mass-eigenstate basis the interaction Lagrangian becomes

$$\begin{aligned}\mathcal{L}^{\texttt{VF}}_{int} =& \frac{e_0}{s_{2\texttt{w}}}\left[s_\gamma^2(\bar\psi_1\gamma^\mu\psi_1)+c_\gamma^2(\bar\psi_2\gamma^\mu\psi_2)+s_\gamma c_\gamma(\bar\psi_1\gamma^\mu\psi_2+\bar\psi_2\gamma^\mu\psi_1)-c_{2\texttt{w}}(\psi^+\gamma^\mu\psi^-)\right]Z_\mu \\ &- e_0(\psi^+\gamma^\mu\psi^-)A_\mu+\frac{e_0}{\sqrt{2}s_\texttt{w}}\left\{\left[s_\gamma(\bar\psi_1\gamma^\mu\psi^-)+c_\gamma(\bar\psi_2\gamma^\mu\psi^-)\right]W^+_\mu+\text{H.c.}\right\} \\ &- \frac{Y_1}{\sqrt{2}}h\left[s_{2\gamma}(\bar\psi_1\psi_1-\bar\psi_2\psi_2)+c_{2\gamma}(\bar\psi_1\psi_2+\bar\psi_2\psi_1)\right],\end{aligned} \tag{3.20}$$

where $s_\gamma = \sin\gamma$, etc., and h is defined in Eq. (3.15). We see that the charged heavy fermions ($\psi^\pm$) have vector-like interactions with Z boson (corresponding $a^0 = c_{2\texttt{w}} \sim 1/2$, $b^0 = 0$ in Eq. (3.1)); the W couplings are also vector-like. Comparing with Table 3.1 we that for $\epsilon = 0.005$ and polarized beams we expect [8] the ILC to be able to measure a^0, b^0 to within $\lesssim 10\%$ at 1σ (ignoring systematic uncertainties).

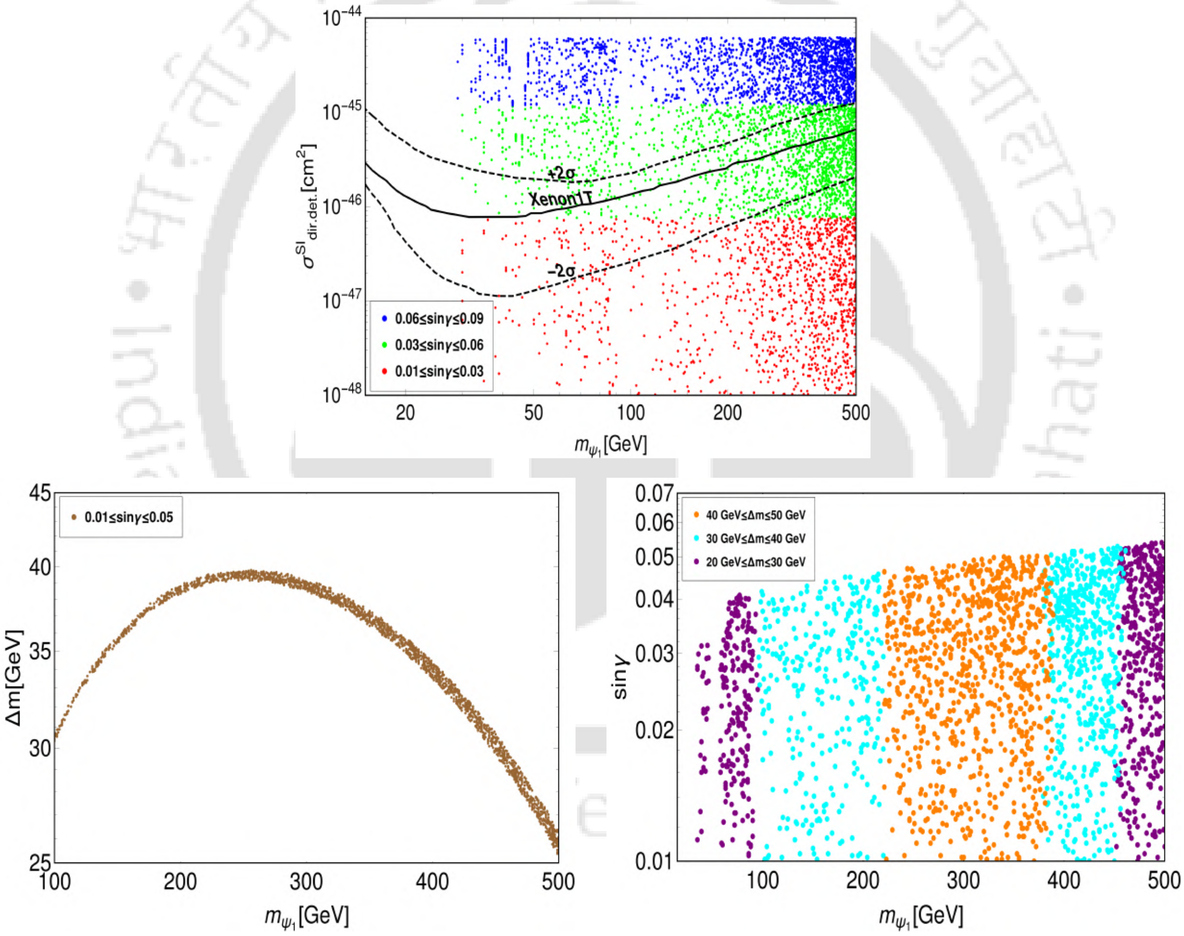

Figure 3.9: Regions allowed by the direct-detection and relic density constraints. Top: in the SI direct-detection cross-section ($\sigma^{\text{SI}}_{\text{DD}}$) vs DM mass ($m_{\psi_1}$) plane for various ranges of $\sin\gamma$. Bottom left: in the $\Delta m - m_{\psi_1}$ plane for $0.01 \le \sin\gamma \le 0.05$; bottom right: in the $\sin\gamma - m_{\psi_1}$ plane for different ranges of Δm.

The strongest limits on the model parameters come from dark matter constraints. The interactions in Eq. (3.20) show that the DM relic density is determined by the

---

[8] The case at hand is similar to $a^0 = 1$, $b^0 = 0$.

h and Z-mediated annihilation and co-annihilation channels, while nuclear scattering, probed by direct-search experiments, is dominated by the Z exchange process alone. The experimental constraint on the spin-independent cross section $\sigma^{\mathtt{SI}}_{\mathtt{dir.\,det.}} \lesssim 10^{-47}\mathrm{cm}^2$ (XENON1T collaboration, [153]), and the fact that this cross section is $\propto \sin^4\gamma$ gives

$$\sin\gamma \lesssim 0.05\;; \tag{3.21}$$

with a weak dependence on the DM mass. This limit on $\sin\gamma$ sharply reduces DM annihilation cross-section via Z mediation, and also via Higgs portal interactions since $Y_1 \;\propto\; \sin(\gamma)$. Though the SM→DM annihilation channels are suppressed, the relic-abundance restriction $\Omega_{\mathtt{DM}}\mathrm{h}^2 = 0.11933 \pm 0.00091$ (PLANCK collaboration [12, 13]) can still be met through co-annihilation channels involving $\psi^{\pm}$, provided $|\Delta m| \ll m_{\psi^{\pm}}$ [154].

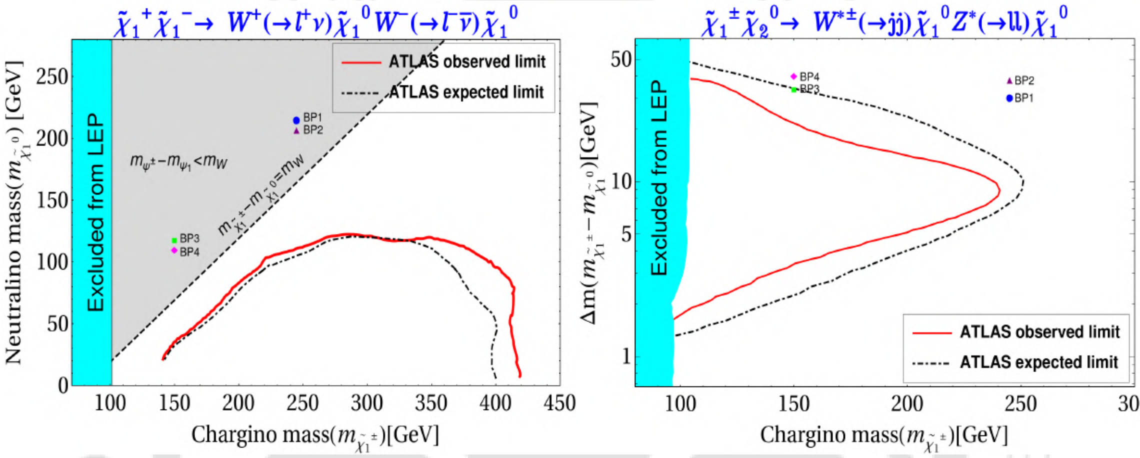

Figure 3.10: Current experimental limits from the LHC for supersymmetric chargino-neutralino production from the dilepton plus missing energy channel [130] (left) and dilepton plus dijet plus missing energy channel [131] (right). The benchmark points for our model (Table 3.4) are included for comparison.

Fig. 3.9 displays various regions allowed by the direct-detection and relic-density constraints. The top panel displays the spin-independent direct-detection cross-section $\sigma^{\mathtt{SI}}_{\mathtt{DD}}$ a function of DM mass (m_{ψ_1}) for various ranges of $\sin\gamma$. The allowed region in the $m_{\psi_1} - \Delta m$ plane is displayed in the bottom left panel, while the allowed region in the $m_{\psi_1} - \sin\gamma$ plane for several ranges of Δm is displayed on the right bottom panel of that figure. The parabola-like region in the bottom left panel is responsible for having two allowed values of m_{ψ_1} for each choice of Δm range on the right bottom panel; this paraboloid shape can be traced to the contribution from co-annihilation channels $\psi^{\pm}\psi_1 \to$SM to the DM annihilation cross-section:

$$\langle\sigma v\rangle_{\mathtt{tot}} \simeq \langle\sigma v\rangle_{\psi_1\bar{\psi}_1\to\mathrm{SM}} + \langle\sigma v\rangle_{\psi_1\psi^{\pm}\to\mathrm{SM}}\left(1+\frac{\Delta m}{m_{\psi_1}}\right)^{3/2} e^{-\Delta m/T} + \cdots \tag{3.22}$$

where T denotes the temperature of the bath, and the ellipses indicate other co-annihilation channels (*e.g.* $\psi^+\psi^- \to$SM, $\psi_1\bar{\psi}_2 \to$SM) with a stronger exponential suppression; for details, see [152]. The relic density is then

$$\Omega_{\mathtt{DM}}\mathrm{h}^2 = \frac{1.09\times10^9\ \mathrm{GeV}^{-1}(m_{\psi_1}/T)}{g_*{}^{1/2}M_{\mathtt{Pl}}}\,\frac{1}{\langle\sigma v\rangle_{\mathtt{tot}}}\bigg|_{T=T_f}\;; \tag{3.23}$$

where $x = T/m_{\psi_1}$, g_* denotes the effective relativistic degrees of freedom, $M_{\texttt{Pl}}$ the Planck mass, and T_f the value of T at freeze-out. From these expressions, it follows that for small Δm the allowed values increase with m_{ψ_1}, but only up to a point beyond which Δm must drop to balance the exponential suppression in Eq. (3.22).

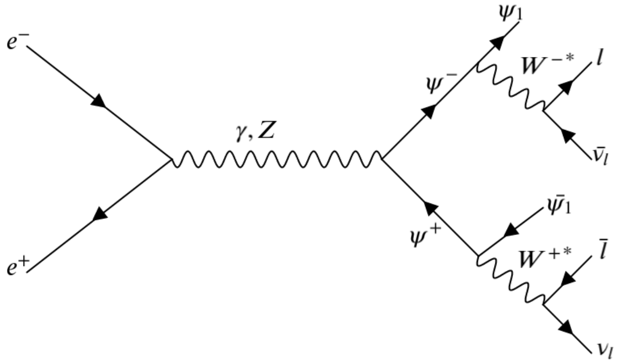

Figure 3.11: Production and decay of the heavy charged fermions at the ILC for the model described in Section 3.5.

Collider data also impose constraints on this model, with the strongest limits from those on the production of chargino pairs [130], or chargino and second neutralino production [131], in supersymmetric theories. Chargino pair production is the exact parallel of the one we study below (see Fig. 3.11 with $\psi^\pm$ replaced by charginos, and ψ_1 by neutralinos), in the limit where the chargino is wino-dominated and the sneutrinos are heavy [9], and assuming the on-shell production of charginos dominates the cross-section. These SUSY limits give

$$m_{\psi_2} + 115\ \text{GeV} \gtrsim m_{\psi^\pm} \quad \text{for } 250\ \text{GeV} > m_{\psi^\pm} > 150\ \text{GeV} \tag{3.24}$$

which, for $m_{\psi^\pm} = 150\,\text{GeV}\,(245\,\text{GeV})$, requires $m_{\psi_1} > 35\,\text{GeV}\,(111\,\text{GeV})$. The model is also consistent with electroweak precision observables, and with the invisible decay widths for the Higgs and Z boson whenever $m_{\psi_1} > m_h/2$, which we assume.

With these constraints in mind, we select several benchmark points, listed in Table 3.4, where all constraints are obeyed and which we will use in our study of the model at the ILC; for these, we also assumed $\Delta m < m_W$, so that the decay of heavy fermion occurs via an off-shell W. We will show that for such relatively small mass splitting there is better segregation of the signal from the SM background at the ILC. The benchmark points are compared with limits from ATLAS [130, 131] [10] in Fig. 3.10.

3.6 Simulation of collider events

We now turn to the ILC collider signatures for this model for the chosen benchmark points (Table 3.4) using the simplest signal: $\psi^\pm$ on-shell pair production with their subsequent decay into DM + opposite-sign leptons (`OSL`) via off-shell W bosons

---

[9] The sneutrinos generate a t-channel graph not present in our model, and other contributions to the charginos generate chiral couplings to the W.

[10] The limits from CMS [155] agree well with Fig. 3.10 and also allow the chosen benchmark points.

Benchmark Points	$m_{\psi^\pm}$ (GeV)	m_{ψ_1} (GeV)	Δm (GeV)
BP1	245	215	30
BP2		207	38
BP3	150	117	33
BP4		110	40

Table 3.4: Benchmark points chosen for collider analysis for singlet-doublet fermion model; in all cases we took $\sin\gamma = 0.05$.

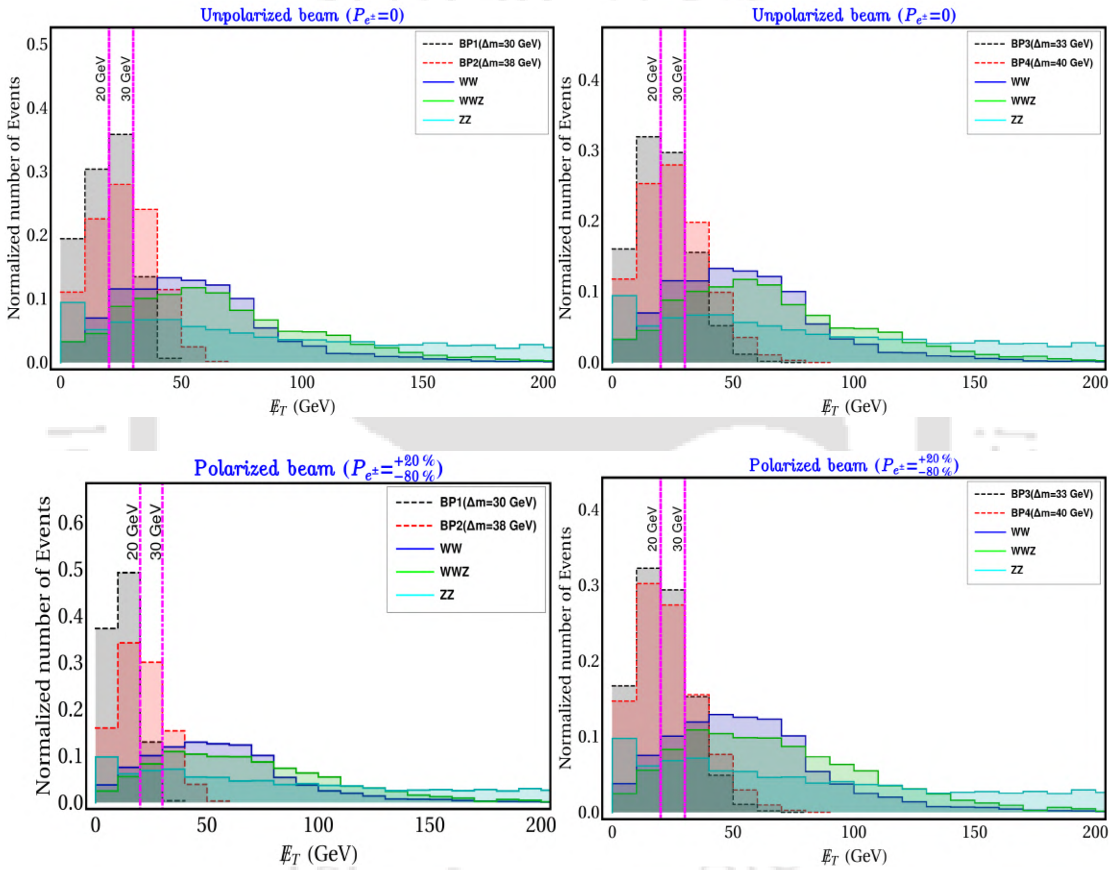

Figure 3.12: Normalized $\not{E}_T$ distribution for the `OSL` final state events at the ILC with $\sqrt{s}$= 500 GeV. Top: results for unpolarized beams; left (right), benchmark points BP1, BP2 (BP3, BP4) (*cf.* Table 3.4). Bottom: same for polarized beams ($P_{e^\pm} = ^{+20\%}_{-80\%}$). The SM background distributions from WW, WWZ, ZZ production are also shown. The cuts $\not{E}_T < 20$, 30 GeV cut used in the analysis are also indicated.

(Fig. 3.11); we adopt the above mass hierarchy, $m_{\psi_2} > m_{\psi^\pm} > m_{\psi_1}$. We note that $\psi_1\,\psi_2$ production, followed by $\psi_2 \to Z\psi_1$ generates a similar final state (`OSL` plus missing energy), but the cross is $\propto \sin^4\gamma$ and significantly smaller. It is also possible to pair produce ψ_1, ψ_2 but the final state signature is different.

We simulated `OSL` events at the ILC with $\sqrt{s} = 500$ GeV as follows: the model was implemented in `Feynrules` [156–158], and parton-level signal events were generated using `CalcHEP` [159], and then showered and analyzed using `Pythia` [160]; SM background events were generated using `MadGraph` [161] and showered using Pythia. For event reconstruction, we use the following criteria:

- Leptons are required to have at least transverse momentum $p_T > 10$ GeV; we consider only electrons and muons with pseudorapidity $|\eta| < 2.4$ – we do not consider τ signals. Two leptons are assumed isolated if $\Delta R_{\ell\ell} = \sqrt{(\Delta\eta)^2 + (\Delta\phi)^2} \geq 0.2$, while a lepton and a jet are assumed isolated if $\Delta R_{\ell j} \geq 0.4$.

- We impose a zero-jet requirement, where jets are reconstructed using the cone jet algorithm around the initiating parton. We further require $p_T > 20$ GeV and $|\eta| < 3.0$.

- Background signal was minimized by imposing cuts at 20 and 30 GeV (see below) on the missing transverse energy, which is defined by

$$\not\!\!E_T = \left|\mathbf{p}_\perp^{\texttt{vis}}\right|^2 \tag{3.25}$$

  where $\mathbf{p}_\perp^{\texttt{vis}}$ is the total visible momentum of leptons, jets, and photons perpendicular to the beam direction.

Background	$\sigma_{\texttt{SM}}^{\psi^+\psi^-}$ (pb)		$\not\!\!E_T$ (GeV)	$\sigma_{\texttt{SM}}^{\texttt{OSL}}$ (fb)	
	$P_{e^\pm} = 0$	$P_{e^\pm} = ^{+20\%}_{-80\%}$		$P_{e^\pm} = 0$	$P_{e^\pm} = ^{+20\%}_{-80\%}$
WW	7.4	15.5	< 20	0.90	2.73
			< 30	0.90	2.73
WWZ	0.04	0.085	< 20	5.3×10^{-4}	1.5×10^{-3}
			<30	1.6×10^{-3}	4.5×10^{-4}
ZZ	0.41	0.66	< 20	3.1×10^{-3}	9.4×10^{-3}
			< 30	4.7×10^{-3}	1.4×10^{-2}

Table 3.5: SM background cross sections for the $\psi^\pm$ and `OSL` final states at the ILC with $\sqrt{s}$=500 GeV with the selection cuts adopted (see text), and for unpolarized and polarized beams ($P_{e^\pm} = ^{+20\%}_{-80\%}$).

We present in Fig. 3.12 the missing transverse energy ($\not\!\!E_T$) distributions (normalized to one event) at the benchmark points for both the signal and the dominant SM background processes events (WW, WWZ, ZZ); and for both polarized and unpolarized beams. Since the intermediate W bosons are off shell, the peak of the missing energy distribution for the signal is at a much smaller value than those SM backgrounds, where W production is on-shell. Based on these distributions we choose upper cuts $\not\!\!E_T < 20, 30$ GeV[11], which retain a significant part of the signal and eliminate most background events, as illustrated in Table 3.5.

The values of the $\psi^\pm$ pair production and signal event cross sections ($\sigma^{\psi^+\psi^-}$ and $\sigma^{\texttt{OSL}}$, respectively) after imposing the above selection criteria and $\not\!\!E_T$ cuts are given

---

[11] ILC projections indicate this collider will be able to measure missing energy very accurately so that the cut used in our analysis is viable [102].

$\sigma^{\psi^+\psi^-}$ (pb)		BPs	$\not{E}_T$ (GeV)	$\sigma^{\texttt{OSL}}$(fb)		Efficiency (ϵ) $\times 10^{-3}$	
$P_{e^\pm} = 0$	$\not{E}_T$			$P_{e^\pm} = 0$	$P_{e^\pm} =^{+20\%}_{-80\%}$	$P_{e^\pm} = 0$	$P_{e^\pm} =^{+20\%}_{-80\%}$
0.14	0.32	BP1	< 20	0.93	2.35	6.43	6.70
			< 30	0.98	2.50	6.98	7.11
		BP2	< 20	0.70	1.80	5.00	5.62
			< 30	0.73	1.88	5.21	5.87
0.45	1.13	BP3	< 20	2.97	7.92	6.60	7.00
			< 30	3.32	8.45	7.37	7.47
		BP4	< 20	2.30	6.05	5.09	5.36
			< 30	2.40	6.32	5.30	5.60

Table 3.6: Signal (`OSL`) and $\psi^\pm$ pair production cross sections and associated signal efficiency ϵ Eq. (3.26) at the ILC for $\sqrt{s} = 500$ GeV with two missing-energy selection cuts and other selection cuts (see text) for unpolarized and polarized beams ($P_{e^\pm} =^{+20\%}_{-80\%}$).

in Table 3.6 for both unpolarized and polarized ($P_{e^\pm} =^{+20\%}_{-80\%}$) beams. Following the discussion in Section 3.3, we define

$$\epsilon = \frac{\sigma^{\texttt{OSL}}}{\sigma^{\psi^+\psi^-}} , \tag{3.26}$$

(see Eq. (3.11)) whose values are listed in Table 3.6. It is clear that $\epsilon \sim 0.001$ used throughout the previous OOT analysis is a conservative choice ($\epsilon \sim 0.005$ more closely corresponds to the results derived in this section).

We also note that signal events are often accompanied by initial state radiation (ISR) and final state radiation (FSR) photons simulated with inbuilt functions in `Pythia` event generator. Using the photon selection criteria $p_T^{\texttt{photon}} > 5$ GeV and $|\eta_{\texttt{photon}}| < 0.24$, the signal cross-section with zero photons, and the inclusive $\leq 1, 2$ photon cross sections are listed in Table 3.7. From this, we can see that the inclusive diphoton cross sections match quite accurately the signal cross-section without photon tagging listed in Table 3.6[12].

We determine the discovery potential of the `OSL` signal at the ILC by plotting signal significance ($S/\sqrt{S+B}$, where S and B denote, respectively the number of signal and SM background events), as a function of luminosity $\mathfrak{L}_{\texttt{int}}$. The results are presented in Fig. 3.13; of particular interest is the advantage provided by using polarized beams, which require a lower luminosity for either the discovery or exclusion of the selected signal; in either case the design luminosity (*cf.* Eq. (3.3) will be sufficient to exclude or detect the NP signal here investigated.

---

[12] With three-photon and four-photon events being very rare, inclusive di-photon event counts match quite accurately to signal cross-section without photon tagging as in Table 3.6.

Benchmark Points	$\not{E}_T$ (GeV)	$\sigma^{\texttt{signal}}$ (fb)					
		OSL + 0 photon		OSL+ ≤ 1 photon		OSL+ ≤ 2 photon	
		$P_{e^\pm} = 0$	$P_{e^\pm} = ^{+20\%}_{-80\%}$	$P_{e^\pm} = 0$	$P_{e^\pm} = ^{+20\%}_{-80\%}$	$P_{e^\pm} = 0$	$P_{e^\pm} = ^{+20\%}_{-80\%}$
BP1	< 20	0.76	2.17	0.84	2.26	0.93	2.35
	< 30	0.80	2.31	0.87	2.39	0.98	2.50
BP2	< 20	0.55	1.79	0.62	1.76	0.70	1.80
	< 30	0.60	1.71	0.67	1.79	0.73	1.88
BP3	< 20	2.82	7.70	2.90	7.81	2.97	7.92
	< 30	2.15	8.21	2.24	8.33	3.32	8.45
BP4	< 20	2.17	5.87	2.23	5.95	2.30	6.05
	< 30	2.26	6.16	2.34	6.23	2.40	6.32

Table 3.7: Signal cross-section including ISR and FSR photon count.

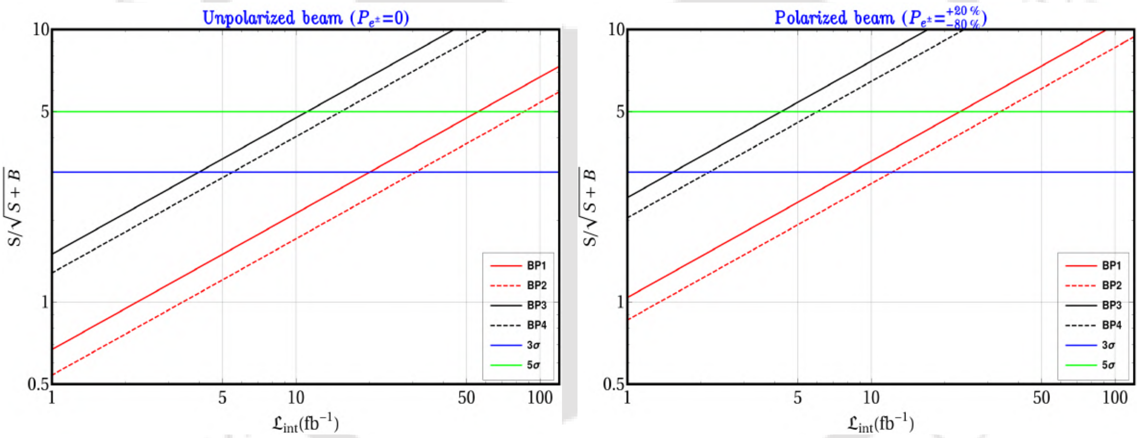

Figure 3.13: Signal significance ($S/\sqrt{S+B}$) for the benchmark points in Table 3.4 for unpolarized (left) and polarized ($P_{e^\pm} = ^{+20\%}_{-80\%}$) beams (right). Blue and green lines correspond to 3σ and 5σ exclusion and discovery limits, respectively.

3.7 Summary

In this chapter, we have analyzed the optimal statistical determination of the parameters of physics beyond the Standard Model, using as a specific example the production of a new heavy charged fermion $\psi^\pm$ that can couple to the Z boson and photon. We assumed for simplicity that the photon coupling is known, and allows for both vector and axial coupling to the Z with couplings a and b respectively. The optimal observable technique generates the minimal statistic uncertainty to which the couplings a, b can be determined. We find that uncertainties for the case where $|a| \sim 1$ are roughly independent of the value of b and smaller than those for the quasi-axial case $|a| \ll 1$. Find, in addition, that, as expected, beam polarization allows for a different distinction of these couplings.

We also studied a sample model where the vector-like case ($b = 0$) is realized; the model consists of an extension of the SM by a fermion isodoublet and a fermion singlet, both assumed odd under a $\mathbb{Z}_2$ symmetry. In addition to providing a realization of the more general optimal observable analysis, this model contains a viable DM candidate. the presence of which can be probed at the ILC through $\psi^{\pm}$ pair production followed by their decays into DM and W bosons. The analysis shows that given the expected ILC luminosity (Eq. (3.3)) this collider will provide early evidence (or provide an early exclusion) of the model here proposed and that this collider will be able to measure the model parameters with an accuracy very close to the optimal one. It is worth noting that the analysis is applicable to supersymmetric chargino pair production in the limit of heavy sneutrino, including our results on the optimal statistical uncertainties for the charged-lepton couplings to the Z in the $a \neq 0, b = 0$ case.

Chapter 4

Examples of SM dominance

Contents

4.1 Introduction

In this chapter we explore the application of the OOT for cases where the SM interference dominates the signal. We study several examples of this kind. In Section 4.3, we investigate the estimation of neutral triple gauge couplings (nTGCs) through $Z\gamma$ production at the ILC and CLIC, in Section 4.4, we examine the same nTGCs via ZZ production at the CLIC, and in Section 4.5, we study SMEFT contribution for $t\bar{t}$ production at ILC. Then we compare SM dominance to NP dominance by considering a UV complete NP set up in Section 4.6, that generates EFT operators contributing to $t\bar{t}$ production.

The production of the processes $e^+e^- \to ZV(V = \gamma, Z)$ have received significant attention over the past few decades. These processes take place via t-channel electron exchange in the SM. The s-channel contribution via Z/γ mediation is forbidden in the SM at the tree level since nTGCs are not allowed at the tree level under the $SU(2)_L \times U(1)_Y$ gauge symmetry. The loop-induced s-channel contribution within SM is also largely suppressed. Therefore, any deviation in the measurements in the process $e^+e^- \to Z\gamma$ from their SM prediction will be a useful hint for NP. $Z\gamma$ production has been extensively studied in the literature in the context of the $e^+\,e^-$ collider [162–172] as well as pp collider [173–180]. We will follow the approach taken by various earlier works [173, 181–185], expressing anomalous nTGCs in terms of model-independent dimension-6 and -8 operators [1]. The dimension-8 operators give rise to anomalous nTGCs at tree-level whereas dimension-6 operators can lead to anomalous nTGCs at one-loop level. We would like to state that in this discussion, we focus only on the dimension-8 operators. However, it should be kept in mind that with a sufficiently high NP scale, the effect of loop-induced anomalous nTGC vertices arising from dimension-6 operators starts making the dominant contribution. Following [181] in particular, we write the Lagrangian for anomalous nTGCs in terms of dimension-8 couplings h_i^V, where $i = 1, ..4$ and $V = \gamma, Z$. $i = 1, 2$ denote CP-violating dimension-6 and -8 couplings, whereas $i = 3, 4$ denote CP-conserving dimension-6 and -8 couplings respectively.

In Section 4.5 and Section 4.6, we will consider two complementary situations: in the first the NP generates a subdominant correction to the SM, while in the second the NP dominates. These two cases can be realized, for example, in 2-HDM, where, in the first, the scale of the non-SM scalars is large compared to the electroweak scale and with the collider energy; while in the second, that same scale is sufficiently low for non-SM particles to be directly produced. The specific illustrations we consider are, for the first case, $t\bar{t}$ production, where the NP contribution arises from dimension-6 SMEFT operators and for the second, production of charged-scalar pairs. The production of charged scalars lie in the BSM dominance category.

To supplement the discussion, in Section 4.2, we discuss relevant dimension-8 effective operators that contribute to the self-interaction of neutral gauge bosons and summarize all the observations in Section 4.7.

4.2 Dimension-8 neutral triple gauge couplings (nTGCs)

4.2.1 Phenomenological framework

The deviation of the self-interactions of gauge bosons from the SM is considered to be one of the most important BSM probe. The self-interaction of gauge bosons[2] within SM framework can be understood by the non-Abelian $SU(2)_L \times U(1)_Y$ gauge theory. The gauge sector Lagrangian involving only gauge bosons within SM is written as

$$\mathcal{L}_{gauge} = -\frac{1}{4}B_{\mu\nu}B^{\mu\nu} - \frac{1}{4}W^i_{\mu\nu}W^{i\mu\nu}. \tag{4.1}$$

Eq. (4.1) provides the necessary gauge boson self-interactions within SM at tree level. The tree-level gauge-boson vertex can be penned down as,

$$V_{W^+_\nu(q)W^-_\lambda(r)V_\mu(p)} = ig_{W^+W^-V}\big(g_{\mu\nu}(p-q)_\lambda + g_{\mu\lambda}(p-q)_\nu + g_{\nu\lambda}(p-q)_\mu\big), \tag{4.2}$$

with $V = \gamma, Z$ and

$$g_{W^+W^-\gamma} = g\sin\theta_w = e_0, \quad g_{W^+W^-Z} = g\cos\theta_w. \tag{4.3}$$

Therefore, we can see that there is no interaction between γ and Z at tree level in SM because Z boson doesn't possess any electromagnetic charge. Therefore, the

---

[1] Studies of anomalous nTGCs regarding flavor-changing-neutral-current (FCNC) have been performed in [186, 187].

[2] Interaction between charged gauge boson ($W^\pm$) with neutral gauge bosons (γ, Z).

interaction between γ and Z which we call nTGCs ($ZZ\gamma$, ZZZ and $Z\gamma\gamma$), play a crucial role in investigating any NP.

The nTGCs are absent in dimension-6 EFT operators at the tree level but they are present in the 1-loop level. On the other hand, dimension-8 operators provide the desired nTGCs at the tree level. We will now focus on the dimension-8 operators contributing to nTGCs. Here, we note that, apart from nTGCs, other vertices involved in the process $e^+ e^- \to Z\gamma$ (ZZ), such as $e^+e^-\gamma/Z$ can get NP contribution from dimension-6 SMEFT operators at tree level. However, from the results of the electroweak precision test at LEP2 and LHC, the deviations of $Zf\bar{f}$ couplings are constrained $\lesssim 0.1\%$ and that of $e^+e^-\gamma$ coupling $\ll 0.1\%$ [188]. Therefore, in this analysis, for optimal measurements of nTGCs through $Z\gamma$ production at the e^+e^- colliders, we have ignored their effect. For t-channel W-mediated $e^+e^- \to \nu\nu\gamma$ final state, will have a negligible contribution to our signal since we demand production of the neutrinos from on-shell Z. In principle, for this process, $e\nu W$ and $WW\gamma$ vertices can also get contributions from dimension-6 SMEFT operators. However, experimental measurements at LEP2 and LHC allow for only $\sim 0.1\%$ deviation for $e\nu W$ coupling from SM, and for $WW\gamma$ coupling, the deviation is $\ll 0.1\%$ [188]. Therefore, the effect of dimension-6 operators' contribution is also neglected in this case.

4.2.2 Dimension eight effective operators

The dimension-8 effective operators that provide $ZZ\gamma$, $Z\gamma\gamma$ and ZZZ couplings can be written as [158]

$$\begin{aligned}
\mathcal{O}_{\tilde{B}W} &= iH^\dagger \tilde{B}_{\mu\nu} W^{\mu\rho}\{D_\rho, D^\nu\}H, \\
\mathcal{O}_{BW} &= iH^\dagger B_{\mu\nu} W^{\mu\rho}\{D_\rho, D^\nu\}H, \\
\mathcal{O}_{WW} &= iH^\dagger W_{\mu\nu} W^{\mu\rho}\{D_\rho, D^\nu\}H, \\
\mathcal{O}_{BB} &= iH^\dagger B_{\mu\nu} B^{\mu\rho}\{D_\rho, D^\nu\}H.
\end{aligned} \tag{4.4}$$

In Eq. (4.4), $\mathcal{O}_{\tilde{B}W}$ is the CP-conserving operator and rest of the three are CP-violating operators. Experimental searches for these nTGCs have been going on in the different colliders but no evidence has been found so far. As discussed above, searches for nTGCs have been carried out at LEP and Tevatron but most stringent bounds come from the ATLAS and CMS experiments at LHC. The ATLAS experiment has put most stringent bounds on $C_{\tilde{B}W}/\Lambda^4$, C_{BW}/Λ^4 and C_{BB}/Λ^4 couplings through the $pp \to Z\gamma \to \nu\bar{\nu}\gamma$ channel at CM energy $\sqrt{s}$ = 13 TeV with integrated luminosity of 36.1 fb^{-1} at the LHC [189] whereas for the C_{WW}/Λ^4 coupling, the tightest limit is given by the CMS experiment through the $pp \to ZZ \to 4\ell$ channel at $\sqrt{s}$ = 13 TeV with integrated luminosity 137 fb^{-1} [190]. The expected 95% C.L. on dimension-8 nTGCs from ATLAS and CMS experiments are presented in Table 4.1.

As we discussed earlier, the dimension-6 operators do not give rise to any nTGCs at the tree level but their contribution becomes important at the one-loop level. However, the order of the contribution from one-loop level in case of dimension-6 operators is roughly $\mathcal{O}(\frac{\alpha_{\rm EM} s}{4\pi\Lambda^2})$, whereas for dimension-8 operators the tree-level contribution becomes $\mathcal{O}(\frac{sv^2}{\Lambda^4})$. Evidently, the contribution of the dimension-8 operators to the $Z\gamma$ or ZZ production supersedes the contribution of dimension-6 operators in the limit of $\Lambda < \sqrt{\frac{4\pi}{\alpha_{\rm EM}}}v \sim 10$ TeV [158]. However, it should be carefully noted

Couplings (TeV^{-4})	95% C.L.	
	$pp \to Z\gamma \to \nu\bar{\nu}\gamma$ (ATLAS)	$pp \to ZZ \to 4\ell$ (CMS)
$C_{\tilde{B}W}/\Lambda^4$	$(-1.10,\ +1.10)$	$(-2.30,\ +2.50)$
C_{WW}/Λ^4	$(-2.30,\ +2.30)$	$(-1.40,\ +1.20)$
C_{BW}/Λ^4	$(-0.65,\ +0.64)$	$(-1.40,\ +1.30)$
C_{BB}/Λ^4	$(-0.24,\ +0.24)$	$(-1.20,\ +1.20)$

Table 4.1: Statistical limits (95% C.L.) from ATLAS [189] and CMS [190] experiments on different dimension-8 nTGCs at LHC.

that, if the loop-induced dimension-6 contribution involves electroweak coupling instead of electromagnetic coupling (depending on the particular loop diagram in consideration), the cut-off on Λ comes down to ~ 5 TeV. The aforementioned limits are derived with the assumption that the Wilson coefficients of the dimension-6 and -8 operators are roughly equal.

The resulting effective Lagrangian that contains anomalous nTGCs from dimension-6 and dimension-8 operators is given by

$$\begin{aligned}
\mathcal{L}_{\text{EFT}} = & \frac{g_e}{m_Z^2}\Bigg[-\left\{f_4^\gamma(\partial_\mu F^{\mu\nu}) + f_4^Z(\partial_\mu F^{\mu\beta})\right\} Z_\alpha(\partial^\alpha Z_\beta) + \left\{f_5^\gamma(\partial^\sigma F_{\sigma\mu}) + f_5^Z(\partial^\sigma Z_{\sigma\mu})\right\}\tilde{Z}^{\mu\beta} Z_\beta \\
& - \left\{h_1^\gamma(\partial^\sigma F_{\sigma\mu}) + h_1^Z(\partial^\sigma Z_{\sigma\mu})\right\} Z_\beta F^{\mu\beta} - \left\{h_3^\gamma(\partial_\sigma F^{\sigma\rho}) + h_3^Z(\partial_\sigma Z^{\sigma\rho})\right\} Z^\alpha \tilde{F}_{\rho\alpha} \\
& - \left\{\frac{h_2^\gamma}{m_Z^2}(\partial_\alpha\partial_\beta\partial^\rho F_{\rho\mu}) + \frac{h_2^Z}{m_Z^2}(\partial_\alpha\partial_\beta(\Box + m_Z^2)Z_\mu)\right\} Z^\alpha F^{\mu\beta} - \Bigg\{\frac{h_4^\gamma}{2m_Z^2}(\Box\partial^\alpha F^{\rho\alpha}) \\
& + \frac{h_4^Z}{2m_Z^2}((\Box + m_Z^2)\partial^\sigma Z^{\rho\alpha})\Bigg\} Z_\alpha \tilde{F}_{\mu\beta}\Bigg],
\end{aligned} \tag{4.5}$$

where $\tilde{Z}_{\mu\nu} = \frac{1}{2}(\epsilon_{\mu\nu\rho\sigma}Z^{\rho\sigma})$ and $Z_{\mu\nu} = (\partial_\mu Z_\nu - \partial_\nu Z_\mu)$ are the field strength tensor. Here, f_3^V, f_4^V, f_5^V $(V = \gamma, Z)$ are dimension-6 couplings and h_3^V, h_4^V, h_5^V are the dimension-8 couplings. The expressions of anomalous nTGCs in terms CP conserving dimension-8 coupling are written as

$$\begin{aligned}
h_3^Z &= \frac{v^2 m_Z^2 C_{\tilde{B}W}}{4c_w s_w \Lambda^4}, \\
h_4^Z &= h_3^\gamma = h_4^\gamma = 0,
\end{aligned} \tag{4.6}$$

whereas, for CP-violating case, the couplings can be written as

$$\begin{aligned}
h_1^Z &= \frac{m_Z^2 v^2\left(-c_w s_w C_{WW} + C_{BW}(c_w^2 - s_w^2) + 4c_w s_w C_{BB}\right)}{4c_w s_w \Lambda^4}, \\
h_1^\gamma &= \frac{m_Z^2 v^2\left(s_w^2 C_{WW} - 2c_w s_w C_{BW} + 4c_w^2 C_{BB}\right)}{4c_w s_w \Lambda^4}, \\
h_2^\gamma &= h_2^Z = 0.
\end{aligned} \tag{4.7}$$

In the next section, we will be discussing the statistical limit on dimension-8 nTGCs considering the highest CM energy ($\sqrt{s}$) and maximum polarization combination of the incoming beams with the same integrated luminosity in the context of the future linear colliders such as the ILC and CLIC. The design details are presented in Table 4.2.

Linear colliders	CM energy ($\sqrt{s}$) (TeV)	luminosity ($\mathfrak{L}_{int}$) (fb^{-1})	beam polarization		
ILC	1	1000	$P_{e^{\pm}} = ^{00\%}_{00\%}$	$P_{e^{\pm}} = ^{-30\%}_{+80\%}$	$P_{e^{\pm}} = ^{+30\%}_{-80\%}$
CLIC	3	1000	$P_{e^{\pm}} = ^{00\%}_{00\%}$	$P_{e^{\pm}} = ^{+00\%}_{+80\%}$	$P_{e^{\pm}} = ^{+00\%}_{-80\%}$

Table 4.2: Design details of ILC and CLIC.

4.3 Probing dimension-8 nTGCs via $Z\gamma$ production

4.3.1 $Z\gamma$ production at the e^+e^- colliders

$Z\gamma$ production at the $e^+\,e^-$ colliders primarily takes place via the t- and u-channel diagrams within the SM as shown in the bottom panel of Fig. 4.1. The BSM contributions to the $Z\gamma$ production via dimension-8 operators written in Eq. (4.4), lead to the s-channel diagram shown in the top panel of Fig. 4.1.

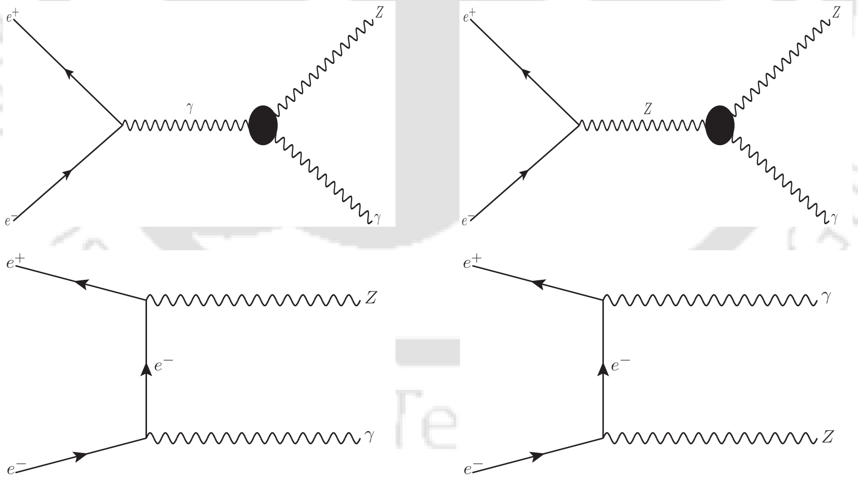

Figure 4.1: $Z\gamma$ production at the $e^+\,e^-$ colliders. Top panel: $ZZ\gamma$ and $Z\gamma\gamma$ contributions from dimension-8 effective operators; Bottom panel: SM contribution.

The variation of the total cross-section with the NP couplings is shown in Fig. 4.2 for unpolarized beams as well as for two different polarization combinations. Total cross-section has one pure SM term, an interference term between SM and dimension-8 operators (C_i/Λ^4) and contribution solely from dimension-8 operators proportional to $(C_i/\Lambda^4)^2$. For both unpolarized and polarized beams, the dominant BSM

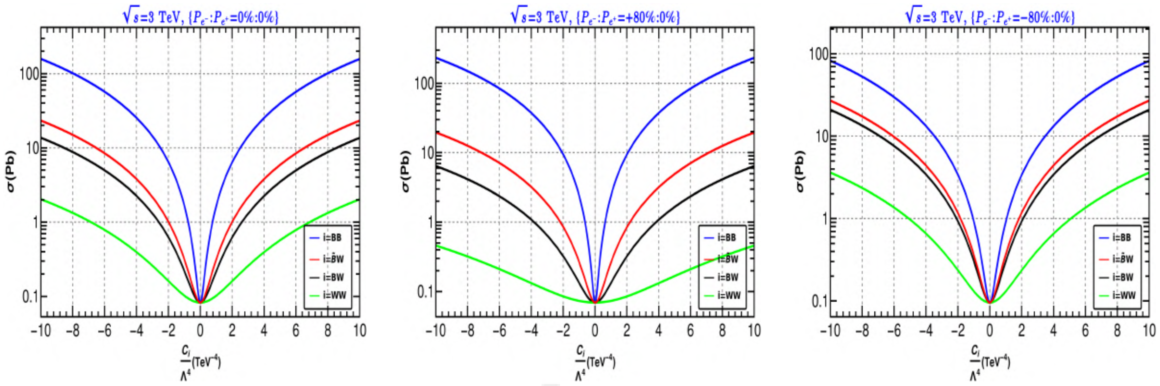

Figure 4.2: Variation of $Z\gamma$ production cross-section with the different dimension-8 couplings at the CLIC. Left: $\{P_{e^-} : P_{e^+} = 0\% : 0\%\}$; Middle: $\{P_{e^-} : P_{e^+} = +80\% : 0\%\}$; Right:$\{P_{e^-} : P_{e^+} = -80\% : 0\%\}$.

contribution to the cross-section will come from the aforementioned interference term as long as the NP couplings are small, so the variation of the cross-section with the NP couplings will not be symmetric in this region. When NP couplings increase further, the NP(squared amplitude) term dominates in the total cross-section. In this region, the cross-section behaves symmetrically with the NP couplings as can be seen in Fig. 4.2. For $C_{\tilde{B}W}/\Lambda^4$, C_{BW}/Λ^4 and C_{WW}/Λ^4, $\{P_{e^-} : P_{e^+} = -80\% : 0\%\}$ beam polarization combination provides increment over the unpolarized cross-section whereas, for C_{BB}/Λ^4 coupling, cross-section increases for the polarization combination $\{P_{e^-} : P_{e^+} = +80\% : 0\%\}$.

4.3.2 Collider simulation

To probe the dimension-8 nTGCs at the colliders, one has to produce a copious number of signal events. At the same time, the signal events have to be significant over and above the non-interfering SM backgrounds to make precision measurements of the anomalous coupling. With this in view, we perform a collider analysis and try to obtain suitable conditions for the most precise estimation of dimension-8 nTGCs. In our analysis, we will consider the signal process ($e^+e^- \to Z(\nu\bar{\nu})\gamma$). This final state has various advantages over the processes where Z decays into charged leptons or hadronic final states. In case of Z decaying to hadrons, the final state will contain large multi-jet background. On the other hand, a larger Z boson branching ratio into neutrinos compared to that into charged leptons provides an opportunity to study the $Z\gamma$ production in high p_T region, where the sensitivity of the anomalous couplings will be higher.
Therefore the signal of our interest is $e^+e^- \to \nu\nu\gamma$ (See Fig. 4.3). We demand exactly one photon with $p_T > 10$ GeV and $|\eta| < 2.5$. In addition, veto on jets with $p_T > 20$ GeV and leptons with $p_T > 10$ GeV are also imposed in the final state. The major background process that gives rise to the same final state is SM $\nu\bar{\nu}\gamma$ where the photon is emitted off a t-channel W boson. This background is irreducible. There are also other backgrounds like $t\bar{t}\gamma$ and $W^+W^-\gamma$ which can contribute to our desired final state when the hadronic/leptonic decay products from the top or W's are very soft and therefore escape the detector. The signal and background events are gen-

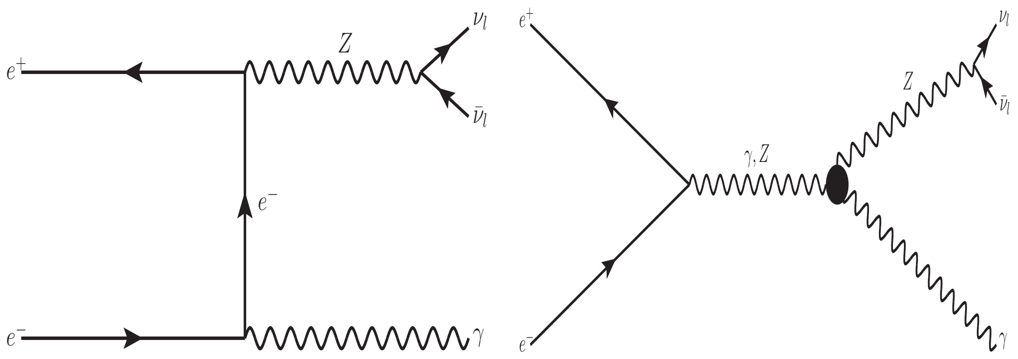

Figure 4.3: Production and decay of $Z\gamma$ final state at e^+e^- colliders; left: SM contribution; right: SMEFT contribution.

erated in `Madgraph5@NLO`. Detector simulation is taken care of by `Delphes`(v3) [191]. The `UFO` file for the NP model has been generated via `Feynrules`. We have plotted two crucial kinematical observables missing energy ($\not{E}$) and missing transverse momenta ($\not{E}_T$) to distinguish signal from the backgrounds. The definition of $\not{E}_T$ is written in Eq. (3.25) and we define $\not{E}$ as

- *Missing Energy or ME ($\not{E}$)*: The energy that is carried away by the missing final state particles, can be identified at the lepton collider given the knowledge of CM energy as
$$\not{E} = \sqrt{s} - \sum_{\ell,j,\gamma} E, \tag{4.8}$$

where E is the total enegy of the visible particles. In Fig. 4.4, we show the kinematical distributions for signal and backgrounds. For signal, we have considered CP-conserving coupling $C_{\tilde{B}W}$ as well as CP-violating couplings C_{BW}, C_{WW} and C_{BB} in the plots. The signal here includes the interference between SM and aNTGC couplings. Amongst the non-interfering backgrounds, the largest cross-section pertains to $\nu\bar{\nu}\gamma$(from t-channel W). However, we can see that though this background is irreducible, it gives rise to a three-body final state as opposed to the signal, which is a two-body final state. Therefore, the $\not{E}$ distribution becomes a narrow peak around $\sqrt{s}/2$ in case of signal, unlike the $\nu\bar{\nu}\gamma$ background. Therefore, a cut on $\not{E}$ reduces this background significantly. On the other hand, $t\bar{t}\gamma$ and $WW\gamma$ backgrounds are suppressed by the lepton and jet-veto. In addition, a moderate $\not{E}_T$ cut improves the signal significance even further. We have found that, with 1440 GeV $< \not{E} < 1560$ GeV and $\not{E}_T > 500$ GeV for the CLIC ($\sqrt{s} = 3$ TeV, $\Lambda = 3.2$ TeV, $C_{\tilde{B}W} = 1$) and 450 GeV $< \not{E} < 560$ GeV and $\not{E}_T > 80$ GeV for ILC ($\sqrt{s} = 1$ TeV, $\Lambda = 1.3$ TeV, $C_{\tilde{B}W} = 1$), the signal dominates strongly over the non-interfering backgrounds. These regions are also very sensitive to the NP couplings. Therefore, in our respective analyses with OOT, we will focus on this region of phase space and use these aforementioned cut values. We mention here that, the NP scale Λ has been chosen to be beyond the reach of the collider experiments in case of the CLIC and ILC to make the EFT valid.

4.3.3 Optimal sensitivity of dimension-8 nTGCs

Using the expression of covariance matrix in Eq. (2.36), optimal statistical sensitivity (95% C.L.) of NP couplings can be obtained from the χ^2 function written in Eq. (2.47)

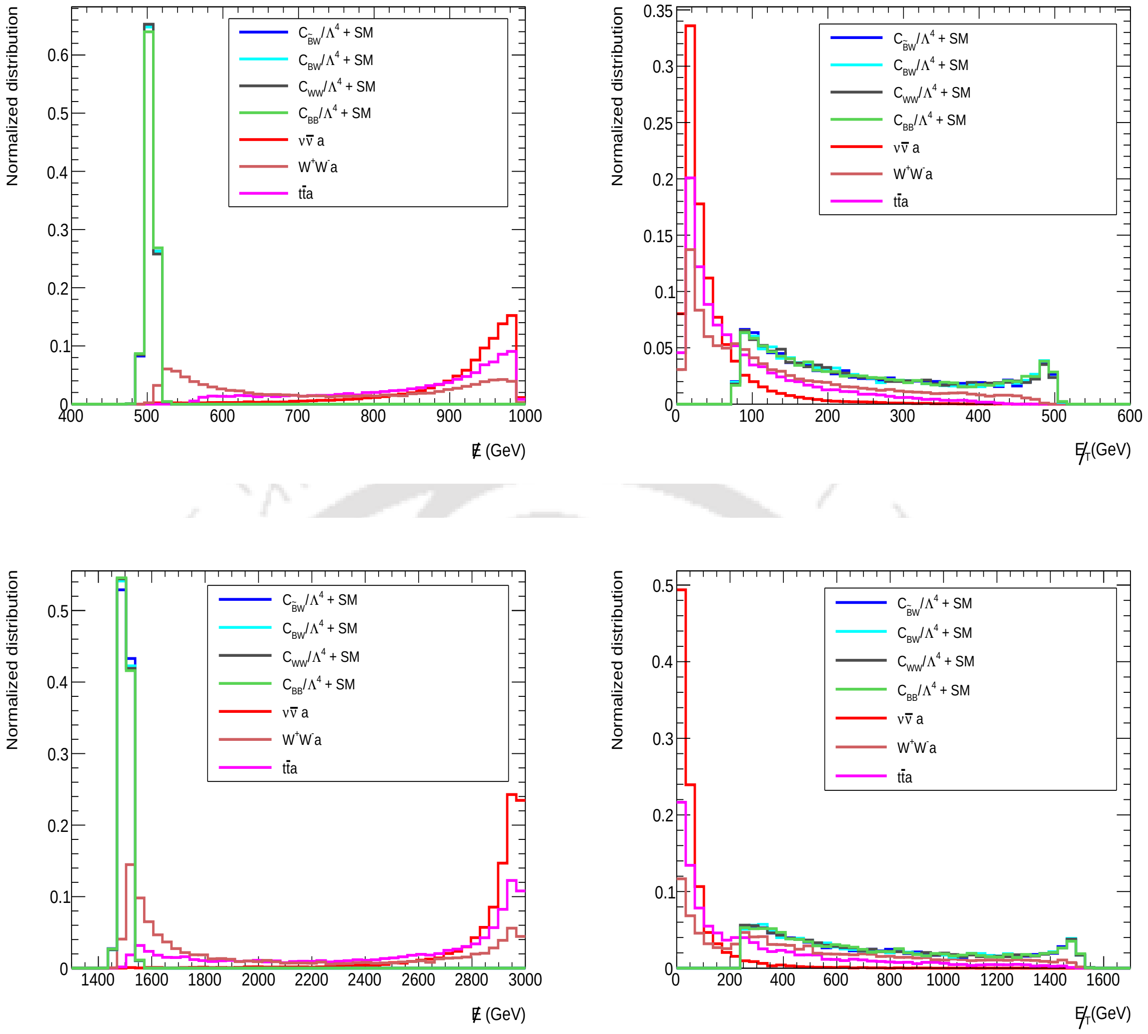

Figure 4.4: Normalized distribution for $e^+e^- \rightarrow Z(\nu\bar{\nu})\gamma$ (SM + dimension-8 nTGCs) and non-interfering SM backgrounds with (top panel) $\sqrt{s} = 1$ TeV (ILC), $\Lambda = 1.3$ TeV, $C_{ij} = 1$ and (bottom panel) $\sqrt{s} = 3$ TeV (CLIC), $\Lambda = 3.2$ TeV, $C_{ij} = 1$ with unpolarized beams. Left: missing energy ($\not{E}$), right: missing transverse energy ($\not{E}_T$).

. We first consider $\sqrt{s} = 1$ TeV and 3 TeV with $\mathfrak{L}_{\texttt{int}} = 1000$ fb^{-1} and show 1-D χ^2 as a function of different NP couplings in Fig. 4.5 and 4.6 respectively. While evaluating the χ^2 function in terms of one NP coupling, the other couplings are kept at zero. 95% C.L. on the NP couplings has been tabulated in Table 4.3. We can see that, different NP couplings are sensitive to different choices of polarization combinations, because of unequal contribution of NP couplings to the various helicity amplitudes. We find that in case of ILC, for $C_{\tilde{B}W}/\Lambda^4$, C_{BW}/Λ^4 and C_{WW}/Λ^4 the best sensitivity is achieved with $\{P_{e^-} : P_{e^+} = -80\% : +30\%\}$, whereas for C_{BB}/Λ^4, $\{P_{e^-} : P_{e^+} = +80\% : -30\%\}$ produces the best result. In context of CLIC, for C_{BB}/Λ^4 we get best sensitivity for $\{P_{e^-} : P_{e^+} = +80\% : 0\%\}$ and for $C_{\tilde{B}W}/\Lambda^4$, C_{BW}/Λ^4 and C_{WW}/Λ^4, the best sensitivity is obtained with $\{P_{e^-} : P_{e^+} = -80\% : 0\%\}$. This phenomenon can be also understood from Fig. 4.2, where the contribution to $Z\gamma$ production cross-section from C_{BB}/Λ^4 is maximum in the polarization combination

$\{P_{e^-} : P_{e^+} = +80\% : 0\%\}$, whereas the other three couplings contribute maximally with $\{P_{e^-} : P_{e^+} = -80\% : 0\%\}$. It is also evident that the initial beam polarization indeed enhances statistical precision in the case of all four dimension-8 nTGCs. In Table 4.3, we have quoted the statistical limits (95% C.L) for all the dimension-8 nTGCs for ILC and CLIC and make a comparison between the two. We can see that due to increased signal cross-section, CLIC yields better sensitivity compared to ILC at the same integrated luminosity. The comparison between ILC, CLIC, and ATLAS sensitivities will be discussed next.

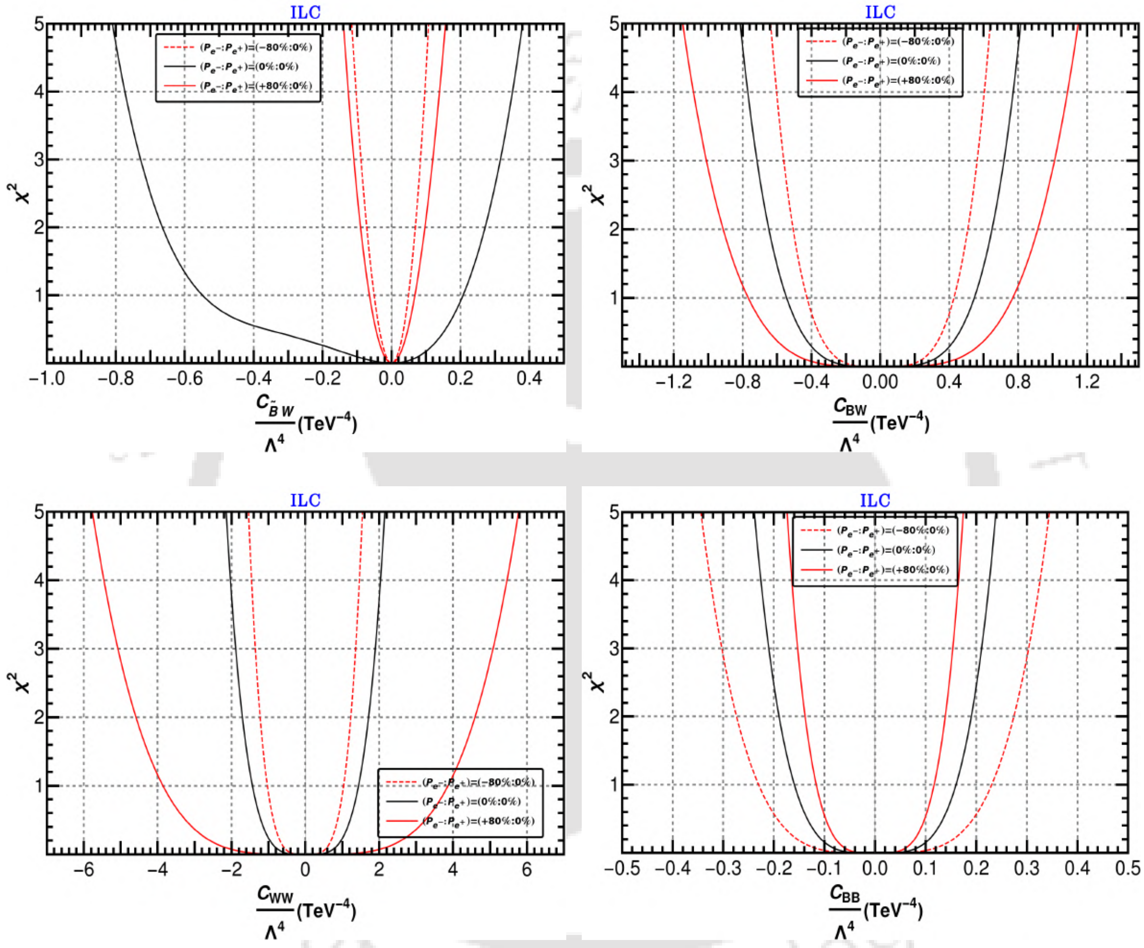

Figure 4.5: χ^2 as a function of different NP couplings for different choices of polarization combination in the context of ILC. All the relevant parameters are written in the inset. Top left: $C_{\tilde{B}W}/\Lambda^4$; top right: C_{BW}/Λ^4; bottom left: C_{WW}/Λ^4; bottom right: C_{BB}/Λ^4.

In Fig. 4.7, we compare the sensitivities achievable at the ILC and CLIC with various polarizations and compare them with the limits obtained with the most recent ATLAS data [189]. One can see that CLIC outperforms both LHC and ILC by at least an order of magnitude for all polarization combinations. However, in case of ILC, for C_{BW}/Λ^4, C_{WW}/Λ^4 and $C_{\tilde{B}W}/\Lambda^4$ polarization combination $\{P_{e^-} : P_{e^+} = -80\% : +30\%\}$ produce better sensitivity compared to ATLAS, whereas for C_{BB}/Λ^4, ILC sensitivities are better than that from ATLAS with $\{P_{e^-} : P_{e^+} = +80\% : -30\%\}$. It is evident from the results that initial beam polarization can improve the level of precision in dimension-8 nTGCs measurement to a large extent.

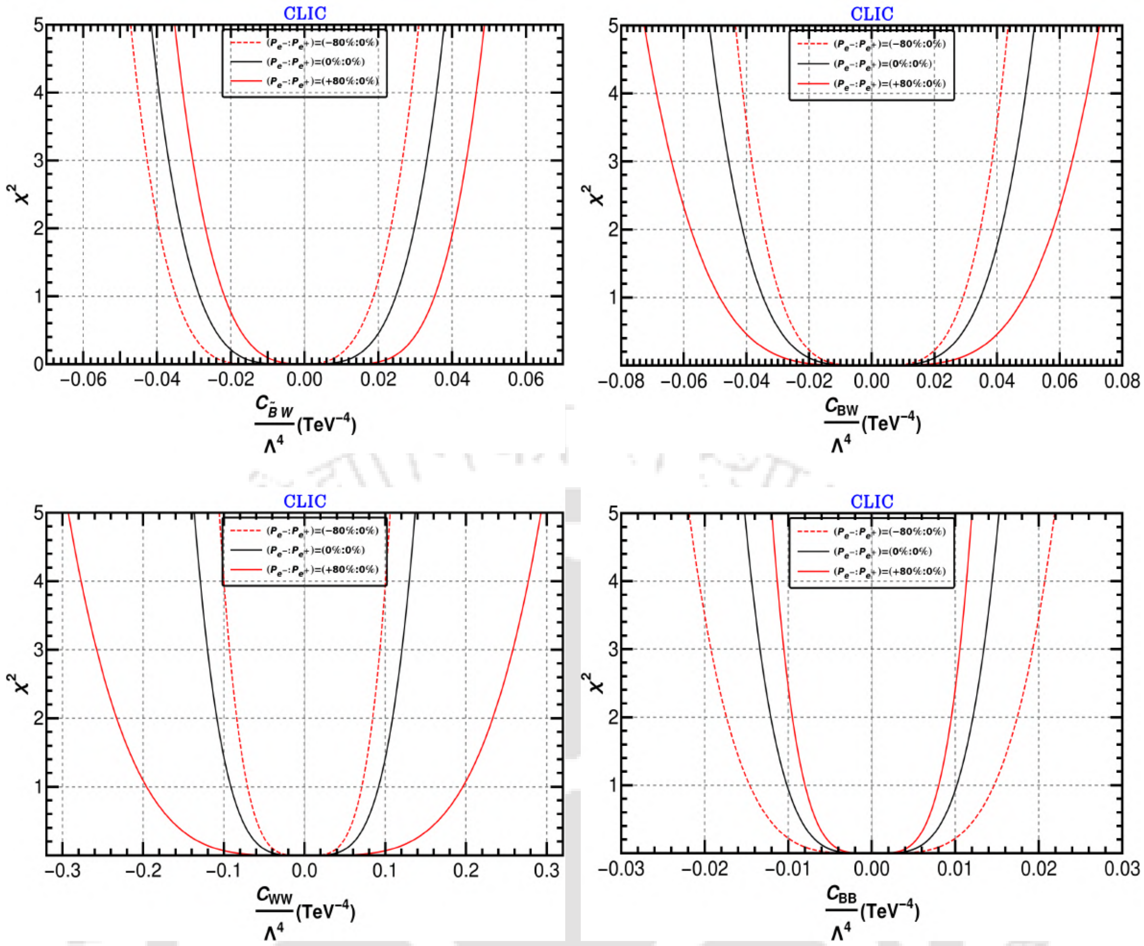

Figure 4.6: Same as Fig. 4.5 but for the CLIC.

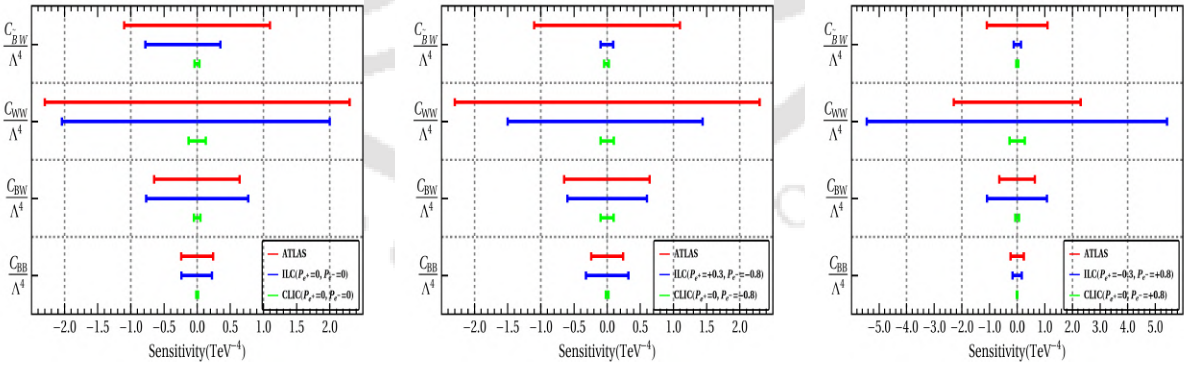

Figure 4.7: Comparison of 95% C.L. limit of dimension-8 nTGCs for three different polarization combinations, in the context of the ILC and CLIC with the existing ATLAS bound. Left: Unpolarized beams; Middle: electron beams are left polarized; Right: electron beams are right polarized. Detailed polarization information are given in the inset.

In Fig. 4.8, we show the variation of statistical limits (95% C.L.) of the NP parameters with the integrated luminosity in the context of both ILC and CLIC. We have allowed the luminosity to vary from 10 fb^{-1} to 1000 fb^{-1}. With the increasing

Couplings (TeV^{-4})	95% C.L. limit					
	ILC			CLIC		
	$P_{e^\pm} = ^{00\%}_{00\%}$	$P_{e^\pm} = ^{+30\%}_{-80\%}$	$P_{e^\pm} = ^{-30\%}_{+80\%}$	$P_{e^\pm} = ^{00\%}_{00\%}$	$P_{e^\pm} = ^{+00\%}_{-80\%}$	$P_{e^\pm} = ^{+00\%}_{+80\%}$
$\frac{C_{\tilde{B}W}}{\Lambda^4}$	$+0.351$ -0.774	$+0.096$ -0.103	$+0.139$ -0.126	$+0.036$ -0.039	$+0.028$ -0.045	$+0.046$ -0.033
$\frac{C_{BW}}{\Lambda^4}$	$+0.770$ -0.770	$+0.603$ -0.603	$+1.086$ -1.086	$+0.049$ -0.049	$+0.041$ -0.041	$+0.069$ -0.069
$\frac{C_{WW}}{\Lambda^4}$	$+2.032$ -2.032	$+1.460$ -1.460	$+5.457$ -5.457	$+0.129$ -0.129	$+0.100$ -0.100	$+0.277$ -0.277
$\frac{C_{BB}}{\Lambda^4}$	$+0.226$ -0.226	$+0.326$ -0.326	$+0.165$ -0.165	$+0.014$ -0.014	$+0.021$ -0.021	$+0.011$ -0.011

Table 4.3: Optimal statistical limit (95% C.L.) on dimension-8 nTGCs at ILC and CLIC for different beam polarization combinations.

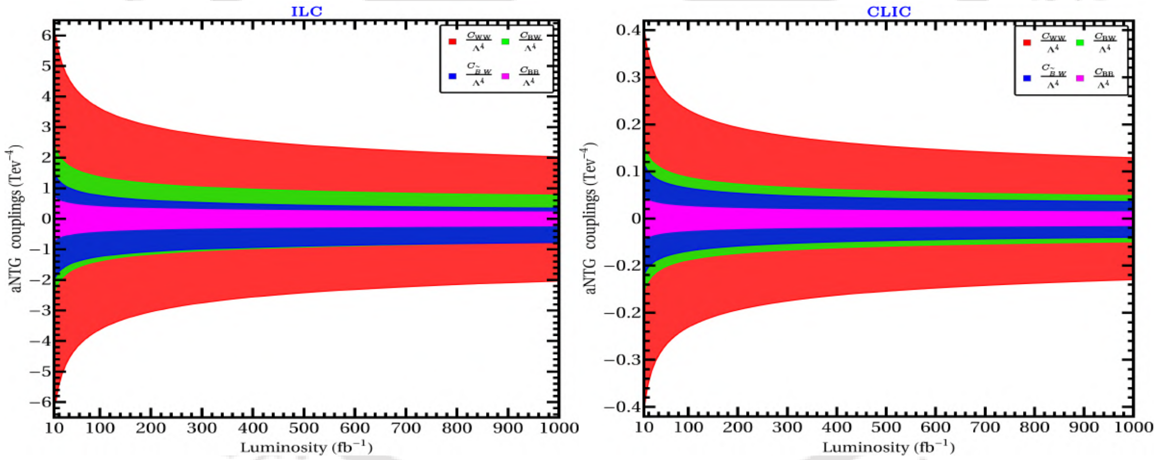

Figure 4.8: Variation of the limits on NP parameters with the integrated luminosity at the e^+e^- colliders. Left: ILC; Right: CLIC.

luminosity, the statistical limit of all the NP parameters is decreased and follow a similar trend. Varying the luminosity from 10 fb^{-1} to 1000 fb^{-1} enhances the statistical limits by 76% (64%), 69% (67%), 67% (65%), and 67% (64%) for $C_{\tilde{B}W}/\Lambda^4$, C_{BW}/Λ^4, C_{WW}/Λ^4, and C_{BB}/Λ^4, respectively for ILC (CLIC).

4.3.4 Correlation of CP-violating dimension-8 nTGCs

Having discussed our results for each individual NP couplings, we will present our two-parameter analysis. The bounds shown in Fig. 4.7 are the most conservative ones. However, there is a possibility that more than one non-zero couplings participate in $e^+e^- \rightarrow Z\gamma$ process. For example, when CP-violation is considered,

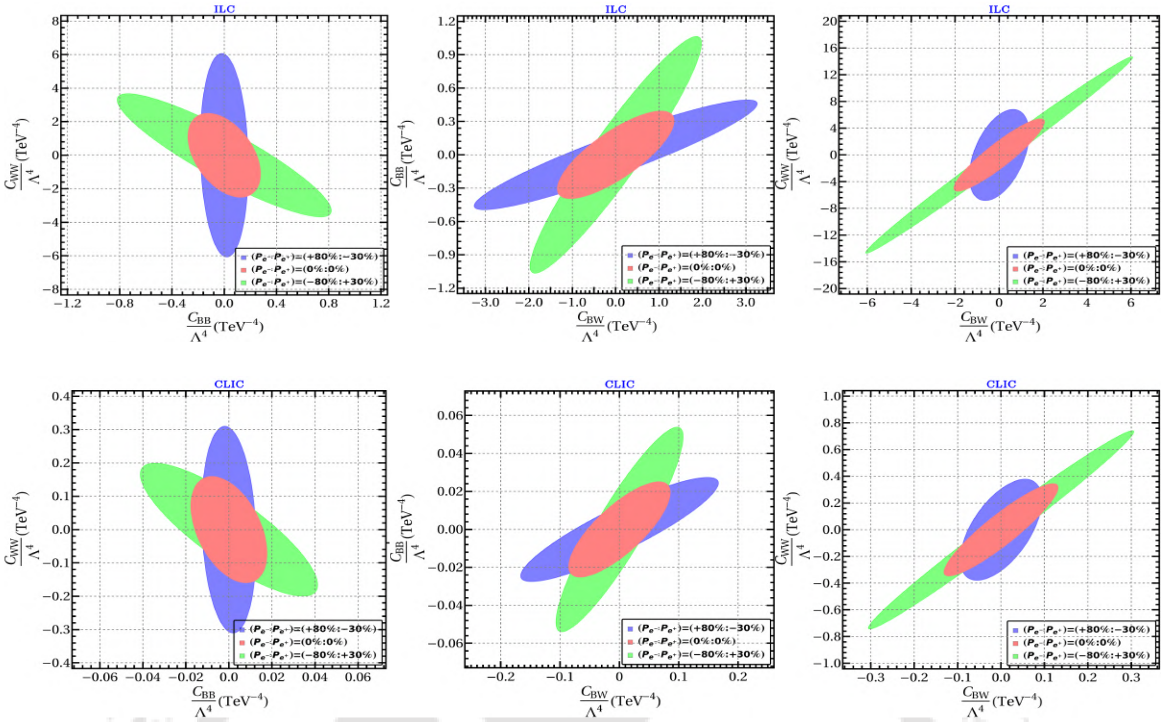

Figure 4.9: 95% C.L. of CP-violating anomalous couplings in 2D parameter space. Left panel: $\left(\frac{C_{WW}}{\Lambda^4}\right)$ & $\left(\frac{C_{BB}}{\Lambda^4}\right)$; middle panel: $\left(\frac{C_{BW}}{\Lambda^4}\right)$ & $\left(\frac{C_{BB}}{\Lambda^4}\right)$. right panel:$\left(\frac{C_{BW}}{\Lambda^4}\right)$ & $\left(\frac{C_{WW}}{\Lambda^4}\right)$. Top:ILC; Bottom:CLIC.

C_{BW}/Λ^4, C_{WW}/Λ^4 and C_{BB}/Λ^4 can contribute simultaneously in $Z\gamma$ production and therefore, the sensitivity in measuring one coupling can be affected by the measurement of the other coupling. In order to capture this non-trivial correlation between these couplings, we have considered two dimension-8 nTGCs non-zero at a time and computed the bound on the parameter space spanned by them. In Fig. 4.9, we show the statistical limits on two-parameters space spanned by $\{C_{BB}/\Lambda^4, C_{WW}/\Lambda^4\}$, $\{C_{BB}/\Lambda^4, C_{BW}/\Lambda^4\}$ and $\{C_{WW}/\Lambda^4, C_{BW}/\Lambda^4\}$ respectively for different polarization combinations. Like one-parameter analysis, here too we can see that CLIC can offer precision at least one order of magnitude higher than that of ILC. Interestingly, we see non-trivial correlation between two parameters, which vary with varying degree of polarization. This happens due to non-trivial interference terms between various couplings. We see, unlike the one-parameter case, here even unpolarized beams can give rise to best sensitivity along certain coupling directions. Therefore, one can say, the two-parameter analysis can provide significantly different sensitivity and polarization-dependence, again owing its origin to the constructive or destructive interference.

In the context of ILC, we have considered the position beam to be both right and left polarized with same degree ($P_{e^+} = \pm 30\%$) whereas for CLIC the positron beam is unpolarized, while in both cases electron beam is supposed to have a higher degree of polarization ($P_{e^-} = \pm 80\%$). Now, from Fig. 4.9, we can see that the is no significant change in the nature of correlation of dimension-8 nTGCs in two-parameters space if we compare the elliptic contours between ILC and CLIC. However, the actual sizes of the contours will definitely depend on the degree of polarization. Therefore, one can infer that the correlation between two couplings will be dominantly governed by on electron beam polarization in case of both ILC and CLIC at the design polarization.

4.3.5 Sensitivity comparison: OOT vs regular binned χ^2 analysis

In this section, we investigate the estimation of the sensitivity of dimension-8 nTGCs through regular binned χ^2 analysis using Eq. (2.6) and compare the results derived from OOT. Therefore, we consider the most constrained dimension-8 effective coupling $i.e.$ C_{BB}/Λ^4 among these four couplings. We again take up the design details of two linear colliders listed in Table 4.2 and show the 95% C.L. statistical limit of C_{BB}/Λ^4 by the cyan color in Fig. 4.10. The 95% C.L are tabulated in Table 4.4. The estimation of the sensitivity via OOT of C_{BB}/Λ^4 is shown in magenta in Fig. 4.10. Now, if we compare the sensitivity of dimension-8 NP coupling, OOT outperforms cut-based analysis by a factor of 1.8.

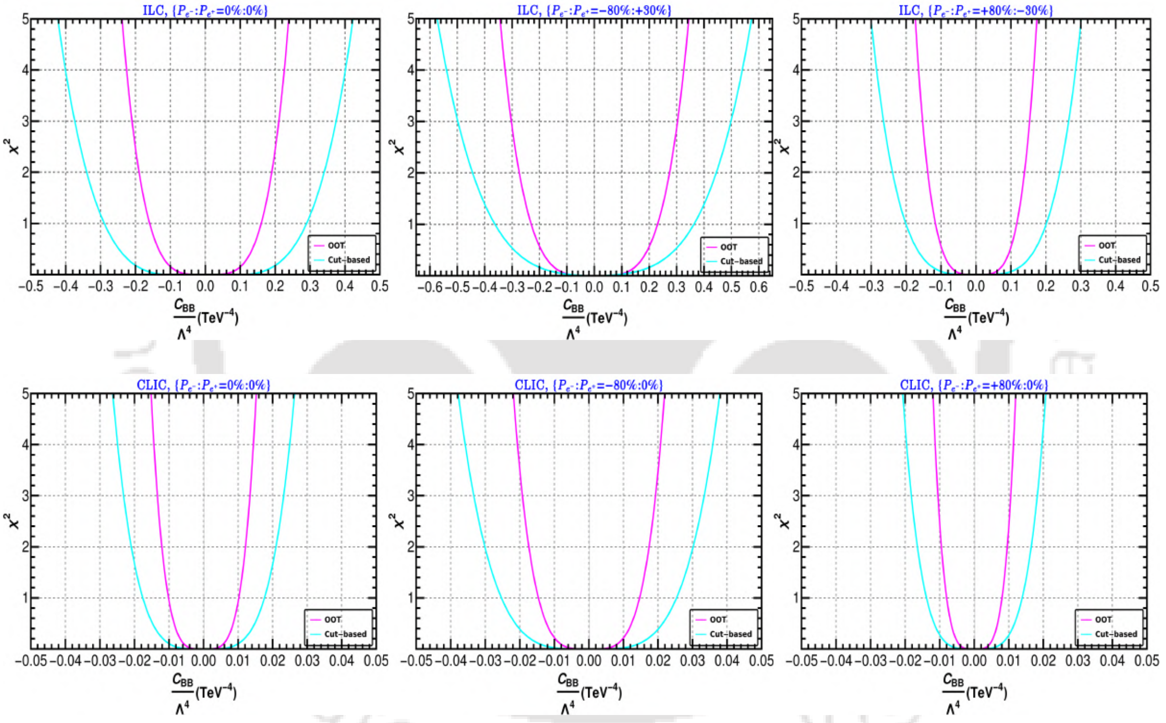

Figure 4.10: Comparison of the sensitivity of C_{BB}/Λ^4 for OOT and cut-based analysis. Beam polarization information is written in the captions of the figures. Top panel: ILC; Bottom panel: CLIC.

We would like to reiterate that our analysis only involves non-zero effects from dimension-8 operators. However, the inclusion of loop-induced NP effects from dimension-6 operators contributes to $Z\gamma$ production cross-section with $\lesssim 50\%$ of that of the tree-level results at CLIC ($\sqrt{s}$ = 3 TeV and Λ = 3.2 TeV) and $\lesssim 8\%$ of the tree-level result at ILC ($\sqrt{s}$ = 1 TeV and Λ = 1.3 TeV). Although the dominant contribution comes from dimension-8 operators, especially the CLIC analysis, the effect of loop effects from dimension-6 operators cannot be neglected. Having said that, in this work, we have obtained the maximum sensitivity that can be achieved for dimension-8 couplings (individual or pair-wise) while all the other couplings are assumed to be zero. The same approach has been taken in [189]. The inclusion

Coupling (TeV^{-4})	95% C.L. limit					
	ILC			CLIC		
	$P_{e^{\pm}} =^{00\%}_{00\%}$	$P_{e^{\pm}} =^{+30\%}_{-80\%}$	$P_{e^{\pm}} =^{-30\%}_{+80\%}$	$P_{e^{\pm}} =^{00\%}_{00\%}$	$P_{e^{\pm}} =^{+00\%}_{-80\%}$	$P_{e^{\pm}} =^{+00\%}_{+80\%}$
$\frac{C_{BB}}{\Lambda^4}$	$+0.401$ -0.401	$+0.540$ -0.540	$+0.285$ -0.285	$+0.025$ -0.025	$+0.036$ -0.036	$+0.020$ -0.020

Table 4.4: 95% C.L. limit of C_{BB}/Λ^4 through cut-based analysis at ILC and CLIC for different beam polarization combinations.

of all dimension-6 and 8 terms in a marginalized analysis will weaken the limits obtained thus far. Obtaining the best possible sensitivity for all the dimension-6 and -8 operators and taking into consideration all the relevant experimental results, can be the topic of a more elaborate future study.

4.4 Probing dimension-8 nTGCs via ZZ production

4.4.1 ZZ production at the CLIC

Pair production of Z-boson at e^+e^- colliders is primarily governed by the electron-mediated t-channel diagram within SM (Fig. 4.12). The BSM contribution from dimension-8 operators to the ZZ production takes place via s-channel γ and Z mediation. Here, we consider that the NP contributions to the process $e^+e^- \to ZZ$ other than nTGCs are negligible. In principle, tree-level dimension-6 SMEFT operators can contribute to the ZZ production via $\gamma f\bar{f}$ and $Zf\bar{f}$ couplings. From the experimental measurements at LEP2 and LHC, the $\gamma f\bar{f}$ ($\propto e_0$) coupling shows $\ll 0.1\%$ deviation from SM whereas for $Zf\bar{f}$ coupling ($\propto g$), the deviation is $\leq 0.1\%$ [188][3]. Therefore, we have neglected the contributions from dimension-6 operators to ZZ production. The variation of the total cross-section with the dimension-8 nTGCs for unpolarized and two different polarization combinations is shown in Fig. 4.11. The total amplitude of the process $e^+e^- \to ZZ$ is

$$|\mathcal{M}_{\texttt{tot}}|^2 = |\mathcal{M}_{\texttt{SM}}|^2 + 2\mathcal{R}\left(\mathcal{M}_{\texttt{SM}}\mathcal{M}^*{}_{\texttt{dimension-8}}\right) + |\mathcal{M}_{\texttt{dimension-8}}|^2. \tag{4.9}$$

The dominant CP-even BSM contribution to the total cross-section arises from the interference term $2\mathcal{R}\left(\mathcal{M}_{\texttt{SM}}\mathcal{M}^*{}_{\texttt{dimension-8}}\right)$ when C_i/Λ^4 are small. As the interference term is proportional to C_i/Λ^4, the cross-section shows asymmetric variation with C_i/Λ^4 in that small interval. In case of large C_i/Λ^4, the dominant contribution to the total cross-section comes from a pure BSM term i.e. $|\mathcal{M}_{\texttt{dimension-8}}|^2$ that is proportional to $(C_i/\Lambda^4)^2$. Therefore, in this range, behavior of the total cross-section is symmetric with C_i/Λ^4. CP violating dimension-8 nTGCs do not interfere with the SM. Therefore, their contributions may stand on a comparable footing or be suppressed by dimension-10 and dimension-12 SMEFT operators. However, in our analysis we assume that no NP effect except dimension-8 operators contribute to ZZ production. The beam polarization plays an important role to enhance or reduce the total

---

[3] e_0 and g are $U(1)_{em}$ and $SU(2)_L$ coupling constants, respectively.

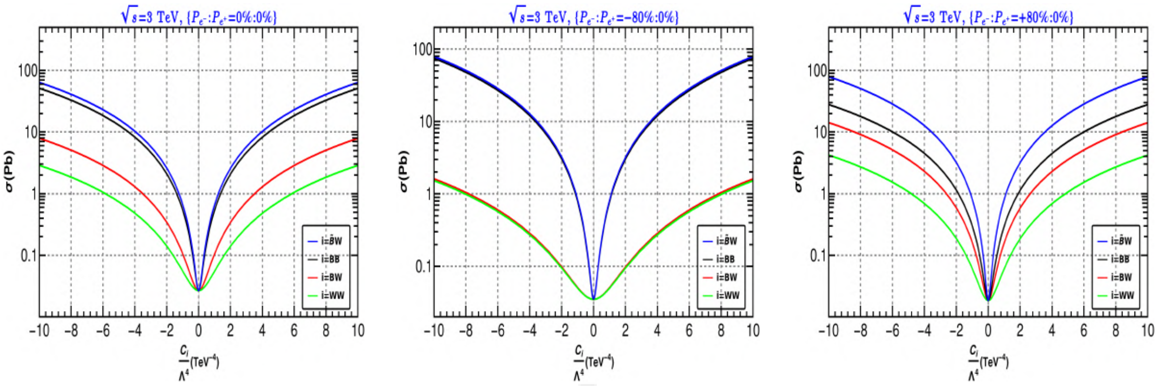

Figure 4.11: Variation of ZZ cross-section with the different dimension-8 effective couplings at the $e^+ e^-$ colliders with $\sqrt{s}$ = 3 TeV. Left: $\{P_{e^-} : P_{e^+} = 0\% : 0\%\}$; Middle: $\{P_{e^-} : P_{e^+} = -80\% : 0\%\}$; Right:$\{P_{e^-} : P_{e^+} = +80\% : 0\%\}$.

cross-section. For $C_i/\Lambda^4\,(i = \tilde{B}W, BW, WW)$ couplings, the ZZ cross-section is increased with $\{P_{e^-} : P_{e^+} = +80\% : 0\%\}$ whereas for C_{BB}/Λ^4 coupling, the opposite polarization provides the enhancement.

4.4.2 Collider analysis

In this section, we will briefly discuss the strategy of estimating signal-background events for ZZ production by reducing the non-interfering SM backgrounds for a specific final state signal of our consideration. The production and subsequent decay final state signal (see Fig. 4.12) for the analysis is given by

$$e^+e^- \to ZZ,\; Z \to \ell^+\ell^-\;(\ell = e, \mu),\; Z \to \nu\bar{\nu}. \tag{4.10}$$

This final state signal provides missing energy through the SM neutrinos which is

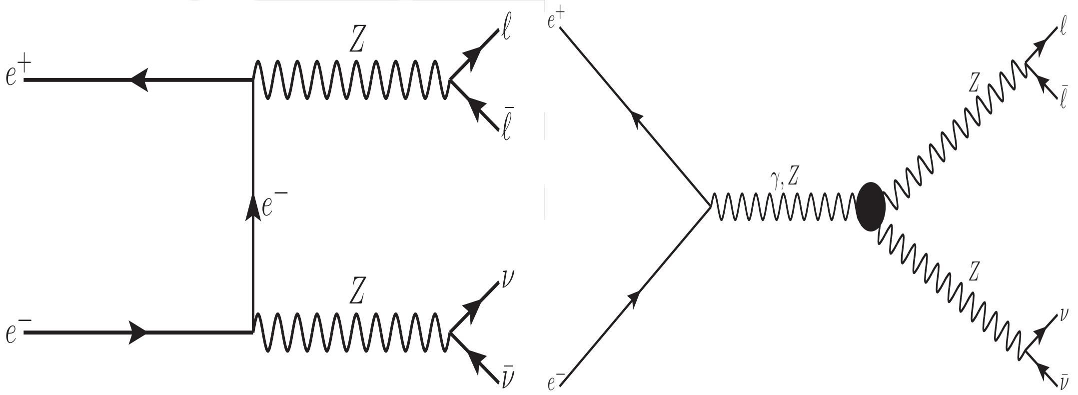

Figure 4.12: Z boson pair production and subsequent decay to `OSL` + missing energy ($E_{\texttt{miss}}$); left: SM, right: dimension-8 SMEFT.

advantageous to discriminate other non-interfering SM backgrounds from the ZZ production. On top of that, as the Z decay to neutrinos has a higher branching ratio compared to charged leptons, this final state produces more statistics. The final state signal process of our interest is `OSL` + missing energy ($E_{\texttt{miss}}$). Dominant non-interfering SM backgrounds arise from 2-body WW and $\ell^+\ell^-(\ell = \tau, \mu)$. There are 3-body non-interfering backgrounds like WWZ, $\nu\nu Z$ and $\ell\ell Z$ but their contribution is $\leq 0.1\%$ compared to WW. Using a suitable cut on $\Delta R_{\ell\ell}$, the $\ell^+\ell^-$ background can be fully reduced without harming the signal. Therefore, in our following analysis, we try to reduce WW as much as possible. In order to mimic the actual collider environment, we use selection criteria on leptons, jets, and photons mentioned in Section 3.6. We take $\not{E}$ and invariant di-lepton mass ($m_{\ell\ell}$) as collider variables for

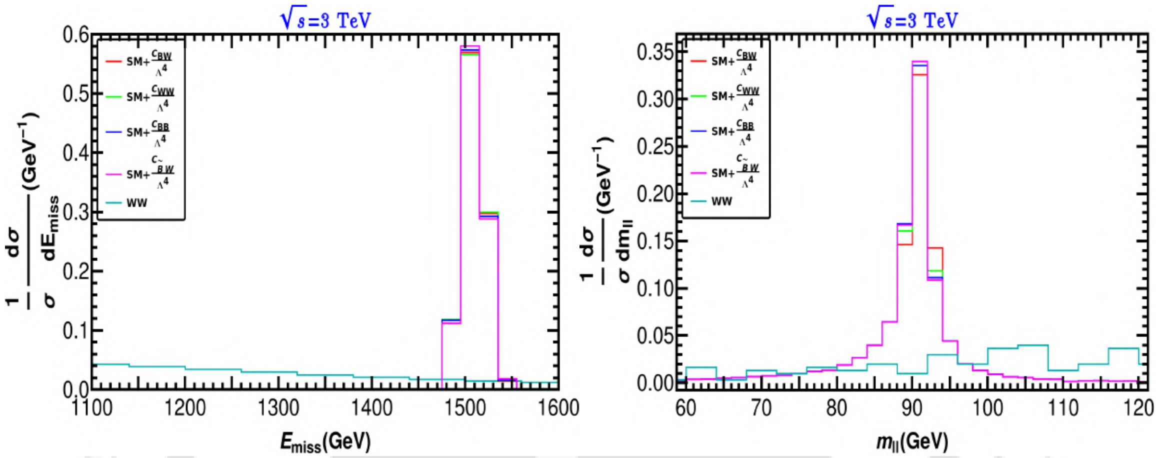

Figure 4.13: Normalized event distribution of `OSL` + missing energy for signal and non-interfering SM background with $\sqrt{s} = 3$ TeV, $C_{ij} = 1$, $\Lambda = 3.2$ TeV and unpolarized beam. Left: missing energy ($E_{\texttt{miss}}$), right: invariant dilepton mass ($m_{\ell\ell}$).

signal back-ground estimation. $\not{E}$ is defined in Eq. (4.8) and $m_{\ell\ell}$ is expressed as

- *Invariant di-lepton mass* ($m_{\ell\ell}$): The construction of an invariant di-lepton mass for two opposite sign leptons can be done by defining:

$$m_{\ell\ell}^2 = (p_{\ell^+} + p_{\ell^-})^2, \tag{4.11}$$

  where p_ℓ is the 4-momentum of ℓ.

We generate signal and background events in `Madgraph` , then showered and analyzed through `Pythia` and the detector simulation is done by `Delphes` . The `UFO` file that is feeded to `Madgraph` is generated through `FeynRules` .

The normalized event distributions for $\not{E}$ and $m_{\ell\ell}$ are shown in Fig. 4.13. The signal distributions shows interference between dimension-8 couplings and the SM. If we look at signal event distributions for missing energy in case of all nTGCs, the distribution peaks near $\sqrt{s}/2$ which is evident as one Z decays to $\nu\bar{\nu}$. Therefore, a cut in the vicinity of $\sqrt{s}/2$ for $E_{\texttt{miss}}$ reduces the irreducible non-interfering SM background significantly. Additionally, a sensible cut on $m_{\ell\ell}$ also helps us to reduce the other backgrounds even further. We observe that, with $1475\,\mathrm{GeV} < \not{E} < 1550$ GeV and $80\,\mathrm{GeV} < m_{\ell\ell} < 98\,\mathrm{GeV}$, all the signal distributions dominate over non-interfering SM backgrounds. This region of phase space is sensitive to study the nTGCs. Here, we note that the choice of the NP scale Λ has been done in such a way that the EFT assumption remains valid. In the following discussion to estimate the sensitivity of dimension-8 nTGCs, we will work in the region of phase space guided by the aforementioned kinematic cut values.

4.4.3 OOT sensitivity of NP couplings

The optimal sensitivity of NP couplings can be determined by using the χ^2 function defined in Eq. (2.47) with the covariance matrix shown in Eq. (2.36). We choose the CM energy $\sqrt{s} = 3$ TeV and $\mathfrak{L}_{int} = 1000\ \text{fb}^{-1}$ and then show χ^2 variation with NP couplings for different choices of polarization combinations in Fig. 4.14. The resulting statistical limits (95% C.L.) for each NP coupling with different beam polarization combinations have been tabulated in Table 4.5. Judicious choices of polarization combination help to estimate the bound on NP couplings in a most stringent way. $\{P_{e^-} : P_{e^+} = -80\% : 0\%\}$ polarization combination provides the most optimal limit for $C_i/\Lambda^4\ (i = \tilde{B}W, BW, WW)$ couplings while for C_{BB}/Λ^4, the opposite polarization combination produces the best result. We can see that given the CM energy and integrated luminosity, CLIC provides much better constraints on NP coupings compared to current experimental bounds. For a careful choice of beam polarization, the most optimal limits of $C_{\tilde{B}W}/\Lambda^4$, C_{BB}/Λ^4, C_{BW}/Λ^4 and C_{WW}/Λ^4 couplings are 29 (60), 6 (29), 8 (16) and 15 (9) times better than the latest experimental limits at ATLAS (CMS), respectively. The statistical sensitivity of NP couplings depends on their impact on the ZZ production. For unpolarized beams, $C_{\tilde{B}W}/\Lambda^4$ maximally contributes, while C_{WW}/Λ^4 has the least influence. Notably, the contribution of $C_{\tilde{B}W}/\Lambda^4$ to ZZ

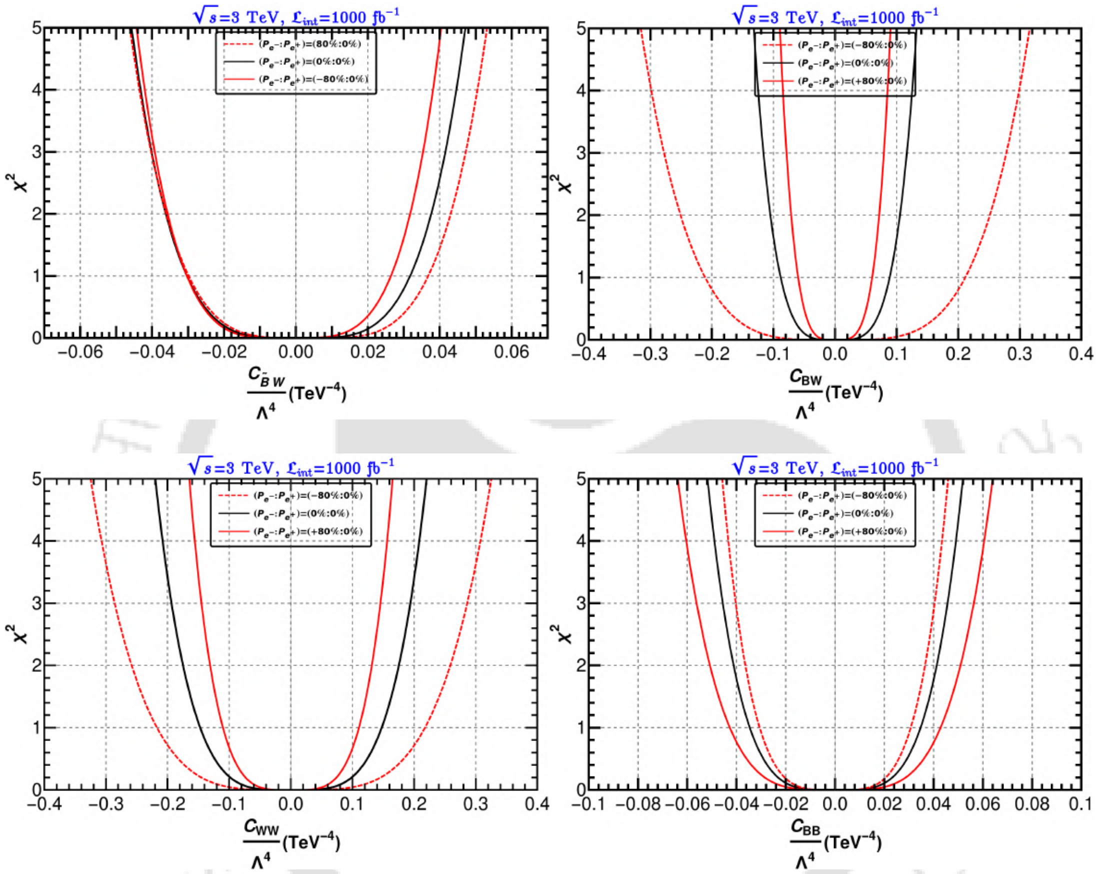

Figure 4.14: χ^2 function of different dimension-8 nTGCs for different choice of polarization combinations at CLIC. Polarization information is written in the inset. Top left: $C_{\tilde{B}W}/\Lambda^4$; top right: C_{BW}/Λ^4; bottom left: C_{WW}/Λ^4; bottom right: C_{BB}/Λ^4. The CM energy is $\sqrt{s} = 3$ TeV and integrated luminosity $\mathfrak{L}_{\texttt{int}} = 1000\ \text{fb}^{-1}$.

production surpasses that of C_{WW}/Λ^4 by a significant factor of thirty. This leads to $C_{\tilde{B}W}/\Lambda^4$ being constrainted approximately 7 times more tightly than C_{WW}/Λ^4 as evident from Table 4.5.

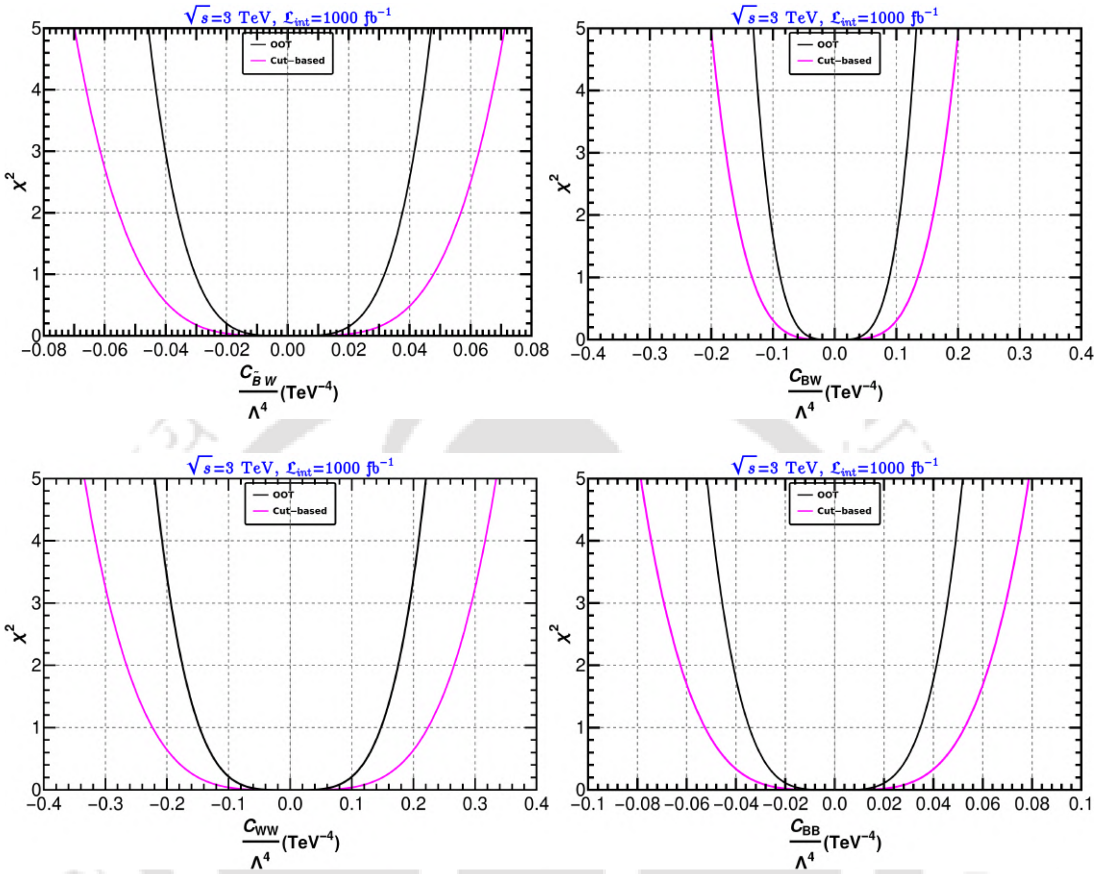

Figure 4.15: Comparison of the variation of the χ^2 function of different NP couplings for unpolarized beam at the CLIC. Top left: $C_{\tilde{B}W}/\Lambda^4$; top right: C_{BW}/Λ^4; bottom left: C_{WW}/Λ^4; bottom right: C_{BB}/Λ^4.

4.4.4 Sensitivity comparison: OOT vs regular binned χ^2 analysis

The statistical limit of NP couplings can also be determined by a contemporary regural binned χ^2 analysis. Here, we discuss the estimation of NP coupling through a cut-based analysis and compare the estimated limit with OOT results. Using Eq. (2.6), the variation of the χ^2 function with NP couplings is shown in Fig. 4.15 by magenta color. The comparison plots clearly show that OOT provides a tighter bound on NP couplings than the regular binned analysis. If we compare the statistical limits, OOT performs better than the regular binned analysis by a factor of 1.7 for each NP coupling.

A comparison of 95% C.L. of dimension-8 couplings between the current experimental constraint from the ATLAS, the cut-based analysis and OOT is shown in Fig. 4.16 for various choices polarization combination where the benefit of the results using OOT can be clearly seen.

Couplings (TeV^{-4})	95% C.L.		
	$P_{e^\pm} = ^{00\%}_{00\%}$	$P_{e^\pm} = ^{+00\%}_{-80\%}$	$P_{e^\pm} = ^{+00\%}_{+80\%}$
$\frac{C_{\tilde{B}W}}{\Lambda^4}$	$+0.044$ -0.043	$+0.050$ -0.043	$+0.038$ -0.042
$\frac{C_{BW}}{\Lambda^4}$	$+0.125$ -0.125	$+0.299$ -0.299	$+0.085$ -0.085
$\frac{C_{WW}}{\Lambda^4}$	$+0.288$ -0.288	$+0.307$ -0.307	$+0.156$ -0.156
$\frac{C_{BB}}{\Lambda^4}$	$+0.049$ -0.049	$+0.043$ -0.043	$+0.060$ -0.060

Table 4.5: Optimal statistical limit (95% C.L.) on dimension-8 nTGCs at CLIC for different beam polarization combinations.

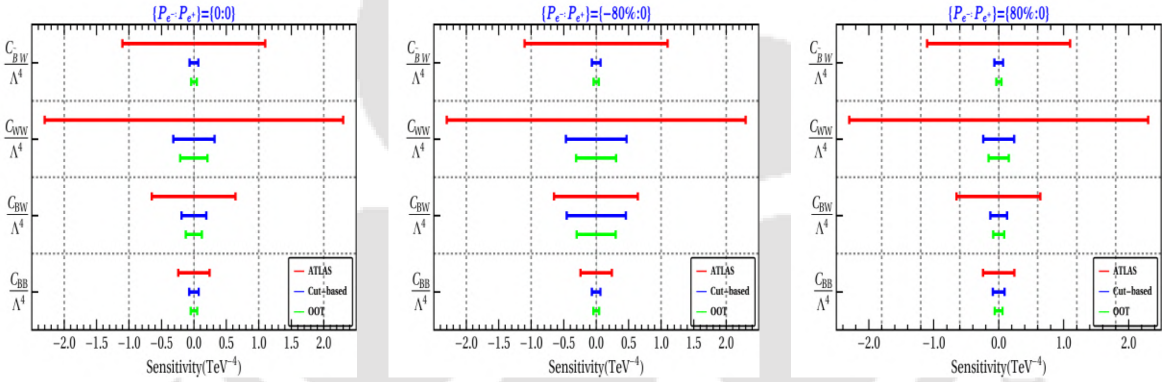

Figure 4.16: Comparison of statistical limit (95% C.L.) of NTGCs between latest ATLAS experiment, OOT and cut-based analysis. The information about beam polarization is written in the headings of the plots.

4.4.5 Correlation between CP violating dimension-8 nTGCs

The expected statistical limits at CLIC discussed above provide the tightest bound on each NP coupling in case of one parameter analysis. In a generic scenario, the estimation of a NP coupling can be affected by the presence of other NP couplings. In our case, all the CP-violating dimnesion-8 NP couplings can contribute simultaneously to the process $e^+e^- \to ZZ$. Therefore, we consider two dimension-8 nTGCs non-zero, at the time keeping the third one fixed at zero in order to estimate the statistical limits and correlation between these two. In Fig. 4.17, we show 95% C.L. in a 2-parameter scenario spanned by planes $\{C_{BW}/\Lambda^4, C_{BB}/\Lambda^4$, $\{C_{WW}/\Lambda^4, C_{BB}/\Lambda^4\}$ and $\{C_{BW}/\Lambda^4, C_{WW}/\Lambda^4\}$, respectively, for all polarization combination. It is worthwhile to notice that the optimal limit on dimension-8 nTGCs in a 2-parameter case is still more stringent than experimental limit by CMS (one parameter analysis). Here, likewise one parameter scenario, the beam polarization plays a crucial roll to con-

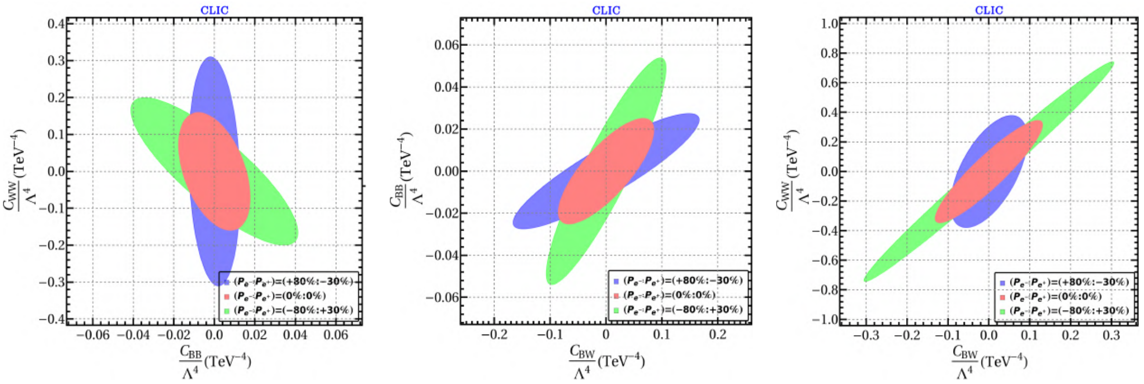

Figure 4.17: Correlation among dimension-8 nTGCs in 2 parameter space. Left:$\{C_{BB}/\Lambda^4, C_{WW}/\Lambda^4\}$, Middle:$\{C_{BW}/\Lambda^4, C_{BB}/\Lambda^4\}$, Right:$\{C_{BW}/\Lambda^4, C_{WW}/\Lambda^4\}$. Polarization information is written in the inset. CM energy and luminosity are written in the headings .

straint a 2-parameter space. As expected, the estimated dimension-8 couplings are abruptly changed due to the presence of others, depending on the constructive or destructive interference between themselves.

4.5 $t\bar{t}$ production production at e^+e^- colliders

Lastly we discuss another example of the OOT where SM interference dominates the signal. We consider $t\bar{t}$ production at an e^+e^- future collider like the ILC assuming any NP contributions stemming from EFT operators are subdominant. These conditions are realized, for example, in the so-called “flipped” 2HDM [192–197] (for a review see [198]) where one scalar doublet couples to down-type quarks, while the second doublet couples to leptons and up-type quarks. If this second doublet is assumed to be heavy [4] it will generate an effective interaction of the form $(\bar{l}e)(\bar{q}u)$ As noted in the Introduction, this situation can be studied in an effective theory approach, with the advantage that the results are not tied to a specific model. Thus, we consider first the possible low-energy manifestation of such UV complete model (*i.e.* below the scale of the heavy scalar) using an effective theory parameterization; within this context we will use the OOT to derive the minimum statistical uncertainty to which the Wilson couplings in the effective theory can be measured.

In the SM, pair-production of top-quark at the e^+ e^- colliders is generated at tree-level by γ and Z mediation, as shown in the left side of Fig. 4.18. The SMEFT contributions can be separated into two classes: those that modify the eeZ and ttZ vertices, and those that generate 4 fermion $eett$ vertices (right side of Fig. 4.18). The relevant

---

[4] More specifically, we assume the second doublet has a small expectation value, large mass, and small mixing with the other doublet.

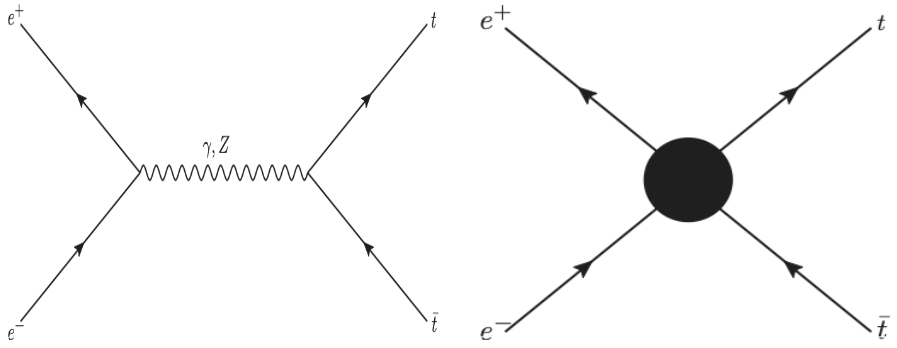

Figure 4.18: Top-quark pair production at $e^+ e^-$ collider. Left: SM contribution; Right: SMEFT contribution.

effective operators (in the so-called Warsaw-basis parameterization [86]) are

group	Operator	vertex
I	$Q^1_{Hl} = (iH^\dagger D_\mu H + \text{H.c.})(\bar{l}_p \gamma^\mu l_r)$	$\frac{1}{2}\text{v}^2 g_\text{z} \bar{e} \not{Z} P_L e$
	$Q^3_{Hl} = (iH^\dagger \tau^I D_\mu H + \text{H.c.})(\bar{l}_p \tau^I \gamma^\mu l_r)$	$-\frac{1}{2}\text{v}^2 g_\text{z} \bar{e} \not{Z} P_L e$
	$Q_{He} = (iH^\dagger D_\mu H + \text{H.c.})(\bar{e}_p \gamma^\mu e_r)$	$\frac{1}{2}\text{v}^2 g_\text{z} \bar{e} \not{Z} P_R e$
II	$Q^1_{Hq} = (iH^\dagger D_\mu H + \text{H.c.})(\bar{q}_p \gamma^\mu q_r)$	$\frac{1}{2}\text{v}^2 g_\text{z} \bar{t} \not{Z} P_L t$
	$Q^3_{Hq} = (iH^\dagger \tau^I D_\mu H + \text{H.c.})(\bar{q}_p \tau^I \gamma^\mu q_r)$	$-\frac{1}{2}\text{v}^2 g_\text{z} \bar{t} \not{Z} P_L t$
	$Q_{Hu} = (iH^\dagger D_\mu H + \text{H.c.})(\bar{u}_p \gamma^\mu u_r)$	$\frac{1}{2}\text{v}^2 g_\text{z} \bar{t} \not{Z} P_R t$
III	$Q^{(1)}_{lq} = (\bar{l}_p \gamma_\mu l_r)(\bar{q}_s \gamma^\mu q_u)$	$(\bar{e}\gamma_\mu P_L e)(\bar{t}\gamma^\mu P_L t)$
	$Q^{(3)}_{lq} = (\bar{l}_p \gamma_\mu \tau^I l_r)(\bar{q}_s \gamma^\mu \tau^I q_u)$	$-(\bar{e}\gamma_\mu P_L e)(\bar{t}\gamma^\mu P_L t)$
	$Q_{lu} = (\bar{l}_p \gamma_\mu l_r)(\bar{u}_s \gamma^\mu u_u)$	$(\bar{e}\gamma_\mu P_L e)(\bar{t}\gamma^\mu P_R t)$
	$Q_{qe} = (\bar{q}_p \gamma_\mu q_r)(\bar{e}_s \gamma^\mu e_u)$	$(\bar{e}\gamma_\mu P_R e)(\bar{t}\gamma^\mu P_L t)$
	$Q_{eu} = (\bar{e}_p \gamma_\mu e_r)(\bar{u}_s \gamma^\mu u_u)$	$(\bar{e}\gamma_\mu P_R e)(\bar{t}\gamma^\mu P_R t)$
IV	$Q^1_{lequ} = (\bar{l}^j_p e_r)\epsilon_{jk}(\bar{q}^k_s u_u)$	$-(\bar{e} P_R e)(\bar{t} P_R t)$
	$Q^3_{lequ} = (\bar{l}^j_p \sigma_{\mu\nu} e_r)\epsilon_{jk}(\bar{q}^k_s \sigma^{\mu\nu} u_u)$	$-(\bar{e}\sigma_{\mu\nu} P_R e)(\bar{t}\sigma^{\mu\nu} P_R t)$

(4.12)

where $g_\text{z} = \sqrt{g^2 + g'^2}$ and $p,\ r,\ s,\ u$ are family indices.

In general the operators in Eq. (4.12) are generated by different types of NP so that they need not have a common scale Λ. The experimental constraints on the Zee coupling allow an $\sim 0.1\%$ deviation from the the SM prediction that corresponds to $\Lambda \sim 7$ TeV (for a unit Wilson coefficient) for group I operators [188]. The constraints on the ttZ coupling (group II) are significantly weaker $\Lambda \sim 1$ TeV [199]; the constraints on the 4-fermion operators (groups III and IV) will be of the same order.

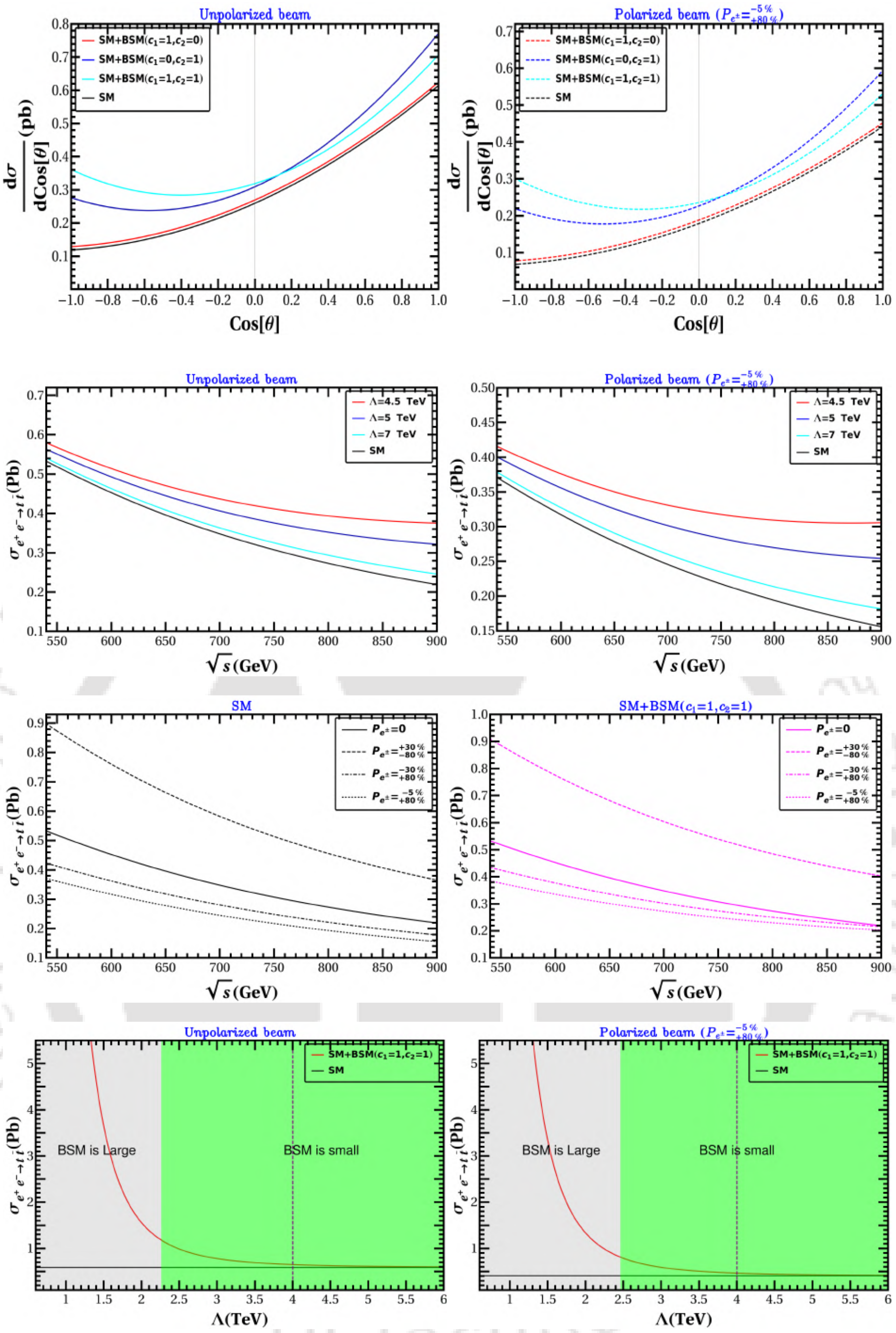

Figure 4.19: Plots of the process $e^+e^- \to \bar{t}t$ cross-section. Top row: angular dependence for CM energy $\sqrt{s} = 500$ GeV, and different values of Λ for unpolarized (left) and polarized with $P_{e^\pm} =^{-5\%}_{+80\%}$ (right) beams. Second row: total cross section as a function of $\sqrt{s}$ for $C_1^0 = C_2^0 = 1$ and several values of Λ, for unpolarized (left) and unpolarized (right) beams. Third row: dependence on the beam polarization for the SM (left) and the SM + EFT with $C_1^0 = C_2^0 = 1$ and $\Lambda = 4$ TeV (right). Bottom row: comparison of the SM total cross section (black horizontal line) with the SM + EFT with $C_1^0 = C_2^0 = 1$ as a function of Λ for unpolarized (left) and polarized (right) beams; the region labeled "BSM small" corresponds to $\sigma_{\texttt{SM+EFT}} < 2\sigma_{\texttt{SM}}$.

Operators in group IV are unique in that, for the process at hand, they do not interfere with the SM, or with the operators in the other groups, and this will allow a future e^+e^- collider to differentiate their contributions from those generated by other types of new physics. These operators offer a convenient method to investigate a class NP effects by suppressing SM contributions in $t\bar{t}$ production for a judicious choice of beam polarization [5]. It is one of the goals of this paper to illustrate this feature using the OOT as a tool; to simplify the discussion we will then consider the effects of these operators, ignoring those that may be generated by those in groups I, II and III. Our effective Lagrangian then takes the form

$$\mathcal{L}_{\mathtt{eff}} = \frac{C_1}{\Lambda^2} Q^1_{lequ} + \frac{C_2}{\Lambda^2} Q^3_{lequ} + \mathrm{H.c.}\,; \tag{4.13}$$

where $C_{1,2}$ are dimensionless (Wilson) coefficients, and Λ is the scale of new physics[6].

The helicity amplitude [7] $M(\lambda_{e^-}, \lambda_{e^+};\, \lambda_t, \lambda_{\bar{t}})$ for this process is given by

$$\begin{aligned}
M(\lambda,\, -\lambda;\, \lambda',\, -\lambda') &= e_0^2 \left(\frac{\lambda\lambda' + \cos\theta}{\beta_z^2} \right) \left[\frac{2}{3}\beta_z^2 - \left(\frac{4s_{\mathtt{w}}^2 - 1 + \lambda}{4s_{2\mathtt{w}}^2} \right) \left(1 - \frac{8}{3}s_{\mathtt{w}}^2 - \beta_t\lambda' \right) \right], \\
M(\lambda,\, \lambda;\, \lambda',\, -\lambda') &= \frac{4C_2 m_t \sqrt{s}}{\Lambda^2}\, \lambda \sin\theta\,, \\
M(\lambda,\, -\lambda;\, \lambda',\, \lambda') &= \frac{2e_0^2 m_t \lambda' \sin\theta}{\sqrt{s}} \left[\frac{2}{3} - \left(\frac{4s_{\mathtt{w}}^2 - 1 + \lambda}{4s_{2\mathtt{w}}^2 \beta_z^2} \right) \left(1 - \frac{8}{3}s_{\mathtt{w}}^2 \right) \right], \\
M(\lambda,\, \lambda;\, \lambda',\, \lambda') &= \frac{s}{2\Lambda^2} (\lambda\lambda'\beta_t - 1)\,(C_1 + 4C_2\lambda\lambda'\,\cos\theta)\,;
\end{aligned} \tag{4.14}$$

where $\lambda_i = \pm 1$ indicates the helicity of particle i, m_t the top-quark mass, m_z the Z-boson mass and

$$\beta_z = \sqrt{1 - \frac{m_z^2}{s}}; \qquad \beta_t = \sqrt{1 - \frac{4m_t^2}{s}}. \tag{4.15}$$

In the above expressions, electron mass has taken to be zero; we also assumed that $C_{1,2}$ are real, if this is not the case then one must replace $C_a \to \mathbf{Re}C_a + i\lambda_e \mathbf{Im}C_a$. We note here that, for zero electron mass, the SM contributes only to the opposite helicity amplitudes $\lambda_{e^-} = -\lambda_{e^+}$, whereas scalar and tensor mediated effective operators contribute only to same helicity amplitudes, so there is no EFT-SM interference; this is not the case for possible contributions from operators in groups I-III in Eq. (4.12).

For $s \gg m_t^2$ and $s_{\mathtt{w}}^2 \simeq 0.25$ it is easy to see that the SM contribution to the total cross section has the form

$$\sigma(P_{e^+},\, P_{e^-})_{\mathtt{SM}} \propto 1 - \mathfrak{a}^2 + (\mathfrak{a} - P_{e^-})\,(\mathfrak{a} + P_{e^+})\;, \quad \mathfrak{a} \sim 0.0652\,; \tag{4.16}$$

which vanishes when $P_{e^+} = P_{e^-} = \pm 1$ and has a maximum when $P_{e^\pm} = \pm 1$; the SM polarized cross section lies above the unpolarized one when $P_{e^-} \lesssim \mathfrak{a}$ and $P_{e^+} \gtrsim -\mathfrak{a}$, or $P_{e^-} \gtrsim \mathfrak{a}$ and $P_{e^+} \lesssim -\mathfrak{a}$.

---

[5] As noted above, operators in group IV are generated by interesting types of new physics; for the current reaction their contributions do not interfere with the SM, which allows a clean evaluation of the effects of polarization – they produce $O(1/\Lambda^4)$ corrections. Operators in the I, II and III are generated by *different* types of new physics (*e.g.* additional Z gauge bosons) and do interfere with the SM, giving rise to $O(1/\Lambda^2)$ contributions. There are also contributions from dimension 8 operators which can generate $O(1/\Lambda^4)$ corrections as well, but these occur only in EFT-SM interference terms and do not correspond to the types of new physics being considered here.

[6] Within the context of the flipped two-Higgs doublet model, Λ denotes the scale of the heavy scalar and c_1 the product of its Yukawa couplings to the leptons and up-type quarks.

[7] For the helicity amplitude calculation see [150].

Explicitly, the SM contribution is given by

$$\begin{aligned}\frac{d\sigma_{\texttt{SM}}}{d\Omega} =& \frac{\alpha_0^2(1-P_{e^-}P_{e^+})}{3s}\Bigg\{1+(\xi_1-P_{\texttt{eff}}\xi_2)+\frac{1}{4}(\xi_1^2-2P_{\texttt{eff}}\xi_1\xi_2+\xi_2^2)\left(\mathfrak{C}^2+\frac{\beta_t^2}{2-\beta_t^2}\right) \\ &-\left[\xi_2(1+\mathfrak{c}\xi_1)-\frac{1}{4}4P_{\texttt{eff}}\left(4\xi_1-(2\xi_1^2-\xi_2^2)\mathfrak{C}\right)\right]\beta_t\cos\theta+ \\ &+\left[1+\mathfrak{C}\left(\xi_1-P_{\texttt{eff}}\xi_2\right)+\frac{2\mathfrak{C}+1}{4}(\xi_1^2-2P_{\texttt{eff}}\xi_1\xi_2+\xi_2^2)+\frac{\mathfrak{C}(2-\mathfrak{C})}{2}P_{\texttt{eff}}\xi_1\xi_2\right]\beta_t^2\cos^2\theta\Bigg\}\,;\end{aligned} \tag{4.17}$$

$$P_{\texttt{eff}}=\frac{P_{e^-}-P_{e^+}}{1-P_{e^-}P_{e^+}}\,,\qquad \xi_1=\frac{1}{s_{2\texttt{w}}^2\beta_z^2},\qquad \xi_2=\frac{4s_{\texttt{w}}^2-1}{2s_{2\texttt{w}}^2\beta_z^2},\qquad \mathfrak{C}=3-12s_{\texttt{w}}^2\,; \tag{4.18}$$

and, using the notation of Eq. (2.27), effective operator contribution is determined by the following choice of f_i and g_i:

$$\begin{aligned}\{f_1,\,f_2,\,f_3\} &= \frac{3\beta_t s}{256\pi^2\Lambda^4}\left\{(1+\beta_t^2),\,16\beta_t\cos\theta,\,32\beta_t^2\cos^2\theta\right\}\,,\\ \{g_1,\,g_2,\,g_3\} &= (1+P_{e^-}P_{e^+})\left\{\left(C_1^2+16\frac{1-\beta_t^2}{1+\beta_t^2}C_2^2\right),\,-C_1C_2,\,C_2^2\right\}\,.\end{aligned} \tag{4.19}$$

We plot in Fig. 4.19 this differential cross section and the associated cross section for various choices of the model parameters and beam polarizations. As expected, the SM cross section decreases as the CM energy $\sqrt{s}$ increases, and the polarized SM cross section for $P_{e^\pm}={}^{-5\%}_{+80\%}$ is smaller than the unpolarized one, in accordance with Eq. (4.16). We therefore will use this choice of beam polarizations for the optimal estimation of the Wilson coefficients, and compare it to that with unpolarized beams.

It also evident that as Λ increases the total cross-section approaches the SM value. We identify a value $\Lambda=\Lambda_{\texttt{boundary}}$ corresponding to $\sigma_{\texttt{tot}}=2\sigma_{\texttt{SM}}$, so that the process is SM-dominated when $\Lambda>\Lambda_{\texttt{boundary}}$; using Fig. 4.19 we find $\Lambda_{\texttt{boundary}}\sim 2$ TeV and, being interested in situations where the EFT represents a correction to the SM, we will consider NP scales above this value. This also shows why $t\bar{t}$ production is such an effective process to probe NP above TeV scale. For our explicit calculations we use the following collider parameters:

$$\Lambda=4\,\text{TeV}\,;\qquad \sqrt{s}=500\,\text{GeV}\,;\qquad \mathfrak{L}_{\texttt{int}}=1000\,\text{fb}^{-1}\,. \tag{4.20}$$

4.5.1 Collider analysis

In this section, we provide an event level signal and background analysis of top quark pair production at e^-e^+ machine. Our main goal here is to determine the efficiency ϵ with which we approximate the optimal observable.

As noted earlier, the SM process is mediated by Z or photon in s-channel exchange, while the NP effects we consider are generated by a contact 4-fermion interaction; as in the previous sections we will restrict ourselves to the NP effects in Eq. (4.13). We will consider only the leptonic decays of the W bosons that follow from the decay of the $\bar{t}\,t$ pair, namely,

$$e^+e^-\longrightarrow t\,\bar{t}\to\left(bW^+\right)\,\left(\bar{b}W^-\right)\to\left(bl'^+\nu_{l'}\right)\,\left(\bar{b}l^-\bar{\nu}_l\right)\;;\quad l,\,l'=e,\,\mu\,, \tag{4.21}$$

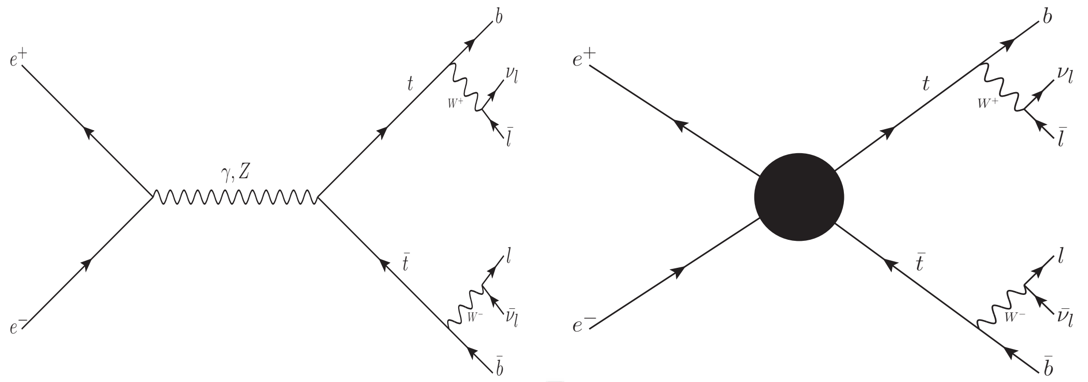

Figure 4.20: Production and decay of top-quark at $e^+ \, e^-$ colliders for $2l \, + 2b +$ missing energy signal.

BPs	Input model	Cross-section (fb)	
		$P_{e^\pm} = 0$	$P_{e^\pm} =^{-5\%}_{+80\%}$
BP1	$C_1^0 = 1, \, C_2^0 = 0$	597.8	415.4
BP2	$C_1^0 = 0, \, C_2^0 = 1$	645.7	461.4
BP3	$C_1^0 = 1, \, C_2^0 = 1$	651.9	467.4

Table 4.6: Total cross-section at e^+e^- collider for different benchmark points for unpolarized and polarized $P_{e^\pm} =^{-5\%}_{+80\%}$ beams with $\sqrt{s} = 500$ GeV. All the benchmark points have $\Lambda = 4$ TeV.

(see Fig. 4.20). Thus the signature will be two opposite-sign leptons of same/different flavors + two b jets+ missing energy ($\not{E}$). The leading (non-interfering) SM background contributions are generated by Zh, ZZ and W^+W^-Z production.

We follow a standard approach, generating parton-level signal events using `CalcHEP` [159]; the events are then showered and analyzed using `Pythia` [161]. For event reconstruction, and lepton and jet identification we use the following criteria:

- Events must have two opposite-sign leptons, and two b jets; the b-tagging efficiency is chosen to be 0.6 in accordance with the ILC TDR [102].
- Lepton transverse momentum: $p_T^l > 10$ GeV.
- Light jet transverse momentum: $p_T^j > 20$ GeV.
- Leptons and light jets must be isolated: $\Delta R_{ll'} > 0.2$, $\Delta R_{jl} > 0.4$ and $\Delta R_{jj'} > 0.4$.
- Exclude events where the dilepton invariant mass is in the range 75 GeV $< m_{ll} < 105$ GeV to reduce the $Z \to \ell^+\ell^-$ background.
- Exclude events where the $b - \bar{b}$ invariant mass is in the range 115 GeV $< m_{bb} < 135$ GeV, to reduce $h \to b\bar{b}$ contamination.

where we defined $\Delta R = \sqrt{\Delta\eta^2 + \Delta\phi^2}$ as the usual distance in the rapidity (η) - azimuthal angle (ϕ) plane. The invariant mass cuts are designed to exclude the

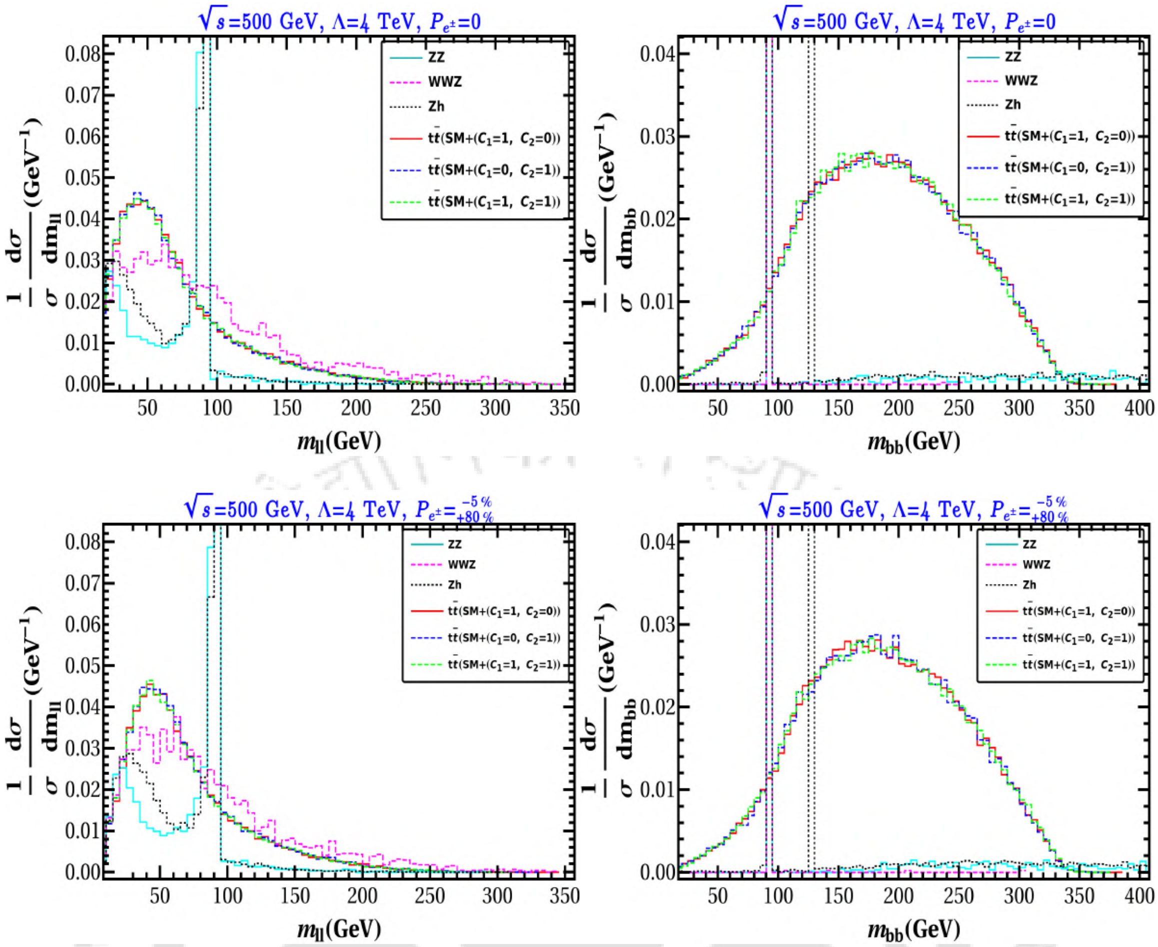

Figure 4.21: Invariant di lepton mass (m_{ll}) (left), Invariant di b-jet mass (m_{bb}) distributions (right) for $2l\ + 2b$ + missing energy final state coming from $t\bar{t}$ signal with EFT ($\Lambda = 4$ TeV) as well as dominant SM backgrounds at the $e^+\,e^-$ collider with $\sqrt{s}$ = 500 GeV. Top panel: Unpolarized beams; bottom panel: polarized beams $P_{e^\pm} =^{-5\%}_{+80\%}$.

SM background; the values selected are based on the event distributions plotted in Fig. 4.21.

Using these selection criteria we determine the efficiency factor ϵ by using Eq. (3.11). For the benchmark points in Table 4.6 we find $\epsilon \sim 0.008$, roughly independent of polarization. In the following we take a conservative approach and use $\epsilon = 0.001$ or $\epsilon = 0.005$.

4.5.2 1σ surfaces of EFT parameter uncertainties

Using Eq. (2.47), we define the optimal 1σ region of the statistical uncertainties of the EFT parameters $C_{1,2}$ for the above described reaction. We choose three different combinations of the NP coupling seed values: $i)$ $C_1^0 = 1, C_2^0 = 0$, $ii)$ $C_1^0 = 0, C_2^0 = 1$, and $iii)$ $C_1^0 = 1, C_2^0 = 1$. The 1σ regions are plotted in Fig. 4.22 for various choices of input values c_i^0 and beam polarizations in $\Delta C_i - \Delta C_j$ plane where $\Delta C_i = C_i - C_i^0$. For this calculation we choose $\sqrt{s}$= 500 GeV and $\mathfrak{L}_{int}$= 1000 fb^{-1}. Note that, even though the SM dominates, the NP effects are significant even for $\Lambda = 4$ TeV.

The 1σ uncertainties for different combination of input values are listed in Ta-

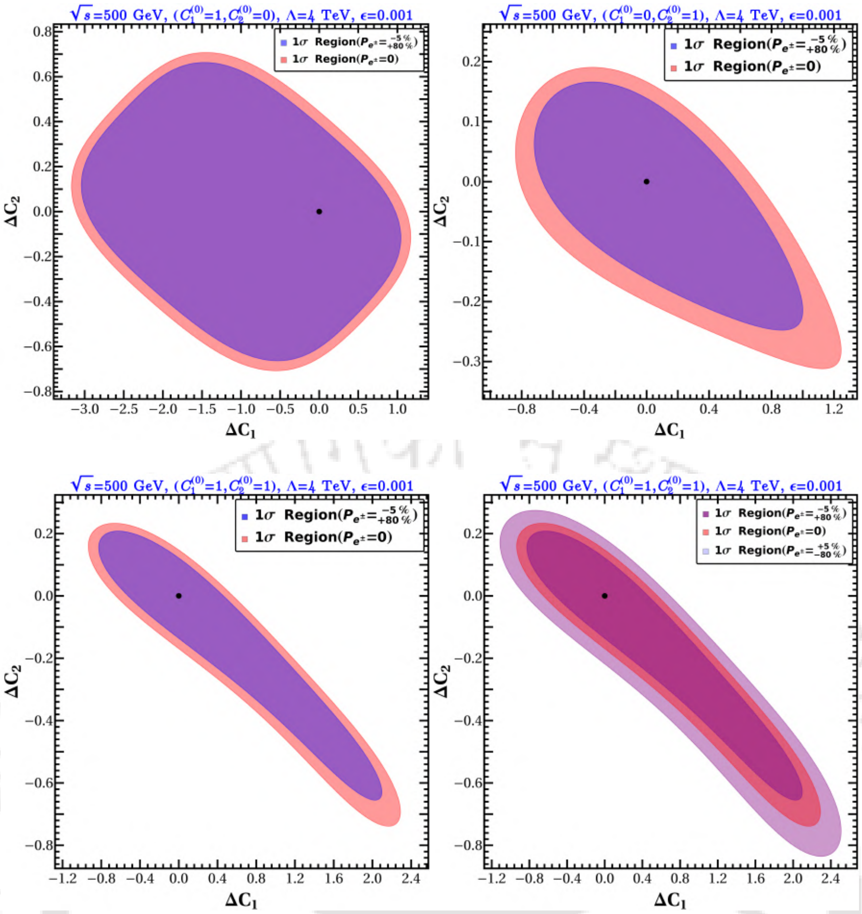

Figure 4.22: Optimal 1σ regions in $\Delta C_1 - \Delta C_2$ plane for various choices of EFT parameters and choices of beam polarization. See figure inset and heading for details.

ble 4.7, while 1σ surfaces are shown in Fig. 4.22. The polarization of the initial beams in the lepton collider play a crucial role in determining the uncertainties of NP couplings. Precise extraction of NP relies on reducing the SM contribution and/or enhancing BSM contribution to the specific process. The uncertainties of NP couplings for different choices of beam polarization (within the possible ranges in accordance to collider TDR) are shown in the bottom right of Fig. 4.22. For $\left(P_{e^\pm} =^{+5\%}_{-80\%}\right)$, both SM and BSM contribution to the top-quark pair production increase, while if we flip the polarization sign, both contributions will decrease. But we observe that $\left(P_{e^\pm} =^{-5\%}_{+80\%}\right)$ provides most constraint surface in $\Delta C_i - \Delta C_j$ plane, which implies that the reduction of SM contribution is more important than the increment in BSM contribution in this scenario. We note that for $\left(P_{e^\pm} =^{+5\%}_{-80\%}\right)$ choice of polarization combination, NP uncertainties are approximately $10 - 20\%$ smaller compared to unpolarized beam. We also note that in all cases the uncertainties for the tensor operator coefficient C_2 are smaller than for the scalar one, as the tensor operator provides larger BSM contribution to $t\bar{t}$ production than the scalar operator. As Λ increases, BSM contribution to the production cross-section is reduced, as a result, the uncertainties of the NP couplings are also increased. This behavior is illustrated in Fig. 4.23.

The OOT done here is primarily signal-based, where we assume that the non-interfering background effects are negligible, which is true to a great extent. However, uncertainty of NP couplings will increase when we include these remaining background effects. We take into account these effects by choosinga lower efficiency ($\epsilon = 0.001$) than the one derived when ignoring such backgrounds ($\epsilon = 0.008$).

Seed parameters	$P_{e^\pm} = 0$				$P_{e^\pm} =^{-5\%}_{+80\%}$			
	$\epsilon = 0.005$		$\epsilon = 0.001$		$\epsilon = 0.005$		$\epsilon = 0.001$	
	$\pm\Delta C_1$	$\pm\Delta C_2$	$\pm\Delta C_1$	$\pm\Delta C_2$	$\pm\Delta C_1$	$\pm\Delta C_2$	$\pm\Delta C_1$	$\pm\Delta C_2$
$C_1^0 = 1, C_2^0 = 0$	$+0.52$ -1.41	$+0.32$ -0.32	$+1.16$ -3.18	$+0.71$ -0.71	$+0.46$ -1.37	$+0.29$ -0.15	$+1.03$ -3.06	$+0.66$ -0.66
$C_1^0 = 0, C_2^0 = 1$	$+0.55$ -0.37	$+0.08$ -0.14	$+1.24$ -0.84	$+0.19$ -0.31	$+0.44$ -0.32	$+0.07$ -0.11	$+1.00$ -0.72	$+0.16$ -0.25
$C_1^0 = 1, C_2^0 = 1$	$+1.02$ -0.42	$+0.10$ -0.33	$+2.29$ -0.94	$+0.23$ -0.74	$+0.55$ -0.37	$+0.09$ -0.14	$+1.24$ -0.84	$+0.19$ -0.31

Table 4.7: Optimal 1σ statistical uncertainties of the C_1 and C_2 couplings for unpolarized and polarized $P_{e^\pm} =^{-5\%}_{+80\%}$ beams, and two values of ϵ; we used the parameters in Eq. (4.20).

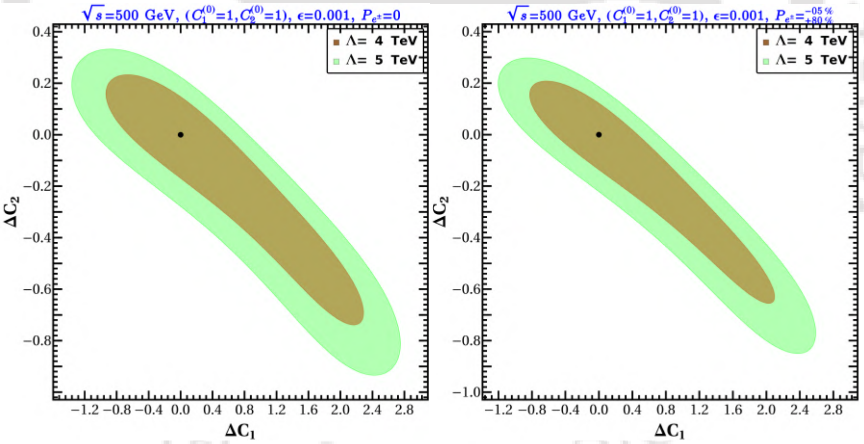

Figure 4.23: 1σ surfaces in $\Delta C_1 - \Delta C_2$ plane for two choices of Λ and unpolarized (left) and polarized $P_{e^\pm} =^{-5\%}_{+80\%}$ (right) beams. See figure inset and heading for details.

4.5.3 Differentiation of hypotheses

We discuss the distinction of different hypotheses from a base hypothesis using Eq. (3.13). We consider $C_1^0 = C_2^0 = 0$ as the base hypothesis (that corresponds to the SM), and various other choices of the seed values of NP couplings (given in the previous section) as alternative hypotheses. The degree of statistical differentiation of the alternate hypotheses from the base hypothesis are shown in Fig. 4.24 and listed in Table 4.8, for both unpolarized and polarized beams. 2σ, 3σ and 5σ regions

Model	ϵ	$\mathfrak{L}_{\text{int}}$ (fb^{-1})	Significance ($\Delta\sigma$)	
			$P_{e^\pm} = 0$	$P_{e^\pm} =^{-5\%}_{+80\%}$
$\bar{C}_1 = 1, \bar{C}_2 = 0$	0.001	1000	0.29	0.35
	0.001	2000	0.41	0.49
	0.005	1000	0.69	0.78
$\bar{C}_1 = 0, \bar{C}_2 = 1$	0.001	1000	2.77	3.36
	0.001	2000	3.92	4.75
	0.005	1000	6.19	7.51
$\bar{C}_1 = 1, \bar{C}_2 = 1$	0.001	1000	3.93	4.83
	0.001	2000	5.56	6.82
	0.005	1000	8.79	10.80

Table 4.8: Statistical significance $\Delta\sigma$ of several hypotheses $\bar{C}_1, \bar{C}_2$ with respect to the SM.

are shown by red, blue and green colours around the base hypothesis. The alternate hypotheses are denoted by cross, square and triangle symbols, respectively. For unpolarized beams, hypothesis I ($\bar{C}_1 = 1, \bar{C}_2 = 0$) is indistinguishable form the SM even if we choose $\epsilon = 0.005$ and $\mathfrak{L}_{int} = 2000$ fb^{-1}. With $\epsilon = 0.001$ (0.005) and $\mathfrak{L}_{int} = 2000$ fb^{-1}, hypothesis II ($\bar{C}_1 = 0, \bar{C}_2 = 1$) lies beyond 3σ (5σ) the exclusion (discovery) limit. Due to larger BSM contribution, hypothesis III ($\bar{C}_1 = 1, \bar{C}_2 = 1$) is easier to distinguish than the other two hypotheses. Appropriate beam polarization, larger ϵ and high luminosity help the differentiation become more significant.

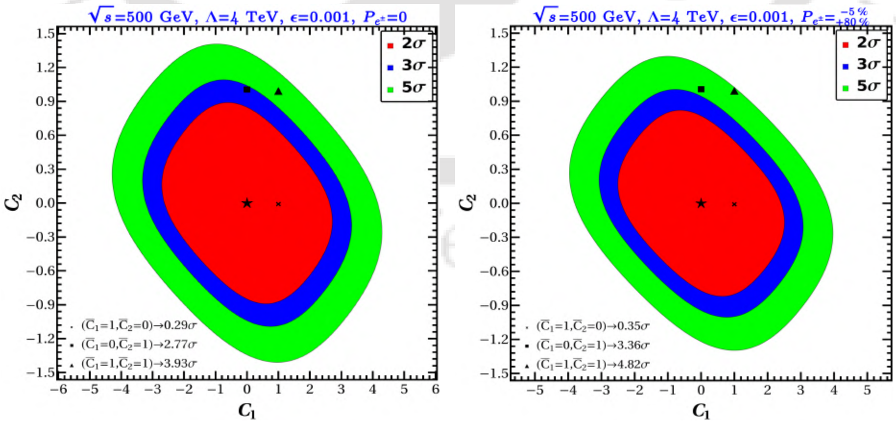

Figure 4.24: Statistical significance (*cf.* Eq. (3.13)) $\Delta\sigma \leq 2,\ 3,\ 5$ (respectively, red, blue and green areas) of alternate models with respect to the SM for unpolarized (left) and polarized $P_{e^\pm} =^{-5\%}_{+80\%}$ beams (right); also noted the statistical significance of 3 specific models. See figure inset and heading for details of the parameter choices.

4.5.4 Optimal versus standard binned χ^2

In this section we provide a comparison of the optimal coefficient uncertainties with those obtained using a basic analysis of collider data using the χ^2 function defined in Eq. (2.6). From this we define the 1σ regions in parameter space by the condition

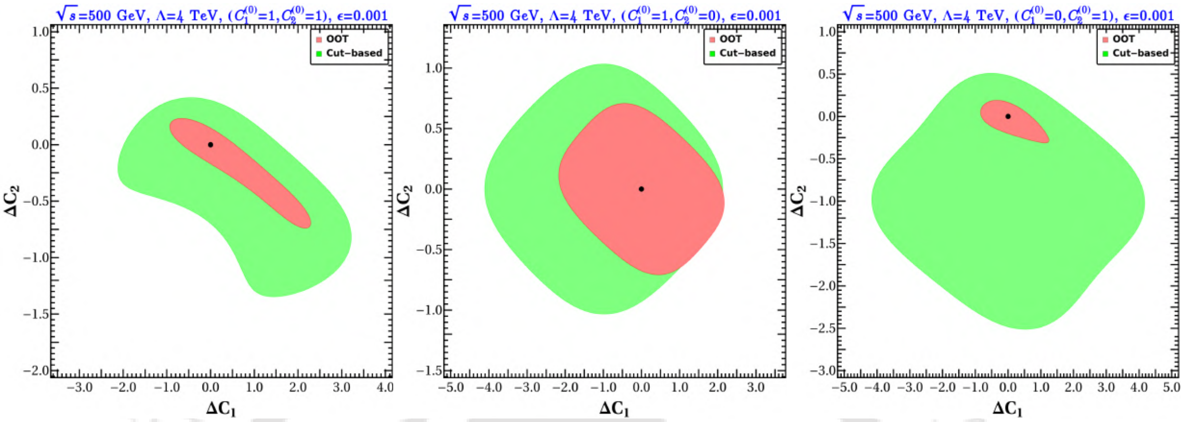

Figure 4.25: Comparison of 1σ surfaces in $\Delta C_1 - \Delta c_2$ plane between OOT (light red) and cut-based analysis as in Eq. (2.6) (in green) for unpolarized beams.

$\chi^2 \leq 1$. The results for three choices of model parameters, and the comparison with the corresponding OOT results are presented in Fig. 4.25. The χ^2 statistic defined in Eq. (2.6) depends on the number of bins, a dependence that is also examined in Fig. 4.25; we find that choosing 5 bins provides the most constrained parameter space [8] and thus we use this choice in the following examples. These results give a measure of the degree to which the analysis based on Eq. (2.6) can be improved. In this case, as BSM contribution is less than SM to the signal final state, the statistical fluctuation in each bin is large, as a consequence, uncertainties in NP couplings estimated from binned analysis is worse than the OOT uncertainties.

4.6 Comparison with BSM dominance

We now consider the determination of NP parameters in cases where the NP dominates over the SM; specifically, we will consider the production of new particles at an e^+e^- collider. For this a specific model must be selected, and we will use the well-understood extension of the SM where an additional doublet is added to the scalar sector, the two-Higgs doublet model[9] (2HDM). As noted in Section 4.5, the so-called 'flipped' 2HDM [192–198] can be used to describe the type of NP effects considered in that section.

The new particles in the 2HDM are a neutral CP-even scalar, a neutral CP-odd scalar, and a pair of charged scalars $H^\pm$; we will also assume the presence of right-handed neutrinos N_R and assume that the N_R and $H^\pm$ are light enough to be produced at the e^+e^- collider. We then will study the degree to which this collider can

---

[8] This choice provides a balance between the number of events with the statistical fluctuations in each bin.

[9] For a recent review see [53, 200].

be expected to determine some of the couplings associated with this extension of the SM.

4.6.1 $t\bar{t}$ production at e^+e^- colliders within flipped-2HDM

We first briefly revisit the process considered in Section 4.5, assuming now that the NP can be directed produced in colliders. In this case the contact interaction on the right-hand diagram on Fig. 4.18 is replaced by the heavy scalar exchange diagram in Fig. 4.26. We consider flipped 2HDM to elucidate this scenario. This model does not generate the effective interaction Q^3_{lequ} in Eq. (4.13), so that $c_2 = 0$. The Yukawa couplings to the CP-even heavy Higgs (H) are given by [198]

$$-\mathcal{L}_{\text{yuk}} = \frac{m_f}{v} y_f \bar{f} f H \,, \tag{4.22}$$

where $y_f = \cos(\beta - \alpha) - \sin(\beta - \alpha)\kappa_f$, with $\kappa_f = \cot\beta = v_1/v_2$ and α is the angle associated with the diagonalization of the neutral CP-even scalar mass matrix.

For this model $C_1 = \frac{m_e m_t}{v^2} k_f$. In order to estimate the the uncertainty of this NP coupling we will consider the resonant production of H and its subsequent decay $\to t\bar{t}$. In the numerical analysis, we consider heavy Higgs mass $m_H = 500$ GeV, $\sin(\beta - \alpha) \sim 1$ in the decoupling limit and small $\tan\beta$ (~ 0.5). In this case we find $C_1 = 5.7 \times 10^{-7}$. Comparing uncertainty in C_1, ΔC_1 in the flipped-2HDM is smaller than in the EFT scenario due to a greater NP contribution to $t\bar{t}$ production.

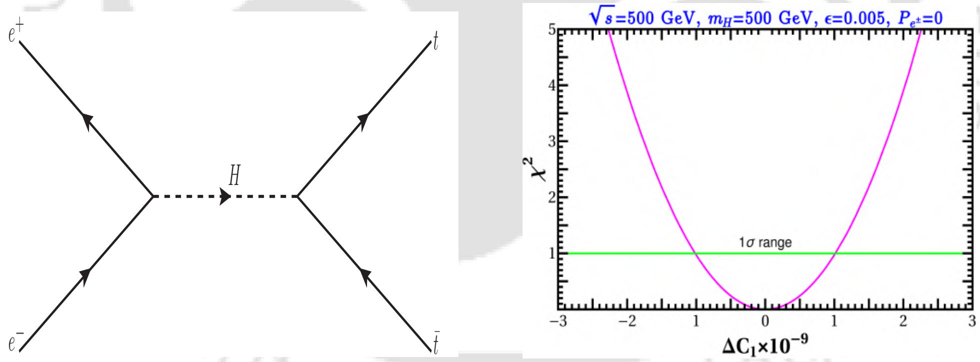

Figure 4.26: Left: NP contribution to $e^+e^- \to t\bar{t}$ in a flipped 2HDM; where H denotes a heavy scalar. Right: dependence of the χ^2 function on the NP coefficient uncertainty ΔC_1, when $C_1^0 = 5.71 \times 10^{-7}$, with the 1σ bound indicated.

4.6.2 H^+H^- production at e^+e^- colliders

We consider next the pair production of $H^\pm$ which provides an additional channel to probe the NP in this model in which the NP contribution dominates. We assume that the $H^\pm$ have the standard minimal coupling to the photon,

$$H^+(p_4)H^-(p_3)\gamma : -ie_0(p_4^\mu - p_3^\mu) \,, \tag{4.23}$$

and parameterize the leptonic-Yukawa[10] and Z couplings as follows:

$$\begin{aligned} H^+(p_4)H^-(p_3)Z &: -\ ia\left(p_4^\mu - p_3^\mu\right)\ , \\ e^+ N_R H^- &: b; \end{aligned} \tag{4.24}$$

where, p_3 and p_4 are the incoming momenta of H^- and H^+, respectively. For definiteness we will consider three different models : the flipped 2 HDM or inert doublet model (IDM) (doublet) [49], the type-II seesaw model (triplet) [201], and the scotogenic model [60]; these are characterized by[11],

Model	a	b
Flipped 2 HDM/Inert-doublet (IDM):	$e_0 \cot(2\theta_{\mathrm{w}}) = 0.21$	0
Scotogenic:	$e_0 \cot(2\theta_{\mathrm{w}}) = 0.21$	0.1
Type II seesaw:	$e_0 \tan(\theta_{\mathrm{w}}) = 0.17$	0

(4.25)

As a concrete application we will consider H^+H^- pair-production at a linear e^+e^- collider; the relevant diagrams are shown in Fig. 4.27. The corresponding helicity amplitudes, $M'(\lambda_{e^-},\, \lambda_{e^+})$, are easily obtained: $M'(\lambda,\, \lambda) = 0$, and

$$M'(\lambda,\, -\lambda) = i\left[e_0^2 + ae_0\left(\frac{4s_{\mathrm{w}}^2-1}{2s_{2\mathrm{w}}} - \lambda\frac{1}{2s_{2\mathrm{w}}}\right)\frac{s}{s-m_{\mathrm{z}}^2} + \frac{(1+\lambda)b^2}{4}\frac{s}{t-m_{\mathrm{N}}^2}\right]\beta_{H^+}\sin\theta\,; \tag{4.26}$$

where θ is the scattering angle of $H^\pm$ from the axis of collision, $\beta_{H^+} = \sqrt{1-4m_{H^+}^2/s}$, and

$$t = \frac{s}{2}\left(1+\beta_{H^+}\cos\theta\right) + m_{H^+}^2\,. \tag{4.27}$$

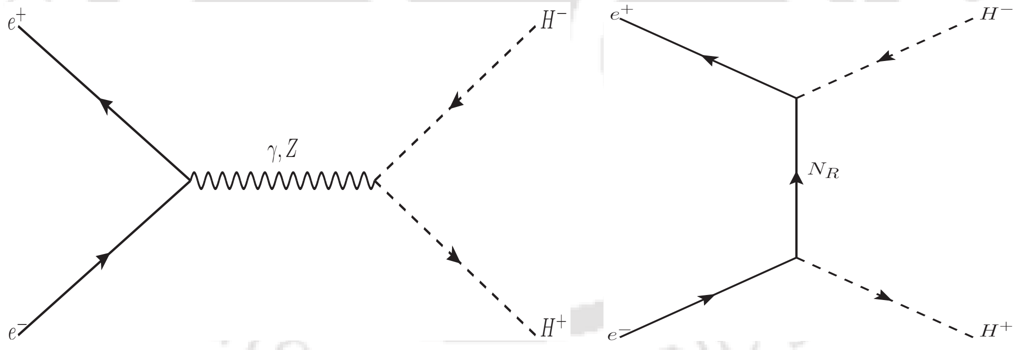

Figure 4.27: Leading pair-production mechanism for singly charged scalar pairs ($H^\pm$) at an $e^\pm$ collider.

In the numerical examples we will choose a charged-Higgs mass of $m_{H^\pm} = 200$ GeV and the right-handed neutrino mass of $m_N = 200$ GeV. As the Z boson couples strongly to left-handed (right-handed) electron (positron) compared to right-handed electron, left polarized electron, and right polarized positron beam enhances the H^+H^- cross-section. We study the effect of beam polarization by comparing the results for unpolarized beams to those with $P_{e^\pm} =^{+30\%}_{-80\%}$ and $P_{e^\pm} =^{+10\%}_{-50\%}$. The plots of the total cross section as a function of the CM energy are presented in Fig. 4.28.

---

[10] We assume that the masses of any other heavy neutrinos are large enough to have negligible effects at the colliders being considered.

[11] Here, b is a free parameter.

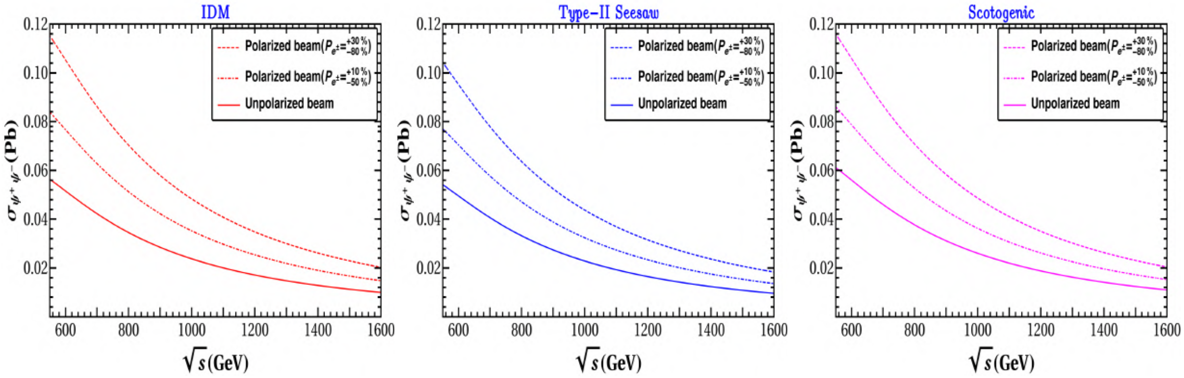

Figure 4.28: The total cross-section for charged scalar pair production as a function of the CM energy ($\sqrt{s}$) at an $e^+ e^-$ collider for unpolarized beams and two different choices of beam polarization. Left: IDM; middle: type-II seesaw; right: scotogenic (see Eq. (4.25)).

4.6.3 Collider analysis of the inert doublet model

In this section we estimate the efficiency factor ϵ for H^+H^- production within the inert doublet model (IDM). This model is one of the simplest extension of the SM where the scalar sector is assumed to include an additional doublet H_2, and an unbroken discrete $\mathbb{Z}_2$ symmetry under which H_2 is odd whereas all other fields are even. This discrete symmetry forbids Yukawa interactions between the inert doublet H_2 and SM fermions and ensures that the lightest physical component of H_2 can serve as a Dark Matter (DM) candidate. The Lagrangian consisting the scalar dark sector can be written as

$$\mathcal{L} = \mathcal{L}_{\text{SM}} + |D_\mu H_2|^2 - V(H_1, H_2), \tag{4.28}$$

where,

$$\begin{aligned} V(H_1, H_2) &= -\mu_H^2(H_1^\dagger H_1) + \lambda_H(H_1^\dagger H_1)^2 + \mu^2(H_2^\dagger H_2) + \lambda(H_2^\dagger H_2)^2 + \lambda_1(H_1^\dagger H_1)(H_2^\dagger H_2) \\ &+ \lambda_2(H_1^\dagger H_2)(H_2^\dagger H_1) + \frac{\lambda_3}{2}[(H_1^\dagger H_2)^2 + \text{H.c.}]. \end{aligned} \tag{4.29}$$

We assume $\mu^2 > 0$ that ensures that the vacuum expection value of the inert doublet vanishes and guarantees that $\mathcal{Z}_2$ remains unbroken. In contrast the SM scalar doublet H_1 does acquire a vacuum expection value v. The physical modes consist of a singly-charged scalar $H^\pm$, a CP-odd neutral scalar A^0, and CP-even neutrals $h,\ H^0$, where h is the physical SM scalar field. The corresponding tree-level masses are given by

$$\begin{aligned} m_{H^0}^2 &= \mu^2 + \lambda_L v^2, \\ m_{H^\pm}^2 &= \mu^2 + \frac{1}{2}\lambda_1 v^2, \\ m_{A^0}^2 &= \mu^2 + \frac{1}{2}(\lambda_1 + \lambda_2 - 2\lambda_3)v^2, \end{aligned} \tag{4.30}$$

where $\lambda_L = \frac{1}{2}(\lambda_1 + \lambda_2 + \lambda_3)$.

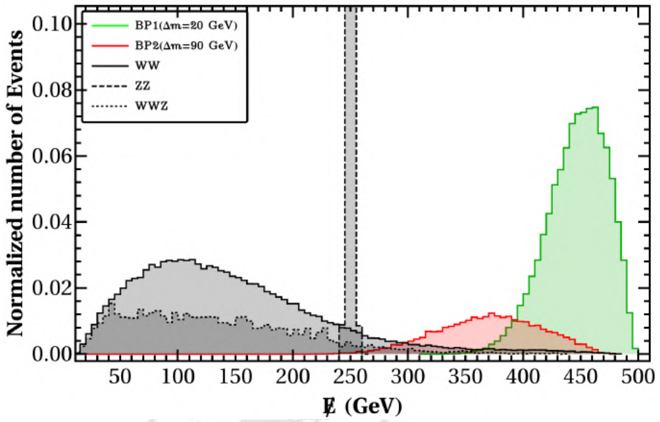

Figure 4.29: Normalized missing energy distribution of OSL + missing energy signal for IDM at the $e^+ e^-$ collider with $\sqrt{s} = 500$ GeV and unpolarized beams.

The signal we will use to identify the production of an H^+H^- pair will be two opposite-sign e or μ leptons (OSL) plus missing energy ($\not{E}$). The decay chain can be written as

$$e^+e^- \to H^+H^-, \quad H^\pm \to H^0W^\pm, \quad W^- \to l^-\bar{\nu}_l\,, \; W^+ \to l^+\nu_l\,; \tag{4.31}$$

where we focus on the leptonic decay modes of W. The dominant (non-interfering) SM background arises from W^+W^-, ZZ and W^+W^-Z production. The analysis of H^+H^- production in an e^+e^- collider for the IDM has been studied in detail in several publications, see, *e.g.*, [202–205].

BPs	Δm	$m_{H^\pm}$	Cross-section (fb)	
			$P_{e^\pm} = 0$	$P_{e^\pm} = ^{+30\%}_{-80\%}$
BP1	20	90	101.2	201.2
BP2	90	160	56.5	112.4

Table 4.9: Total cross-section of charged scalar pair-production ($H^+ H^-$) for different benchmark points for unpolarized and polarized ($P_{e^\pm} = ^{+30\%}_{-80\%}$) beams.

We use the criteria for events reconstruction as in section 4.5.1 in order to reduce the SM background we impose the following cuts:

- $\mathcal{C}_1$: events must contain two opposite sign leptons in the final state.
- $\mathcal{C}_2$: missing energy $\not{E} \leq 370\,(300)$ for BP1 (BP2).

It follows form Fig. 4.29 that $\mathcal{C}_{1,2}$ strongly reduce the (non-interfering) SM backgrounds. We also chose charged scalar masses equal to $m_{H^\pm}$ = 90 GeV and 160 GeV in view of the latest bounds [206]. Using the the definition of ϵ in Eq. (3.11), the efficiency factor for the two benchmark points is tabulated in Table 4.10. These results justify the conservative choice $\epsilon = 0.005$ we used above for all the different NP scenarios.

Cuts	Cross-section					Efficiency factor (ϵ)	
	Signal		SM background				
	BP1 (fb)	BP2 (fb)	W^+W^- (fb)	ZZ (fb)	W^+W^-Z (fb)	ϵ^{BP1}	ϵ^{BP2}
$\mathcal{C}_1$	2.02	1.13	211.4	11.2	0.8	0.02	0.02
$\mathcal{C}_2$	1.96	0.85	4.01	0.0	0.002	0.019	0.015

Table 4.10: Event cross-section and efficiency factor (ϵ) for two different benchmark points of IDM and corresponding SM background estimation background estimation for unpolarized beams with CM energy ($\sqrt{s}$) = 500 GeV.

4.6.4 1σ surfaces in the $a - b$ plane

We now apply the OOT to obtain the the optimal statistical uncertainty regions for the NP couplings (a, b); the results are presented in Table 4.11 and the corresponding 1σ regions are shown in Fig. 4.30 with CM energy ($\sqrt{s}$) = 500 GeV, luminosity ($\mathfrak{L}_{int}$) = 1000 fb^{-1} and signal efficiency (ϵ) = 0.005. For the IDM and type II models the uncertainties in NP couplings are similar since the cross sections are almost equal. For the scotogenic model where $b \neq 0$, the t-channel diagram contributes and enhances the cross section, resulting in an increased sensitivity to b. In Table 4.11, 1σ uncertainties of NP couplings for two different charged Higgs masses ($m_{H^\pm} = 90, 160$ GeV) are listed. For $m_{H^\pm}$ =160 GeV, due to smaller production cross-section, the uncertainties of NP couplings are increased by approximately 30% compared to the case of $m_{H^\pm} = 90$ GeV. We can also see that a judicious choice of polarization also enhances the cross section, leading to a reduced statistical uncertainty in the determination of the NP coefficients. For $P_{e^\pm} =^{+30\%}_{-80\%}$ the uncertainty in the parameter a (b) is reduced by approximately 50-55% (25-40%). Finally, as a function of the luminosity $\mathfrak{L}_{int}$ and the efficiency ϵ, the uncertainties scale as $1/(\sqrt{\mathfrak{L}_{int}\epsilon})$ with the expected result that a larger luminosity and/or efficiency also lead to reduction of the uncertainties.

4.6.5 Differentiation of models

We can now follow the same approach as in Section 4.5.3 and use the OOT to estimate the extent to which different hypotheses can be distinguished. Specifically, given a "base" and alternate hypotheses, $\{a^0, b^0\}$ and $\{\bar{a}, \bar{b}\}$, respectively, we define the significance as in Eq. (3.13) (where now $g_i^0 = g_i(a^0, b^0)$, $\bar{g}_i = g_i(\bar{a}, \bar{b})$) and again assume that these hypotheses can be distinguished at the $\geq \ell\sigma$ level if $\Delta\sigma \geq \ell$.

Taking $a^0 = b^0 = 0$ (similar to the SM) as a base hypothesis, we determine the statistical separation of the models listed above. For CM energy $\sqrt{s} = 500$ GeV, $\mathfrak{L}_{int} = 1000$ fb^{-1}, $m_{H^\pm} = 160$ GeV, and $\epsilon = 0.005$, the separation significance are listed in Table 4.12 and corresponding plots are shown in Fig. 4.31. For unpolarized beams, we can see that for both inert doublet and type-II seesaw models are under discovery limit (that is, $\Delta\sigma < 5$), but the scotogenic model is above this limit due to the enhancement of the cross-section by the t-channel N_R contribution. Polarized beams ($P_{e^\pm} =^{+30\%}_{-80\%}$) enhances the production cross-section, which in turn provides a clear distinction (above 5σ) of the three different models from the base hypothesis.

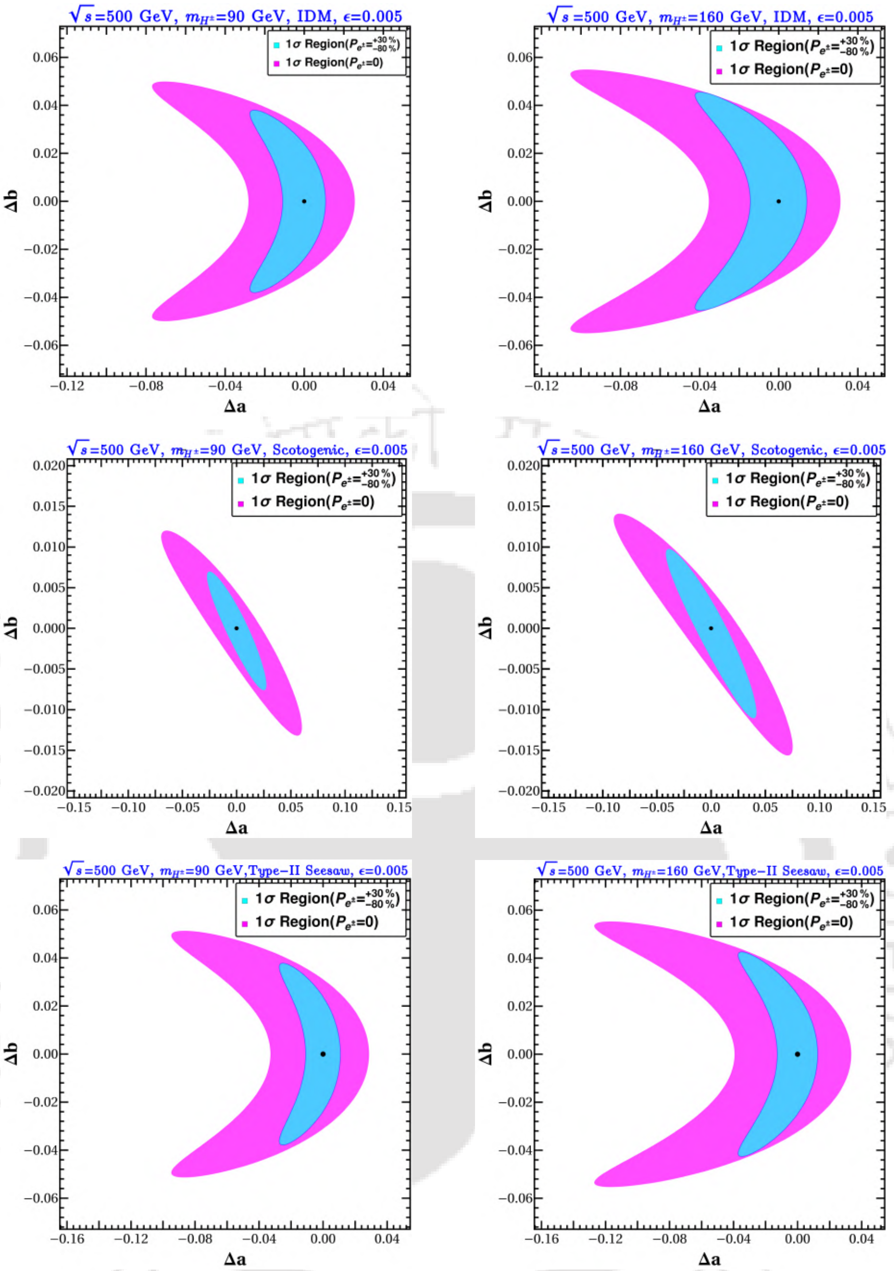

Figure 4.30: Optimal 1σ surfaces for different models with unpolarized and polarized beams $P_{e^\pm} = ^{+30\%}_{-80\%}$, $\epsilon = 0.005$, and $m_{H^\pm} = 90$ GeV (left column) or $m_{H^\pm} = 160$ GeV (right column).

Also note that with larger luminosity, total number of events increases to provide higher significance.

4.6.6 Comparison between optimal and standard χ^2

The statistical uncertainties obtained using the OOT can be compared to those obtained using a basic collider analysis based on Eq. (2.6), as was done in Section 4.5.4. Here also we consider the differential cross-section as our collider observable for the binned analysis. The resulting 1σ regions in the $a - b$ plane for three different

		Uncertainties			
		$P_{e^\pm}=0$		$P_{e^\pm}=^{+30\%}_{-80\%}$	
Model	$m_{H^\pm}$(GeV)	$\pm\Delta a$	$\pm\Delta b$	$\pm\Delta a$	$\pm\Delta b$
Inert doublet	90	$+0.025$	$+0.050$	$+0.011$	$+0.038$
		-0.077	-0.050	-0.027	-0.038
	160	$+0.033$	$+0.058$	$+0.014$	$+0.046$
		-0.117	-0.058	-0.042	-0.046
Scotogenic	90	$+0.060$	$+0.012$	$+0.028$	$+0.007$
		-0.070	-0.012	-0.028	-0.007
	160	$+0.085$	$+0.016$	$+0.041$	$+0.010$
		-0.105	-0.016	-0.042	-0.010
Type-II Seesaw	90	$+0.028$	$+0.050$	$+0.017$	$+0.038$
		-0.095	-0.050	-0.028	-0.038
	160	$+0.037$	$+0.058$	$+0.015$	$+0.046$
		-0.157	-0.058	-0.043	-0.046

Table 4.11: Optimal 1σ statistical uncertainty in the a, b couplings for both unpolarized and polarized $P_{e^\pm}=^{+30\%}_{-80\%}$ beams with $\epsilon = 0.005$.

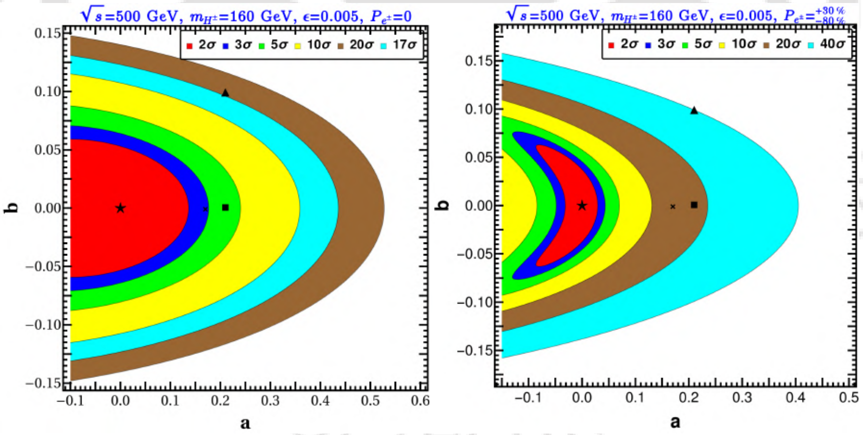

Figure 4.31: Statistical significance of alternate models with respect to the $a^0 = b^0 = 0$ model (*cf.* Eq. (3.13)), $\Delta\sigma \le \ell$, for various choices of ℓ. Cross, square and triangle correspond to the IDM, type-II seesaw and scotogenic models, respectively. Left: unpolarized beams, right: polarized beams $P_{e^\pm}=^{+30\%}_{-80\%}$.

models are shown in Fig. 4.32 for both the binned and OOT analyses (the collider parameters as in Section 4.6.3). The 1σ contours for binned analysis (OOT) are shown by green (pink) color contours. In this scenario, with purely NP productions, the cross-section is larger, statistical fluctuation in each bin is less, making the NP uncertainties determined through binned analysis close to OOT.

Models	significance ($\Delta\sigma$)	
	$P_{e^{\pm}} = 0$	$P_{e^{\pm}} = ^{+30\%}_{-80\%}$
Inert doublet	4σ	17σ
Type-II Seesaw	2.82σ	13σ
Scotogenic	17σ	40σ

Table 4.12: Statistical significance of three different models with respect to the $a^0 = b^0 = 0$ model.

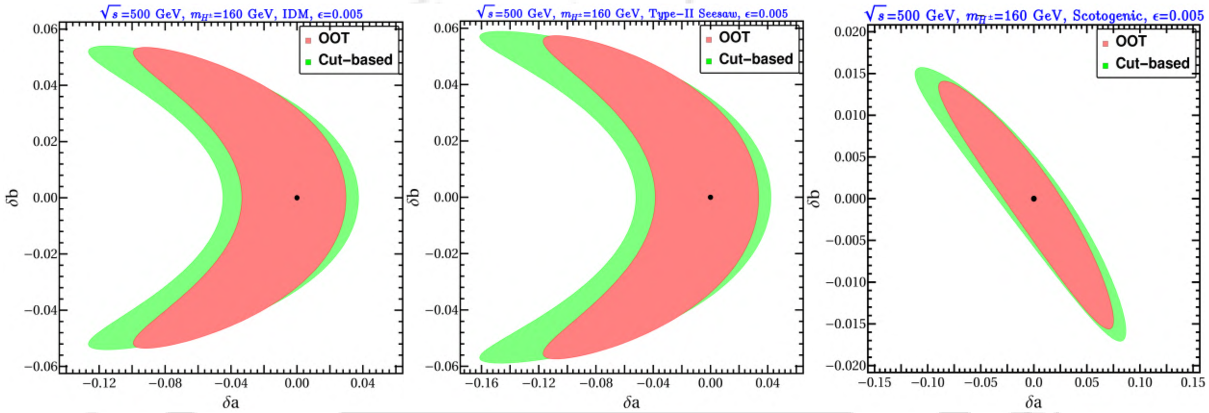

Figure 4.32: Comparison of 1σ statistical limit for OOT (pink) and collider (green) χ^2 in $a-b$ plane for charged scalar pair production at e^+e^- colliders for unpolarized beam. All the relevant parameters are written in the caption. Left: IDM; middle: type-II seesaw; right: scotogenic model (see Eq. (4.25)).

4.7 Summary

In this Chapter 4, we have discussed the estimation of NP couplings in several cases where SM interference dominates the signal. In Section 4.3, we have considered dimension-8 SMEFT operators, which can give rise to anomalous neutral triple gauge couplings, namely $ZZ\gamma$ and $Z\gamma\gamma$. For this purpose, we have considered $Z\gamma$ production at the linear e^+e^- colliders to probe physics beyond SM. We have analyzed mono-photon + missing energy as the final state signal and used cuts on missing energy ($\not{E}$) and missing transverse energy ($\not{E}_T$) to segregate the signal from non-interfering SM backgrounds. Using OOT we find optimal sensitivity that can be achieved in the measurement of dimension-8 nTGCs at the experiments. We have considered the differential cross-section of $Z\gamma$ production as the observable of the OOT, to estimate the 95% C.L. limit on the dimension-8 nTGCs. On one hand, we have performed individual one-dimensional analysis for all the couplings, on the other hand, the two-parameter analysis has also been performed in order to explore the non-trivial correlation between different NP couplings. A comparative analysis of NP couplings between our predictions for future colliders, namely, ILC and CLIC, and the most stringent limits obtained so far from ATLAS has been performed. While both linear colliders outperform ATLAS with certain polarization combinations, CLIC offers at least ten times improvement over ILC sensitivities. For all the cases, the non-trivial effect of beam polarization can be noted. It is worthwhile to mention that different combinations of polarized beams are sensitive to different couplings. Considering the choice of beam polarization that provides the most stringent limit at CLIC, we have observed that the optimal limit on dimension-8 nTGCs is at least fifteen times better than the current experimental limit.

In Section 4.4, we have discussed determination of dimension-8 nTGCs via the process $e^+e^- \to ZZ$ which is a parallel search along with $Z\gamma$ production. Considering `OSL` + missing energy as the final state signal, signal background estimation has been done using missing energy and invariant dilepton mass. We have determined that $C_{\tilde{B}W}/\Lambda^4$ is the most stringent NP coupling compared to other three couplings. For a careful choice of polarization, $C_{\tilde{B}W}/\Lambda^4$ is approximately thirty time more tighter than the ATLAS limit. With an appropriate choice of beam polarization, the statistical limit of NP couplings is approximately 15% to 45% more precise compared to the unpolarized beam.

In Section 4.5, we have studied two limits of the OOT, one in SMEFT ($t\bar{t}$ production in an e^+e^- collider) where the SM dominates over the NP contribution, and one in UV complete NP models (H^+H^- production in an e^+e^- collider) where SM contribution is subdominant. For the first application we used an EFT parameterization of the NP effects, including for simplicity only those operators that do not interfere with the SM contributions in this process. We find that for realistic collider parameters the 1σ statistical uncertainty of the NP parameters lie in the 20% to 100% range (depending on the values of the coefficients, the beam polarizations and the efficiency of signal background estimation). The possibility of distinguishing different NP models (defined by their values of the NP coefficients) is equally modest, with a significance below 5σ in all cases studied. In the second application the NP particles are assumed to be light enough to be directly produced. Here we find that the sensitivity is much higher so that the NP parameters could be measured to a precision of 1% to 10% (depending on the values of the coefficients, the beam polarizations and the efficiency). Moreover, different models can be easily distinguished, provided the beams are strongly polarized, which provides a useful comparison of how efficiently the NP couplings can be extracted at the proposed future $e^+ e^-$ colliders. The calculations for both applications require the estimation of an efficiency factor ϵ which we obtain by performing standard collider analyses of the corresponding reactions by studying a cut based signal background analysis. The statistical uncertainties in the NP coefficients obtained using the OOT are $O(0.5)$ in the first case we considered (Section 4.5), white significantly smaller, $O(0.05)$, for the second example (Section 4.6). This is imply due to the different values of the NP contributions to the cross sections in each case: in the first the NP effects are small, this leads to a relatively small inverse-correlation matrix M in Eq. (2.26), while in the second example NP effects dominate leading ot a larger M and correspondingly smaller uncertainties. We also compared the OOT results with those obtained a simple collider estimate of the parameter uncertainties based on the χ^2 statistic of Eq. (2.6). We found that the optimal uncertainties are significantly smaller in the case where the NP effects are subdominant, but that in the case where the NP dominates the results are comparable. The collider analysis, however, can be improved by optimizing the data binning, and possibly by selecting a better suited statistic; such investigations, however, lie outside the scope of this paper.

Chapter 5

OOT with non-interfering SM background: Example 1

Contents

5.1 Introduction

In this chapter, we discuss the estimation of NP sensitivity with substantial non-interfering SM background. In the previous chapters, non-interfering SM backgrounds was ignored in the OOT, assuming their presence to alter the conclusions marginally. However, we must note here that the presence of SM background was considered before as well, to do event simulations and to evaluate the signal efficiency ϵ_s after background reduction. Here, we consider the SM background events in constructing the optimal covariance matrix folded with appropriate efficiency factor ϵ_b after the cuts.

The example at hand has flavour constraints which has important implications to the collider observability. Precision tests carried out at low energies play a crucial role in exploring flavour violating NP effects under SMEFT framework. FCNC processes such as $b \to s(d)$ transitions are one of the most important probes in this connection, as there is no such interactions within the SM at the tree level. Such flavour observables therefore provide an important bound on the corresponding SMEFT operators [207–211]. In addition, there are processes that are GIM suppressed [212]. At the one-loop level, flavour changing (FC) productions involving up type quarks are even less prominent than those involving down type quarks. Hence, FC transitions involving up type quarks provide an important window to search for NP. Along with flavor observables, top-quark physics also plays an important role under SMEFT framework as it has $O(1)$ Yukawa coupling, which is crucial to explain the origin of EWSB. Several analyses under SMEFT framework in the top-quark sector have been performed in [213, 214]. This motivates us to choose tc production as an example process to study.

As we know that the renormalization-group equations (RGE) allow one to compute the running and mixing between the BSM scale down to the electroweak scale and further down to the scale of low-energy precision experiments, the SMEFT can be matched to a low energy EFT. It could be done following a two step matching procedure. The coefficients C_i's generated at the scale Λ will be related to their values at the electroweak scale $v \sim 246$ GeV, and these coefficients can further be related to the WCs of a low-energy EFT through RGE running. Therefore, any constraints obtained on the WCs from low energy data will in turn limit $C_i(\Lambda)$s at any given BSM scale Λ. The flavour changing neutral current (FCNC) processes are loop suppressed in the SM, and any tree level NP contributions to such processes will have limited parameter spaces allowed by the data. Similarly, the availability of precise data on the flavour changing charged current (FCCC) processes at the low energy could play an essential role to constrain the NP parameter space contributing to such processes at the tree level. Therefore, the study of FCNC and FCCC processes at the low energy will play a crucial role in exploring flavour violating NP effects under SMEFT framework.

The stringent constraint on the dimension-6 effective operators derived from the flavour observables indicate that their production at the LHC is small, while the SM background is huge and mostly irreducible, so that a prediction requires thorough analysis. It is also difficult to probe them in a future electron-positron collider with a maximum centre-of-mass (CM) energy of 3 TeV. Therefore we examine the process at high energy muon collider [118]. Muons, being fundamental particles, provide the advantage of directing their entire energy towards short-distance scattering rather than having it distributed among the partons. As a result, a 14 TeV muon collider can exhibit effectiveness on par with a 100 TeV proton-proton collider [215]. This high-energy capability is particularly advantageous for both the exploration of new heavy particles along with indirect measurements at elevated energy levels. Hence, a multi-TeV moun collider acts as both discovery and precision machine altogether. Limited studies on tc production at lepton colliders have been documented in the existing literature [216–219]. In a somewhat similar analysis [219], the flavor constraints are obtained from rare B decay processes, applicable to vector operators only, while ours is done considering all possible observables applicable to all of vector, scalar and tensor type four-Fermi operators.

This chapter is arranged in the following way. In Section 5.2, we discuss the relevant phenomenological framework for our analysis. Then in Section 5.3, we study the constraints from flavour physics. Collider simulation is presented in Section 5.4. Finally, we summarize our conclusion in Section 5.5.

5.2 Phenomenological framework

Our goal of the analysis is to probe the dimension-6 flavor violating effective (EFT) operators that contributes to tc $(\bar{t}c + t\bar{c})$ production at the future muon collider. The Feynman graphs for the $t\bar{c}$ production is shown in Fig. 5.1 ($\bar{t}c$ graphs are similar with same contributions and not shown here). There are essentially two different contributions: (i) via Ztc vertex and (ii) four-fermi $\mu\mu tc$ contact interaction. As elaborated later, operators contributing to Ztc affect the process very mildly, while the main contribution arises from the four-Fermi operators.

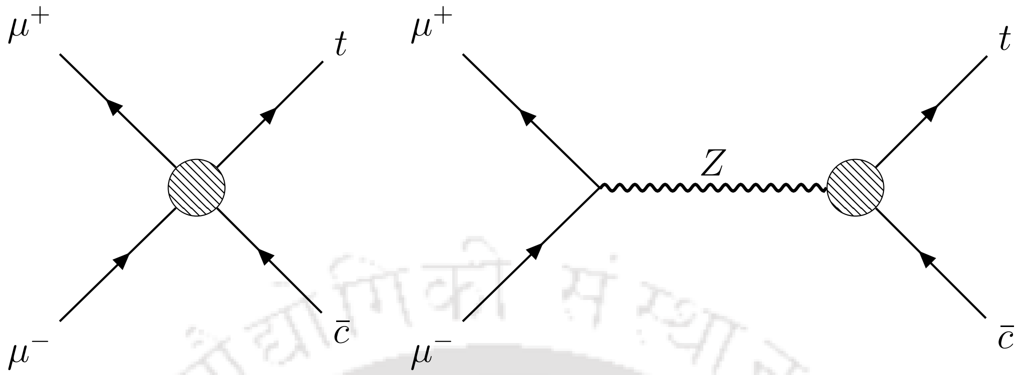

Figure 5.1: Feynman diagrams that induce $t\,\bar{c}$ production at the muon collider; left: effective four-Fermi ($\mu\mu tc$) couplings, right: effective Ztc couplings. The conjugate processes look alike with exactly same cross-section.

There are three types of four-Fermi operators containing i) four leptons, ii) four quarks and iii) two leptons and two quarks, where the last one serves our purpose. There are seven operators that contribute to the $\mu^+\mu^- \to tc$ production, as given by [86, 218]

$$\begin{aligned}
\mathcal{O}_{lq}^{(1)} &= (\bar{l}_p\gamma^\mu l_r)(\bar{q}_s\gamma_\mu q_t), \\
\mathcal{O}_{lq}^{(3)} &= (\bar{l}_p\gamma^\mu\tau^I l_r)(\bar{q}_s\gamma_\mu\tau^I q_t), \\
\mathcal{O}_{eu} &= (\bar{e}_p\gamma^\mu e_r)(\bar{u}_s\gamma_\mu u_t), \\
\mathcal{O}_{lu} &= (\bar{l}_p\gamma^\mu l_r)(\bar{u}_s\gamma_\mu u_t), \\
\mathcal{O}_{qe} &= (\bar{q}_p\gamma^\mu q_r)(\bar{e}_S\gamma_\mu e_t), \\
\mathcal{O}_{lequ}^{(1)} &= (\bar{l}_p^j e_r)\epsilon_{jk}(q_s^k u_t), \\
\mathcal{O}_{lequ}^{(3)} &= (\bar{l}_p^j\sigma^{\mu\nu} e_r)\epsilon_{jk}(q_s^k\sigma_{\mu\nu} u_t),
\end{aligned} \tag{5.1}$$

where l (e) is the left (right)-handed lepton doublet (singlet), q is the left-handed quark doublet, and u (d) is the up (down)-type right-handed quark singlets. Apart, p, r, s, t indicates flavour indices, τ^I are the Pauli matrices, $\epsilon = -i\tau_2$, $\sigma^{\mu\nu} = \frac{i}{2}[\gamma^\mu, \gamma^\nu]$. The operators as in Eq. (5.1) has been mentioned time and again in the thesis, but it's still useful to refer them here in explicit. Using Eq. (5.1), the most general four-Fermi effective Lagrangian for $\mu\mu tc$ contact interaction can be written as

$$\mathcal{L}_{\mu\mu tc} = \frac{1}{\Lambda^2}\sum_{i,j=L,R}\left[V_{ij}(\bar{\mu}\gamma_\mu P_i\mu)(\bar{t}\gamma^\mu P_j c) + S_{ij}(\bar{\mu}P_i\mu)(\bar{t}P_j c) + T_{ij}(\bar{\mu}\sigma_{\mu\nu}P_i\mu)(\bar{t}\sigma^{\mu\nu}P_j c)\right], \tag{5.2}$$

where vector-like (V_{ij}), scalar-like (S_{ij}) and tensor-like (T_{ij}) couplings can be expressed in terms of the Wilson coefficients (WCs) of the seven four-Fermi operators as in Eq. (5.1) as

$$\begin{aligned}
&V_{LL} = (C_{lq}^{(1)} - C_{lq}^{(3)}), \quad V_{LR} = C_{lu}, \quad V_{RR} = C_{eu}, \quad V_{RL} = C_{qe},\\
&S_{RR} = -C_{lequ}^{(1)}, \quad S_{LL} = S_{LR} = S_{RL} = 0,\\
&T_{RR} = -C_{lequ}^{(3)}, \quad T_{LL} = T_{LR} = T_{RL} = 0.
\end{aligned} \tag{5.3}$$

Note that for vector operators we have all the helicity combination of fermions appear for both lepton and quarks, while for the scalar and tensor couplings only RR combination is non zero. The above parametrisation will be used for the collider simulation later.

The tree-level dimension-6 SMEFT operators that contribute to effective Ztc vertex are

$$\begin{aligned}
\mathcal{O}_{Hq}^{(1)} &= i(H^\dagger D^\mu H)(\bar{q}_s \gamma_\mu q_t),\\
\mathcal{O}_{Hq}^{(3)} &= i(H^\dagger D^\mu \tau^I H)(\bar{q}_s \gamma_\mu \tau^I q_t),\\
\mathcal{O}_{Hu} &= i(H^\dagger D^\mu H)(\bar{u}_s \gamma_\mu u_t).
\end{aligned} \tag{5.4}$$

Therefore, the effective Lagrangian containing Ztc vertex[1] is

$$\mathcal{L}_{Ztc} = g\frac{v^2}{\Lambda^2}\bar{t}\gamma^\mu(a_L^Z P_L + a_R^Z P_R)cZ_\mu\,, \tag{5.5}$$

where a_L and a_R are the functions of $C_{Hq}^{(1)}$, $C_{Hq}^{(3)}$ and C_{Hu} as,

$$a_L^Z = \frac{1}{4c_w}(C_{Hq}^{(1)} - C_{Hq}^{(3)})\,, \quad a_L^Z = \frac{1}{4c_w}C_{Hu}. \tag{5.6}$$

5.3 Flavour constraints and predictions

In this section, we study all possible flavour and top quark related experimental constraints that put bound on the dimension-6 effective couplings of our interest as described above. We then make some observable predictions for some rare processes based on the constraints obtained for the effective operators.

5.3.1 Flavour and top-quark constraints

Note that the operators defined in Eq. (5.1) will contribute to various low energy observables related to FCNC and FCCC processes. In the following we will discuss different inputs which we have considered in this analysis.

FCNC processes: Most important constraints will be obtained from the semileptonic and leptonic decays of via $b \to s\ell^+\ell^-$ decays. The corresponding low energy effective Hamiltonian is given by [220, 221]

$$\begin{aligned}
\mathcal{H}_{\text{eff}} = \mathcal{H}_{\text{eff}}^{\text{SM}} - \frac{4G_F}{\sqrt{2}}\lambda_q\frac{e_0^2}{16\pi^2}\Big(&\Delta C_9^\ell O_9^\ell + \Delta C_{10}^\ell O_{10}^\ell + C_9^{\prime\ell} O_9^{\prime\ell} + C_{10}^{\prime\ell} O_{10}^{\prime\ell} + C_S^\ell O_S^\ell + C_P^\ell O_P^\ell\\
&+ C_S^{\prime\ell} O_S^{\prime\ell} + C_P^{\prime\ell} O_P^{\prime\ell}\Big),
\end{aligned} \tag{5.7}$$

---

[1] γtc vertex is forbidden by $U(1)$ gauge invariance.

where ℓ stands here for all the three lepton fields: e, μ and τ. Here, e_0 and G_F are the $U(1)_{em}$ and Fermi coupling constants, $\lambda_q = V_{qb}V^*_{qs}$ is the CKM combination. The four-Fermi operators as in Eq. (5.7) are expressed as

$$\begin{aligned} O^\ell_9 &= (\bar{s}\gamma_\mu P_L b)(\bar{\ell}\gamma^\mu \ell), \qquad & O^\ell_S &= (\bar{s}P_R b)(\bar{\ell}\ell)\,, \\ O^\ell_{10} &= (\bar{s}\gamma_\mu P_L b)(\bar{\ell}\gamma^\mu\gamma^5 l), \qquad & O^\ell_P &= (\bar{s}P_R b)(\bar{\ell}\gamma^5 l)\,. \end{aligned} \tag{5.8}$$

The O' operators can be obtained by interchanging $\{L \leftrightarrow R\}$ from the operators O as above in Eq. (5.8). The SM Hamiltonian ($\mathcal{H}^{SM}$) already incorporates O^l_9 and O^l_{10} operators with WCs $C^{\texttt{SM}}_9$ and $C^{\texttt{SM}}_{10}$. Therefore, ΔC^l_9 and ΔC^l_{10} denote the WCs corresponding to O^l_9 and O^l_{10} operators stemming from NP. Remaining effective operators are absent in the SM framework thus comes purely from NP contribution. We will use Eq. (5.7) and Eq. (5.8) to obtain limits from $b \to s$ and $b \to d$ transitions and translate them in terms of the Wilson coefficients of our notation as in Eq. (5.1). Following a tree level matching procedure, one can express the WCs defined in Eq. (5.1) in terms of the WCs of in the low energy effective Hamiltonian given above [222].

- $b \to s\mu\mu$ decay: $b \to s$ transitions are absent at the tree level within the SM; therefore observables having such transitions provide intriguing indications of potential NP effects through ΔC^μ_9 and ΔC^μ_{10} [223–227]. They stem from several experimental observations like $B \to K\mu\mu$, $B \to K^*\mu\mu$, and $B_s \to \phi\mu\mu$, which have been considered in this analysis [228–237]. The latest experimental results from the LHCb on lepton flavor university (LFU) ratio R_K and R^*_K [238, 239] are in great agreement with the SM prediction which indicates a tighter constraint on ΔC^μ_9 and ΔC^μ_{10}. After matching dimension-6 effective couplings in Eq. (5.1) with the Hamiltonian written in Eq. (5.7), we get [222]

$$\begin{aligned} \Delta C^\mu_9 &= \left(\frac{\alpha}{\lambda^d_t \pi}\right)\left(\frac{v^2}{\Lambda^2}\right)\left(C^{(1)}_{lq} + C^{(3)}_{lq} + C_{qe}\right), \\ \Delta C^\mu_{10} &= \left(\frac{\alpha}{\lambda^d_t \pi}\right)\left(\frac{v^2}{\Lambda^2}\right)\left(C^{(1)}_{lq} - C^{(3)}_{lq} - C_{qe}\right), \end{aligned} \tag{5.9}$$

  where $\alpha = e_0^2/4\pi$ is fine structure constant, $\lambda_q = V^*_{tb}V_{ts}$ and v is the VEV of the SM Higgs. We can see that $\mathcal{O}^{(1)}_{lq}$, $\mathcal{O}^{(3)}_{lq}$, and $\mathcal{O}_{qe}$ are the three dimension-6 SMEFT operators that contribute to $b \to s\mu\mu$ transition. Since we have analysed the constraints by choosing one operator at a time, therefore, for $\mathcal{O}^{(1)}_{lq}$ and $\mathcal{O}^{(3)}_{lq}$ operators, $\Delta C^\ell_9 = -\Delta C^\ell_{10}$; whereas for $\mathcal{O}_{qe}$, we have $\Delta C^\ell_9 = \Delta C^\ell_{10}$. Following the analysis discussed in [227], we obtain $\Delta C^\mu_9 = -0.23$ and transmitting this limit to couplings of dimension-6 SMEFT operator using Eq. (5.9), the constraints are noted in Table 5.1.

- $b \to d\mu\mu$ decay: $b \to d\mu\mu$ transition is another FCNC process which also plays an important role to constrain NP scenarios [240, 241]. Like $b \to s\mu\mu$ transition, here also $\mathcal{O}^{(1)}_{lq}$, $\mathcal{O}^{(3)}_{lq}$, and $\mathcal{O}_{qe}$ operators contribute. Consequently, the relations between the WCs in two different parametrizations are similar to that in Eq. (5.25), just with a trivial substitution of $\lambda_q = V^*_{tb}V_{td}$. We utilize the experimentally determined value of $\Delta C_9 = -0.53$ from the global fits of $B^+ \to \pi^+\mu^+\mu^-$, $B^0_s \to \bar{K}^{*0}\mu^+\mu^-$, $B^0 \to \mu^+\mu^-$, and radiative $B \to X_d\gamma$ decays data sourced from [241], to relate the dimension-6 effective couplings of our choice (Eq. (5.25)). The constraints from this decay channel for these three dimension-6 effective couplings are tabulated in Table 5.1.

- $K_L \to \mu\mu$ decay: The expression for the branching ratio of $K_L \to \mu^+\mu^-$ decay using the Hamiltonian in Eq. (5.7) can be expressed as [242, 243]

$$\text{BR}(K_L \to \mu^+\mu^-) = \tau_L \frac{f_K^2 m_K^3 \beta_\mu}{16\pi} \left| N_L^{SD} - \left(\frac{2m_\mu}{m_K}\right) \frac{G_F \alpha_e}{\sqrt{2}\pi} \text{Re}\left[-\lambda_c \frac{Y_c}{s_W^2} + \lambda_t C_{10} \right] \right|^2 . \tag{5.10}$$

In the above Eq. (5.10), τ_L represents the mean life of the K_L meson, m_μ and m_K denote the masses of the muon and kaon respectively, G_F and α_e stand respectively for the Fermi constant and the fine structure constant, and β_μ and λ_q are defined as:

$$\beta_\mu = \sqrt{1 - \frac{4m_\mu^2}{m_K^2}}, \qquad \lambda_q = V_{qd}^* V_{qs}. \tag{5.11}$$

Y_c indicate short-distance contribution from SM while $N_L^{SD} = \pm[0.54(77) - 3.95i] \times 10^{-11}$ in GeV^{-2} is the short distance contribution [244] and $C_{10} = C_{10}^{\text{SM}} + \Delta C_{10}^{\mu}$. The relevant operators are $\mathcal{O}_{lq}^{(1)}$, $\mathcal{O}_{lq}^{(3)}$ and $\mathcal{O}_{qe}$ that contribute to this observables. ΔC_{10}^{μ} respects Eq. (5.9). Resulting limits on dimension-6 effective couplings are written in Table 5.1.

- $B_q - \bar{B}_q$ mixing (with $q = d, s$): B^0 or B_s mesons exhibit oscillatory behaviour between particle and antiparticle states, a phenomenon arising from the influence of flavour-changing weak interactions. These meson-antimeson mixings are the $\Delta B = 2$ FCNC processes. In presence of NP, the mixing amplitude or the frequency of meson-antimeson oscillations is defined as,

$$\Delta M_q = 2|M_{12}^q| = 2|M_{12}^{q,SM} + M_{12}^{q,NP}|, \tag{5.12}$$

with

$$M_{12}^q = \frac{\langle B_q | \mathcal{H}_{eff}^{\Delta B=2} | \bar{B}_q \rangle}{2M_{B_q}} . \tag{5.13}$$

The dominant contribution to $M_{12}^{q,SM}$ in the SM arises from the top mediated box diagrams [245–247], and the corresponding contribution is given by

$$M_{12}^{q,SM} = \frac{G_F^2}{24\pi^2} m_{B_q} f_{B_q}^2 \hat{B}_q \eta_B f(x^2) (\lambda_t^q)^2 . \tag{5.14}$$

Here, $m_{B_d}(m_{B_s})$ and $f_{B^0_{d(s)}} = 190.0\ (230.3)$ MeV are the masses and decay constants, $\hat{B}_{d(s)} = 1.222\ (1.232)$ is the brag factor of $B^0_{d(s)}$ meson respectively, $\eta_B = 0.55$ is the QCD correlation factor [248], and $\lambda_t^{d(s)} = V_{tb} V_{td(s)}^*$. The Inami-Lim function $f(x)$ is given by [249]

$$f(x) = x\left(\frac{1}{4} + \frac{9}{4(1-x)} - \frac{3}{2(1-x)^2}\right) - \frac{3x^3 \log x}{(1-x)^3}, \qquad x = \frac{m_t}{m_W}. \tag{5.15}$$

We already mentioned that the SMEFT operators in Eq. (5.1) contribute to FCNC processes like $b \to s\ell^+\ell^-$ and $b \to d\ell^+\ell^-$. The four fermi operators in

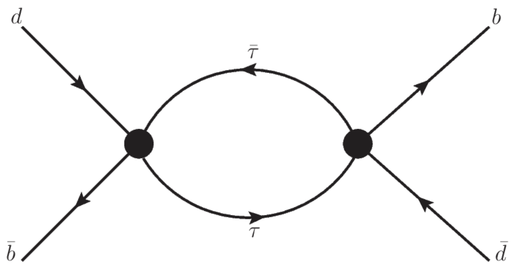

Figure 5.2: τ mediated 1-loop NP contribution to $\Delta m_{B_d^0}$.

Eqs. (5.7) and (5.8), may contribute to $B_s - \bar{B}_s$ and $B^0 - \bar{B}^0$ mixing amplitudes respectively via the diagram shown in Fig. 5.2. In our scenario, the dispersive part of the diagram in Fig. 5.2 will contribute to M_{12}^q. The dominant contribution will arise from a τ mediated loop via the insertion of operators $\mathcal{O}_9$ and $\mathcal{O}_{10}$. From the dispersive part of the diagram in Fig. 5.2, we obtain

$$\begin{aligned} M_{12}^{q,NP} = &-\frac{G_F^2\alpha^2}{8\pi^2} m_{B_i} f_{B_i}^2 \hat{B}_i \eta_B (\lambda_t^i)^2 \Bigg[4\left((\Delta C_9^2 + \Delta C_{10}^2) m_b^2 + 4\Delta C_{10}^2 m_\tau^2\right) \log\frac{\Lambda^2}{m_\tau^2} \\ &+ (2m_b^2(\Delta C_9^2 + \Delta C_{10}^2) + m_\tau^2(3\Delta C_{10}^2 - \Delta C_9^2))\mathrm{DiscB}[2\mathrm{m_b^2}, \mathrm{m}_\tau, \mathrm{m}_\tau] \\ &+ 4(\Delta C_9^2 + \Delta C_{10}^2) m_b^2 - 2m_\tau^2(\Delta C_9^2 - 7\Delta C_{10}^2) \Bigg]. \end{aligned} \tag{5.16}$$

The expression of `DisB[a,b,c]` function is written in the Appendix A.4. As we have discussed earlier, the contributions to $b \to s\tau^+\tau^-$ will come from $\mathcal{O}_{lq}^{(1)}$, $\mathcal{O}_{lq}^{(3)}$ and $\mathcal{O}_{qe}$.The amplitude is calculated using the Hamiltonian described in Eq. (5.7). Therefore, effective couplings related to these operators obey Eq. (5.9). The relevant constraints from this observable are presented in Table 5.1.

- $B_s^0 \to \mu\mu$ decay: Following Eq. (5.7), the branching ratio of $B_s^0 \to \mu^+\mu^-$ turns out [250],

$$\mathrm{BR}(B_s^0 \to \mu^+\mu^-) = \tau_{B_s} \frac{G_F^2 \alpha^2 M_{B_s} f_{B_s}^2 m_\mu^2 (\lambda_q^{sd})^2}{16\pi^3} \sqrt{1 - \frac{4m_\mu^2}{M_{B_s}^2}} |C_{10}^\ell|^2. \tag{5.17}$$

The branching ratio of this rare decay is $\left(2.69^{+0.37}_{-0.35}\right) \times 10^{-9}$ [248, 251]. Understandably, $\mathcal{O}_{lq}^{(1)}$, $\mathcal{O}_{lq}^{(3)}$, and $\mathcal{O}_{qe}$ contribute to this branching ratio. Using Eq. (5.9), the constraints obtained on the effective couplings for the relevant operators are tabulated in Table 5.1.

- $K^\pm \to \pi^\pm\nu\nu$ decay: The effective Hamiltonian relevant to $s \to d$ transitions is parameterized as [252, 253]

$$\mathcal{H}_{\mathtt{eff}}^{s\to d} = \frac{G_F}{\sqrt{2}} \lambda_t^{sd} \left(\sum_{i=1}^{10} C_i O_i + \sum_{\ell=e,\mu,\tau} C_{\nu_\ell}^L O_{\nu_\ell}^L \right), \tag{5.18}$$

where $\lambda_t^{sd} = V_{ts} V_{td}^*$. The details of $O_1 - O_{10}$ operators are discussed in [252]. The operator relevant to $K^\pm \to \pi^\pm\nu\nu$ decay is

$$\begin{aligned} O_{\nu_\ell}^L &= \alpha(\bar{d}\gamma^\mu(1-\gamma5)s)(\bar{\nu}_\ell\gamma_\mu(1-\gamma5)\nu_\ell), \\ O_{\nu_\ell}^R &= \alpha(\bar{d}\gamma^\mu(1+\gamma5)s)(\bar{\nu}_\ell\gamma_\mu(1-\gamma5)\nu_\ell). \end{aligned} \tag{5.19}$$

The WC is $C^L_{\nu_\ell} = C^{L,\text{SM}}_{\nu_\ell} + \delta C^L_{\nu_\ell}$ with SM contribution

$$C^{L,\text{SM}}_{\nu_\ell} = \frac{1}{2\pi s_w^2}\left(\frac{\lambda_c^{sd}}{\lambda_t^{sd}} X_c^\ell + X_t\right), \tag{5.20}$$

where $X_t = 1.48$ is the short-distance NLO QCD correction arises from top-quark, $X_c^e \simeq X_c^\mu = 1.04 \times 10^{-3}$ and $X_c^\tau = 0.70 \times 10^{-3}$ are the short-distance charm contribution with the NLO logarithmic approximation [253, 254]. By correlating the dimension-6 effective operators from Eq. (5.1) with those specified in Eq. (5.20), we can express the dimension-6 effective couplings [255] as

$$\delta C^L_{\nu_\ell} = \frac{2\pi}{e_0^2 \lambda_t^{sd}} \frac{v^2}{\Lambda^2}\left[C^{(1)}_{lq} - C^{(3)}_{lq}\right], \qquad \delta C^R_{\nu_\ell} = 0. \tag{5.21}$$

The branching ratio of $B^+ \to \pi^+ \nu\nu$ decay is expressed as [255, 256]

$$\mathcal{B}(K^+ \to \pi^+ \nu\bar{\nu}) = \frac{2\alpha^2 |\lambda_t^{sd}|^2 \mathcal{B}(K^+ \to \pi^0 e^+ \nu_e)}{|V_{us}|^2} \sum_{\ell=e,\mu,\tau} |C^L_{\nu_\ell} + C^R_{\nu_\ell}|^2 . \tag{5.22}$$

We take $\mathcal{B}(K^+ \to \pi^0 e^+ \nu_e) = (5.07 \pm 0.04) \times 10^{-2}$ and $\mathcal{B}(K^+ \to \pi^+ \nu\nu) = (1.14^{+0.40}_{-0.33}) \times 10^{-10}$ from the PDG average [188], and obtain $\delta C_{\nu_\ell} = -3.31$. Following Eq. (5.20), constraints on dimension-6 effective couplings are noted in Table 5.1.

FCCC processes:

- $b \to q\ell\nu$ decay: The most general effective Hamiltonian for $b \to c(u)\ell\nu_\ell$ transitions is written as [258]

$$\mathcal{H}^{b\to q\ell\bar{\nu}_\ell}_{\text{eff}} = \frac{4G_F}{\sqrt{2}} V_{qb}[(1 + C^l_{V_1})\mathcal{O}^l_{V_1} + C^l_{V_2}\mathcal{O}^l_{V_2} + C^l_{S_1}\mathcal{O}^l_{S_1} + C^l_{S_2}\mathcal{O}^l_{S_2} + C^l_T\mathcal{O}^l_T], \tag{5.23}$$

with the operators

$$\begin{aligned}
\mathcal{O}^l_{V_1} &= (\bar{q}_L \gamma^\mu b_L)(\bar{l}_L \gamma_\mu \nu_{lL}), \\
\mathcal{O}^l_{V_2} &= (\bar{q}_R \gamma^\mu b_R)(\bar{l}_L \gamma_\mu \nu_{lL}), \\
\mathcal{O}^l_{S_1} &= (\bar{q}_L b_R)(\bar{l}_R \nu_{lL}), \\
\mathcal{O}^l_{S_2} &= (\bar{q}_R b_L)(\bar{l}_R \nu_{lL}), \\
\mathcal{O}^l_T &= (\bar{q}_R \sigma^{\mu\nu} b_L)(\bar{l}_R \sigma_{\mu\nu} \nu_{lL}),
\end{aligned} \tag{5.24}$$

with $q = u$ or c. If we match the ones in Eq. (5.23) with those mentioned in Eq. (5.1), we find the following relations between the couplings [222]

$$\frac{C^{(3)}_{lq}}{\Lambda^2} = -\frac{V_{cb}}{V_{cs}}\left(\frac{C_{V_1}}{v^2}\right), \quad \frac{C^{(1)}_{lequ}}{\Lambda^2} = -2\frac{V_{cb}}{V_{tb}}\left(\frac{C_{S_2}}{v^2}\right), \quad \frac{C^{(3)}_{lequ}}{\Lambda^2} = -2\frac{V_{cb}}{V_{tb}}\left(\frac{C_T}{v^2}\right). \tag{5.25}$$

FCCC processes like $b \to q\ell\nu$ have been widely studied on [257, 259, 260]. In this analysis, we borrow the constraints from [257], where the experimental results of $\bar{B} \to D(D^*)\ell^-\bar{\nu}_\ell$, $R(D^{(*)})$,$\bar{B} \to \pi\ell^-\bar{\nu}_\ell$ ($\ell = \mu,\ e$) along with lattice

NP couplings	Related processes/ Observables	Constraints (GeV^{-2})	Simultaneous fit (GeV^{-2})
$C_{lq}^{(1)}/\Lambda^2$	$b \to s\mu\mu$	$-(3.98 \pm 1.20) \times 10^{-10}$	$-(9.96 \pm 0.03) \times 10^{-10}$
	$b \to d\mu\mu$	$-(1.90^{+0.65}_{-0.68}) \times 10^{-10}$ [241]	
	$\mathcal{B}(K_L \to \mu^+\mu^-)$	$-(1.21^{+0.33}_{-0.31}) \times 10^{-10}$	
	$\mathcal{B}(B_s^0 \to \mu^+\mu^-)$	$-(7.39^{+0.41}_{-0.44}) \times 10^{-10}$	
	$\mathcal{B}(K^+ \to \pi^+\nu\bar{\nu})$	$-(3.50^{+0.55}_{-0.80}) \times 10^{-10}$	
	$\Delta m_{B_d^0}$	$-(1.81 \pm 0.05) \times 10^{-8}$	
	$\Delta m_{B_s^0}$	$-(3.08 \pm 0.01) \times 10^{-8}$	
$C_{lq}^{(3)}/\Lambda^2$	$B \to D^{(*)}\tau\nu_\tau$	$-(0.35 \pm 0.15) \times 10^{-7}$ [257]	$-(9.99 \pm 0.03) \times 10^{-9}$
	$B \to D^{(*)}\mu(e)\nu$	$(0.14 \pm 0.09) \times 10^{-7}$ [257]	
	$B \to \pi\mu\nu_\mu$	$(0.06 \pm 0.20) \times 10^{-7}$ [257]	
	$b \to s\mu\mu$	$-(3.98 \pm 1.20) \times 10^{-10}$	
	$b \to d\mu\mu$	$-(1.90^{+0.65}_{-0.68}) \times 10^{-10}$ [241]	
	$\mathcal{B}(K_L \to \mu^+\mu^-)$	$-(1.21^{+0.33}_{-0.31}) \times 10^{-10}$	
	$\mathcal{B}(B_s^0 \to \mu^+\mu^-)$	$-(7.39^{+0.41}_{-0.44}) \times 10^{-10}$	
	$\mathcal{B}(K^+ \to \pi^+\nu\bar{\nu})$	$(3.50^{+0.55}_{-0.80}) \times 10^{-10}$	
	$\mathcal{B}(\pi^\pm \to \mu\nu_\mu)$	$(1.28 \pm 0.81) \times 10^{-8}$	
	$\mathcal{B}(K^\pm \to \mu\nu_\mu)$	$(2.21 \pm 0.74) \times 10^{-8}$	
	$\mathcal{B}(B^\pm \to \tau\nu_\tau)$	$(1.27 \pm 0.43) \times 10^{-7}$	
	$\mathcal{B}(D_s^\pm \to \mu\nu_\mu)$	$(6.02 \pm 9.94) \times 10^{-9}$	
	$\mathcal{B}(D^\pm \to \mu\nu_\mu)$	$-(1.14 \pm 1.52) \times 10^{-8}$	
	$\Delta m_{B_d^0}$	$-(1.81 \pm 0.05) \times 10^{-8}$	
	$\Delta m_{B_s^0}$	$-(1.10 \pm 0.01) \times 10^{-8}$	
	$\mathcal{B}(t \to b\ell\nu_\ell)$	$(7.13 \pm 0.37) \times 10^{-7}$	
C_{eu}/Λ^2	$t \to c\ell\ell$	$< 10^{-5}$ [214]	-
C_{lu}/Λ^2	$t \to c\ell\ell$	$< 10^{-5}$ [214]	-
C_{qe}/Λ^2	$b \to s\mu\mu$	$-(1.24 \pm 0.26) \times 10^{-9}$	$-(1.04 \pm 0.03) \times 10^{-9}$
	$b \to d\mu\mu$	$(0.68^{+2.72}_{-2.79}) \times 10^{-10}$ [241]	
	$\mathcal{B}(K_L \to \mu^+\mu^-)$	$-(1.213^{+0.334}_{-0.310}) \times 10^{-10}$	
	$\mathcal{B}(B_s^0 \to \mu^+\mu^-)$	$-(7.39^{+0.415}_{-0.445}) \times 10^{-10}$	
	$\Delta m_{B_d^0}$	$-(1.81 \pm 0.05) \times 10^{-8}$	
	$\Delta m_{B_s^0}$	$-(1.10 \pm 0.01) \times 10^{-8}$	

Table 5.1: Constraints on the different dimension-6 effective vector couplings from various flavour and top-quark processes and decay modes. For the details on observables concerning $b \to s\mu^+\mu^-$ and $b \to d\mu^+\mu^-$ transitions, see references [227, 241] and for the measurements see the text.

inputs are taken into account. We find that from $b \to c\mu\nu_\mu$ and $b \to u\mu\nu_\mu$ decays, the constraints on $\mathcal{O}_{lequ}^{(1)}$ are $C_{lequ}^{(1)}/\Lambda^2 = (0.09 \pm 0.58) \times 10^{-7}$ GeV^{-2} and $C_{lequ}^{(1)}/\Lambda^2 = (0.02 \pm 0.12) \times 10^{-7}$ GeV^{-2} respectively. As the uncertainties are very high here, we may infer that the corresponding operator is insensitive to

NP couplings	Related processes/ Observables	Constraints (GeV^{-2})	Simultaneous fit (GeV^{-2})
$C^{(1)}_{\ell equ}/\Lambda^2$	$B \to D^{(*)}\tau\nu_\tau$	$(1.81 \pm 0.06) \times 10^{-7}$ [257]	$-(6.61 \pm 0.17) \times 10^{-10}$
	$B \to D^{(*)}\mu\nu_\mu$ $B \to D^{(*)}e\nu_e$	$(0.09 \pm 0.58) \times 10^{-7}$ [257]	
	$B \to \pi\mu\nu_\mu$ $B \to \pi e\nu_e$	$(0.03 \pm 0.18) \times 10^{-7}$ [257]	
	$\mathcal{B}(\pi^\pm \to \mu\nu_\mu)$	$-(5.82 \pm 0.31) \times 10^{-10}$	
	$\mathcal{B}(K^\pm \to \mu\nu_\mu)$	$-(1.83 \pm 0.05) \times 10^{-9}$	
	$\mathcal{B}(B^\pm \to \tau\nu_\tau)$	$-(6.64 \pm 0.21) \times 10^{-9}$	
	$\mathcal{B}(D_s^\pm \to \mu\nu_\mu)$	$-(4.36 \pm 3.17) \times 10^{-10}$	
	$\mathcal{B}(D^\pm \to \mu\nu_\mu)$	$(8.61 \pm 11.71) \times 10^{-10}$	
$C^{(3)}_{\ell equ}/\Lambda^2$	$B \to D^{(*)}\tau\nu_\tau$	$(0.62 \pm 0.17) \times 10^{-7}$ [257]	$(0.72 \pm 6.51) \times 10^{-10}$
	$B \to D^{(*)}\mu\nu_\mu$ $B \to D^{(*)}e\nu_e$	$-(0.33 \pm 6.61) \times 10^{-10}$ [257]	
	$B \to \pi\mu\nu_\mu$ $B \to \pi e\nu_e$	$(0.07 \pm 0.16) \times 10^{-7}$ [257]	

Table 5.2: Constraints of scalar and tensor mediated dimension-6 effective couplings from various flavour observables, see text for details.

these decays and zero consistent. $\mathcal{O}^{(3)}_{lequ}$ is also insensitive for these two decay modes for the same reason.

- $P \to \ell\nu_\ell$ decay: Leptonic decays from psudoscalar mesons (P) provide one of cleanest probes to constrain NP. The hadronic matrix elements for these decays with different Lorentz structures are defined as [261]

$$\langle 0|\bar{q}_1\gamma^\mu\gamma_5 q_2|P(p)\rangle = if_P p^\mu, \qquad \langle 0|\bar{q}_1\gamma_5 q_2|P(p)\rangle = -if_P\frac{M_P}{m_{q_1}+m_{q_2}}, \tag{5.26}$$

where m_P, f_P, and $m_{q_{1(2)}}$ are the mass, decay constant, and mass of constituent quarks of P-meson. These inputs for different pseudoscalar mesons are taken from FLAG review [248]. $\mathcal{O}^{(3)}_{lq}$ and $\mathcal{O}^{(1)}_{lequ}$ operators contribute to this decay. Using the effective Hamiltonian in Eq. (5.23), the branching ratio of $P \to \ell\nu_\ell$ is expressed as

$$\mathcal{B}(P \to \ell\nu_\ell) = \tau_P\frac{m_P m_\ell f_P^2 G_f^2 V_{q_1q_2}}{8\pi}\left(1-\frac{m_\ell^2}{m_P^2}\right)^2\left|1 - C_{V_1} + \frac{m_P^2}{m_\ell(m_{q_1}+m_{q_2})}C_{S_2}\right|^2, \tag{5.27}$$

where, τ_P is the lifetime of P meson, m_ℓ is the mass of the lepton (ℓ), and $V_{q_1q_2}$ is CKM matrix element. C_{V_1} and C_{S_2} follow same relations as expressed in Eq. (5.25). Constraints on C_{V_1} and C_{S_2} couplings are tabulated in Table 5.3. Using these observables, we note the constraints on C_i/Λ^2 in Table 5.1 and 5.2 following Eq. (5.25).

- $t \to b\ell\nu_\ell$ decay: Along with the flavour observable described above, semi leptonic decays of top quark is instrumental in constraining NP. The $t \to b\ell\nu_\ell$

Decay modes	Branching ratio	Constraints (GeV^{-2})	
		C_{V_1}	C_{S_2}
$\pi^\pm \to \mu\nu_\mu$	$(99.9877 \pm 0.00004) \times 10^{-2}$	$-(1.77 \pm 0.6) \times 10^{-2}$	$(4.33 \pm 0.23) \times 10^{-4}$
$K^\pm \to \mu\nu_\mu$	$(63.56 \pm 0.11) \times 10^{-2}$	$-(3.21 \pm 1.08) \times 10^{-2}$	$(1.36 \pm 0.04) \times 10^{-3}$
$B^\pm \to \tau\nu_\tau$	$(1.09 \pm 0.24) \times 10^{-4}$	$-(1.85 \pm 0.62) \times 10^{-1}$	$(4.94 \pm 1.60) \times 10^{-2}$
$D_s^\pm \to \mu\nu_\mu$	$(5.43 \pm 0.15) \times 10^{-3}$	$-(8.74 \pm 14.43) \times 10^{-3}$	$(3.25 \pm 2.36) \times 10^{-4}$
$D^\pm \to \mu\nu_\mu$	$(3.74 \pm 0.17) \times 10^{-4}$	$(1.66 \pm 2.21) \times 10^{-2}$	$-(6.40 \pm 8.71) \times 10^{-4}$

Table 5.3: Constraints on C_{V_1} and C_{S_2} from $\mathcal{B}(P \to \ell\nu_\ell)$. Experimental inputs for different $P \to \ell\nu_\ell$ branching ratios are adopted from PDG average [188].

decay gets contribution from few operators in Eq. (5.1), thereby imposing constraints on the associated dimension six effective couplings. This decay process is governed by W mediated charge current interaction within SM whereas for NP contribution arises from $\mathcal{O}_{lq}^{(3)}$, $\mathcal{O}_{lequ}^{(1)}$, and $\mathcal{O}_{lequ}^{(3)}$ operators. The total decay width (Γ^t) for this process is given by

$$\Gamma^t = \frac{1}{64\pi^3 m_t} \int_{E_\ell=0}^{\frac{m_t}{2}} \left(\int_{E_b=(\frac{m_t}{2}-E_\ell)}^{\frac{m_t}{2}} \left|\mathcal{M}_{\mathtt{tot}}^t\right|^2 dE_b \right) dE_\ell, \tag{5.28}$$

where m_t is mass of top quark, E_b and E_ℓ are the energy of b-quark and lepton (ℓ). SM and NP contribution to the total amplitude are written in the Appendix A.4. Constaints on $\mathcal{O}_{lq}^{(1)}$ from this decay is tabulated in Table 5.1. For scalar ($C_{\ell equ}^{(3)}/\Lambda^2$) and tensor ($C_{\ell equ}^{(3)}/\Lambda^2$) mediated couplings, orders of the constraints are 10^{-3} and 10^{-4} respectively. For $t \to c\ell\ell$ decay (Eq. (5.29)), upper limit of these operstors is 10^{-5}. Therefore constraints obtained from $t \to b\ell\nu$ on $C_{\ell equ}^{(1)}/\Lambda^2$ and $C_{\ell equ}^{(3)}/\Lambda^2$ are ruled out from the upper limit of $t \to c\ell\ell$ decay.

We would like to note that no suitable observable has been found to constrain $\mathcal{O}_{\ell u}$ and $\mathcal{O}_{eu}$ operators. An upper bound is noted for this two operators form $t \to c\ell\ell$ decay in Table 5.1, and we make predictions for $t \to c\ell\ell$ as we discuss below.

5.3.2 Prediction on different observables

Using the constraints on the EFT operators obtained in Table 5.1, Table 5.2 and Table 5.3, we provide future prediction of following observables, with numerical estimates noted in Table 5.4.

- $\underline{\mathcal{B}(t \to c\ell\ell)}$: The branching ratio of $t \to c\ell\ell$ decay is given by[2]

$$\mathcal{B}(t \to c\ell\ell) = \frac{m_t^5}{6144\pi^3\Lambda^4\Gamma_{\mathtt{tot}}^t} \left(4(C_{lq}^{(1)} +_{lq}^{(3)})^2 + (C_{eu}^2 + C_{lu}^2 + C_{qe}^2 + C_{le\ell q}^{(1)^2} + 72 C_{le\ell q}^{(3)^2} \right) . \tag{5.29}$$

---

[2] The expression of $\mathcal{B}(t \to c\ell\ell)$ is calculated in the limit of $m_c, m_\ell \to 0$, but in numerical evaluation all masses are taken into account.

As of now, there hasn't been any specific experimental searches conducted to observe $t \to c\ell\ell$ decays. However, an indirect upper limit on $t \to c\ell\ell$ decays can be obtained by $t \to Zq$ searches at ATLAS [262]. At 95 % C.L., bounds on $t \to c\ell\ell$ branching ratios are [214]

$$\begin{aligned} \mathcal{B}(t \to c e^+ e^-) &< 2.1 \times 10^{-4}, \\ \mathcal{B}(t \to c \mu^+ \mu^-) &< 1.5 \times 10^{-4}. \end{aligned} \tag{5.30}$$

These upper limits of the branching ratio provide upper bounds on the dimension-6 effective vector and scalar operators on the order of 10^{-5} whereas for tensor operator the upper bound is 10^{-7}. Constraints determined from experimental inputs on dimension-6 effective couplings listed in Table 5.1 and 5.2 respect this upper bound. Using the obtained constraints on dimension-6 effective couplings, we provide the prediction on this observable in Table 5.4.

- $\mathcal{B}(K_L \to \pi^0 \ell\bar{\ell})$: The branching fraction of $K_L \to \pi^0 \ell\bar{\ell}$ can be expressed as [263, 264]

  $$\mathcal{B}(K_L \to \pi^0 \ell\bar{\ell}) = \left(C^\ell_{\rm dir} \pm C^\ell_{\rm int}|a_S| + C^\ell_{\rm mix}|a_S|^2 + C^\ell_{\gamma\gamma}\right) \cdot 10^{-12}\,, \tag{5.31}$$

  The details of a_s, $C^\ell_{\mathtt{dir}}$, $C^\ell_{\mathtt{int}}$, $C^\ell_{\mathtt{mix}}$ and $C^\ell_{\gamma\gamma}$ are discussed in [263, 264]. Constraint on $C^{(1)}_{lq}/\Lambda^2$ and $C^{(3)}_{lq}/\Lambda^2$ couplings provide prediction on this observable.

- $\mathcal{B}(D^0 \to \mu\mu)$: Branching ratio of $D^0 \to \mu\mu$ decay is noted as [265]

  $$\mathcal{B}(D^0 \to \mu\mu) = \frac{M_D}{8\pi\Gamma_D\Lambda^4}\sqrt{1 - \frac{4m_\ell^2}{M_D^2}}\left[(1 - \frac{4m_\ell^2}{M_D^2})|A|^2 + |B|^2\right], \tag{5.32}$$

  with

  $$\begin{aligned} A =& \frac{G_f f_D M_D^2}{2m_c} C^{(1)}_{lequ}, \\ B =& \frac{G_f f_D m_\mu}{2m_c}(C^{(1)}_{lq} + C^{(3)}_{lq} - C_{lu} + C_{qe})), \end{aligned} \tag{5.33}$$

  where m_c is the mass of charm quark, M_D and f_D are the mass and decay constant of D^0, respectively. Tensor mediated operator does not contribute to this observable as $\left\langle \ell^+\ell^- | \mathcal{O}^{(3)}_{lequ} | D^0 \right\rangle = 0$. Constraints on operators written in Eq. (5.33) provide prediction on this observable.

- $\mathcal{B}(t \to c\gamma)$: Scalar mediated dimension-6 effective couplings provide a prediction on BR($t \to c\gamma$) through τ mediated 1-loop diagram as in Fig. 5.3. Vector and tensor mediated operators do not contribute to this observable as $\langle c\gamma | \mathcal{O}^v_i | t \rangle = 0$[3] and $\left\langle c\gamma | \mathcal{O}^{(3)}_{lequ} | t \right\rangle = 0$. The expression of $\mathcal{B}(t \to c\gamma)$ is given by

  $$\mathcal{B}(t \to c\gamma) = \frac{8e_0^2 m_\tau^6}{9\Gamma^t(m_t^2 - m_c^2)}\left(\frac{C^{(1)}_{lequ}}{\Lambda^2}\right)^2\left(1 + 2\mathrm{Log}\left[\frac{\Lambda}{m_\tau}\right]\right)^2(m_c^4 + 7m_c^2 m_t^2 + m_t^4). \tag{5.34}$$

Prediction on different observables noted in Table 5.4 suggest that all the experimental predictions on dimension-6 effective couplings are consistent with existing upper bounds.

---

[3] $\mathcal{O}^v_i$ is any vector operator in Eq. (5.1).

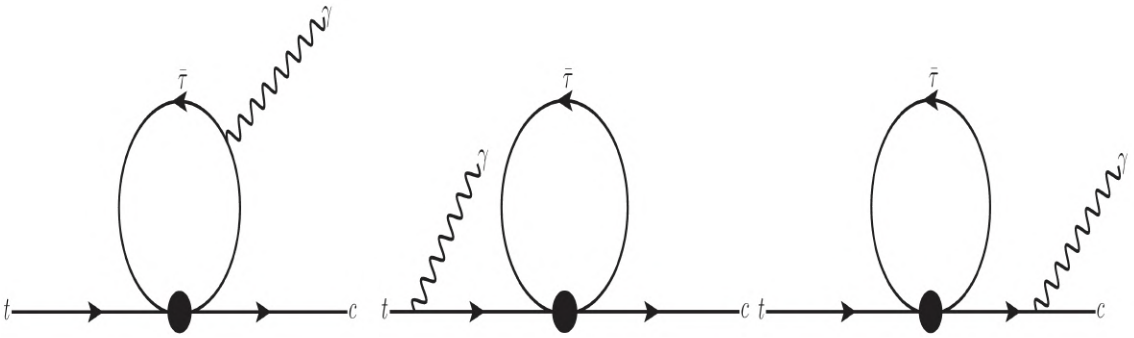

Figure 5.3: τ mediated 1-loop scalar mediated operator $\mathcal{O}_{lequ}^{(1)}$ contribution to $t \to c\gamma$ decay.

Dimension-6 couplings	Observables	Branching ratio	
		Prediction	Upper bound
$\frac{C_{lq}^{(1)}}{\Lambda^2}$	$\mathcal{B}(K_L \to \pi^0 e^+ e^-)$	7.38×10^{-11}	2.8×10^{-10} [266]
	$\mathcal{B}K_L \to \pi^0 \mu^+ \mu^-$	8.43×10^{-11}	3.8×10^{-10} [267]
	$\mathcal{B}(D^0 \to \mu\mu)$	4.63×10^{-23}	3.1×10^{-9} [268]
	$\mathcal{B}(t \to cee)$	1.28×10^{-11}	2.1×10^{-4} [214]
	$\mathcal{B}(t \to c\mu\mu)$	1.30×10^{-11}	1.5×10^{-4} [214]
$\frac{C_{lq}^{(3)}}{\Lambda^2}$	$\mathcal{B}(K_L \to \pi^0 e^+ e^-)$	7.42×10^{-11}	2.8×10^{-10} [266]
	$\mathcal{B}(K_L \to \pi^0 \mu^+ \mu^-)$	8.46×10^{-11}	3.8×10^{-10} [267]
	$\mathcal{B}(D^0 \to \mu\mu)$	4.63×10^{-21}	3.1×10^{-9} [268]
	$\mathcal{B}(t \to cee)$	1.31×10^{-11}	2.1×10^{-4} [214]
	$\mathcal{B}(t \to c\mu\mu)$	1.33×10^{-11}	1.5×10^{-4} [214]
$\frac{C_{qe}}{\Lambda^2}$	$\mathcal{B}(D^0 \to \mu\mu)$	4.04×10^{-21}	3.1×10^{-9} [268]
	$\mathcal{B}(t \to cee)$	2.79×10^{-12}	2.1×10^{-4} [214]
	$\mathcal{B}(t \to c\mu\mu)$	2.82×10^{-12}	1.5×10^{-4} [214]
$\frac{C_{lequ}^{(1)}}{\Lambda^2}$	$\mathcal{B}(t \to cee)$	2.34×10^{-13}	2.1×10^{-4} [214]
	$\mathcal{B}(t \to c\mu\mu)$	2.37×10^{-13}	1.5×10^{-4} [214]
	$\mathcal{B}(t \to c\gamma)$	4.30×10^{-17}	1.8×10^{-4}[269]
$\frac{C_{lelu}^{(3)}}{\Lambda^2}$	$\mathcal{B}(t \to cee)$	2.84×10^{-13}	2.1×10^{-4} [214]
	$\mathcal{B}(t \to c\mu\mu)$	2.86×10^{-13}	1.5×10^{-4} [214]

Table 5.4: Prediction of different observables from the simultaneous fit and existing upper bound.

5.4 Collider Analysis

In this section, we analyse the possibility of probing the NP at collider in terms of the effective operators as in Eq. (5.1). For that we focus on those most stringent limits of the dimension-6 effective operators stemmed from the flavour observables. If the most stringent limits on the NP couplings can be probed for a given $\sqrt{s}$ then the others can be probed at a smaller $\sqrt{s}$. From Table 5.1, we see that the flavor constraint on $C_{lelq}^{(3)}/\Lambda^2$, the tensor coupling is one of the most stringent ones which are on the order of $\sim 10^{-11}$ GeV^{-2} followed by $C^{(1)}_{lelq}/\Lambda^2 \sim 10^{-10}$ GeV^{-2} and $C^{(1)}_{lq}/\Lambda^2 \sim 10^{-9}$ GeV^{-2}. Therefore, in our subsequent analysis, we will focus on these three WCs mostly. From Eq. (5.36), it is clear that the signal cross-section exhibits a linear growth with the square of the CM energy, conversely, SM background processes are expected to decrease as $\sqrt{s}$ increases. Therefore, at high $\sqrt{s}$, a muon collider should have the capability to detect a such NP scenarios where the CM energy of the machine is expected to go upto 30 TeV. For our analysis, we consider $\sqrt{s} = 10$ TeV with an integrated luminosity ($\mathfrak{L}_{\texttt{int}}$) of 1 ab^{-1}. This choice is within the reach of the future muon collider projections [118]. We further note that when we are probing $C/\Lambda^2 \sim 10^{-11}$ GeV^{-2} at $\sqrt{s} = 10$ TeV, we assume, $\Lambda \gtrsim 10$ TeV, so that the Wilson coefficient $C \gtrsim 10^{-3}$, to keep the effective theory framework validated.

5.4.1 tc ($\bar{t}c + t\bar{c}$) production cross-section

The differential $t\bar{c}(\bar{t}c)$ production cross-section at $\mu^+\mu^-$ collider, governed by the effective four-fermi contact interaction as shown in Fig. 5.1, in terms of vector, scalar and tensor couplings is given by[4]

$$\begin{aligned}\frac{d\sigma}{d\cos\theta} = \frac{3\mathcal{F}}{8}\Big[&2(V_{RR}^2 + V_{LL}^2)\left(1 + (1+\beta)\cos\theta + \beta\cos^2\theta\right)\\ &+ 2(V_{RL}^2 + V_{LR}^2)\left(1 - (1+\beta)\cos\theta + \beta\cos^2\theta\right)\\ &+ S_{RR}^2(1+\beta) - 4S_{RR}T_{RR}(1+\beta)\cos\theta + 16T_{RR}^2(1-\beta+2\beta\cos^2\theta)\Big],\end{aligned} \tag{5.35}$$

where $\mathcal{F} = \frac{s}{\Lambda^4}\frac{\beta^2}{4\pi(1+\beta^3)}$ and $\beta = \frac{s-m_t^2}{s+m_t^2}$. Therefore, total production cross-section is

$$\sigma_{\texttt{prod}} = \mathcal{F}\left[8T_{RR}^2(3-\beta) + \frac{3}{2}S_{RR}^2 + (V_{LL}^2 + V_{RR}^2 + V_{LR}^2 + V_{RL}^2)(3+\beta)\right]. \tag{5.36}$$

The variation of the signal cross-section ($\sigma_{\texttt{prod}}$) for the vector, scalar and tensor four Fermi operators used in this model with CM energy ($\sqrt{s}$) is shown in the right side of the Fig. 5.4. Here, $\Lambda = 50$ TeV and Wilson coefficients ($C = 1$) are kept constants. From Eq. (5.36) we see that the total cross-section ($\sigma_{\texttt{prod}}$) is proportional to s/Λ^4, therefore, larger ($\sqrt{s}$) yields larger cross-section, provided we are in the effective theory limit, i.e. $\sqrt{s} < \Lambda$. We also note from Fig. 5.4, that the production cross-section is largest for the tensor coupling and the lowest for the vector coupling. For vector coupling, the cross-section ~ 0.1 fb at $\sqrt{s} = 5$ TeV and that is down to 0.001 fb at $\sqrt{s} = 1$ TeV for $C/\Lambda^2 \sim 10^{-10}$ GeV^{-2}, making it a necessity to probe these couplings at $\sqrt{s} = 10$ TeV.The variation is shown in one operator scenario, that implies $\sigma_{\texttt{prod}} \propto C_i^2/\Lambda^4$. Therefore the variation of total cross-section with C/Λ^2 is symmetric as depicted in the left side of Fig. 5.1. Apart from the four-fermi couplings, Ztc couplings (a_L^Z and a_R^Z) via $\mathcal{O}^{(1)}_{Hq}$, $\mathcal{O}^{(3)}_{Hq}$ and $\mathcal{O}_{Hu}$ also contribute to tc production by interfering with the four-fermi vector couplings V_{ij}. The contribution of Ztc couplings can be incorporated to the total cross-section by redefining

$$V_{ij} \to V_{ij} + 4c_i^Z a_j^Z\left(\frac{m_W m_Z}{s - m_Z^2}\right) \quad \text{with} \quad a_L^Z = \frac{1}{4c_w}(C^{(1)}_{Hq} - C^{(3)}_{Hq}), \quad a_L^Z = \frac{1}{4c_w}C_{Hu}, \tag{5.37}$$

where $i, j = L, R$, and $c_L^Z = -1/2 + s_w^2$ and $c_R^Z = s_w^2$ are the couplings to a left or right

---

[4] In the expression of differential cross-section, muon mass is neglected.

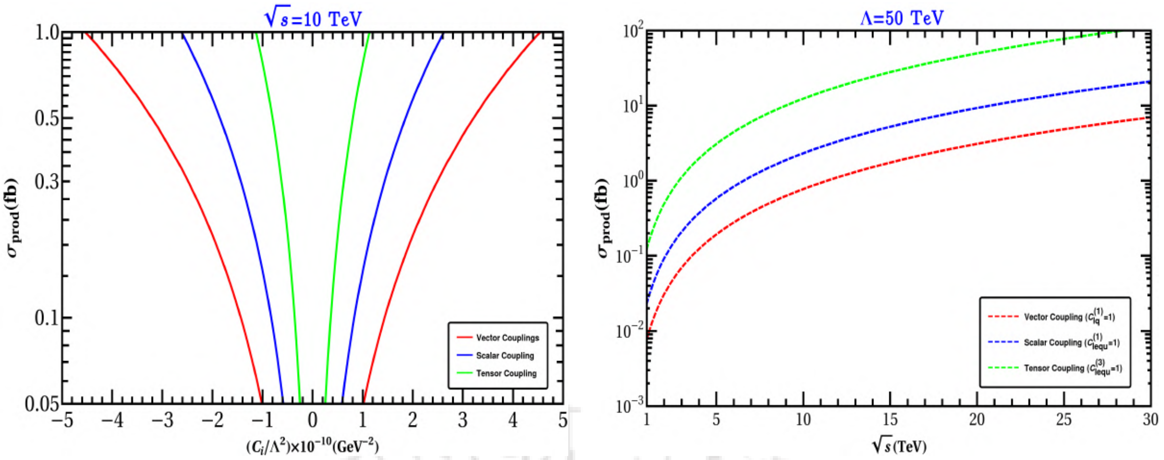

Figure 5.4: Variation of total cross-section of tc production at $\mu^+\mu^-$ collider with different choices of C/Λ^2 (GeV^{-2}) (left) and CM energy ($\sqrt{s}$) for $\Lambda = 50$ TeV (right).

handed electron, respectively. On contrary to four-fermi couplings, the cross-section via Z mediation drops as $\sim 1/s$ due to the s-channel mediation. In the left side of Fig. 5.4, we show the variation of $\sigma_{\texttt{prod}}$ with varying C/Λ^2 in GeV^{-2}. From the figure, we again see that the tensor mediated four-fermi coupling (T_{RR}) provides the maximum contribution to the tc production and vector mediated production provides the least. In one operator scenario, all the vector operator contribute equally to the total cross-section. If we assume Ztc effective couplings to be of the same order to

Couplings (GeV^{-2})	Cross-section ($\sigma_{\texttt{prod}}$) (fb)
$C_{lq}^{(1)}/\Lambda^2$	4.8×10^{-2}
$C_{lequ}^{(1)}/\Lambda^2$	0.15
$C_{lequ}^{(3)}/\Lambda^2$	0.77
$C_{Hq}^{(1)}/\Lambda^2$	1.71×10^{-10}

Table 5.5: $t\bar{c}(t\bar{c})$ production cross-section ($\sigma_{\texttt{prod}}$) at muon collider for vector ($C_{lq}^{(1)}/\Lambda^2$), scalar ($C_{lequ}^{(1)}/\Lambda^2$), tensor ($C_{lequ}^{(3)}/\Lambda^2$), and Ztc ($C_{Hq}^{(1)}/\Lambda^2$) effective couplings. We consider $\sqrt{s}$ = 10 TeV and $C/\Lambda^2 = 10^{-10}$ GeV^{-2} for all the operators.

that of vector coupling, $C/\Lambda^2 \sim 10^{-9}$ GeV^{-2}, then the contribution from Ztc is way milder than the four fermi operator contribution, see Table 5.5, where we see that the production cross-section ($\sigma_{\texttt{prod}}$) for vector coupling surpasses that of Ztc coupling by an order of 10^8 in fb at 10 TeV muon collider. Therefore in the following analysis we neglect the contribution of Ztc and study the four fermi operators.

5.4.2 Signal and background processes

In high-energy muon colliders, collision events take place at a center-of-mass (CM) energy surpassing that achieved by the present LHC (parton level) or potential future electron-positron colliders. Consequently, it is anticipated that jets that are closely clustered together in these collisions will exhibit collimation, effectively coalescing into a singular, consolidated jet. A notable illustration of this behavior can be observed in the jets stemming from the hadronic decay processes of top quarks or W/Z bosons, where they converge to form a single "top" or "W/Z" jet [270]. Since the signal process is $\mu^-\mu^+ \to tc$, for this analysis, we consider a dijet signal with no leptons. The corresponding SM background processes are $\mu^-\mu^+ \to t\bar{t}$, $\mu^-\mu^+ \to q\bar{q}$, $\mu^-\mu^+ \to c\bar{c}$, $\mu^-\mu^+ \to b\bar{b}$, $\mu^-\mu^+ \to W^+W^-$ and $\mu^-\mu^+ \to ZZ$.

Event simulation

The signal and background events are generated in `MadGraph5`. For the EFT signal process, the `UFO` model file is generated using `FeynRules`. The benchmark points (BPs) we consider for collider analysis are:

- BP1 (Vector) : $C_{lq}^{(1)}/\Lambda^2 = -9.96 \times 10^{-10}$ GeV^{-2},
- BP2 (Scalar) : $C_{lequ}^{(1)}/\Lambda^2 = -6.61 \times 10^{-10}$ GeV^{-2},
- BP3 (Tensor) : $C_{lequ}^{(3)}/\Lambda^2 = 7.24 \times 10^{-11}$ GeV^{-2}.

These BPs are most stringent flavor constrained vector, scalar, and tensor couplings as noted in Table 5.1 and 5.2. Using these numerical inputs, MC generated events are fed into `Pythia8` and `Delphes3` for parton showering and detector simulation respectively.

- We use the leptons and jets selection criteria described in Section 3.6.
- The jet clustering has been done in `Fastjet3` [271] using `anti-kt` algorithm [272]. The jet radius is taken to be 0.5 with the minimum p_T of the jet set as 20 GeV. The jet reconstruction is done using `Delphes3`.

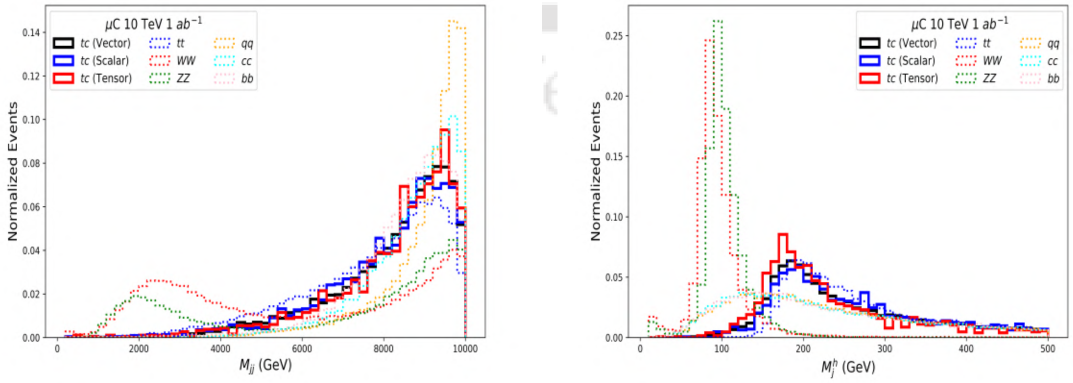

Figure 5.5: Normalized event distribution for dijet final state containing signal and background processes at muon collider with $\sqrt{s} = 10$ TeV and $\mathfrak{L}_{\texttt{int}} = 1$ ab^{-1}.

5.4.3 Cut based Analysis

For the analysis, we use the following sequential cuts for the signal and background processes:

- Cut 1: $N_j = 2$ and $N_l = 0$.
- Cut 2: $M_{jj} > 8$ TeV.
- Cut 3: $M_j^h > 160$ GeV.

Here, M_{jj} is the invariant mass of the dijet, M_j^h is the invariant masses of the reconstructed particles of the heavier jet. The major background, in case of our analysis, are the diboson processes. In Cut 1, which is our signal selection cut, we demand only processes with 2 jets. We further remove events with detected leptons. This will remove the detected leptonic and semi-leptonic decay processes for W^+W^-, ZZ as well as $t\bar{t}$. The invariant mass of the dijet pair is expected to peak near the centre of mass energy of the incoming particles for jets coming from the production level processes. For jets coming from branching or radiation, the invariant mass is expected to peak at a lower value. Imposing Cut 2, we can remove futher semileptonic and leptonic processes from diboson production, where the leptons were not detected. Now, due to the collimation of boosted jets in high energies, as we mention above, we expect multiple jets branching from top or W/Z to appear as a single jet in the detector. The invariant mass of the reconstructed particles of such jets are expected to peak at the mass of their respective sources, i.e. top mass or W/Z mass. In tc signal process, the heavier jet is expected to peak at the top mass, as such Cut 3, will significantly remove W^+W^- and ZZ backgrounds as evident from the distribution in Fig. 5.5. The signal can be further separated from the background by using a charm tagging algorithm on the lighter jet of tc signal process. However, with the current c-tagging efficiency at LHC [273, 274], it looks like a far-fetched possibility. This is primarily due to high miss-tagging efficiency of the b-jets as c-jets. After employing sequential cuts as mentioned above, signal significance $S/\sqrt{S+B}$ and efficiency factor[5] $\epsilon_{s(b)} = \sigma^{\texttt{sig}}_{s(b)}/\sigma^{\texttt{prod}}_{s(b)}$ are noted in Table 5.6. We see that the benchmark point with vector couplings have most signal significance, while the tensor one has the least.

5.4.4 OOT Sensitivities

In general, a collider observable ($e.g.$, differential cross-section) contains contribution from both the signal and background. The expression of the observable $i.e.$, differential corss-section follows Eq. (2.37). The presence of the second term in Eq. (2.37), i.e. the SM background makes an important distinction of this OOT analysis from the previous ones. Here g_i are the non-linear functions of NP couplings and f_i are the function of phase-space co-ordinate ϕ and ϵ_s (ϵ_b) is the signal (background) efficiencies in estimating the signal (and background) after using judicious cuts as tabulated in Table 5.6. In this analysis as our focus on $2 \to 2$ processes, the phase space co-ordinate will be $\phi = \cos\theta$, where θ is angle between the outgoing particles

---

[5] $\sigma^{\texttt{sig}}_{s(b)}$ is the final state cross-section after final for signal (background) whereas $\sigma^{\texttt{prod}}_{s(b)}$ is the production cross-section for signal (background).

Process	No Cuts	Cut 1	Cut 2	Cut 3	$\epsilon_{s/b}$	Significance
$\mu^-\mu^+ \to tc$ (BP1)	6432	1339	891	809	0.12	
$\mu^-\mu^+ \to tc$ (BP2)	2130	467	302	278	0.13	
$\mu^-\mu^+ \to tc$ (BP3)	140	30	20	18	0.13	BP1: 18.40
$\mu^-\mu^+ \to t\bar{t}$	1730	352	191	183	0.10	
$\mu^-\mu^+ \to q\bar{q}$	3555	746	650	433	0.12	BP2: 7.42
$\mu^-\mu^+ \to c\bar{c}$	1728	363	290	190	0.11	
$\mu^-\mu^+ \to b\bar{b}$	914	194	143	93	0.10	BP3: 0.53
$\mu^-\mu^+ \to W^+W^-$	58860	22882	7258	215	0.004	
$\mu^-\mu^+ \to ZZ$	3284	1238	454	10	0.003	

Table 5.6: Cut flow and signal significance for signal at the chosen benchmark points and background processes for analysis at muon collider at 10 TeV and 1 ab^{-1}. Here $\epsilon_{s/b}$ denotes the cut efficiency for signal and background following the final cut (Cut 3).

with respect to the beam axis. However, the choice of ϕ can vary depending on the specific process. We importantly note that the signal of the processes under consideration are essentially dijet events (as elaborated in the previous section), stemming from the produced particles in the high CM energy of the muon collider, enabling us to use Eq. (2.7), without much problem. However, for processes where the decay products are not collimated, say for example, at smaller CM energy, the usage of Eq. (2.7) is limited.

Here, we discuss the optimal uncertainties and correlations of different dimension-6 effective operators in context of $t\bar{c}(\bar{t}c)$ production. As mentioned before, we focus on the probe of most stringent vector, scalar, and tensor mediated couplings that contribute to the tc production at the $\mu^+\mu^-$ colliders. The χ^2 variation dimension-6

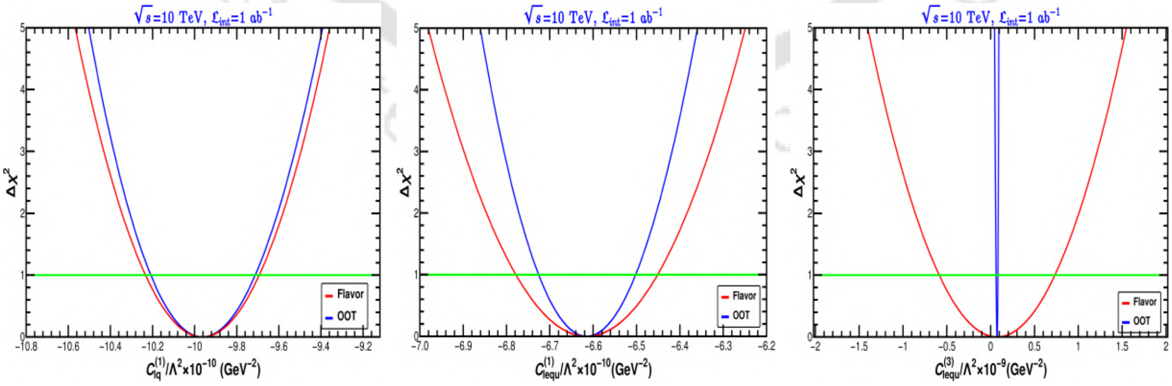

Figure 5.6: The $\Delta\chi^2$ variation as a function of dimension-6 effective couplings; left: $C^{(1)}_{lq}/\Lambda^2$ (Vector), middle: $C^{(1)}_{lequ}/\Lambda^2$ (Scalar), right: $C^{(3)}_{lequ}/\Lambda^2$ (Tensor). The units of C/Λ^2 is in GeV^{-2}. The horizontal axis denote $\Delta\chi^2 = 1$.

effective operators are shown in the Fig. 5.6. At CM energy $\sqrt{s}$=10 TeV and luminosity $\mathfrak{L}_{\texttt{int}} = 1\ \text{ab}^{-1}$, we observe that for all the couplings, optimal uncertainty is narrower than flavor uncertainty. It is intriguing to note that for the tensor-mediated operator $C^{(3)}_{lequ}/\Lambda^2$, the flavour uncertainty is way larger than the optimal collider sensitivity of this coupling at muon collider (see the right most panel in Fig. 5.6). This suggests that the pertinent operator is less-consistent in flavour observable, yet in a collider scenario, it can be measured with larger precision. This is because the tensor operator having most stringent flavour bound, has the largest contribution to the tc production compared to scalar and vector operators, as already evidenced by Fig. 5.4 and Table 5.5.

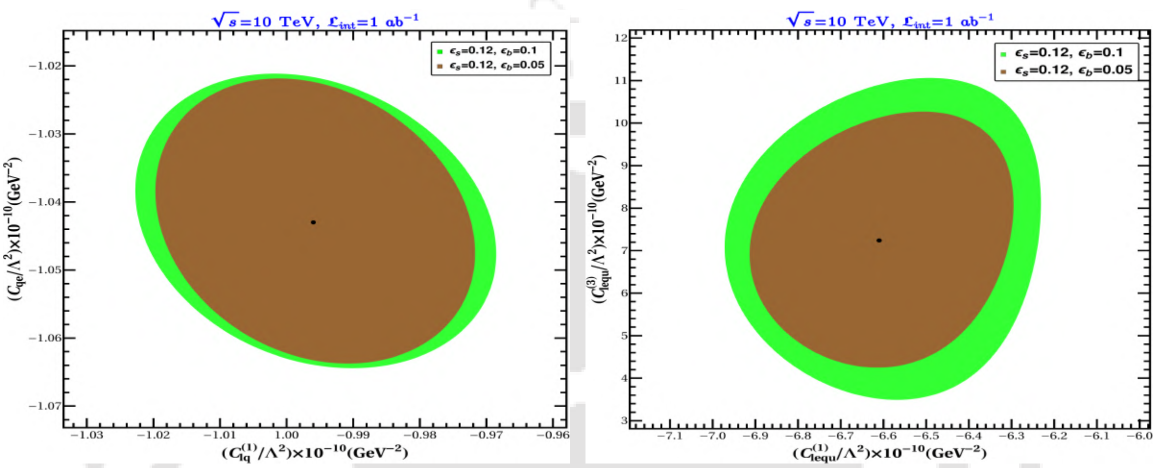

Figure 5.7: Optimal 1σ allowed parameter space in 2D plane. Left: $C^{(1)}_{lq}/\Lambda^2 - C_{qe}/\Lambda^2$ plane; right: $C^{(1)}_{lequ}/\Lambda^2 - C^{(3)}_{lequ}/\Lambda^2$ plane. Variation of background efficiency (ϵ_b) is also shown in both cases. See inset and headings for details. The flavor inputs are taken from the case-III mentioned in Table 5.7.

The correlations between the two vector couplings and correlations among scalar and tensor couplings for different background efficiencies ($\epsilon_b = \{0.1, 0.05\}$) are shown in Fig. 5.7. The benchmark cases with seed values are listed in Table 5.7. It is clear that the presence of background via ϵ_b plays a crucial role in determining the optimal uncertainty of NP couplings, the lesser the contamination, the better the precision. Moreover, the optimal uncertainty of NP couplings depends on the relative NP signal and non-interfering SM background contribution to the final state. Contribution to the final state from two vectors operators is greater than the scalar and tensor operators together by a factor of 25 (Table 5.6), due to the choice of the seed values of the benchmark points. Therefore, the relative NP signal is larger than the background contribution for the vector operators than the scalar and tensor ones. That is why the vector operator correlation is less affected by the change in background contamination as shown in the Fig. 5.7.

In Fig. 5.8 we show the variation of 1σ regions for different CM energies and integrated luminosities. In our scenario, the increase of CM energy ($\sqrt{s}$) is more effective than the increase of integrated luminosity. If we increase the CM energy twice, then the signal cross-section is increased by a factor of 4 which in turn suggest four times enhancement in signal events. However, we must remember that when we enhance $\sqrt{s}$, we choose $\Lambda > \sqrt{s}$ to be consistent with EFT framework, reducing the WC appropriately to keep C/Λ^2 is same ballpark. Larger CM energy also reduces the non-interfering SM backgrounds. However, if we double the luminosity, both the signal and background events will enhance twice, suggesting larger CM energy helps reducing optimal uncertainty for EFT frameworks as considered here.

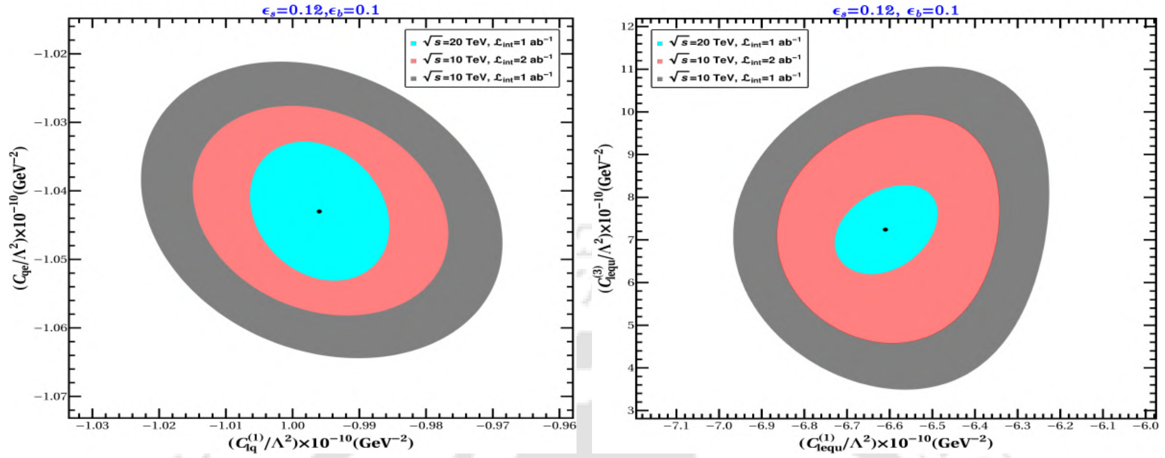

Figure 5.8: Comparison of optimal 1σ surfaces for CM energy ($\sqrt{s}$) and luminosity ($\mathfrak{L}_{\texttt{int}}$); Left: $C_{lq}^{(1)}/\Lambda^2 - C_{qe}/\Lambda^2$ plane; right: $C_{lequ}^{(1)}/\Lambda^2 - C_{lequ}^{(3)}/\Lambda^2$ plane. The flavor inputs are taken from the case-III mentioned in Table 5.7.

Cases	Vector ops. combination	Scalar and tensor ops. combination
I	$\frac{C_{lq}^{(1)}}{\Lambda^2} = -9.96 \times 10^{-10}\ \text{GeV}^{-2}$, $\frac{C_{qe}}{\Lambda^2} = 0$	$\frac{C_{lequ}^{(1)}}{\Lambda^2} = -6.61 \times 10^{-10}\ \text{GeV}^{-2}$, $\frac{C_{lequ}^{(3)}}{\Lambda^2} = 0$
II	$\frac{C_{lq}^{(1)}}{\Lambda^2} = 0$, $\frac{C_{qe}}{\Lambda^2} = -1.04 \times 10^{-9}\ \text{GeV}^{-2}$	$\frac{C_{lequ}^{(1)}}{\Lambda^2} = 0$ $\frac{C_{lequ}^{(3)}}{\Lambda^2} = 7.24 \times 10^{-11}\ \text{GeV}^{-2}$
III	$\frac{C_{lq}^{(1)}}{\Lambda^2} = -9.96 \times 10^{-10}\ \text{GeV}^{-2}$, $\frac{C_{qe}}{\Lambda^2} = -1.04 \times 10^{-9}\ \text{GeV}^{-2}$	$\frac{C_{lequ}^{(1)}}{\Lambda^2} = -6.61 \times 10^{-10}\ \text{GeV}^{-2}$, $\frac{C_{lequ}^{(3)}}{\Lambda^2} = 7.24 \times 10^{-11}\ \text{GeV}^{-2}$

Table 5.7: Different benchmark cases of combination of operators studied for optimal correlations and separability from SM.

In Fig. 5.9, we show the optimal statistical separation of different cases listed in Table 5.7 from the 'base model' SM. Here, Case-I and Case-II are followed from flavour constraints noted in Table 5.1 and 5.2 and case-III is considered to show the correlations among different operators. We consider the CM energy $\sqrt{s}$ = 10 TeV and integrated luminosity $\mathfrak{L}_{\texttt{int}}$= 1 ab^{-1}. We determine that for various vector (scalar and tensor) operator combinations, Case-I, Case-II, and Case-III are 28.18σ (11.63σ), 76.97σ (1.78σ), and 87.34σ (12.67σ) away from SM respectively, so that the distinction of vector operators is comparatively easier than the scalar and tensor operators once we adhere to the benchmark points respecting flavour constraints. Estimated values of vector, scalar, and tensor couplings are noted in Table 5.8 for diferent CM energies

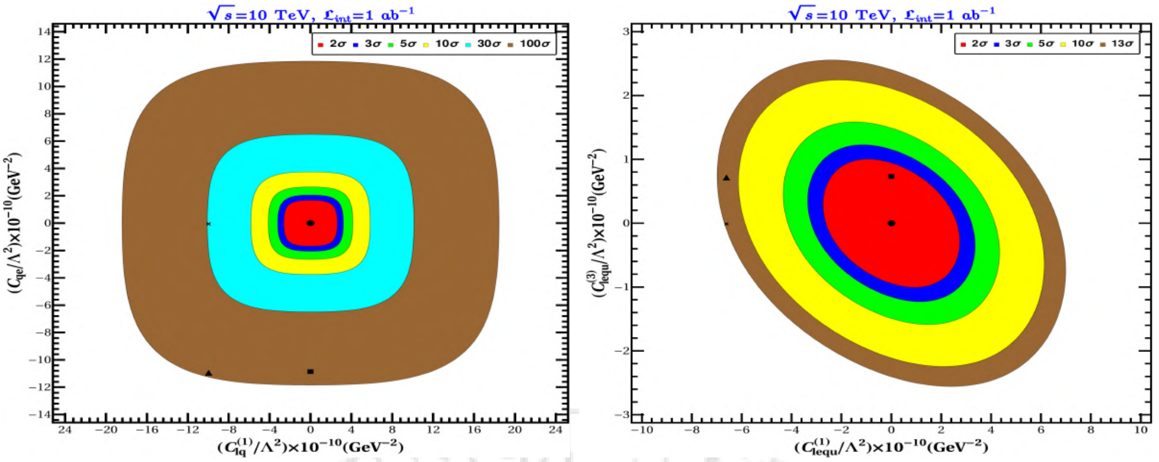

Figure 5.9: Seperation of different cases mentioned in Table 5.7; Left: $C_{lq}^{(1)}/\Lambda^2 - C_{qe}/\Lambda^2$ plane, right: $C_{lequ}^{(1)}/\Lambda^2 - C_{lequ}^{(3)}/\Lambda^2$ plane. The representative points related to case-I, case-II, and case-III are denoted by cross (×), triangle (△), and square (□). The 'base model' SM is represented by the dot (•). Different $n\sigma$ regions are presented in the inset of the figures.

and luminosities at 5σ separation. To acheive the 5σ separation for tensor operator with current flavor bound, we require 18 ab^{-1} integrated luminosity for 10 TeV CM energy.

Couplings (GeV^{-2})	$\sqrt{s} = 10$ TeV, $\mathfrak{L}_{\texttt{int}}$=1 ab^{-1}	$\sqrt{s} = 10$ TeV, $\mathfrak{L}_{\texttt{int}}$=10 ab^{-1}	$\sqrt{s} = 30$ TeV, $\mathfrak{L}_{\texttt{int}}$=1 ab^{-1}	$\sqrt{s} = 30$ TeV, $\mathfrak{L}_{\texttt{int}}$=10 ab^{-1}
$C_{lq}^{(1)}/\Lambda^2$	-4.13×10^{-10}	-3.14×10^{-10}	-7.92×10^{-11}	-4.45×10^{-11}
$C_{lequ}^{(1)}/\Lambda^2$	-7.88×10^{-11}	-2.33×10^{-11}	-7.88×10^{-11}	-4.43×10^{-11}
$C_{lequ}^{(3)}/\Lambda^2$	14.93×10^{-11}	8.39×10^{-11}	2.81×10^{-11}	1.58×10^{-11}

Table 5.8: Values of vector ($C_{lq}^{(1)}/\Lambda^2$), scalar ($C_{lequ}^{(1)}/\Lambda^2$), and tensor ($C_{lequ}^{(3)}/\Lambda^2$) couplings at different CM energies and luminosities at 5σ separation.

5.5 Summary

In this chapter, we have explored the SMEFT operators that contribute to tc $(\bar{t}c + t\bar{c})$ production at colliders. The most significant contribution arises from the quark flavour violating four fermi operators. The other operator which provides modification to Ztc vertex has much less contribution at high CM energy and have thus been ignored in this analysis. Such four fermi operators contribute significantly to low energy flavour dependent processes and are thus heavily constrained by them. We study all such FCNC and FCCC processes including $b \to s(d)$ transitions, $P \to \ell\nu$, $K_L \to \mu\mu$, $B - \bar{B}$ mixing, top decays etc., to constrain the four fermi SMEFT operators. The most stringent bound arises on the tensor operator, having $C_{lelq}^{(3)}/\Lambda^2 \sim 10^{-11}$ GeV^{-2}, followed by scalar operator $C_{lelq}^{(3)}/\Lambda^2 \sim 10^{-10}$ GeV^{-2} and vector operator $C_{lq}^{(1)}/\Lambda^2 \sim 10^{-9}\ \mathrm{GeV}^{-2}$. We also predict observational sensitivities of the processes like $K_L \to \pi_0 \ell\ell$, $D_0 \to \mu\mu$, $t \to c\ell\ell$ and $t \to c\gamma$ from the obtained limits and show that they are consistent with the existing upper bounds.

Using these constraints, we have examined the future probe of these SMEFT operators at multi-TeV moun collider through tc $(\bar{t}c + t\bar{c})$ production. The required CM energy is 10 TeV where the production cross-section is of the order of fb, respecting EFT constraint $\Lambda > \sqrt{s}$. Given the high CM energy, the process basically yields dijet final state (a 'top' jet and a 'charm' jet) with no leptons stemming from the top decay. There is apparently a little chance of tagging them as well, which incorporates several SM backgrounds. There exists very little number of variables at disposal to segregate the signal from background, amongst which invariant di-jet mass and invariant mass of the heavy jet plays an important role to achieve a satisfactory signal significance for vector and scalar operator benchmarks in particular, at high luminosity 1 ab^{-1}.

Using OOT, we have determined the optimal uncertainties of the vector, scalar and tensor type SMEFTs at the benchmarks respecting flavour constraints. We see that at 10 TeV CM energy muon collider with 1 ab^{-1} integrated luminosity optimal uncertainty of the effective C/Λ^2 is better than the flavor uncertainty. Relative contribution between NP signal and non-interfering SM background play an important role in NP estimation, the less the background, the better the estimation. The dependence of the uncertainty on the CM energy and luminosity has also been compared and the advantages of CM energy to estimate optimal uncertainty pertaining to EFT limit is discussed. Considering SM as a base model, distinction of different operators from SM has also been studied. We have observed that at 10 TeV CM energy, 30 fb^{-1} luminosity is required to segregate (at 5 σ level) vector ($\mathcal{O}_{lq}^{(1)}$) operators from the SM, whereas for scalar ($\mathcal{O}_{lequ}^{(1)}$) and tensor ($\mathcal{O}_{lequ}^{(3)}$) operators we need 155 fb^{-1} and 18 ab^{-1} integrated luminosity, respectively, after obeying flavour constraints.

Chapter 6

OOT with non-interfering SM background: Example 2

Contents

6.1 Introduction

In this chapter we again explore the optimal estimation of NP couplings in presence of non-interfering SM backgrounds. However, here our approach will be much more generic. In previous analyses, an analytical expression for a hard process is obtained followed by the introduction of an efficiency factor to mimic the final signal after experimental cuts and branching ratios. The same methodology was used in the previous chapter for SM backgrounds. Unfortunately this approximation is not always reliable, nor can it be systematically improved. In order to sidestep these problems we develop a straightforward numerical procedure for calculating covariance matrix including all final-state effects and experimental cuts without approximation (beyond those involved in the numerical calculations), and which can be applied in any reaction irrespective of the strength of the SM background, and in any collider environment. This numerical procedure has already been discussed in Section 2.2.3, which we use here. In collider experiments, a realistic comparison of the confidence regions obtained using the likelihood function and the OOT approach must include all relevant SM background contributions, which can significantly affect the results. The main goal of this chapter is to provide such a realistic comparison, to use these results to gauge how close are the results obtained using the standard likelihood technique to the optimal ones, and to provide a tool to determine the collider parameters (such as beam polarization) that can enhance the sensitivity to a specific type of NP; upcoming e^+e^- colliders will serve as precision machines, where the analysis is best suited.

6.2 Signal background analysis

We illustrate the method using a simple model where the NP consists of heavy charged and neutral fermions, $\psi^{\pm}$ and ψ_1, respectively, having $\psi_1\psi^{\pm}W^{\mp}$ coupling. These particles appear in extensions of the SM with a fermion isodoublet $\Psi = (\psi^0, \psi^-)^T$ having hypercharge $Y_\Psi = -1$ and a singlet χ, specifically in a vector-like singlet-doublet model [151], providing a viable DM in the form of ψ_1, when they are stabilized by a $\mathbb{Z}_2$ symmetry (see Section 3.5). Here we take on a purely phenomenological approach, considering $\psi^{\pm}$ to have general chiral couplings to the Z boson parameterized by two NP couplings, a and b, but minimal coupling to photon [275],

$$\psi^+\psi^- Z : -\frac{ie_0}{2s_w c_w}\gamma^\mu\left(a + b\gamma^5\right) \;,\; \psi^+\psi^-\gamma : -\, ie_0\gamma^\mu . \tag{6.1}$$

We now calculate the optimal (*i.e.* minimal) statistical uncertainty when measuring the NP couplings a, b in the pair production of $\psi^{\pm}$ (with their subsequent decays) at an e^+e^- collider (see Fig. 3.1):

$$e^+e^- \to \psi^+\psi^- \to W^+W^-\psi_1\bar{\psi}_1 \;,\; W \to \ell\nu\, . \tag{6.2}$$

with $\ell = e, \mu$. We assume the $\psi_1\bar{\psi}_1$ are assumed to be stable DM candidates that escapes detection, so that the signal consists of missing energy $\not{E}$ plus opposite sign dileptons (OSL) [1]. We include all possible 2-body and 3-body SM backgrounds: $e^+e^- \to WW$, ZZ, $\mu\mu$, $\tau\tau$, WWZ, $\ell\ell Z$, with the subsequent leptonic decays of the W, Z and τ. We sum over e and μ final states. In order to suppress the backgrounds we impose thee following cuts [2]:

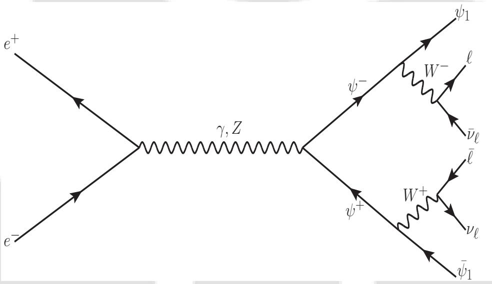

Figure 6.1: Pair-production of heavy charged fermions ($\psi^+\psi^-$) and their subsequent decay at an e^+ e^- collider.

- $\mathcal{C}_1$: $p_T^\ell > 10$ GeV, $N_{\texttt{lep}} = 2$, $|m_{\ell\ell} - m_Z| > 15$ GeV and $\Delta R_{\ell\ell} < 3.0$,
- $\mathcal{C}_2$: $\not{E} > 325$ GeV.

where $N_{\texttt{lep}}$ is the number of light charged leptons in the final state, $m_{\ell\ell}$ the invariant mass of the two final charged leptons, and $\Delta R_{\ell\ell}$ is the angular seperation between two opposie sign leptons. $\mathcal{C}_1$ reduces the (dominant) W background, while $\mathcal{C}_2$ suppresses the Z, μ and τ backgrounds; see Fig. 6.2.

---

[1] A similar analysis has been done in [275], but without including the SM background.

[2] The ideal choice of cuts (those that minimize the area of the 1σ regions) are model-dependent; we will not study here the optimization of such cuts, restricting ourselves to reasonable choices based on physical considerations.

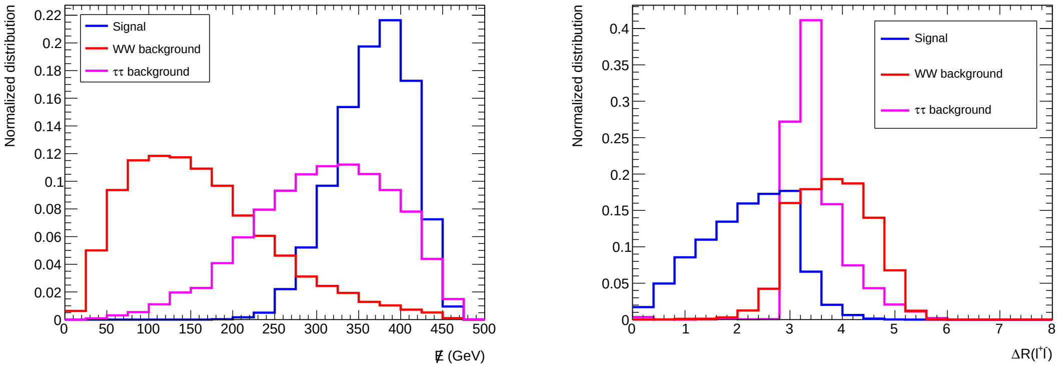

Figure 6.2: Normalized $\not\!\!E$ distribution (left) and $\Delta R(\ell^+\ell^-)$ (right) for signal and dominating backgrounds of the reaction in Fig. 3.1; see text for details. We assumed $\sqrt{s} = 500$ GeV, $m_{\psi^\pm} = 210$ GeV (consistent with LEP bound [126]) and $m_{\psi_1} = 60$ GeV.

Processes	Production cross-section (fb)		Number of events after final cuts	
	$P_{e^\pm} = ^{-30\%}_{+80\%}$	$P_{e^\pm} = ^{+30\%}_{-80\%}$	$P_{e^\pm} = ^{-30\%}_{+80\%}$	$P_{e^\pm} = ^{+30\%}_{-80\%}$
$a^0 = 1, b^0 = 0$	5.2	55.7	4791	50832
$a^0 = 0, b^0 = 1$	19.6	20.4	17685	18479
$a^0 = 1, b^0 = 1$	7.0	58.2	6457	53250
WW	51	798	1558	18030
$\tau\tau/\mu\mu$	57	68	286	360
ZZ	8.8	18.9	21	44
$\nu\nu Z$	3.4	50	72	1190
$\ell\ell Z$	16.5	22.4	18	4
WWZ	0.063	0.87	21	248

Table 6.1: Production cross sections with $\mathcal{C}_1$ imposed, and final event numbers after cuts $\mathcal{C}_1 + \mathcal{C}_2$, for signal and background contributions to the reaction in Fig. 3.1. We took CM energy $\sqrt{s} = 500$ GeV, integrated luminosity $\mathfrak{L}_{\tt int} = 2000\ \text{fb}^{-1}$ and two polarization choices; we assumed $m_{\psi^\pm} = 210$ GeV and $m_{\psi_1} = 60$ GeV.

We now determine the accuracy to which a and b can be measured, assuming these couplings have one of the following seed values: • $a^0 = 0$, $b^0 = 1$ (pure axial coupling), • $a^0 = 1$, $b^0 = 0$ (pure vector coupling), • $a^0 = 1$, $b^0 = 1$ (chiral coupling).

We list in Table 6.1 the results for both signal and background event numbers, and the corresponding production cross sections (note that for this reaction there is no SM-DM interference); the results illustrate the effectiveness of the cuts imposed in reducing the background, and also the effects of the beam polarization. We assumed the the CM collider energy is $\sqrt{s} = 500$ GeV and an integrated luminosity of $\mathfrak{L}_{\tt int} =$

$2000\,\text{fb}^{-1}$, and took $m_{\psi^\pm} = 210\,\text{GeV}$, $m_{\psi_1} = 60\,\text{GeV}$.

The choice of beam polarization plays a crucial role in optimizing signal to noise ratio, that in turn helps in reducing the uncertainty of the coupling estimates. For example, the choice $P_{e^\pm} = ^{+30\%}_{-80\%}$ (consistent with the ILC design [102]), increases the signal cross-section when $a^0 = 1,\ b^0 = 0$ (it also increases the WW background, but this is suppressed by $\mathcal{C}_2$); this results in smaller uncertainties than those obtained using unpolarized beams. For $a^0 = 0, b^0 = 1$ the choice $P_{e^\pm} = ^{-30\%}_{+80\%}$ enhances the signal cross-section, and also suppresses the WW background.

6.3 1σ regions

The optimal 1σ regions, dictated by Eq. (2.47), for the above three choices of $\{a^0,\ b^0\}$ begin considered are shown in the Fig. 6.3, for the signal-only with $\mathcal{C}_1$ and $\mathcal{C}_2$ imposed (green), for the full signal+background after applying $\mathcal{C}_1$ only (light red), and for the full signal+background after applying $\mathcal{C}_1$ and $\mathcal{C}_2$ (blue); this illustrates the degradation of the (optimal) precision to which the NP parameters can be estimated once the background is included (a feature absent in several previous analyses that used the OOT).

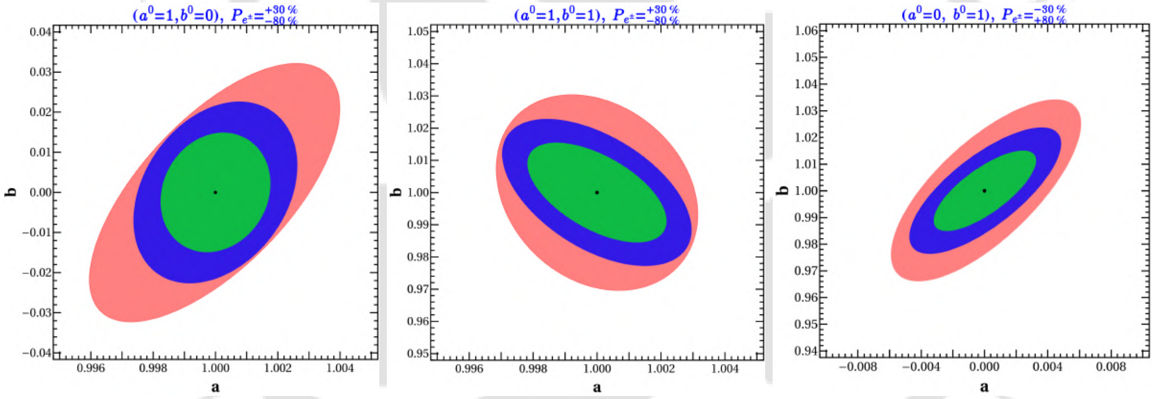

Figure 6.3: 1σ surfaces for different hypotheses, $a^0 = 1, b^0 = 0$ (left), $a^0 = 1, b^0 = 1$ (middle) and $a^0 = 0, b^0 = 1$ (right) after implementation of cuts, $\mathcal{C}_1$ (light red), $\mathcal{C}_2$ (blue) as described in the text, and signal only case in green. All the relevant parameters are written in the caption.

It should be noted that the shape and orientation of the $\chi^2_{\text{t}} = 1$ ellipses has a complicated dependence on the NP parameters $a^0,\ b^0$, as well as on the polarization and the specific choices made for $\mathcal{C}_{1,2}$. These features cannot be mimicked using an efficiency factor multiplying the signal and background cross sections. Such a simplification is appropriate in cases where the background is ignorable, or when its cross section is approximately proportional to that of the signal, which is occurs only in a limited number of situations. In the general case, it is more accurate and reliable to follow the above procedure than the efficiency approximation.

In Fig. 6.4, we present a comparison of the the 1σ regions from both OOT and regular χ^2_{e} analyses for three different hypotheses listed above. The figures also provide a measure of the level of improvement needed in the regular χ^2_{e} analysis to reach the minimal uncertainties derived using the OOT; the reason the χ^2_{e} result is close to the optimal on for $a^0 = 0,\ b^0 = 1$ is that in this case the background is the smallest, whence the event distribution closely mimics the pure signal. This situation will re-

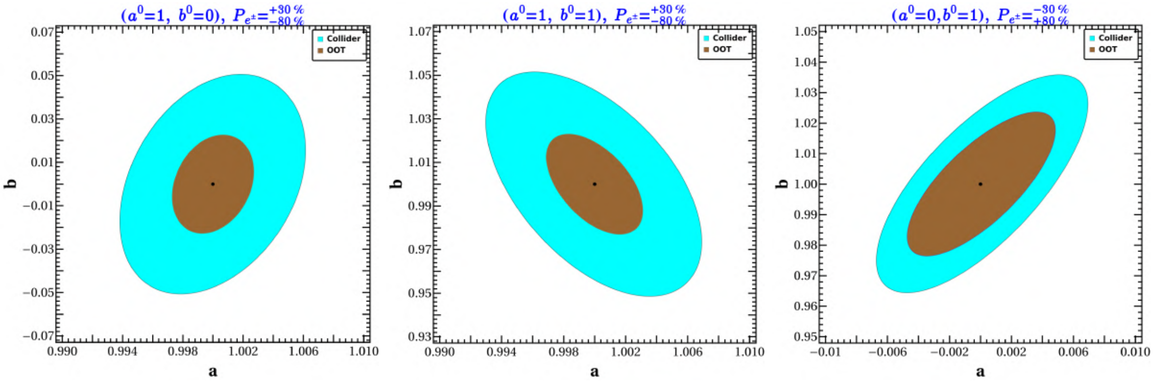

Figure 6.4: Comparison of 1σ regions between collider (cyan) and OOT (brown) for three different hypotheses mentioned at the caption.

peat in all cases where we have the signal dominates the background (after the cuts are imposed).

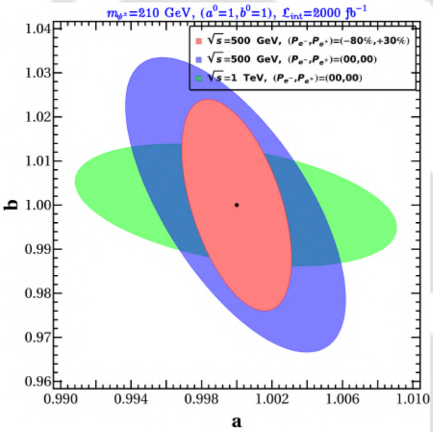

Figure 6.5: Comparison of 1σ surfaces for different CM energy and beam polarization.

It is worthwhile studying how the uncertainty and correlation of NP couplings depend on the CM energy and beam polarization. An illustrative example is presented in Fig. 6.5, from which we can infer that the covariance matrix can be strongly dependent on $\sqrt{s}$ (for this particular case, the uncertainty in b drops, while a enhances); while, as noted previously, the overall uncertainty can be significantly reduced by an appropriate choice of polarizations. The ability of the OOT to determine the effects that changes in both polarization and CM energy have on the precision to which NP parameters can be extracted provides a useful guide in in selecting future collider designs.

6.4 Summary

In this chapter, we have discussed the optimal precision of NP couplings in presence of non-interfering SM background in the most generic way. This approach allows a determination of the maximal statistical precision when measuring NP parameters in any given collider process, incorporating all experimental cuts and including all possible SM backgrounds in a numerical way, without worrying much about the analytical cross-sections of the processes. The results obtained provide a useful gauge of the degree of optimization reached by standard data analysis techniques, and of the effects of collider parameters, such as CM energy and beam polarization (when available) in the precision that can be reached. This last can be used to compare different collider proposals, for example, a $\mu^+\mu^-$ collider with relatively high CM energy, but no polarized beam, agains an e^+e^- collider of lower energy but with polarized beams. Finally, we reiterate that the approach here described is much preferable to the "efficiency approximation" where experimental cuts and branching ratios are mimicked by multiplying the hard cross sections by a fixed factor. This also enables us to apply the OOT technique for any collider environment and any kind of NP estimation.

Chapter 7

Summary and future prospects

Despite the tremendous success that the SM of particle physics has achieved, several theoretical and experimental outcomes suggest the existence of BSM physics, although no signal has been observed yet. It's therefore crucial to explore unique signals and innovative methods/experiments to search for NP. Thanks to the clean environment, upcoming lepton colliders stand out as highly promising instruments for identifying any hints of NP. Apart from the conventional binned analysis, powerful statistical techniques such as OOT, multivariate analysis, matrix element method, machine learning, etc., will play a pivotal role in pinpointing NP. In this thesis, we have explored the estimation of NP couplings for different BSM scenarios at future lepton colliders using OOT as well as binned analyses. The OOT methodology has been developed for three cases, when (i) signal is dominated by NP, (ii) SM interference dominates the signal, and (iii) non-interfering SM background is significant. We develop a numerical technique for the third case, hitherto unavailable in the literature.

After Introduction in Chapter 1 and a detailed discussion of OOT in Chapter 2, in Chapter 3, we have examined the optimal precision of NP couplings in the case of a BSM-dominated scenario. Here we considered pair-production of heavy charged fermions $\psi^{\pm}$ that couple to photon and Z boson. We parameterize the coupling with Z boson by a (vector) and b (axial-vector) couplings, assuming that to photon is known. Pair production of heavy $\psi^{\pm}$ at the e^+e^- collider by helicity amplitude technique have been calculated to employ OOT to estimate optimal estimation of NP parameters. It turns out that vector coupling is slightly easier to probe than axial vector coupling. The advantages of appropriate beam polarization have been highlighted. We also show that segregation of the NP cases from the base model (SM) is also possible at high luminosity. A UV complete model with a DM (singlet-doublet model) matches with a hypothesis ($a \sim 1, b = 0$), for which the detailed signal background analysis is done to find out the efficiency of the final signal (ϵ_s), after branching ratios and required cut effects, an important ingredient for OOT estimates.

Chapter 4 describes the estimation of NP couplings for SM domination in signal. We take up several examples of such kind. In Section 4.3 of this chapter, we have taken the process $e^+e^- \to Z\gamma$. Dominant SM contribution to this process arises from electron-mediated t-channel diagram and the BSM contribution stems from dimension-8 SMEFT operators. These dim-8 effective operators produce self-interaction between neutral gauge bosons. Optimal sensitivity of these dimension-8 nTGCs through mono-photon + missing energy final state signal. The correlation between CP-violating dimension-8 effective couplings has been studied as well. We have also drawn the comparison between optimal and binned sensitivity of dimension-8 nTGCs. In Section 4.4, we have discussed the statistical sensitivity of the same sets of dimension-8 nTGCs through ZZ production at the CLIC. This channel serves as a complementary search for dimension-8 nTGCs. This search in turn gives a complete picture of the understanding of nTGCs. In Section 4.5, we study top-quark pair production at the e^+e^- collider governed by photon and Z mediated s-channel diagrams along with scalar and tensor-mediated dim-6 four-Fermi operators via contact interaction. Considering di-lepton + di-bjet + missing energy as final state signal we have determined the optimal uncertainty of the NP couplings. Invariant di-lepton mass and invariant di-bjet mass are the useful observables for signal-background distinction. The scalar coupling turns easier to probe than the tensor one. For the sake of comparison, we have elaborated on the UV completion of the scalar-mediated operator where via flipped 2HDM model. We have also found out that the OOT is advantageous compared to binned analysis in the case of SM-dominated scenarios.

In Chapter 5, we have explored an example of OOT, where SM background turns important, but the ϵ approximation works. The methodology relies on the fact that the covariance matrix has an added non-interfering SM contribution, but the cut efficiencies do not alter the phase space orientation, just change the overall efficiency. This example explores the probing of flavor constraints on dimension-6 four-Fermi SMEFT operators contributing to tc production at the muon collider. We have FCNC transitions, FCCC transitions, particle anti-particle mixing, leptonic decay of pseudoscalar mesons, and top quark decays to constrain the corresponding effective couplings, which have been evaluated by performing simultaneous fits based on relevant observables. The most stringent constraint on dimension-6 effective couplings is on the order of 10^{-10} GeV^{-2}. Therefore, we need very high CM energy and high luminosity to probe these couplings. Muon collider at 10 TeV CM energy and 1 ab^{-1} integrated luminosity turns useful for that. At that high energy, the final state just presumes as di-jet events, so that one can use ϵ approximation after having both the signal and background. The optimal uncertainty of NP couplings provides a clear indication that vector-like couplings have less uncertainty than scalar and tensor ones. We have also shown that optimal sensitivity turns more precise than flavour uncertainties.

In Chapter 6 we finally study the optimal uncertainty of NP couplings in presence of non-interfering SM backgrounds in the most generic and elegant way. Instead of using the efficiency factors for signal and background processes, we propose to use final state events including background in bins to estimate the optimal covariance matrix. The methodology has been elaborated again with the same model as in Chapter 3 via opposite sign lepton (`OSL`) + missing energy to estimate the Z couplings of the heavy charged fermions at the e^+e^- collider. A comparison has been drawn between CM energy and luminosity to estimate the sensitivity of NP couplings. Optimal sensitivity is compared with the usual binned analysis in presence of non-interfering backgrounds and turns better, significantly when the NP contribution is large, marginal when the NP contribution is weaker. But most importantly, the methodology enables us to use OOT in the context of any NP signal in presence of any SM backgrounds and in the context of any collider environment.

In summary, we thus have discussed several NP scenarios to be explored in the future LCs. At 500 GeV ILC, Z coupling of heavy charged fermions and singly charged scalar particles in multi-Higgs models are explored; CLIC with 3 TeV demonstrates superior sensitivity to nTGCs via $Z\gamma$ and ZZ productions (compared to LHC). The discovery potential of the models is subject to several conditions. For example, the beam polarization facility of ILC will be super useful in probing the heavy vector like fermion, or scalar couplings, to suppress the SM background contribution in particular. The relative precision by which the NP couplings can be extracted depend further on the production cross-section, more importantly the NP contribution to the signal. In this way, fermion couplings are easier to probe than the scalar ones. Also the vector like couplings are easier to probe than the axial vector ones. On the other hand, seeing the requirement of heavy NP, one requires high CM energy as accessible in muon collider. For example, flavour violating operators after stringent flavor constraints, $c/\Lambda^2 \sim O(10^{-10})\ \mathrm{GeV}^{-2}$, requires 10 TeV muon collider for probing.

The analyses put up in this thesis show the usefulness of OOT in guiding which kind of NP can be estimated well and how it depends on the interfering and non-interfering SM contributions. This brings out how and when beam polarization does play more important role than CM energy or luminosity, or otherwise. We also do compare the standard likelihood analysis to OOT to show when they do similar, and where there is a significant distinction between them. Apart, the results of the individual NP cases also turn important, be it the charged fermions (or scalars), nTGCs, or top quark pair production. There are several examples still left to be explored. For example, the trilinear Higgs coupling (λ_{hhh}), plays a pivotal role in elucidating the configuration of the Higgs potential. One immediate goal is to estimate the optimal sensitivity of this coupling at future colliders. Another interesting task is to measure the sensitivity of DM-SM couplings at future colliders via mono-X ($X = \gamma, Z, j$) + missing energy signal. The same needs to be done in the context of Axion and axion-like particles (ALPs) as well. It is also important to compare it with other statistical methods like multivariate analysis [276–279], matrix element methods [280–283] etc., which we plan to take up next.

Appendix **A**

Appendix

A.1 Optimal Analysis with other CM energies

In this appendix, we repeat the analysis of Section 3.4 for both lower and higher CM energies and different charged-fermion masses. The results are presented in Fig. A.1: optimal 1σ regions for $\sqrt{s} = 250$ GeV, $m_{\psi^\pm} = 110$ GeV (left column), and $\sqrt{s} = 2$ TeV, $m_{\psi^\pm} = 900$ GeV (right column). Note that as $m_{\psi^\pm}$ and $\sqrt{s}$ increase the cross-section drops (Drell-Yann process falls like $\sim 1/\sqrt{s}$, see Eq. (3.7)) and the eigenvalues of the covariance matrix increase (since $V^{-1} \sim M \sim 1/\sigma$, *cf.* Eq. (2.26) and (2.47)); the 1σ regions are corresponding larger. The two cases where $a, b \neq 0$, the 1σ regions are very asymmetric because the probability distribution of NP couplings are heavily distorted from the normal distribution.

A.2 χ^2 ellipsoids in g_i plane

If the g_i are taken as the NP parameters, then the $\chi^2 = 1$ regions become ellipsoids in this space, as illustrated in Fig. A.2 for two examples. In general V_0 is not diagonal, so that the g_i's are correlated, however, one can always choose alternative coefficients, linear combinations of the g_i, which are uncorrelated and whose (1σ) statistical uncertainties equal the square-root of the eigenvalues of V_0. That is, if $g_i = R_{ij}\tilde{g}_i$, one can always find R orthogonal which diagonalizes V_0, whence (Eq. (2.47)) becomes $\chi^2 = \epsilon \sum(\delta\tilde{g}_i)^2/\bar{V}_0^i$, where the eigenvalues of V_0 are denoted by $\bar{V}_0^i$ and $\delta\tilde{g}_i$ is the statistical uncertainty of the $\bar{g}_i$. An example is given in Table A.1 and corresponding 1σ ellipsoids are shown in Fig. A.2.

	Uncertainties $\times 10^{-6}$ ($\epsilon = 0.001$)			Uncertainties $\times 10^{-6}$ ($\epsilon = 0.005$)		
Seed parameters $\times 10^{-5}$	$\lvert\delta\tilde{g}_1\rvert$	$\lvert\delta\tilde{g}_2\rvert$	$\lvert\delta\tilde{g}_3\rvert$	$\lvert\delta\tilde{g}_1\rvert$	$\lvert\delta\tilde{g}_2\rvert$	$\lvert\delta\tilde{g}_3\rvert$
$g_1^0 = g_2^0 = 1;\ g_3^0 = 1$	1.07	18.40	179.06	0.48	8.23	80.07
$g_1^0 = g_2^0 = 1;\ g_3^0 = -1$	1.06	18.18	177.16	0.47	8.13	79.23

Table A.1: 1σ statistical uncertainties for the uncorrelated parameters $\tilde{g}_i$ (see text) for the indicated seed parameters and efficiencies; we assume unpolarized beams.

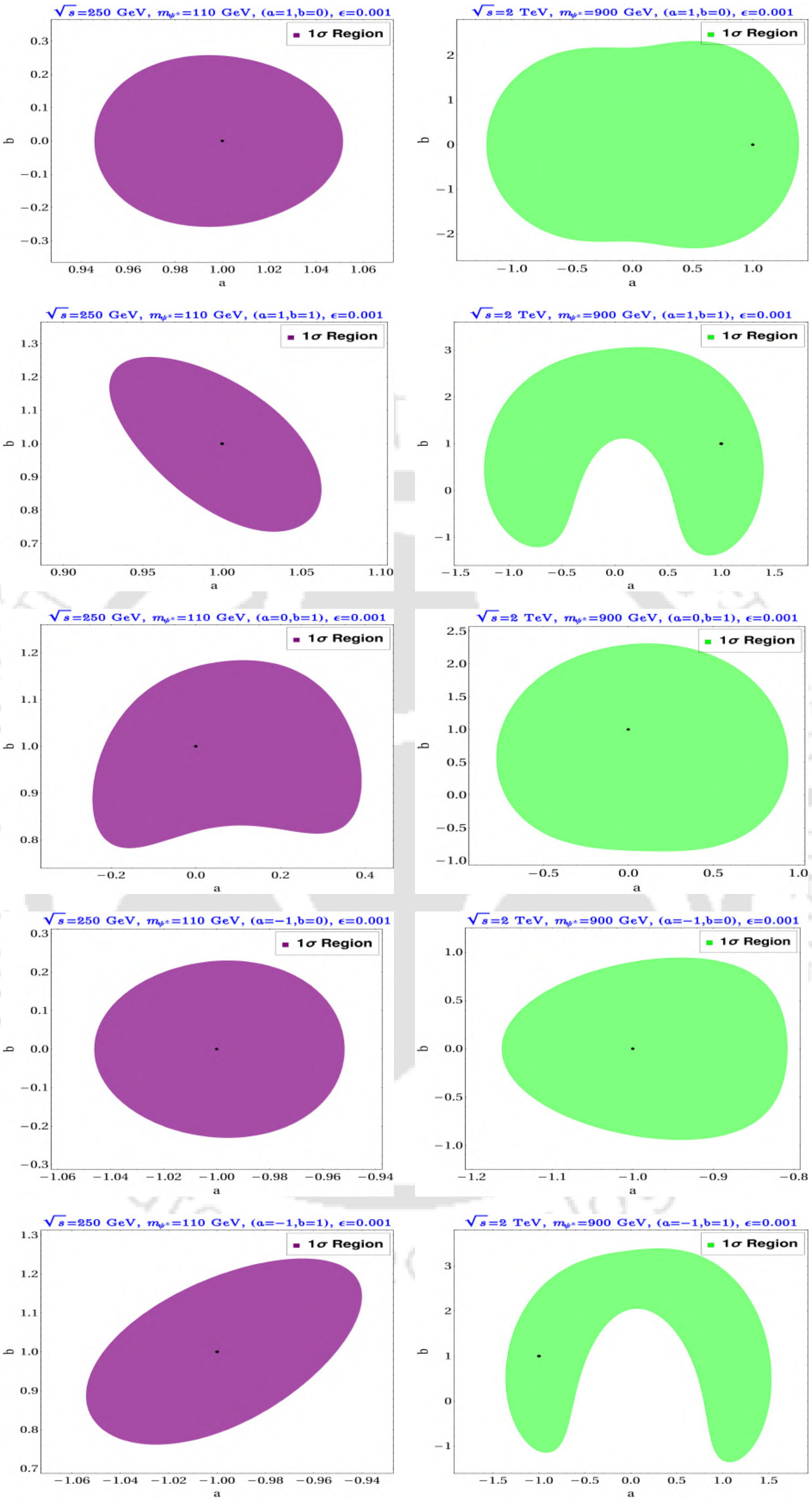

Figure A.1: $\chi^2 \leq 1$ regions for unpolarized beams. Left column: $\sqrt{s} = 250$ GeV and $m_{\psi^\pm} = 110$ GeV; right column: $\sqrt{s} = 2$ TeV and $m_{\psi^\pm} = 900$ GeV.

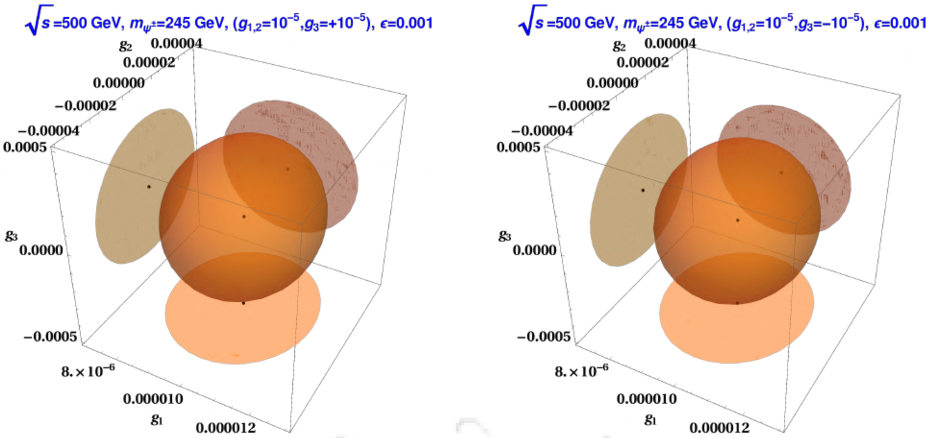

Figure A.2: $\chi^2 = 1$ ellipsoids in g_i space for $g^0_{1,2} = 10^{-5}$, $g^0_3 = \pm 10^{-5}$ and unpolarized beams. The 2-dimension projections are also drawn.

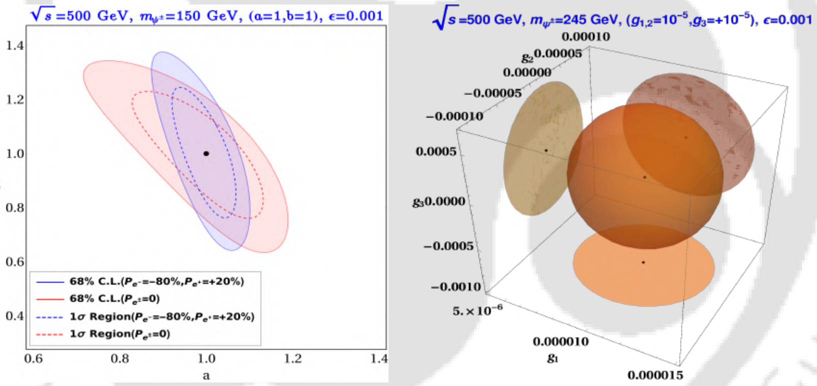

Figure A.3: 68.3% C.L. in two-parameter and three-parameter distributions; $\chi^2 \leq 2.3$ (left) for $a - b$ plane for $(a = 1, b = 1)$ case (with dotted lines denoting 1σ surfaces) and $\chi^2 \leq 3.5$ (right) for $g_i = 10^{-5}$ $(i = 1, 2, 3)$.

A.3 68.3% C.L. in two-parameter and three-parameter distributions

For $n = 2\,(3)$ parameter, a 68.3% C.L. corresponds to $\chi^2 = 2.3\,(3.5)$. The 68.3% C.L. contours are plotted in Fig. A.3 when $a^0 = b^0 = 1$ (left panel) and for $g^0_i = 10^{-5}$ (right panel); a comparison with the $\chi^2 \leq 1$ region is also provided. It is quite evident that 68.3% C.L. regions are larger than 1σ surfaces.

A.4 Loop function for $B_q - \overline{B}_q$ mixings and amplitudes of $t \to b\ell\nu$

- Loop function:

$$\mathtt{DiscB}(\mathtt{a},\mathtt{b},\mathtt{c}) = \frac{1}{\mathrm{a}}\lambda(\mathrm{a},\mathrm{b}^2,\mathrm{c}^2)\mathrm{Log}\left[\frac{-\mathrm{a}+\mathrm{b}^2+\mathrm{c}^2+\sqrt{\lambda(\mathrm{a},\mathrm{b}^2,\mathrm{c}^2)}}{2\mathrm{bc}}\right], \tag{A.1}$$

where $\lambda(x,y,z) = x^2 + y^2 + z^2 - 2(xy + yz + zx)$.

- $t \to b\ell\nu_\ell$ decay: The SM and BSM contributions to the $t(p) \to b(k)\ell(k_1)\nu(k_2)$ decay amplitude are written as

$$\begin{aligned}
\mathcal{M}^t_{\mathtt{SM}} =& \frac{g^2}{2\sqrt{2}((q^2 - m_W^2) + i\Gamma_W m_W)}\bar{u}(k)\gamma^\mu P_L u(p)\bar{u}(k_2)\gamma^\mu P_L v(k_1), \\
\mathcal{M}^t_{\mathtt{NP}} =& -\frac{C^{(3)}_{lq}}{\Lambda^2}\bar{u}(k)\gamma^\mu P_L u(p)\bar{u}(k_2)\gamma^\mu P_L v(k_1), \\
&+ \frac{C^{(1)}_{lequ}}{\Lambda^2}\left(\bar{u}(k_1)P_R v(k_2)\right)\left(\bar{v}(p_2)P_R u(p_1)\right), \\
&+ \frac{C^{(3)}_{lequ}}{\Lambda^2}\left(\bar{u}(k_1)\sigma^{\mu\nu}P_R v(k_2)\right)\left(\bar{v}(p_2)\sigma_{\mu\nu}P_R u(p_1)\right).
\end{aligned} \tag{A.2}$$

A.5 Renormalization Group (RG) Equations

The renormalization group equations of the relevant SMEFT couplings are written as [284]

$$\frac{dC_i}{d\ln\mu} = \frac{1}{16\pi^2}\beta_i, \tag{A.3}$$

where $C_i = \left\{C_{lq}^{(1)}/\Lambda^2, C_{lequ}^{(1)}/\Lambda^2, C_{lequ}^{(3)}/\Lambda^2\right\}$ are the SMEFT coefficients and $\beta_i = \{\beta_{lq}^{(1)}, \beta_{lequ}^{(1)}, \beta_{lequ}^{(3)}\}$ are the respective 1-loop β functions of the SMEFT operators. The β functions are:

$$
\begin{aligned}
\left[\beta_{lq}^{(1)}\right]_{\mu\mu tc} &= \frac{2}{3}g'^2\left[\frac{C_{lq}^{(1)}}{\Lambda^2}\right]_{wwtc}\delta_{\mu\mu} - g'^2\left[\frac{C_{lq}^{(1)}}{\Lambda^2}\right]_{\mu\mu tc} + [\gamma_q]_{tw}\left[\frac{C_{lq}^{(1)}}{\Lambda^2}\right]_{\mu\mu wc} + \left[\frac{C_{lq}^{(1)}}{\Lambda^2}\right]_{\mu\mu tw}[\gamma_q]_{wc}\,,\\
&= \left(g'^2 + \frac{1}{2}y_t^2\right)\left[\frac{C_{lq}^{(1)}}{\Lambda^2}\right]_{\mu\mu tc}\,,\\
\left[\beta_{lequ}^{(1)}\right]_{\mu\mu tc} &= -\left(\frac{11}{3}g'^2 + 8g_S^2\right)\left[\frac{C_{lequ}^{(1)}}{\Lambda^2}\right]_{\mu\mu tc} + [\gamma_q]_{tv}\left[\frac{C_{lequ}^{(1)}}{\Lambda^2}\right]_{\mu\mu vc} + [\gamma_u]_{vc}\left[\frac{C_{lequ}^{(1)}}{\Lambda^2}\right]_{\mu\mu tv}\\
&= -\left(\frac{11}{3}g'^2 + 8g_S^2 - \frac{1}{2}y_t^2\right)\left[\frac{C_{lequ}^{(1)}}{\Lambda^2}\right]_{\mu\mu tc}\,,\\
\left[\beta_{lequ}^{(3)}\right]_{\mu\mu tc} &= -\left(\frac{2}{9}g'^2 - 3g^2 + \frac{8}{3}g_S^2\right)\left[\frac{C_{lequ}^{(3)}}{\Lambda^2}\right]_{\mu\mu tc} + [\gamma_q]_{tv}\left[\frac{C_{lequ}^{(3)}}{\Lambda^2}\right]_{\mu\mu vc} + [\gamma_u]_{vc}\left[\frac{C_{lequ}^{(3)}}{\Lambda^2}\right]_{\mu\mu tv}\,,\\
&= -\left(\frac{2}{9}g'^2 - 3g^2 + \frac{8}{3}g_S^2 - \frac{1}{2}y_t^2\right)\left[\frac{C_{lequ}^{(3)}}{\Lambda^2}\right]_{\mu\mu tc}\,.
\end{aligned}
\tag{A.4}
$$

Here $\gamma_q = \frac{1}{2}\left(y_u y_u^\dagger + y_d y_d^\dagger\right)$ and $\gamma_u = \left(y_u y_u^\dagger\right)$. We consider, $y_u = y_d = 0$ except for y_t. The RGEs for the Standard Model parameters are noted below:

$$
\begin{aligned}
\frac{dg}{d\ln\mu} &= \frac{1}{16\pi^2}\left(-\frac{19}{6}g^3\right),\\
\frac{dg'}{d\ln\mu} &= \frac{1}{16\pi^2}\left(\frac{41}{6}g'^3\right),\\
\frac{dg_S}{d\ln\mu} &= \frac{1}{16\pi^2}\left(-7g_S^2\right),\\
\frac{dy_t}{d\ln\mu} &= \frac{y_t}{16\pi^2}\left(\frac{9}{4}g^2 - \frac{17}{12}g'^2 - 8g_S^2 + \frac{9}{2}y_t^2\right).
\end{aligned}
\tag{A.5}
$$

Utilizing the aforementioned equations, we illustrate the evolution of dimension-six vector ($C_{lq}^{(1)}/\Lambda^2$), scalar ($C_{lequ}^{(1)}/\Lambda^2$), and tensor ($C_{lequ}^{(3)}/\Lambda^2$) couplings with the energy scale ranging from 1 GeV to 10 TeV. This representation is depicted in Fig. A.4, taking into account the flavor inputs as noted in Table 5.1 and 5.2.

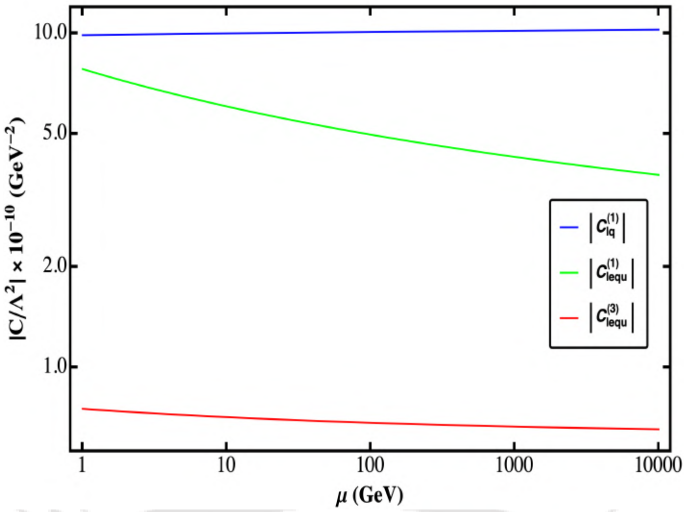

Figure A.4: RG running for dimension-six vector ($C_{lq}^{(1)}/\Lambda^2$), scalar ($C_{lequ}^{(1)}/\Lambda^2$), and tensor ($C_{lequ}^{(3)}/\Lambda^2$) couplings.

Bibliography

[1] P. W. Higgs, *Broken Symmetries and the Masses of Gauge Bosons*, *Phys. Rev. Lett.* **13** (1964) 508.

[2] F. Englert and R. Brout, *Broken Symmetry and the Mass of Gauge Vector Mesons*, *Phys. Rev. Lett.* **13** (1964) 321.

[3] G. S. Guralnik, C. R. Hagen and T. W. B. Kibble, *Global Conservation Laws and Massless Particles*, *Phys. Rev. Lett.* **13** (1964) 585.

[4] P. W. Higgs, *Spontaneous Symmetry Breakdown without Massless Bosons*, *Phys. Rev.* **145** (1966) 1156.

[5] T. W. B. Kibble, *Symmetry breaking in nonAbelian gauge theories*, *Phys. Rev.* **155** (1967) 1554.

[6] ATLAS collaboration, *Observation of a new particle in the search for the Standard Model Higgs boson with the ATLAS detector at the LHC*, *Phys. Lett. B* **716** (2012) 1 [`1207.7214`].

[7] CMS collaboration, *Observation of a New Boson at a Mass of 125 GeV with the CMS Experiment at the LHC*, *Phys. Lett. B* **716** (2012) 30 [`1207.7235`].

[8] P. Grange', J.-F. Mathiot, B. Mutet and E. Werner, *Aspects of fine-tuning of the Higgs mass within finite field theories*, *Phys. Rev. D* **88** (2013) 125015 [`1312.5278`].

[9] K. G. Begeman, A. H. Broeils and R. H. Sanders, *Extended rotation curves of spiral galaxies: Dark haloes and modified dynamics*, *Mon. Not. Roy. Astron. Soc.* **249** (1991) 523.

[10] D. Clowe, M. Bradac, A. H. Gonzalez, M. Markevitch, S. W. Randall, C. Jones et al., *A direct empirical proof of the existence of dark matter*, *Astrophys. J. Lett.* **648** (2006) L109 [`astro-ph/0608407`].

[11] J. R. Primack, *Dark matter and structure formation*, in *Midrasha Mathematicae in Jerusalem: Winter School in Dynamical Systems*, 7, 1997, `astro-ph/9707285`.

[12] Planck collaboration, *Planck 2013 results. XVI. Cosmological parameters*, *Astron. Astrophys.* **571** (2014) A16 [`1303.5076`].

[13] Planck collaboration, *Planck 2018 results. VI. Cosmological parameters*, *Astron. Astrophys.* **641** (2020) A6 [`1807.06209`].

[14] Super-Kamiokande collaboration, *Constraints on neutrino oscillations using 1258 days of Super-Kamiokande solar neutrino data*, *Phys. Rev. Lett.* **86** (2001) 5656 [`hep-ex/0103033`].

[15] SNO collaboration, *Direct evidence for neutrino flavor transformation from neutral current interactions in the Sudbury Neutrino Observatory*, *Phys. Rev. Lett.* **89** (2002) 011301 [`nucl-ex/0204008`].

[16] KamLAND collaboration, *Precision Measurement of Neutrino Oscillation Parameters with KamLAND*, *Phys. Rev. Lett.* **100** (2008) 221803 [`0801.4589`].

[17] P. Minkowski, *$\mu \to e\gamma$ at a Rate of One Out of 10^9 Muon Decays?*, *Phys. Lett. B* **67** (1977) 421.

[18] R. N. Mohapatra and G. Senjanovic, *Neutrino Mass and Spontaneous Parity Nonconservation*, *Phys. Rev. Lett.* **44** (1980) 912.

[19] J. Schechter and J. W. F. Valle, *Neutrino Masses in SU(2) x U(1) Theories*, *Phys. Rev. D* **22** (1980) 2227.

[20] T. P. Cheng and L.-F. Li, *Neutrino Masses, Mixings and Oscillations in SU(2) x U(1) Models of Electroweak Interactions*, *Phys. Rev. D* **22** (1980) 2860.

[21] R. N. Mohapatra and G. Senjanovic, *Neutrino Masses and Mixings in Gauge Models with Spontaneous Parity Violation*, *Phys. Rev. D* **23** (1981) 165.

[22] R. Foot, H. Lew, X. G. He and G. C. Joshi, *Seesaw Neutrino Masses Induced by a Triplet of Leptons*, *Z. Phys. C* **44** (1989) 441.

[23] E. Ma, *Pathways to naturally small neutrino masses*, *Phys. Rev. Lett.* **81** (1998) 1171 [`hep-ph/9805219`].

[24] I. Esteban, M. C. Gonzalez-Garcia, M. Maltoni, T. Schwetz and A. Zhou, *The fate of hints: updated global analysis of three-flavor neutrino oscillations*, *JHEP* **09** (2020) 178 [`2007.14792`].

[25] Planck collaboration, *Planck 2018 results. VI. Cosmological parameters*, *Astron. Astrophys.* **641** (2020) A6 [`1807.06209`].

[26] E. W. Kolb and M. S. Turner, *The Early Universe*, vol. 69. 1990, 10.1201/9780429492860.

[27] M. Trodden, *Electroweak baryogenesis*, *Rev. Mod. Phys.* **71** (1999) 1463 [`hep-ph/9803479`].

[28] A. D. Sakharov, *Violation of CP Invariance, C asymmetry, and baryon asymmetry of the universe*, *Pisma Zh. Eksp. Teor. Fiz.* **5** (1967) 32.

[29] M. Fukugita and T. Yanagida, *Baryogenesis Without Grand Unification*, *Phys. Lett. B* **174** (1986) 45.

[30] A. Pilaftsis and T. E. J. Underwood, *Resonant leptogenesis*, *Nucl. Phys. B* **692** (2004) 303 [`hep-ph/0309342`].

[31] V. A. Kuzmin, V. A. Rubakov and M. E. Shaposhnikov, *On the Anomalous Electroweak Baryon Number Nonconservation in the Early Universe*, *Phys. Lett. B* **155** (1985) 36.

[32] Muon g-2 collaboration, *Measurement of the Positive Muon Anomalous Magnetic Moment to 0.46 ppm*, *Phys. Rev. Lett.* **126** (2021) 141801 [`2104.03281`].

[33] LHCb collaboration, *Test of Lepton Flavor Universality by the measurement of the $B^0 \to D^{*-}\tau^+\nu_\tau$ branching fraction using three-prong τ decays*, *Phys. Rev. D* **97** (2018) 072013 [`1711.02505`].

[34] LHCb collaboration, *Test of lepton flavor universality using $B^0 \to D^{*-}\tau^+\nu_{tau}$ decays with hadronic τ channels*, *Phys. Rev. D* **108** (2023) 012018 [`2305.01463`].

[35] CMS, ATLAS collaboration, *Evidence for the Higgs boson decay to a Z boson and a photon at the LHC*, `2309.03501`.

[36] CMS collaboration, *Search for a standard model-like Higgs boson in the mass range between 70 and 110 GeV in the diphoton final state in proton-proton collisions at $\sqrt{s} = 8$ and 13 TeV*, *Phys. Lett. B* **793** (2019) 320 [`1811.08459`].

[37] S. Weinberg, *Nonabelian Gauge Theories of the Strong Interactions*, *Phys. Rev. Lett.* **31** (1973) 494.

[38] R. Jackiw and C. Rebbi, *Vacuum Periodicity in a Yang-Mills Quantum Theory*, *Phys. Rev. Lett.* **37** (1976) 172.

[39] N. S. Manton, *A New Six-Dimensional Approach to the Weinberg-Salam Model*, *Nucl. Phys. B* **158** (1979) 141.

[40] D. B. Fairlie, *Higgs' Fields and the Determination of the Weinberg Angle*, *Phys. Lett. B* **82** (1979) 97.

[41] Y. Hosotani, *Dynamical Mass Generation by Compact Extra Dimensions*, *Phys. Lett. B* **126** (1983) 309.

[42] Y. Hosotani, *Dynamics of Nonintegrable Phases and Gauge Symmetry Breaking*, *Annals Phys.* **190** (1989) 233.

[43] G. Isidori, G. Ridolfi and A. Strumia, *On the metastability of the standard model vacuum*, *Nucl. Phys. B* **609** (2001) 387 [`hep-ph/0104016`].

[44] J. Ellis, J. R. Espinosa, G. F. Giudice, A. Hoecker and A. Riotto, *The Probable Fate of the Standard Model*, *Phys. Lett. B* **679** (2009) 369 [`0906.0954`].

[45] S. Alekhin, A. Djouadi and S. Moch, *The top quark and Higgs boson masses and the stability of the electroweak vacuum*, *Phys. Lett. B* **716** (2012) 214 [`1207.0980`].

[46] P. Fayet, *Supergauge Invariant Extension of the Higgs Mechanism and a Model for the electron and Its Neutrino*, *Nucl. Phys. B* **90** (1975) 104.

[47] P. Fayet, *Supersymmetry and Weak, Electromagnetic and Strong Interactions*, *Phys. Lett. B* **64** (1976) 159.

[48] P. Fayet, *Spontaneously Broken Supersymmetric Theories of Weak, Electromagnetic and Strong Interactions*, *Phys. Lett. B* **69** (1977) 489.

[49] N. G. Deshpande and E. Ma, *Pattern of Symmetry Breaking with Two Higgs Doublets*, *Phys. Rev. D* **18** (1978) 2574.

[50] J. F. Donoghue and L. F. Li, *Properties of Charged Higgs Bosons*, *Phys. Rev. D* **19** (1979) 945.

[51] L. F. Abbott, P. Sikivie and M. B. Wise, *Constraints on Charged Higgs Couplings*, *Phys. Rev. D* **21** (1980) 1393.

[52] J. F. Gunion, H. E. Haber, G. L. Kane and S. Dawson, *The Higgs Hunter's Guide*, vol. 80. 2000.

[53] G. Bhattacharyya and D. Das, *Scalar sector of two-Higgs-doublet models: A minireview*, *Pramana* **87** (2016) 40 [`1507.06424`].

[54] F. Mahmoudi and O. Stal, *Flavor constraints on the two-Higgs-doublet model with general Yukawa couplings*, *Phys. Rev. D* **81** (2010) 035016 [`0907.1791`].

[55] A. Crivellin, A. Kokulu and C. Greub, *Flavor-phenomenology of two-Higgs-doublet models with generic Yukawa structure*, *Phys. Rev. D* **87** (2013) 094031 [`1303.5877`].

[56] M. A. Arroyo-Ureña, J. L. Diaz-Cruz, E. Díaz and J. A. Orduz-Ducuara, *Flavor violating Higgs signals in the Texturized Two-Higgs Doublet Model (THDM-Tx)*, *Chin. Phys. C* **40** (2016) 123103 [`1306.2343`].

[57] B. Altunkaynak, W.-S. Hou, C. Kao, M. Kohda and B. McCoy, *Flavor Changing Heavy Higgs Interactions at the LHC*, *Phys. Lett. B* **751** (2015) 135 [`1506.00651`].

[58] J. M. Alves, F. J. Botella, G. C. Branco, F. Cornet-Gomez and M. Nebot, *Controlled Flavour Changing Neutral Couplings in Two Higgs Doublet Models*, *Eur. Phys. J. C* **77** (2017) 585 [`1703.03796`].

[59] Z.-j. Tao, *Radiative seesaw mechanism at weak scale*, *Phys. Rev. D* **54** (1996) 5693 [`hep-ph/9603309`].

[60] E. Ma, *Verifiable radiative seesaw mechanism of neutrino mass and dark matter*, *Phys. Rev. D* **73** (2006) 077301 [`hep-ph/0601225`].

[61] J. McDonald, *Gauge singlet scalars as cold dark matter*, *Phys. Rev. D* **50** (1994) 3637 [`hep-ph/0702143`].

[62] H. Davoudiasl, R. Kitano, T. Li and H. Murayama, *The New minimal standard model*, *Phys. Lett. B* **609** (2005) 117 [`hep-ph/0405097`].

[63] G. Cacciapaglia and F. Sannino, *Fundamental Composite (Goldstone) Higgs Dynamics*, *JHEP* **04** (2014) 111 [`1402.0233`].

[64] S. Bhattacharya, P. Poulose and P. Ghosh, *Multipartite Interacting Scalar Dark Matter in the light of updated LUX data*, JCAP **04** (2017) 043 [1607.08461].

[65] C. E. Yaguna, *The Singlet Scalar as FIMP Dark Matter*, JHEP **08** (2011) 060 [1105.1654].

[66] Z. Kang, *View FImP miracle (by scale invariance) à la self-interaction*, Phys. Lett. B **751** (2015) 201 [1505.06554].

[67] A. Hietanen, R. Lewis, C. Pica and F. Sannino, *Fundamental Composite Higgs Dynamics on the Lattice: SU(2) with Two Flavors*, JHEP **07** (2014) 116 [1404.2794].

[68] N. Arkani-Hamed, S. Dimopoulos and G. R. Dvali, *The Hierarchy problem and new dimensions at a millimeter*, Phys. Lett. B **429** (1998) 263 [hep-ph/9803315].

[69] I. Antoniadis, N. Arkani-Hamed, S. Dimopoulos and G. R. Dvali, *New dimensions at a millimeter to a Fermi and superstrings at a TeV*, Phys. Lett. B **436** (1998) 257 [hep-ph/9804398].

[70] J. C. Pati and A. Salam, *Lepton Number as the Fourth Color*, Phys. Rev. D **10** (1974) 275.

[71] R. N. Mohapatra and J. C. Pati, *Left-Right Gauge Symmetry and an Isoconjugate Model of CP Violation*, Phys. Rev. D **11** (1975) 566.

[72] R. N. Mohapatra and J. C. Pati, *A Natural Left-Right Symmetry*, Phys. Rev. D **11** (1975) 2558.

[73] G. Senjanovic and R. N. Mohapatra, *Exact Left-Right Symmetry and Spontaneous Violation of Parity*, Phys. Rev. D **12** (1975) 1502.

[74] A. Davidson, *$B - L$ as the fourth color within an $\mathrm{SU}(2)_L \times \mathrm{U}(1)_R \times \mathrm{U}(1)$ model*, Phys. Rev. D **20** (1979) 776.

[75] R. N. Mohapatra and R. E. Marshak, *Local B-L Symmetry of Electroweak Interactions, Majorana Neutrinos and Neutron Oscillations*, Phys. Rev. Lett. **44** (1980) 1316.

[76] R. E. Marshak and R. N. Mohapatra, *Quark - Lepton Symmetry and B-L as the U(1) Generator of the Electroweak Symmetry Group*, Phys. Lett. B **91** (1980) 222.

[77] A. Masiero, J. F. Nieves and T. Yanagida, *$B^{-}l$ Violating Proton Decay and Late Cosmological Baryon Production*, Phys. Lett. B **116** (1982) 11.

[78] E. Ma, *Gauged B - 3L(tau) and radiative neutrino masses*, Phys. Lett. B **433** (1998) 74 [hep-ph/9709474].

[79] E. Ma and U. Sarkar, *Gauged B - 3L(tau) and baryogenesis*, Phys. Lett. B **439** (1998) 95 [hep-ph/9807307].

[80] L. N. Chang, O. Lebedev, W. Loinaz and T. Takeuchi, *Constraints on gauged B - 3 L(tau) and related theories*, Phys. Rev. D **63** (2001) 074013 [hep-ph/0010118].

[81] P. B. Pal and U. Sarkar, *Gauged B - 3L(tau), low-energy unification and proton decay*, *Phys. Lett. B* **573** (2003) 147 [`hep-ph/0306088`].

[82] X. G. He, G. C. Joshi, H. Lew and R. R. Volkas, *NEW Z-prime PHENOMENOLOGY*, *Phys. Rev. D* **43** (1991) 22.

[83] X.-G. He, G. C. Joshi, H. Lew and R. R. Volkas, *Simplest Z-prime model*, *Phys. Rev. D* **44** (1991) 2118.

[84] R. Foot, *New Physics From Electric Charge Quantization?*, *Mod. Phys. Lett. A* **6** (1991) 527.

[85] W. Buchmuller and D. Wyler, *Effective Lagrangian Analysis of New Interactions and Flavor Conservation*, *Nucl. Phys. B* **268** (1986) 621.

[86] B. Grzadkowski, M. Iskrzynski, M. Misiak and J. Rosiek, *Dimension-Six Terms in the Standard Model Lagrangian*, *JHEP* **10** (2010) 085 [`1008.4884`].

[87] L. Lehman, *Extending the Standard Model Effective Field Theory with the Complete Set of Dimension-7 Operators*, *Phys. Rev. D* **90** (2014) 125023 [`1410.4193`].

[88] C. W. Murphy, *Dimension-8 operators in the Standard Model Eective Field Theory*, *JHEP* **10** (2020) 174 [`2005.00059`].

[89] H.-L. Li, Z. Ren, J. Shu, M.-L. Xiao, J.-H. Yu and Y.-H. Zheng, *Complete set of dimension-eight operators in the standard model effective field theory*, *Phys. Rev. D* **104** (2021) 015026 [`2005.00008`].

[90] S. Weinberg, *Baryon and Lepton Nonconserving Processes*, *Phys. Rev. Lett.* **43** (1979) 1566.

[91] G. F. Giudice, C. Grojean, A. Pomarol and R. Rattazzi, *The Strongly-Interacting Light Higgs*, *JHEP* **06** (2007) 045 [`hep-ph/0703164`].

[92] K. Hagiwara, S. Ishihara, R. Szalapski and D. Zeppenfeld, *Low-energy effects of new interactions in the electroweak boson sector*, *Phys. Rev. D* **48** (1993) 2182.

[93] C. Arzt, M. B. Einhorn and J. Wudka, *Patterns of deviation from the standard model*, *Nucl. Phys. B* **433** (1995) 41 [`hep-ph/9405214`].

[94] S. Bhattacharya and J. Wudka, *Dimension-seven operators in the standard model with right handed neutrinos*, *Phys. Rev. D* **94** (2016) 055022 [`1505.05264`].

[95] Y. Liao, X.-D. Ma and Q.-Y. Wang, *Extending low energy effective field theory with a complete set of dimension-7 operators*, *JHEP* **08** (2020) 162 [`2005.08013`].

[96] Y. Liao and X.-D. Ma, *An explicit construction of the dimension-9 operator basis in the standard model effective field theory*, *JHEP* **11** (2020) 152 [`2007.08125`].

[97] T. Cohen, N. Craig, X. Lu and D. Sutherland, *Is SMEFT Enough?*, *JHEP* **03** (2021) 237 [`2008.08597`].

[98] F. Feruglio, *The Chiral approach to the electroweak interactions*, *Int. J. Mod. Phys. A* **8** (1993) 4937 [`hep-ph/9301281`].

[99] B. Grinstein and M. Trott, *A Higgs-Higgs bound state due to new physics at a TeV*, *Phys. Rev. D* **76** (2007) 073002 [`0704.1505`].

[100] P. Zerwas, ed., *Proceedings, Workshop on e^+e^- Collisions at 500 GeV: The Physics Potential, Part A: Munich, Germany, February 4, 1991*, (Hamburg, Germany), DESY, 1991. 10.3204/PUBDB-2016-05691.

[101] C. Friberg, *Gamma gamma physics at linear colliders*, in *Workshop on the Development of Future Linear Electron-Positron Colliders for Particle Physics Studies and for Research Using Free Electron Lasers*, pp. 241–247, 11, 1999, `hep-ph/9911444`.

[102] *The International Linear Collider Technical Design Report - Volume 1: Executive Summary*, `1306.6327`.

[103] *The International Linear Collider Technical Design Report - Volume 2: Physics*, `1306.6352`.

[104] ILC collaboration, *The International Linear Collider. A Global Project*, `1901.09829`.

[105] ILC INTERNATIONAL DEVELOPMENT TEAM collaboration, *The International Linear Collider: Report to Snowmass 2021*, `2203.07622`.

[106] CLICDP, CLIC collaboration, *The Compact Linear Collider (CLIC) - 2018 Summary Report*, `1812.06018`.

[107] CLIC, CLICDP collaboration, *The Compact Linear e^+e^- Collider (CLIC): Physics Potential*, `1812.07986`.

[108] CLIC ACCELERATOR collaboration, *The Compact Linear Collider (CLIC) - Project Implementation Plan*, `1903.08655`.

[109] O. Brunner et al., *The CLIC project*, `2203.09186`.

[110] M. Ahmad et al., *CEPC-SPPC Preliminary Conceptual Design Report. 1. Physics and Detector*, .

[111] *CEPC-SPPC Preliminary Conceptual Design Report. 2. Accelerator*, .

[112] CEPC PHYSICS STUDY GROUP collaboration, *The Physics potential of the CEPC. Prepared for the US Snowmass Community Planning Exercise (Snowmass 2021)*, in *Snowmass 2021*, 5, 2022, `2205.08553`.

[113] TLEP DESIGN STUDY WORKING GROUP collaboration, *First Look at the Physics Case of TLEP*, *JHEP* **01** (2014) 164 [`1308.6176`].

[114] FCC collaboration, *FCC-ee: The Lepton Collider: Future Circular Collider Conceptual Design Report Volume 2*, *Eur. Phys. J. ST* **228** (2019) 261.

[115] I. Agapov et al., *Future Circular Lepton Collider FCC-ee: Overview and Status*, in *Snowmass 2021*, 3, 2022, `2203.08310`.

[116] C. Aime et al., *Muon Collider Physics Summary*, `2203.07256`.

[117] Muon Collider collaboration, *The physics case of a 3 TeV muon collider stage*, 2203.07261.

[118] K. M. Black et al., *Muon Collider Forum Report*, 2209.01318.

[119] J. P. Delahaye, M. Diemoz, K. Long, B. Mansoulié, N. Pastrone, L. Rivkin et al., *Muon Colliders*, 1901.06150.

[120] D. Atwood and A. Soni, *Analysis for magnetic moment and electric dipole moment form-factors of the top quark via $e^+e^- \to t\bar{t}$*, *Phys. Rev. D* **45** (1992) 2405.

[121] M. Davier, L. Duflot, F. Le Diberder and A. Rouge, *The Optimal method for the measurement of tau polarization*, *Phys. Lett. B* **306** (1993) 411.

[122] M. Diehl and O. Nachtmann, *Optimal observables for the measurement of three gauge boson couplings in e^+e^- —> W^+W^-*, *Z. Phys. C* **62** (1994) 397.

[123] J. F. Gunion, B. Grzadkowski and X.-G. He, *Determining the $t\bar{t}$ and ZZ couplings of a neutral Higgs boson of arbitrary CP nature at the NLC*, *Phys. Rev. Lett.* **77** (1996) 5172 [hep-ph/9605326].

[124] A. Das, S. Mandal and T. Modak, *Testing triplet fermions at the electron-positron and electron-proton colliders using fat jet signatures*, *Phys. Rev. D* **102** (2020) 033001 [2005.02267].

[125] A. Das and S. Mandal, *Bounds on the triplet fermions in type-III seesaw and implications for collider searches*, *Nucl. Phys. B* **966** (2021) 115374 [2006.04123].

[126] L3 collaboration, *Search for heavy neutral and charged leptons in e^+e^- annihilation at LEP*, *Phys. Lett. B* **517** (2001) 75 [hep-ex/0107015].

[127] Particle Data Group collaboration, *Review of Particle Physics*, *Phys. Rev. D* **98** (2018) 030001.

[128] CMS collaboration, *Search for Evidence of the Type-III Seesaw Mechanism in Multilepton Final States in Proton-Proton Collisions at $\sqrt{s} = 13$ TeV*, *Phys. Rev. Lett.* **119** (2017) 221802 [1708.07962].

[129] CMS collaboration, *Searches for Long-Lived Charged Particles in pp Collisions at $\sqrt{s}$=7 and 8 TeV*, *JHEP* **07** (2013) 122 [1305.0491].

[130] ATLAS collaboration, *Search for electroweak production of charginos and sleptons decaying into final states with two leptons and missing transverse momentum in $\sqrt{s} = 13$ TeV pp collisions using the ATLAS detector*, *Eur. Phys. J. C* **80** (2020) 123 [1908.08215].

[131] ATLAS collaboration, *Searches for electroweak production of supersymmetric particles with compressed mass spectra in $\sqrt{s} = 13$ TeV pp collisions with the ATLAS detector*, *Phys. Rev. D* **101** (2020) 052005 [1911.12606].

[132] K. Hagiwara, S. Ishihara, J. Kamoshita and B. A. Kniehl, *Prospects of measuring general Higgs couplings at e^+e^- linear colliders*, *Eur. Phys. J. C* **14** (2000) 457 [hep-ph/0002043].

[133] S. Dutta, K. Hagiwara and Y. Matsumoto, *Measuring the Higgs-Vector boson Couplings at Linear e^+e^- Collider*, *Phys. Rev. D* **78** (2008) 115016 [`0808.0477`].

[134] B. Grzadkowski and Z. Hioki, *CP violating lepton energy correlation in e^-e^+ —> $t\bar{t}$*, *Phys. Lett. B* **391** (1997) 172 [`hep-ph/9608306`].

[135] B. Grzadkowski, Z. Hioki and M. Szafranski, *Four Fermi effective operators in top quark production and decay*, *Phys. Rev. D* **58** (1998) 035002 [`hep-ph/9712357`].

[136] B. Grzadkowski and Z. Hioki, *Probing top quark couplings at polarized NLC*, *Phys. Rev. D* **61** (2000) 014013 [`hep-ph/9805318`].

[137] B. Grzadkowski and J. Pliszka, *Testing top quark Yukawa interactions in e^+e^- —> $t\bar{t}Z$*, *Phys. Rev. D* **60** (1999) 115018 [`hep-ph/9907206`].

[138] B. Grzadkowski and Z. Hioki, *Optimal observable analysis of the angular and energy distributions for top quark decay products at polarized linear colliders*, *Nucl. Phys. B* **585** (2000) 3 [`hep-ph/0004223`].

[139] B. Grzadkowski, Z. Hioki, K. Ohkuma and J. Wudka, *Probing anomalous top quark couplings induced by dimension-six operators at photon colliders*, *Nucl. Phys. B* **689** (2004) 108 [`hep-ph/0310159`].

[140] B. Grzadkowski, Z. Hioki, K. Ohkuma and J. Wudka, *Optimal-observable analysis of possible new physics using the b quark in $\gamma\gamma$ —> $t\bar{t}$ —> bX*, *Phys. Lett. B* **593** (2004) 189 [`hep-ph/0403174`].

[141] B. Grzadkowski, Z. Hioki, K. Ohkuma and J. Wudka, *Optimal beam polarizations for new-physics search through $\gamma\gamma$ —> $t\bar{t}$ —> lX/bX*, *JHEP* **11** (2005) 029 [`hep-ph/0508183`].

[142] Z. Hioki, T. Konishi and K. Ohkuma, *Studying possible CP-violating Higgs couplings through top-quark pair productions at muon colliders*, *JHEP* **07** (2007) 082 [`0706.4346`].

[143] J. F. Gunion and J. Pliszka, *Determining the relative size of the CP even and CP odd Higgs boson couplings to a fermion at the LHC*, *Phys. Lett. B* **444** (1998) 136 [`hep-ph/9809306`].

[144] Z. Hioki and K. Ohkuma, *Optimal-observable Analysis of Possible Non-standard Top-quark Couplings in $pp- > t\bar{t}X- > l^+X'$*, *Phys. Lett. B* **716** (2012) 310 [`1206.2413`].

[145] Z. Hioki and K. Ohkuma, *Final charged-lepton angular distribution and possible anomalous top-quark couplings in $pp \to t\bar{t}X \to \ell^+X'$*, *Phys. Lett. B* **736** (2014) 1 [`1406.2475`].

[146] S. Bhattacharya, S. Nandi and S. K. Patra, *Optimal-observable analysis of possible new physics in $B \to D^{(*)}\tau\nu_\tau$*, *Phys. Rev. D* **93** (2016) 034011 [`1509.07259`].

[147] Z. Calcuttawala, A. Kundu, S. Nandi and S. K. Patra, *Optimal observable analysis for the decay $b \to s$ plus missing energy*, *Eur. Phys. J. C* **77** (2017) 650 [`1702.06679`].

[148] Z. Calcuttawala, A. Kundu, S. Nandi and S. Kumar Patra, *New physics with the lepton flavor violating decay $\tau \to 3\mu$*, Phys. Rev. D **97** (2018) 095009 [1802.09218].

[149] Q.-H. Cao and J. Wudka, *Search for new physics via single top production at TeV energy e gamma colliders*, Phys. Rev. D **74** (2006) 094015 [hep-ph/0608331].

[150] R. Vega and J. Wudka, *A Covariant method for calculating helicity amplitudes*, Phys. Rev. D **53** (1996) 5286 [hep-ph/9511318].

[151] S. Bhattacharya, N. Sahoo and N. Sahu, *Minimal vectorlike leptonic dark matter and signatures at the LHC*, Phys. Rev. D **93** (2016) 115040 [1510.02760].

[152] S. Bhattacharya, P. Ghosh, N. Sahoo and N. Sahu, *Mini Review on Vector-Like Leptonic Dark Matter, Neutrino Mass, and Collider Signatures*, Front. in Phys. **7** (2019) 80 [1812.06505].

[153] XENON collaboration, *Dark Matter Search Results from a One Ton-Year Exposure of XENON1T*, Phys. Rev. Lett. **121** (2018) 111302 [1805.12562].

[154] S. Bhattacharya, P. Ghosh and N. Sahu, *Multipartite Dark Matter with Scalars, Fermions and signatures at LHC*, JHEP **02** (2019) 059 [1809.07474].

[155] CMS collaboration, *Search for supersymmetry in final states with two oppositely charged same-flavor leptons and missing transverse momentum in proton-proton collisions at $\sqrt{s} = 13$ TeV*, JHEP **04** (2021) 123 [2012.08600].

[156] A. Alloul, N. D. Christensen, C. Degrande, C. Duhr and B. Fuks, *FeynRules 2.0 - A complete toolbox for tree-level phenomenology*, Comput. Phys. Commun. **185** (2014) 2250 [1310.1921].

[157] N. D. Christensen and C. Duhr, *FeynRules - Feynman rules made easy*, Comput. Phys. Commun. **180** (2009) 1614 [0806.4194].

[158] C. Degrande, *A basis of dimension-eight operators for anomalous neutral triple gauge boson interactions*, JHEP **02** (2014) 101 [1308.6323].

[159] A. Belyaev, N. D. Christensen and A. Pukhov, *CalcHEP 3.4 for collider physics within and beyond the Standard Model*, Comput. Phys. Commun. **184** (2013) 1729 [1207.6082].

[160] T. Sjostrand, S. Mrenna and P. Z. Skands, *PYTHIA 6.4 Physics and Manual*, JHEP **05** (2006) 026 [hep-ph/0603175].

[161] J. Alwall, R. Frederix, S. Frixione, V. Hirschi, F. Maltoni, O. Mattelaer et al., *The automated computation of tree-level and next-to-leading order differential cross sections, and their matching to parton shower simulations*, JHEP **07** (2014) 079 [1405.0301].

[162] D. Choudhury and S. D. Rindani, *Test of CP violating neutral gauge boson vertices in $e^+e^- \to \gamma Z$*, Phys. Lett. B **335** (1994) 198 [hep-ph/9405242].

[163] S. Atag and I. Sahin, *$ZZ\gamma$ and $Z\gamma\gamma$ couplings at linear $e^+ e^-$ collider energies with the effects of Z polarization and initial state radiation*, Phys. Rev. D **70** (2004) 053014 [hep-ph/0408163].

[164] I. Ots, H. Uibo, H. Liivat, R. Saar and R. K. Loide, *Possible anomalous $ZZ\gamma$ and $Z\gamma\gamma$ couplings and Z boson spin orientation in $e^+e^- \to Z\gamma$*, Nucl. Phys. B **702** (2004) 346.

[165] I. Ots, H. Uibo, H. Liivat, R. Saar and R. K. Loide, *Possible anomalous $ZZ\gamma$ and $Z\gamma\gamma$ couplings and Z boson spin orientation in $e^+e^- \to Z\gamma$: The role of transverse polarization*, Nucl. Phys. B **740** (2006) 212.

[166] A. Gutierrez-Rodriguez, M. A. Hernandez-Ruiz and M. A. Perez, *Probing the $ZZ\gamma$ and $Z\gamma\gamma$ Couplings Through the Process $e^+e^- \to \nu\bar{\nu}\gamma$*, Phys. Rev. D **80** (2009) 017301 [0808.0945].

[167] B. Ananthanarayan, S. K. Garg, M. Patra and S. D. Rindani, *Isolating CP-violating γ ZZ coupling in $e^+e^- \to \gamma$ Z with transverse beam polarizations*, Phys. Rev. D **85** (2012) 034006 [1104.3645].

[168] B. Ananthanarayan, J. Lahiri, M. Patra and S. D. Rindani, *New physics in $e^+e^- \to Z\gamma$ at the ILC with polarized beams: explorations beyond conventional anomalous triple gauge boson couplings*, JHEP **08** (2014) 124 [1404.4845].

[169] R. Rahaman and R. K. Singh, *On polarization parameters of spin-1 particles and anomalous couplings in $e^+e^- \to ZZ/Z\gamma$*, Eur. Phys. J. C **76** (2016) 539 [1604.06677].

[170] R. Rahaman and R. K. Singh, *On the choice of beam polarization in $e^+e^- \to ZZ/Z\gamma$ and anomalous triple gauge-boson couplings*, Eur. Phys. J. C **77** (2017) 521 [1703.06437].

[171] J. Ellis, S.-F. Ge, H.-J. He and R.-Q. Xiao, *Probing the scale of new physics in the $ZZ\gamma$ coupling at e^+e^- colliders*, Chin. Phys. C **44** (2020) 063106 [1902.06631].

[172] J. Ellis, H.-J. He and R.-Q. Xiao, *Probing new physics in dimension-8 neutral gauge couplings at e^+e^- colliders*, Sci. China Phys. Mech. Astron. **64** (2021) 221062 [2008.04298].

[173] U. Baur and E. L. Berger, *Probing the weak boson sector in $Z\gamma$ production at hadron colliders*, Phys. Rev. D **47** (1993) 4889.

[174] J. Ellison and J. Wudka, *Study of trilinear gauge boson couplings at the Tevatron collider*, Ann. Rev. Nucl. Part. Sci. **48** (1998) 33 [hep-ph/9804322].

[175] A. Senol, H. Denizli, A. Yilmaz, I. Turk Cakir, K. Y. Oyulmaz, O. Karadeniz et al., *Probing the Effects of Dimension-eight Operators Describing Anomalous Neutral Triple Gauge Boson Interactions at FCC-hh*, Nucl. Phys. B **935** (2018) 365 [1805.03475].

[176] A. Yilmaz, A. Senol, H. Denizli, I. Turk Cakir and O. Cakir, *Sensitivity on Anomalous Neutral Triple Gauge Couplings via ZZ Production at FCC-hh*, Eur. Phys. J. C **80** (2020) 173 [1906.03911].

[177] A. Senol, H. Denizli, A. Yilmaz, I. Turk Cakir and O. Cakir, *The projections on $ZZ\gamma$ and $Z\gamma\gamma$ couplings via $\nu\bar{\nu}\gamma$ production in HL-LHC and HE-LHC*, *Phys. Lett. B* **802** (2020) 135255 [`1910.03843`].

[178] A. Yilmaz, *Search for the limits on anomalous neutral triple gauge couplings via ZZ production in the $\ell\ell\nu\nu$ channel at FCC-hh*, *Nucl. Phys. B* **969** (2021) 115471 [`2102.01989`].

[179] R. Rahaman and R. K. Singh, *Anomalous triple gauge boson couplings in ZZ production at the LHC and the role of Z boson polarizations*, *Nucl. Phys. B* **948** (2019) 114754 [`1810.11657`].

[180] J. Ellis, H.-J. He and R.-Q. Xiao, *Probing Neutral Triple Gauge Couplings at the LHC and Future Hadron Colliders*, `2206.11676`.

[181] K. Hagiwara, R. D. Peccei, D. Zeppenfeld and K. Hikasa, *Probing the Weak Boson Sector in $e^+e^- \to W^+W^-$*, *Nucl. Phys. B* **282** (1987) 253.

[182] F. M. Renard, *Tests of Neutral Gauge Boson Selfcouplings With $e^+e^- \to \gamma Z$*, *Nucl. Phys. B* **196** (1982) 93.

[183] G. Gounaris, R. Kogerler and D. Schildknecht, *ON $Z0 - -- > e^+e^-\gamma$ DECAYS*, *Phys. Lett. B* **137** (1984) 261.

[184] G. Gounaris et al., *Triple gauge boson couplings*, in *AGS / RHIC Users Annual Meeting*, 1, 1996, `hep-ph/9601233`.

[185] G. J. Gounaris, J. Layssac and F. M. Renard, *Signatures of the anomalous Z_γ and ZZ production at the lepton and hadron colliders*, *Phys. Rev. D* **61** (2000) 073013 [`hep-ph/9910395`].

[186] A. I. Hernández-Juárez, A. Moyotl and G. Tavares-Velasco, *Contributions to ZZV^* $(V = \gamma, Z, Z')$ couplings from CP violating flavor changing couplings*, *Eur. Phys. J. C* **81** (2021) 304 [`2102.02197`].

[187] A. I. Hernández-Juárez and G. Tavares-Velasco, *Non-diagonal contributions to $Z\gamma V^*$ vertex and bounds on $Z\bar{t}q$ couplings*, `2203.16819`.

[188] Particle Data Group collaboration, *Review of Particle Physics*, *PTEP* **2022** (2022) 083C01.

[189] ATLAS collaboration, *Measurement of the $Z\gamma \to \nu\bar{\nu}\gamma$ production cross section in pp collisions at $\sqrt{s} = 13$ TeV with the ATLAS detector and limits on anomalous triple gauge-boson couplings*, *JHEP* **12** (2018) 010 [`1810.04995`].

[190] CMS collaboration, *Measurements of $\mathrm{pp} \to \mathrm{ZZ}$ production cross sections and constraints on anomalous triple gauge couplings at $\sqrt{s} = 13\,\mathrm{TeV}$*, *Eur. Phys. J. C* **81** (2021) 200 [`2009.01186`].

[191] DELPHES 3 collaboration, *DELPHES 3, A modular framework for fast simulation of a generic collider experiment*, *JHEP* **02** (2014) 057 [`1307.6346`].

[192] V. D. Barger, J. L. Hewett and R. J. N. Phillips, *New Constraints on the Charged Higgs Sector in Two Higgs Doublet Models*, *Phys. Rev. D* **41** (1990) 3421.

[193] Y. Grossman, *Phenomenology of models with more than two Higgs doublets*, *Nucl. Phys. B* **426** (1994) 355 [`hep-ph/9401311`].

[194] A. G. Akeroyd and W. J. Stirling, *Light charged Higgs scalars at high-energy e^+e^- colliders*, *Nucl. Phys. B* **447** (1995) 3.

[195] A. G. Akeroyd, *Nonminimal neutral Higgs bosons at LEP-2*, *Phys. Lett. B* **377** (1996) 95 [`hep-ph/9603445`].

[196] A. G. Akeroyd, *Fermiophobic and other nonminimal neutral Higgs bosons at the LHC*, *J. Phys. G* **24** (1998) 1983 [`hep-ph/9803324`].

[197] M. Aoki, S. Kanemura, K. Tsumura and K. Yagyu, *Models of Yukawa interaction in the two Higgs doublet model, and their collider phenomenology*, *Phys. Rev. D* **80** (2009) 015017 [`0902.4665`].

[198] L. Wang, J. M. Yang and Y. Zhang, *Two-Higgs-doublet models in light of current experiments: a brief review*, *Commun. Theor. Phys.* **74** (2022) 097202 [`2203.07244`].

[199] CMS collaboration, *Probing effective field theory operators in the associated production of top quarks with a Z boson in multilepton final states at $\sqrt{s}$ = 13 TeV*, *JHEP* **12** (2021) 083 [`2107.13896`].

[200] M. Krawczyk, N. Darvishi and D. Sokolowska, *The Inert Doublet Model and its extensions*, *Acta Phys. Polon. B* **47** (2016) 183 [`1512.06437`].

[201] J. Schechter and J. W. F. Valle, *Neutrino Decay and Spontaneous Violation of Lepton Number*, *Phys. Rev. D* **25** (1982) 774.

[202] M. Aoki, S. Kanemura and H. Yokoya, *Reconstruction of Inert Doublet Scalars at the International Linear Collider*, *Phys. Lett. B* **725** (2013) 302 [`1303.6191`].

[203] M. Hashemi, M. Krawczyk, S. Najjari and A. F. Żarnecki, *Production of Inert Scalars at the high energy e^+e^- colliders*, *JHEP* **02** (2016) 187 [`1512.01175`].

[204] J. Kalinowski, W. Kotlarski, T. Robens, D. Sokolowska and A. F. Zarnecki, *Benchmarking the Inert Doublet Model for e^+e^- colliders*, *JHEP* **12** (2018) 081 [`1809.07712`].

[205] J. Kalinowski, W. Kotlarski, T. Robens, D. Sokolowska and A. F. Zarnecki, *Exploring Inert Scalars at CLIC*, *JHEP* **07** (2019) 053 [`1811.06952`].

[206] A. Pierce and J. Thaler, *Natural Dark Matter from an Unnatural Higgs Boson and New Colored Particles at the TeV Scale*, *JHEP* **08** (2007) 026 [`hep-ph/0703056`].

[207] R. Aoude, T. Hurth, S. Renner and W. Shepherd, *The impact of flavour data on global fits of the MFV SMEFT*, *JHEP* **12** (2020) 113 [`2003.05432`].

[208] S. Bißmann, C. Grunwald, G. Hiller and K. Kröninger, *Top and Beauty synergies in SMEFT-fits at present and future colliders*, *JHEP* **06** (2021) 010 [2012.10456].

[209] J. Alda, J. Guasch and S. Penaranda, *Anomalies in B mesons decays: a phenomenological approach*, *Eur. Phys. J. Plus* **137** (2022) 217 [2012.14799].

[210] S. Bruggisser, R. Schäfer, D. van Dyk and S. Westhoff, *The Flavor of UV Physics*, *JHEP* **05** (2021) 257 [2101.07273].

[211] C. Grunwald, G. Hiller, K. Kröninger and L. Nollen, *More Synergies from Beauty, Top, Z and Drell-Yan Measurements in SMEFT*, 2304.12837.

[212] S. L. Glashow, J. Iliopoulos and L. Maiani, *Weak Interactions with Lepton-Hadron Symmetry*, *Phys. Rev. D* **2** (1970) 1285.

[213] S. Bibmann, J. Erdmann, C. Grunwald, G. Hiller and K. Kröninger, *Constraining top-quark couplings combining top-quark and $\boldsymbol{B}$ decay observables*, *Eur. Phys. J. C* **80** (2020) 136 [1909.13632].

[214] W. Altmannshofer, S. Gori, B. V. Lehmann and J. Zuo, *UV physics from IR features: New prospects from top flavor violation*, *Phys. Rev. D* **107** (2023) 095025 [2303.00781].

[215] V. Shiltsev and F. Zimmermann, *Modern and Future Colliders*, *Rev. Mod. Phys.* **93** (2021) 015006 [2003.09084].

[216] S. Bar-Shalom, G. Eilam, A. Soni and J. Wudka, *Probing the flavor changing tc vertex via tree level processes: e+ e- —> t anti-c electron-neutrino anti-electron-neutrino, t anti-c e+ e- and t —> c W+ W-*, *Phys. Rev. Lett.* **79** (1997) 1217 [hep-ph/9703221].

[217] S. Bar-Shalom, G. Eilam, A. Soni and J. Wudka, *Implications of a W+ W- (Z Z) - Higgs - t anti-c interaction for e+ e- —> t anti-c electron-neutrino anti-electron-neutrino, t anti-c e+ e-, t anti-c Z and for t —> c W+ W-, c Z Z in a two Higgs doublet model*, *Phys. Rev. D* **57** (1998) 2957 [hep-ph/9708358].

[218] S. Bar-Shalom and J. Wudka, *Flavor changing single top quark production channels at e+ e- colliders in the effective Lagrangian description*, *Phys. Rev. D* **60** (1999) 094016 [hep-ph/9905407].

[219] S. Sun, Q.-S. Yan, X. Zhao and Z. Zhao, *Constraining rare B decays by $\mu^+\mu^- \to tc$ at future lepton colliders*, *Phys. Rev. D* **108** (2023) 075016 [2302.01143].

[220] C. Bobeth, M. Misiak and J. Urban, *Photonic penguins at two loops and m_t dependence of $BR[B \to X_s l^+ l^-]$*, *Nucl. Phys. B* **574** (2000) 291 [hep-ph/9910220].

[221] W. Altmannshofer, P. Ball, A. Bharucha, A. J. Buras, D. M. Straub and M. Wick, *Symmetries and Asymmetries of $B \to K^* \mu^+ \mu^-$ Decays in the Standard Model and Beyond*, *JHEP* **01** (2009) 019 [0811.1214].

[222] J. Aebischer, A. Crivellin, M. Fael and C. Greub, *Matching of gauge invariant dimension-six operators for $b \to s$ and $b \to c$ transitions*, JHEP **05** (2016) 037 [1512.02830].

[223] S. Descotes-Genon, J. Matias, M. Ramon and J. Virto, *Implications from clean observables for the binned analysis of $B- > K * \mu^+\mu^-$ at large recoil*, JHEP **01** (2013) 048 [1207.2753].

[224] S. Descotes-Genon, T. Hurth, J. Matias and J. Virto, *Optimizing the basis of $B \to K^*ll$ observables in the full kinematic range*, JHEP **05** (2013) 137 [1303.5794].

[225] R. R. Horgan, Z. Liu, S. Meinel and M. Wingate, *Calculation of $B^0 \to K^{*0}\mu^+\mu^-$ and $B_s^0 \to \phi\mu^+\mu^-$ observables using form factors from lattice QCD*, Phys. Rev. Lett. **112** (2014) 212003 [1310.3887].

[226] A. Bharucha, D. M. Straub and R. Zwicky, *$B \to V\ell^+\ell^-$ in the Standard Model from light-cone sum rules*, JHEP **08** (2016) 098 [1503.05534].

[227] A. Biswas, S. Nandi, S. K. Patra and I. Ray, *New physics in $b \to \ell\ell$ decays with complex wilson coefficients*, Nucl. Phys. B **969** (2021) 115479 [2004.14687].

[228] CDF collaboration, *Measurements of the Angular Distributions in the Decays $B \to K^{(*)}\mu^+\mu^-$ at CDF*, Phys. Rev. Lett. **108** (2012) 081807 [1108.0695].

[229] LHCb collaboration, *Measurement of the CP asymmetry in $B^+ \to K^+\mu^+\mu^-$ decays*, Phys. Rev. Lett. **111** (2013) 151801 [1308.1340].

[230] LHCb collaboration, *Differential branching fractions and isospin asymmetries of $B \to K^{(*)}\mu^+\mu^-$ decays*, JHEP **06** (2014) 133 [1403.8044].

[231] LHCb collaboration, *Test of lepton universality using $B^+ \to K^+\ell^+\ell^-$ decays*, Phys. Rev. Lett. **113** (2014) 151601 [1406.6482].

[232] LHCb collaboration, *Angular analysis of the $B^0 \to K^{*0}\mu^+\mu^-$ decay using 3 fb^{-1} of integrated luminosity*, JHEP **02** (2016) 104 [1512.04442].

[233] Belle collaboration, *Lepton-Flavor-Dependent Angular Analysis of $B \to K^*\ell^+\ell^-$*, Phys. Rev. Lett. **118** (2017) 111801 [1612.05014].

[234] CMS collaboration, *Measurement of angular parameters from the decay $\mathrm{B}^0 \to \mathrm{K}^{*0}\mu^+\mu^-$ in proton-proton collisions at $\sqrt{s} = 8$ TeV*, Phys. Lett. B **781** (2018) 517 [1710.02846].

[235] ATLAS collaboration, *Angular analysis of $B_d^0 \to K^*\mu^+\mu^-$ decays in pp collisions at $\sqrt{s} = 8$ TeV with the ATLAS detector*, JHEP **10** (2018) 047 [1805.04000].

[236] LHCb collaboration, *Angular Analysis of the $B^+ \to K^{*+}\mu^+\mu^-$ Decay*, Phys. Rev. Lett. **126** (2021) 161802 [2012.13241].

[237] LHCb collaboration, *Branching Fraction Measurements of the Rare $B_s^0 \to \phi\mu^+\mu^-$ and $B_s^0 \to f_2'(1525)\mu^+\mu^-$- Decays*, Phys. Rev. Lett. **127** (2021) 151801 [2105.14007].

[238] LHCb collaboration, *Test of lepton universality in $b \to s\ell^+\ell^-$ decays*, *Phys. Rev. Lett.* **131** (2023) 051803 [2212.09152].

[239] LHCb collaboration, *Measurement of lepton universality parameters in $B^+ \to K^+\ell^+\ell^-$ and $B^0 \to K^{*0}\ell^+\ell^-$ decays*, *Phys. Rev. D* **108** (2023) 032002 [2212.09153].

[240] A. V. Rusov, *Probing New Physics in $b \to d$ transitions*, *JHEP* **07** (2020) 158 [1911.12819].

[241] R. Bause, H. Gisbert, M. Golz and G. Hiller, *Model-independent analysis of $b \to d$ processes*, *Eur. Phys. J. C* **83** (2023) 419 [2209.04457].

[242] G. Isidori and R. Unterdorfer, *On the short distance constraints from K(L,S) —> mu+ mu-*, *JHEP* **01** (2004) 009 [hep-ph/0311084].

[243] V. Chobanova, G. D'Ambrosio, T. Kitahara, M. Lucio Martinez, D. Martinez Santos, I. S. Fernandez et al., *Probing SUSY effects in $K^0_S \to \mu^+\mu^-$*, *JHEP* **05** (2018) 024 [1711.11030].

[244] G. D'Ambrosio, A. M. Iyer, F. Mahmoudi and S. Neshatpour, *Anatomy of kaon decays and prospects for lepton flavour universality violation*, *JHEP* **09** (2022) 148 [2206.14748].

[245] J. S. Hagelin, *Mass Mixing and CP Violation in the $B^0 - \bar{B}^0$ system*, *Nucl. Phys. B* **193** (1981) 123.

[246] A. Ali and C. Jarlskog, *Signatures of $B(s)0$ $\bar{B}(s)0$ Mixings in $p\bar{p}$ and e^+e^- Collisions*, *Phys. Lett. B* **144** (1984) 266.

[247] L.-L. Chau and W.-Y. Keung, *Implications From the b Decay Measurements*, *Phys. Rev. D* **29** (1984) 592.

[248] FLAVOUR LATTICE AVERAGING GROUP (FLAG) collaboration, *FLAG Review 2021*, *Eur. Phys. J. C* **82** (2022) 869 [2111.09849].

[249] C. Gay, *B mixing*, *Ann. Rev. Nucl. Part. Sci.* **50** (2000) 577 [hep-ex/0103016].

[250] D. Becirevic, N. Kosnik, F. Mescia and E. Schneider, *Complementarity of the constraints on New Physics from $B_s \to \mu^+\mu^-$ and from $B \to Kl^+l^-$ decays*, *Phys. Rev. D* **86** (2012) 034034 [1205.5811].

[251] CMS, LHCb collaboration, *Observation of the rare $B^0_s \to \mu^+\mu^-$ decay from the combined analysis of CMS and LHCb data*, *Nature* **522** (2015) 68 [1411.4413].

[252] V. Cirigliano, G. Ecker, H. Neufeld, A. Pich and J. Portoles, *Kaon Decays in the Standard Model*, *Rev. Mod. Phys.* **84** (2012) 399 [1107.6001].

[253] G. Buchalla and A. J. Buras, *The rare decays $K \to \pi\nu\bar{\nu}$, $B \to X\nu\bar{\nu}$ and $B \to l^+l^-$: An Update*, *Nucl. Phys. B* **548** (1999) 309 [hep-ph/9901288].

[254] G. Buchalla, A. J. Buras and M. E. Lautenbacher, *Weak decays beyond leading logarithms*, *Rev. Mod. Phys.* **68** (1996) 1125 [hep-ph/9512380].

[255] L.-S. Geng, J. M. Camalich and R.-X. Shi, *New physics in $s \to d$ semileptonic transitions: rare hyperon vs. kaon decays*, *JHEP* **02** (2022) 178 [`2112.11979`].

[256] A. Buras, *Gauge Theory of Weak Decays*. Cambridge University Press, 6, 2020, 10.1017/9781139524100.

[257] I. Ray and S. Nandi, *Test of new physics effects in $\bar{B} \to (D^{(*)}, \pi)\ell^- \bar{\nu}_\ell$ decays with heavy and light leptons*, `2305.11855`.

[258] Y. Sakaki, M. Tanaka, A. Tayduganov and R. Watanabe, *Testing leptoquark models in $\bar{B} \to D^{(*)}\tau\bar{\nu}$*, *Phys. Rev. D* **88** (2013) 094012 [`1309.0301`].

[259] S. Bhattacharya, S. Nandi and S. Kumar Patra, *$b \to c\tau\nu_\tau$ Decays: a catalogue to compare, constrain, and correlate new physics effects*, *Eur. Phys. J. C* **79** (2019) 268 [`1805.08222`].

[260] Z.-R. Huang, Y. Li, C.-D. Lu, M. A. Paracha and C. Wang, *Footprints of New Physics in $b \to c\tau\nu$ Transitions*, *Phys. Rev. D* **98** (2018) 095018 [`1808.03565`].

[261] D. Bečirević, F. Jaffredo, A. Peñuelas and O. Sumensari, *New Physics effects in leptonic and semileptonic decays*, *JHEP* **05** (2021) 175 [`2012.09872`].

[262] ATLAS collaboration, *Search for flavour-changing neutral current top-quark decays $t \to qZ$ in proton-proton collisions at $\sqrt{s} = 13$ TeV with the ATLAS detector*, *JHEP* **07** (2018) 176 [`1803.09923`].

[263] G. Ecker, A. Pich and E. de Rafael, *Radiative Kaon Decays and CP Violation in Chiral Perturbation Theory*, *Nucl. Phys. B* **303** (1988) 665.

[264] G. Ecker, A. Pich and E. de Rafael, *K —> pi Lepton+ Lepton- Decays in the Effective Chiral Lagrangian of the Standard Model*, *Nucl. Phys. B* **291** (1987) 692.

[265] E. Golowich, J. Hewett, S. Pakvasa and A. A. Petrov, *Relating D0-anti-D0 Mixing and D0 —> l+ l- with New Physics*, *Phys. Rev. D* **79** (2009) 114030 [`0903.2830`].

[266] KTeV collaboration, *Search for the rare decay K(L) —> pi0 e+ e-*, *Phys. Rev. Lett.* **93** (2004) 021805 [`hep-ex/0309072`].

[267] KTEV collaboration, *Search for the Decay $K_L \to \pi^0\mu^+\mu^-$*, *Phys. Rev. Lett.* **84** (2000) 5279 [`hep-ex/0001006`].

[268] LHCb collaboration, *Search for Rare Decays of D0 Mesons into Two Muons*, *Phys. Rev. Lett.* **131** (2023) 041804 [`2212.11203`].

[269] ATLAS collaboration, *Search for flavour-changing neutral currents in processes with one top quark and a photon using 81 fb^{-1} of pp collisions at $\sqrt{s} = 13$ TeV with the ATLAS experiment*, *Phys. Lett. B* **800** (2020) 135082 [`1908.08461`].

[270] J. Duan, Y. Gao, C.-Y. Ji, S. Sun, Y. Yao and Y.-L. Zhang, *Resonant electric probe to axionic dark matter*, *Phys. Rev. D* **107** (2023) 015019 [`2206.13543`].

[271] M. Cacciari, G. P. Salam and G. Soyez, *FastJet User Manual*, *Eur. Phys. J. C* **72** (2012) 1896 [`1111.6097`].

[272] M. Cacciari, G. P. Salam and G. Soyez, *The anti-k_t jet clustering algorithm*, *JHEP* **04** (2008) 063 [0802.1189].

[273] ATLAS collaboration, *Performance and Calibration of the JetFitterCharm Algorithm for c-Jet Identification*, .

[274] CMS collaboration, *Identification of c-quark jets at the CMS experiment*, .

[275] S. Bhattacharya, S. Jahedi and J. Wudka, *Probing heavy charged fermions at e^+e^- collider using the optimal observable technique*, *JHEP* **05** (2022) 009 [2106.02846].

[276] L. Holmstrom, S. R. Sain and H. E. Miettinen, *A New multivariate technique for top quark search*, *Comput. Phys. Commun.* **88** (1995) 195.

[277] TMVA collaboration, *TMVA - Toolkit for Multivariate Data Analysis*, physics/0703039.

[278] H. Voss, A. Hocker, J. Stelzer and F. Tegenfeldt, *TMVA, the Toolkit for Multivariate Data Analysis with ROOT*, *PoS* **ACAT** (2007) 040.

[279] P. C. Bhat, *Multivariate Analysis Methods in Particle Physics*, *Ann. Rev. Nucl. Part. Sci.* **61** (2011) 281.

[280] Do collaboration, *A precision measurement of the mass of the top quark*, *Nature* **429** (2004) 638 [hep-ex/0406031].

[281] Do collaboration, *Helicity of the W boson in lepton + jets $t\bar{t}$ events*, *Phys. Lett. B* **617** (2005) 1 [hep-ex/0404040].

[282] F. Fiedler, A. Grohsjean, P. Haefner and P. Schieferdecker, *The Matrix Element Method and its Application in Measurements of the Top Quark Mass*, *Nucl. Instrum. Meth. A* **624** (2010) 203 [1003.1316].

[283] P. Artoisenet, V. Lemaitre, F. Maltoni and O. Mattelaer, *Automation of the matrix element reweighting method*, *JHEP* **12** (2010) 068 [1007.3300].

[284] A. Celis, J. Fuentes-Martin, A. Vicente and J. Virto, *DsixTools: The Standard Model Effective Field Theory Toolkit*, *Eur. Phys. J. C* **77** (2017) 405 [1704.04504].